Evaluation of Platinum Nanoparticles on Human Platelets

Pushpa Patel

A thesis submitted to

The University of Birmingham for the degree of

DOCTOR OF PHILOSOPHY

Centre for Doctoral Training in Fuel Cells and their Fuels

School of Chemical Engineering

College of Engineering and Physical Sciences

University of Birmingham

November 2023

Abstract

Platinum nanoparticles (PtNPs) are the key catalyst of proton exchange membrane fuel cells (PEMFC); however, their degradation may pose a potential health risk if they are inhaled and translocate across the lungs gaining access to the bloodstream, where they will encounter platelets. Platelets are critical to the cardiovascular system where they maintain haemostasis (leading to cessation of bleeding). On the other hand, excessive activation of platelets underlies a variety of thrombotic diseases including ischaemic stroke and heart attack. Activation of platelets has been observed by nanoparticles including diesel exhaust particles *in vitro*, nonetheless, not much is known on how the physicochemical properties of the nanoparticles influence platelet activation. This thesis aims to create an array of PtNPs exhibiting negative, positive, and neutral charges, and to investigate their ability to induce activation of human platelets including aggregation. Citrate capped PtNPs were synthesised and characterised by TEM, DLS, zeta potential and XPS for size, surface charge and surface composition. Alkane and polyethylene glycol (PEG) thiols and other surface modifying compounds were used to functionalise these PtNPs to exhibit negative, positive, and neutral charges via ligand exchange and synthesis methods. Following characterisation, functionalisation of PtNPs was met with varying degrees of success. It was revealed the negatively and neutrally charged PtNPs were only partially functionalised by the alkane and PEGylated thiols. Positively charged PtNPs were found to be unstable. Albeit these partially functionalised PtNPs were assessed in platelet activation and aggregation. Negatively charged and neutrally charged PtNPs were unable to induce platelet aggregation, while platelet aggregation was observed by citrate capped PtNP. Platelet aggregation was found to be influenced by the zeta potential of PtNPs.

Acknowledgements

Firstly, I would like to express my infinite gratitude to my supervisor Professor Paula Mendes for taking a chance on me when I decided to change my discipline and enter the exciting world of nanotechnology. Thank you for giving me creative freedom, which in turn has given me great confidence as a scientist. Your continuous support and guidance has been invaluable. To my second supervisor Professor Steve Watson, thank you for all of your expertise and guidance with the platelet work. Likewise, thank you for coming into the lab and telling bad jokes, it was never the `thyme or plaice'.

A special thank you to the past and present members of the Mendes group that have supported me and have been part of this journey, Craig, Francia, Marcos, Nasim, Josh, Barbara, Dario, Laura, Charlie, Miguel, Terri-Anne, Hannah, Daniel C, Daniel K, Julian, Imen, Sona, Santino, and Thorben. My favourite moments with you have been our karaoke sessions.

To my friends and colleagues in the Fuel Cell labs, a huge thank you to Abu, Zeyu, Pete, Bhargav, Naser, Abdul, Chris H, Sam E, Yousif, Elvin and Ahmed. Thank you for all the entertaining moments, especially at JESS.

In the Birmingham Platelet lab, I am especially grateful to Gina and Rich, thank you for all your kindness and help with ploughing out the experiments. Thank you to Pip for providing antibodies and noticing my safety goggles, to Lourdes for helping me with the initial platelet experiments and Beata for your kindness and support.

In the School of Chemical Engineering, I would like to thank Elaine Mitchell, Dave Boylen and Lynne Draper for helping me get started. I would also like to thank Zoe Simon and Adam McCabe for all their help and support especially with the last experiment. A special thank you to Andy Ingram, Matt Keith, Claire Moran, and Eddie Pelan for all the lovely chats.

I would like to thank the lovely friends I've made in Chemical Engineering, Nicole Rosik for all our corridor chats and coffees, Aneesa Nabi for all your positive energy and encouragement, Jarrod Thomas for all the coffee morning chats during my brief stint in Biochem Eng. A very special thank you to Dan Baiocco for being welcoming since the very beginning of my PhD.

In the School of Chemistry, I would like to thank Michael Butlin and Owen Jones (Mowen) for all the monthly gastronomic outings with Abu.

I would like to express my gratitude to Dr Nicholas Davidson in the School of Geography for allowing me to work out of hours to complete all my experiments. In the School of Physics, thank you to Munir Ahmed (Chow) for all his unconditional help and wise words of wisdom. Additionally, I would like to thank Ian Bodfish and Brian Thomas in Mech Eng stores for their constant banter.

A very special thank you to Natalie Allock at the University of Leicester's Electron Microscopy Facility, your continuous support and advice with TEM imaging has been invaluable. Equally, to Dr Mark Isaacs at Harwell XPS, thank you for all your expertise and constant help with XPS fittings.

To Dr Melissa Grant in the School of Dentistry, thank you for offering me employment, I am forever grateful for your support, advice, and kindness. Your willingness to help others is inspiring.

To my beautiful friends who are dotted far and wide, Chris A, Bhav, Chiara, Richard and Kimmy, thank you all for your constant encouragement and being supportive throughout this PhD.

Finally, I would like to say a special thank you to my family. Dad, thank you for always supporting my decisions and being there for me. Also, thank you for coming to visit me for our breakfast catch ups at the Country girl in Selly Oak. To my sisters Prethi and Bhav, thanks for the constant support throughout this PhD, especially during the challenging moments. Rish, thank you for the banter and Diya thank you for making me smile with your cheeky antics. Thank you for being so patient with me, I promise no more degrees.

And thank you, for reading this far.

Good luck with the rest!

Dedication

To my friend, the `Queen'

Dr Margret Goodall

(1943-2022)

It was an honour to have worked with you,

miss your wicked sense of humour.

`I am inevitable.' Thanos

`And I am Iron Man.' Tony Stark

COVID statement

My PhD research was affected by the COVID-19 pandemic and limited my access to laboratories; therefore, I was unable to complete the original planned experiments. As a result, I was unable to conduct functionalisation experiments at different time points and I was not able to optimise nanoparticle synthesis conditions for subsequent functionalisation experiments.

Abbreviations

ACD	Acid-citrate-dextrose
ADP	Adenosine diphosphate
AgNP	Silver nanoparticle
ApoE	Apolipoprotein E
AuNP	Gold nanoparticle
AuNR	Gold nanoparticle
AuNP-S-AB	Gold nanoparticle- thioabiraterone
CLEC-2	C-type lectin 2
CSH	Cysteamine hydrochloride
DEA	2-Diethylaminoethanethiol
DEP	Diesel exhaust particle
DLS	Dynamic light scattering
DMSO	Dimethyl sulfoxide
DT	1-Decanethiol
DTT	1-Dodecanethiol
DVLO	Derjaguin, Landau, Verwey and Overbeek
ECL	Enhanced chemiluminescence
EDL	Electric double layer
EDX	Energy dispersive X-ray
EGTA	(Ethylene glycol-bis(β-aminoethyl ether)-*N*,*N*,*N*′,*N*′-tetraacetic acid)
FEG-SEM	Field emission gun scanning electron microscopy

GPVI	Glycoprotein IV
$H_2PtCl_6.6H_2O$	Chloroplatinic acid hexahydrate
HOR	Hydrogen oxidation reaction
HSA	Human serum albumin
ICP-MS	Inductively coupled plasma mass spectrometry
LDH	Lactate dehydrogenase
LiTEBH	Lithium triethylborohydride
LTA	Light transmission aggregometry
MMP-1	Matrix metalloproteinase-1
MTS	(2,3-Bis-(2-Methoxy-4-nitro-5-sulfophenyl)-2H-tetrazolium-5-carboxanilide)
MTT	3-(4,5-Dimethylthiazol-2-yl)-2,5-diphenyltetrazolium bromide
NiONP	Nickel oxide nanoparticle
ORR	Oxidation reduction reaction
ODT	Octandecanethiol
OT	1-Octanethiol
PBS	Phosphate buffered saline
PDI	Polydispersity index
PEG	Polyethylene glycol
PEI	Polyethylenimine
PEMFC	Proton exchange membrane fuel cells
PGI_2	Prostacyclin
PPh_3	Triphenylphosphine
PP2	1-Tert-Butyl-3-(4-chlorophenyl)-1H-pyrazolo[3.4-d]pyrimidin-4-amine

PRP	Platelet rich plasma
PRT-060318	2-(((1R,2S)-2-aminocyclohexyl)amino)-4-(m-tolylamino)pyrimidine-5-carboxamide
PsNP	Polystyrene nanoparticle
PtNP	Platinum nanoparticle
PVDF	Polyvinylidene difluoride
RT-PCR	Real-time polymerase chain reaction
S-AB	Thiobiraterone
SAM	Self-assembled monolayer
SDS-PAGE	Sodium dodecyl sulphate polyacrylamide gel electrophoresis
SHS	Second-harmonic light scattering
SiNP	Silica nanoparticle
SPION	Superparamagnetic iron oxide nanoparticle
TA	Thioctic acid
TBST	Tris buffered saline-Tween
TEM	Transmission electron microscopy
THF	Tetrahydrofuran
TiONP	Titanium oxide nanoparticle
VWF	von Willebrand factor
XPS	X-ray photoelectron spectroscopy
2-MEE	2-{2-[2-(2-Mercaptoethoxy)ethoxy]ethoxy}ethanol
2-MOHA	O-(2-Carboxyethyl)-O'-(2-mercaptoethyl)heptaethylene glycol
2-PF	2-Photon fluorescence

3-MPS	3-Mercapto-1-propanesulfonic acid
3-MTP	3-Mercaptopropionate
6-AHT	6-Amino-1-Hexanethiol
6-MHA	6-Mercaptohexanoic acid
6-MCH	6-Mercapto-1-hexanol
6-ATA	(6-Aminohexyl)trimethylammonium
8-MOA	8-Mercaptoctanoic acid
11-AUT	11-Amino-1-undecanethiol hydrochloride
11-MUDA	11-Mercaptoundecanoic acid
11-MUHEG	11-Mercaptoundecyl)hexa(ethylene glycol)
11-MABr	(11-Mercaptoundecyl)-N,N,N-trimethylammonium bromide
16-MHDA	16-Mercaptohexadecanoic acid

Contents

Chapter 1 Introduction 1

1.1 Nanotechnology 1

1.2 Applications in Nanotechnology 2

1.3 Synthesis and functionalised nanoparticles 6

1.4 Nanoparticles for biological interactions 18

1.5 Health risk of nanoparticles 25

1.6 Platelets 28

1.7 Concluding remarks 37

1.8 Aims 37

1.9 Hypothesis 38

Chapter 2 Theory of Experimental Techniques 39

2.1 Physicochemical characterisation 40

2.2 Physiological and biochemical assays 50

Chapter 3 Materials and Methods 54

3.1 Materials & Chemicals 54

3.2 Platinum nanoparticle synthesis 54

3.3 Functionalisation of PtNP 56

3.4 Nanoparticle characterisation 61

3.5 Physiological and biochemical assays 64

Chapter 4 Synthesis and Characterisation of Platinum Nanoparticles 70

4.1 Introduction 71

4.2 Results and Discussion 73

4.3 Conclusion 95

Chapter 5 Functionalisation of Platinum Nanoparticles with Negatively Charged Thiol Compounds 97

5.1 Introduction 98

5.2 Results and Discussion 100

5.3 Conclusion 139

5.4 Further work 139

Chapter 6 Synthesis and Functionalisation of Positively Charged Platinum Nanoparticles ... 141

6.1 Introduction 142

6.2 Results and Discussion 144

6.3 Conclusion 164

Chapter 7 Functionalisation of Platinum Nanoparticles with Neutrally Charged Thiol Compounds 167

7.1 Introduction 168

7.2 Results and Discussion 170

7.3 Conclusion 199

7.4 Further work 200

Chapter 8 Platinum Nanoparticle Human Platelet Interactions 201

8.1 Introduction 202

8.2 Results and Discussion 204

8.1 Conclusions 227

8.2 Further work 228

Chapter 9 Conclusions 230

and Future Work 230

9.1 Conclusions 230

9.2 Further work 234

Chapter 10 References 236

Chapter 11 Appendix 254

11.1 Platinum nanoparticles surface area calculations 254

11.2 Surface coverage of nanoparticles by alkanethiols calculations 259

11.3 PtNP preparation for platelet experiments 264

List of Figures

Figure 1.1 Applications of nanotechnology. Nanotechnology has been applied in various different fields, these include medicine, fuel cells, electronics, industrial, environmental and food agriculture. 2

Figure 1.2 Platinum nanoparticles as catalysts for proton exchange membrane fuel cells. PtNPs of 3 – 5 nm on carbon black are located on the anode and cathode of the PEMFC and catalyse both hydrogen oxidation reaction (HOR) and the oxygen reduction reaction (ORR). 6

Figure 1.3 Illustration of top-down and bottom-up approaches for nanoparticle synthesis. Top-down approaches involve physical methods such as laser ablation or chemical etching. Bottom-down approaches use chemical synthesis methods such as chemical synthesis or sol-gel. 7

Figure 1.4 Seed mediated synthesis for metallic nanoparticles. (a) metallic seed synthesis, (b) metallic nanoparticle synthesis and (c) capping agents' sodium citrate and thiols. 9

Figure 1.5 Self-assembled monolayer monomer structure on a gold substrate. (a) a typical SAM monomer exhibits a head group that binds to the substrate, a chain which is the spacer and a functional group. (b) an alkanethiol SAM monomer has a mercapto group which binds to the gold substrate, an alkanethiol chain and a functional group with a negative charge. 11

Figure 1.6 Phases of self-assembled monolayer formation by the alkanethiol 6-mercaptohexanoic acid (6-MHA) on a gold substrate. (a) Physisorption of 6-MHA, (b) chemisorption of 6-MHA and (c) rearrangement of 6-MHA. 12

Figure 1.7 Protein corona. Proteins with a high binding affinity bind onto the nanoparticle surface first to form a hard corona, this is followed by proteins with a low binding affinity which form a soft corona. 22

Figure 1.8. Degradation mechanism of platinum nanoparticles in proton exchange membrane fuel cells. (a) carbon corrosion, (b) platinum dissolution and (c) migration and sintering.....26

Figure 1.9 Haemostatic plug. At the site of vessel injury, platelets are recruited to exposed collagen and endothelial cells to form a haemostatic plug with fibrin. As the platelets become activated, they transform from their resting state and change shape, when they are fully aggregated, they form projections. 29

Figure 1.10 Activation of platelets by nanoparticles. Platelets have been shown to be activated by numerous nanoparticles of different materials, morphologies and size, these include gold, silver, carbon nanotubes and polystyrene nanoparticles. 31

Figure 1.11 Platelet surface receptors. There are several main platelet receptors expressed on the surface of platelets that have differing structures, these include GPVI, integrin αIIbβ3, Clec-2, PEAR-1, and G protein-coupled receptors PAR1, PAR4, P2Y1 and P2Y12. 36

Figure 2.1 Overview of experimental techniques employed for the physicochemical characterisation of PtNPs and the physiological and biochemical assays used to assess the PtNP-platelet interactions. 40

Figure 2.2 A typical transmission electron microscopy set up. The prepared TEM grid sample is placed into the instrument, a high energy beam of electrons is fired and then passed through a series of electromagnetic lenses, and the images are projected onto a fluorescent screen. 41

Figure 2.3 A dynamic light scattering set up. The helium laser hits the sample cuvette containing the colloidal particles and produces a scattered light intensity profile which then passes through a correlator creating a histogram of the data. 43

Figure 2.4 A zeta potential representation. Zeta potential measures the electric potential difference from the nanoparticle surface to the edge of the slipping plane which together make the EDL. 44

Figure 2.5 A typical zeta potential set up. Zeta potential is measured using a helium laser that splits into a reference and incident beam, the incident beam continues passing through the attenuator and then the folded capillary cell to enable zeta potential measurements. The optics of both beams are combined and pass to a detector which relays the data to the digital signal process to give the zeta potential data. 45

Figure 2.6 Zeta potential magnitude. Zeta potential values indicate colloidal stability of particles. 46

Figure 2.7 A gel electrophoresis set up. The agarose gel matrix and the voltage applied allow the separation of nucleic acids at different molecular weights. 47

Figure 2.8 A typical X-ray photoelectron spectroscopy set up. A sample is positioned onto a platform within an ultra-high vacuum chamber. Monochromatic Kα X-rays produced from either magnesium or aluminium probes is directed onto the sample causing an ejection of photoelectrons. These photoelectrons are collected by the electron lens and detector to create an XPS spectra of the sample. 48

Figure 2.9 Photoelectron emission. (a) The sample is bombarded with an X-ray causing the emission of a photoelectron from 1s2 orbital. (b) An electron from a higher energy will occupy the vacancy generating an energy release. This energy will either be released as an X-ray or an Auger electron. 49

Figure 2.10 Light transmission aggregometry of platelets. An increased light transmission is observed as platelets activated and finally aggregated; this is demonstrated by the aggregation trace. 51

Figure 2.11 Western blotting overview. (a) Protein lysates are produced from cells ready for electrophoresis using lysis buffers, (b) proteins are separated by their molecular weight using electrophoresis, (c) separated proteins are transferred to a PVDF membrane by electroblotting, (d) the membrane is blocked and incubated with a primary antibody specific to the protein of interest followed by a secondary antibody conjugated to enzyme or fluorescent probe and (e) finally an X-ray film is exposed onto the PVDF membrane to detect the protein of interest. ..53

Figure 3.1 Aggregation stimulation timeline. 67

Figure 4.1 Overview of PtNP synthesis. (a) Pt seeds are synthesised by the reduction of ($H_2PtCl_6.6H_2O$) with sodium borohydride, (b) the Pt seeds are used as template to grow larger PtNPs using a milder reducing agent L-ascorbic acid. 73

Figure 4.2 Pt seed characterisation of the 50 mL reaction. (a) synthesis of Pt seeds by the reduction of $H_2PtCl_6.6H_2O$, (b) Pt seeds after synthesis reaction, (c), (d) & (e) TEM images (f), particle size distribution from TEM, (g) particle size intensity by DLS, representative of 1 measurement (h) Pt seeds after centrifugation. Results presented from 1 synthesis reaction (n=1). 75

Figure 4.3 Pt seed synthesis characterisation of 5x reaction scale. (a) - (c) TEM images (d), particle size distribution and (e) particle size intensity by DLS, representative of 1 measurement. Results presented from 1 synthesis reaction (n=1). 77

Figure 4.4 Characterisation of 20 nm c-PtNPs. (a-d) TEM images from each reaction scale, (e-h) particle size distribution from each reaction scale, (i) average diameters by TEM, (j) average

hydrodynamic diameters & (k) average zeta potentials. Results presented from 1 synthesis reaction for each reaction scale (n=1). 79

Figure 4.5 Characterisation of 60 nm c-PtNP. (a-d) TEM images from each reaction scale, (e-h) particle size distribution from each reaction scale, (i) average diameters by TEM, (j) average hydrodynamic diameters & (k) average zeta potentials. Results presented from 1 synthesis reaction for each reaction scale (n=1). 82

Figure 4.6 Characterisation of 20 c-PtNP synthesised from four batches. (a-d) TEM images from each reaction batch, (e-h) particle size distribution from each batch, (i) average diameters by TEM, (j) average hydrodynamic diameters & (k) average zeta potentials. Results presented from 4 synthesis reactions (n=1 per batch synthesised). 85

Figure 4.7 High-resolution XPS spectra of a copper substrate. (a) oxidised copper substrate and (b) reduced copper substrate using hydrogen and nitrogen gases. 87

Figure 4.8 High-resolution XPS spectra of a copper substrate and c-PtNPs on a copper substrate. (a) Pt 4f - Cu substrate, (b) Pt 4f – c-PtNPs on Cu substrate, (c) Cu 2p - Cu substrate, (d) Cu 2p – c-PtNPs on Cu substrate, (e) C 1s - Cu substrate, (f) C 1s – c-PtNPs on Cu substrate, (g) O 1s - Cu substrate and (h) O 1s – c-PtNPs on Cu substrate (n=1). 90

Figure 4.9 Structure of citrate ion with different carbon and oxygen species. 91

Figure 4.10 c-PtNP physiological buffer interactions. (a) hydrodynamic diameters and (b) zeta potentials & (c) c-PtNPs in Tyrodes-HEPES buffer and (d) c-PtNPs in PBS. Results presented from 3 experiments (n=3) and presented as mean ± SD. 94

Figure 5.1 Negatively charged carboxyl-terminated alkanethiols. (a) 6-mercaptohexanoic acid (6-MHA), (b) 8-mercaptooctanoic acid (8-MOA) and (c) thioctic acid (TA). 100

Figure 5.2 Ligand exchange of citrate ions on the 20 nm c-PtNP by 6-MHA. Note figure not to scale. 102

Figure 5.3 Characterisation of PtNP-6-MHA. (a) hydrodynamic diameters, (b) zeta potentials (c) pH and (d) gel electrophoresis. Results (except electrophoresis) are representative of 3 experiments (n=3) and presented as mean ± SD. 104

Figure 5.4 High resolution XPS spectra of 6-MHA and PtNP-6-MHA on a copper substrate. (a) Pt 4f - 6-MHA, (b) Pt 4f - PtNP-6-MHA, (c) Cu 2p - 6-MHA, (d) Cu 2p – PtNP-6-MHA, (e) C 1s – 6-MHA, (f) C 1s – PtNP-6-MHA, (g) O 1s – 6-MHA, (h) O 1s – PtNP-6-MHA (i) S 2p – 6-MHA and (j) S 2p – PtNP-6-MHA (n=1)..... 108

Figure 5.5 Ligand exchange of citrate ions on the 20 nm c-PtNP by 8-MOA. Note figure not to scale. 112

Figure 5.6 Characterisation of PtNP-8-MOA, (a) hydrodynamic diameters, (b) zeta potentials (c) pH and (d) gel electrophoresis. Results (except electrophoresis) are representative of 3 experiments (n=3) and presented as mean ± SD. 113

Figure 5.7 High resolution XPS spectra of 8-MOA and PtNP-8-MOA on a copper substrate. (a) Pt 4f - 8-MOA, (b) Pt 4f - PtNP-8-MOA, (c) Cu 2p - 8-MOA, (d) Cu 2p – PtNP-8-MOA, (e) C 1s – 8-MOA, (f) C 1sPtNP-8-MOA, (g) O 1s – 8-MOA, (h) O 1s – PtNP-8-MOA, (i) S 2p – 8-MOA and (j) S 2p – PtNP-8-MOA (n=1)..... 118

Figure 5.8 Ligand exchange of citrate ions on the 20 nm c-PtNP by TA. Note figure not to scale. 121

Figure 5.9 Characterisation of PtNP-TA. (a) hydrodynamic diameters, (b) zeta potentials (c) pH and (d) gel electrophoresis. Results (except electrophoresis) are representative of 3 experiments (n=3) and presented as mean ± SD. 122

Figure 5.10 High resolution XPS spectra of TA and PtNP-TA on a copper substrate. (a) Pt 4f - TA, (b) Pt 4f - PtNP-TA, (c) Cu 2p - TA, (d) Cu 2p – PtNP-TA, (e) C 1s – TA, (f) C 1s – PtNP-TA, (g) O 1s – TA, (h) O 1s – PtNP-TA (i) S 2p – TA and (j) S 2p – PtNP-TA, (n=1). 126

Figure 5.11 Structure of O-(2-carboxyethyl)-O'-(2-mercaptoethyl)heptaethylene glycol (2-MOHA). 130

Figure 5.12 Ligand exchange of citrate ions on the 20 nm c-PtNP by 2-MOHA. Note figure not to scale. 131

Figure 5.13 Characterisation of PtNP-2-MOHA. (a) hydrodynamic diameters, (b) zeta potentials (c) pH and (d) gel electrophoresis. Results (except electrophoresis) are representative of 3 experiments (n=3) and presented as mean ± SD. Note *: overspill 132

Figure 5.14 High resolution XPS spectra of 2-MOHA and PtNP-2-MOHA on a copper substrate. (a) Pt 4f – 2-MOHA, (b) Pt 4f - PtNP-2-MOHA, (c) Cu 2p - 2-MOHA, (d) Cu 2p – PtNP-2-MOHA, (e) C 1s – 2-MOHA, (f) C 1s – PtNP-2-MOHA, (g) O 1s – 2-MOHA, (h) O 1s – PtNP-2-MOHA, (i) S 2p – 2-MOHA and (j) S 2p – PtNP-2-MOHA, (n=1). 137

Figure 6.1 Amino terminated alkanethiols. (a) cysteamine hydrochloride, (b) 6-amino-1-hexamethiol and (c) 11-amino-1-undecanethiol hydrochloride 144

Figure 6.2 Simultaneous binding of 6-AHT to 20 nm c-PtNPs. 145

Figure 6.3 c-PtNP with 6-AHT. (a) c-PtNP particle size distribution, (b) c-PtNP with 6-AHT particle size distribution, (c) c-PtNPs (left vial), c-PtNPs with 6-AHT (right vial), (d) c-PtNP aggregation by 6-AHT. Results are from 1 experiment (n=1). 146

Figure 6.4 Structure of cetrimethylammonium bromide (CTAB). 147

Figure 6.5 Synthesis and characterisation of PtNP-CTAB and c-PtNPs. (a) addition of CTAB, (b) reduction of $H_2PtCl_6.6H_2O$, (c & d) TEM images of PtNP-CTAB, (e) particle size distribution of

PtNP-CTAB, (f & g) TEM images of citrate PtNPs, (h) particle size distribution of citrate PtNPs. Results are from 1 experiment (n=1). 149

Figure 6.6 PtNP-CTAB and c-PtNP characterisation by DLS and zeta potential. (a) average hydrodynamic diameters & (b) average zeta potentials. Results are respresentitive of 1 experiment (n=1). 151

Figure 6.7 Structure of (6-mercaptohexyl)trimethylammonium bromide (6-MTAB)..... 153

Figure 6.8 Structure of (6-aminohexyl)trimethylammonium bromide hydrobromide (6-ATA). 154

Figure 6.9 PtNP-CTAB ligand exchange with 6-ATA. Note figure not to scale..... 155

Figure 6.10 6-ATA characterisation by (a) DLS (b) zeta potential and (c) pH. Results are respresentitive of 1 experiment (n=1). 156

Figure 6.11 PtNP surface modified with 70 µM 6-ATA. (a & b) PtNP + 70 µM 6-ATA post surface modification and (c & d) PtNP + 70 µM 6-ATA day after surface modification. Results are representative of 1 experiment (n=1). 157

Figure 6.12 Structure of 2-diethylaminoethanethiol hydrochloride (DEA). 158

Figure 6.13 Schematic of synthesis of positively charged PtNPs by reduction of sodium borohydride with DEA as a capping agent. Note figure not to scale. 159

Figure 6.14 Synthesis of positively charged PtNPs with DEA as a capping agent. (a) reaction A with $H_2PtCl_6.6H_2O$ prepared in dH_2O at pH 2 and reaction B $H_2PtCl_6.6H_2O$ prepared in just dH_2O, (b) reactions A and B after 20 hours, (c) & (d) TEM images of reaction A, (e) frequency distribution of reaction A and (f) & (g) TEM images of reaction B. Results are representative of 1 experiment (n=1). 160

Figure 6.15 PtNP-DEA synthesis and characterisation by (a) DLS, (b) zeta potential and (c) reaction A and B the day after synthesis. Results are representative of 1 experiment (n=1). 162

Figure 6.16 Hypothetical arrangement of DEA on the PtNP surface, not to scale. 164

Figure 6.17 Structure of (11-mercaptoundecyl)-N,N,N-trimethylammonium bromide (11-MABr). 165

Figure 6.18 Structure of polyethyleneimine (PEI). 166

Figure 7.1 Structure of 6-mercaptohexanol (6-MCH). 170

Figure 7.2 Ligand exchange of citrate ions on 20 nm c-PtNP by 6-MCH. Note figure not to scale. 171

Figure 7.3 Characterisation of PtNP-6-MCH. (a) hydrodynamic diameters, (b) zeta potentials and (c) pH. Results are representative of 3 experiments (n=3) and presented as mean ± SD. 172

Figure 7.4 Schematic of synthesis of neutrally charged PtNPs with 6-MCH as a capping agent. Note Figure to scale. 174

Figure 7.5 Synthesis of PtNP with 6-MCH as a capping agent. (a) with L-ascorbic acid, (b) with sodium borohydride and (c) with sodium citrate and L-ascorbic acid. Results are from 1 experiment (n=1). 175

Figure 7.6 Structure of 2-[2-[2-(2-mercaptoethoxy)ethoxy]ethoxy]ethanol (2-MEE)..... 177

Figure 7.7 Ligand exchange of citrate ions on 20 nm c-PtNP by 2-[2-[2-(2-mercaptoethoxy)ethoxy]ethoxy]ethanol. 178

Figure 7.8 Characterisation of PtNP-2-MEE. (a) hydrodynamic diameters, (b) zeta potentials (c) pH and (d) gel electrophoresis. Results (except electrophoresis) are representative of 3 experiments (n=3) and presented as mean ± SD. Note *: overspill 179

Figure 7.9 High resolution XPS spectra of 2-MEE and PtNP-2-MEE on a copper substrate. (a) Pt 4f –2-MEE, (b) Pt 4f - PtNP-2-MEE, (c) Cu 2p - 2-MEE, (d) Cu 2p – PtNP-2-MEE, (e) C 1s – 2-MEE, (f) C 1s – PtNP-2-MEE, (g) O 1s – 2-MEE, (h) O 1s – PtNP-2-MEE, (i) S 2p – 2-MEE and (j) S 2p – PtNP-2-MEE, (n=1). 183

Figure 7.10 Structure of 11-(mercaptoundecyl)hexa(ethylene glycol) (11-MUHEG). 188

Figure 7.11 Ligand exchange of citrate ions on 20 nm c-PtNPs by 11-MUHEG. Note figure not to scale. 189

Figure 7.12 Characterisation of PtNP-11-MUHEG. (a) hydrodynamic diameters, (b) zeta potentials (c) pH and (d) gel electrophoresis. Results (except electrophoresis) are representative of 3 experiments (n=3) and presented as mean ± SD. Note *: overspill 190

Figure 7.13 High resolution XPS spectra of 11-MUHEG and PtNP-11-MUHEG on a copper substrate. (a) Pt 4f –11-MUHEG, (b) Pt 4f - PtNP-11-MUHEG, (c) Cu 2p - 11-MUHEG, (d) Cu 2p – PtNP-11-MUHEG, (e) C 1s – 11-MUHEG (f) C 1s – PtNP-11-MUHEG, (g) O 1s – 11-MUHEG, (h) O 1s – PtNP-11-MUHEG, (i) S 2p – 11-MUHEG and (j) S 2p – PtNP-11-MUHEG, (n=1). 196

Figure 8.1 Functionalised PtNP with Tyrodes-HEPES buffer. (a) hydrodynamic diameters with Tyrodes-HEPES buffer, (b) zeta potentials with Tyrodes-HEPES buffer and (c) pH with Tyrodes-HEPES buffer. Results presented from 1 experiment (n=1). 206

Figure 8.2 Structure of PEGylated thiols used to functionalise PtNPs. (a) O-(2-carboxyethyl)-O'-(2-mercaptoethyl) heptaethylene glycol (2-MOHA) and (b) 11-mercaptoundecyl)hexa(ethylene glycol) (11-MUHEG). 209

Figure 8.3 Human platelet aggregations with c-PtNPs. (a) representative control aggregation trace to 1U/mL Thrombin, (b) representative aggregation traces to c-PtNPs (4.1 – 59.2 μg/mL), (c) representative aggregation trace to sodium citrate 11 μM, (d) quantification of dose-

response aggregations to c-PtNPs (4.1 – 59.2 μg/mL) presented as mean ± SEM. Results are representative of 3 experiments (n=3). 212
Figure 8.4 Structure of glycoprotein VI (GPVI). 213
Figure 8.5 Human platelet aggregations with functionalised PtNP-2-MOHA and PtNP-11-MUHEG. (a) representative aggregation traces to PtNP-2-MOHA (59.2 μg/mL), (b) representative aggregation traces to 2-MOHA (70 μM), (c) representative aggregation traces to PtNP-11-MUHEG (59.2 μg/mL) and (d) representative aggregation traces to 11-MUHEG (59.2 μg/mL). Results are representative of 3 experiments (n=3). 215
Figure 8.6 GPVI signalling pathway. 217
Figure 8.7 Human platelet aggregations with c-PtNPs and Src and Syk inhibitors. (a) representative control aggregation trace to 3 μg/mL CRP following pre-incubation with 20 μM PP2 and 3 μM PRT-060318, (b) representative trace to 59.2 μg/mL c-PtNP following pre-incubation with 20 μM PP2 and 3 μM PRT-060318, (c) quantification of maximal aggregation by CRP and c-PtNP with pre-incubation of with 20 μM PP2 and 3 μM PRT-060318 presented as mean ± SEM, (P<0.001). Results are representative of 3 experiments (n=3). 218
Figure 8.8 Expression of phospho-tyrosine, phospho-Syk and phospho-LAT from platelet whole cell lysates treated with EGTA, pre-incubated with Src and Syk inhibitors with PtNP stimulation. Results are representative of 3 experiments (n=3). 221
Figure 8.9 Human platelet rich plasma aggregations with PtNPs (a) representative aggregation traces to PAR1 peptide 50 μM, (b) representative aggregation traces to PtNP 59.2 μg/mL, (c) quantification of platelet aggregation in PRP with PtNPs. Results are representative of 3 experiments (n=3) and presented as mean ± SEM (P<0.001). 223

Figure 8.10 Protein corona of functionalised PtNPs. (a) hydrodynamic diameters with human plasma and (b) zeta potentials with human plasma. Results presented from 1 experiment (n=1). 225

List of Tables

Table 1.1 Common ligands used to coat metallic and metal oxide nanoparticles. 10

Table 1.2 Metallic nanoparticle platelet interactions. This summary is from an opinion article co-written by the author of this thesis.[89] Platelet studies were performed in washed platelets (WP) and/or platelet-rich plasma (PRP) and assessed through light transmission aggregometry (LTA) or flow cytometry. 32

Table 1.3 Non-metallic nanoparticle platelet interactions. This summary is from an opinion article co-written by the author of this thesis.[89] Platelet studies were performed in WP and/or PRP and assessed through light transmission aggregometry (LTA) or flow cytometry. 33

Table 3.1 Alkane and PEGylated thiols used for functionalisation experiments. 56

Table 3.2 Final concentration and volume of alkanethiol added to coat platinum nanoparticles. 58

Table 3.3 Final concentration and volume of PEGylated thiols added to coat platinum nanoparticles. 58

Table 3.4 Final concentration and volume of 6-ATA added to coat PtNP-CTAB. 59

Table 3.5 Vecstar Split Tube Furnace settings for oxide reduction. 63

Table 3.6 Agonists used in platelet and platelet-rich plasma aggregations. 64

Table 3.7 Inhibitors used in platelet aggregations and phosphorylation experiments. 64

Table 3.8 Primary antibodies used in Western blotting. 65

Table 3.9 Secondary antibodies used in Western blotting. 65

Table 4.1 20 nm c-PtNP scaled up reactions, volumes, diameters, and calculated surface areas/mL. 80

Table 4.2 60 nm c-PtNP scaled up reactions, volumes, diameters, and calculated surface areas/mL. 83

Table 4.3 20 nm c-PtNP synthesised from four batches, TEM diameters and calculated surface areas/mL. 86

Table 4.4 Components of Tyrodes-HEPES buffer. 94

Table 4.5 Components of 1x PBS. 94

Table 5.1 - % of bound and unbound S 2 p in 6-MHA and PtNP-6-MHA. 111

Table 5.2 - % of bound and unbound S 2p in 8-MOA and PtNP-8-MOA. 120

Table 5.3 % of bound and unbound S 2 p in TA and PtNP-TA. 128

Table 6.1 PtNP-DEA synthesis reaction ratios of precursor, capping and reducing agent. 159

Table 7.1 -% of bound and unbound S 2p in 2-MEE and PtNP-2-MEE. 187

Table 7.2 -% of bound and unbound S 2p in 11-MUHEG and PtNP-11-MUHEG. 198

Table 8.1 Functionalised platinum nanoparticles. 204

Table 11.1 Surface coverage calculations for PtNP with 6-mercaptohexanoic acid (6-MHA). 261

Table 11.2 Surface coverage calculations for PtNP with 8-mercaptooctanoic acid (8-MOA) . 261

Table 11.3 Surface coverage calculations for PtNP with thioctic acid (TA) 262

Table 11.4 Surface coverage calculations for PtNP with O-(2-carboxyethyl)-O'-(2-mercaptoethyl)heptaethylene glycol (2-MOHA) 262

Table 11.5 Surface coverage calculations for PtNP with (6-aminohexyl)trimethylammonium bromide hydrobromide (6-ATA) 262

Table 11.6 Surface coverage calculations for PtNP with 6-mercaptohexanol 263

Table 11.7 Surface coverage calculations for PtNP with 2-{2-[2-(2-Mercaptoethoxy)ethoxy]ethoxy}ethanol (2-MEE) 263

Table 11.8 Surface coverage calculations for PtNP with 11-Mercaptoundecyl)hexa(ethylene glycol) (11-MUHEG) 263

Chapter 1 Introduction

1.1 Nanotechnology

Nanotechnology is a rapidly evolving field with a plethora of applications in medicine, biology, engineering, chemistry, and physics. It is described as the science, engineering and technology executed on the nanoscale. For a particle to be classed as a `nanoparticle' it must exhibit at least one dimension within the 1 – 100 nm range, thus allowing for nanoparticles of different geometries.[1, 2] The concept of nanotechnology was first introduced by American physicist and later Nobel Prize Laurette Richard Feyman in his 1959 lecture `*There's Plenty of Room at the Bottom*'.[3]

While nanotechnology seems relatively new, it has been around since the early 4th century. The earliest example and most extraordinary piece of nanotechnology is the Roman artefact the Lycurgus cup. A remarkable feature of this cup is its colour, the cup consists of 70 nm colloidal gold and silver nanoparticles dispersed throughout the glass which contribute to its dichroic effect. In scattered light the Lycurgus cup appears green due to the silver nanoparticles (AgNPs) and in transmitted light it appears red from the presence of gold nanoparticles (AuNPs).[4] Artisans would often create objects unaware that they were using nanotechnology in their work. Another example dating back to 900 AD is Damascus steel. Remnants of cementite or iron carbide nanowires encapsulated by carbon nanotubes were discovered in an ancient Damascus sabre. It was assumed that these nanomaterials contributed to the mechanical properties of the sabre.[5]

1.2 Applications in Nanotechnology

Today nanotechnology has influenced all aspects of science. The nature of nanoparticles has provided fundamental developments in medicine, biology, electronics and hydrogen fuel cells to name a few, see Figure 1.1. This is largely due to its attractive feature of large surface area to volume ratios compared with bulk materials.[6] In the next section, the applications of nanotechnology will be discussed in further detail.

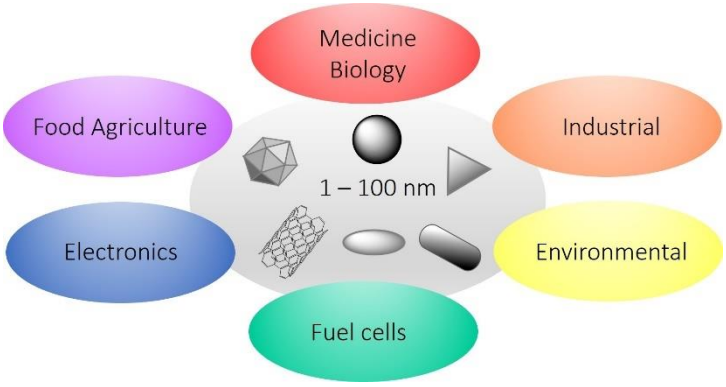

Figure 1.1 Applications of nanotechnology. Nanotechnology has been applied in various different fields, these include medicine, fuel cells, electronics, industrial, environmental and food agriculture.

1.2.1 Nanomedicine

As the name suggests, nanomedicine is an application of nanotechnology in biomedicine. The most explored nanoparticles in nanomedicine are gold, silver, iron, and platinum. As a result of their low toxicity, simple synthesis and high versatility, AuNPs have been heavily explored in nanomedicine, especially in drug delivery. Recent work by Salamone et al.[7] demonstrated the promising potential of AuNPs with the anticancer therapy drug methotrexate (MTX) in neuroblastoma cells. AuNPs were synthesised with the hydrophilic thiol 3-mercapto-1-propanesulfonic acid (3-MPS) to enable the uptake of MTX molecules on the nanoparticle

surface to form a AuNP-MTX conjugate. *In vitro* assessment of cell viability in neuroblastoma cells, found AuNP-MTX to be more effective compared to free MTX alone and free AuNPs which had no effect at all. Amongst the different metallic nanoparticles, AgNPs have shown exceptional antimicrobial activity. In a comparison study of negatively and positively charged AgNPs, high bactericidal activity was observed by the positively charged AgNPs on gram-positive and gram-negative bacteria. The study proposed that the effectiveness of antibacterial activity was due to the electrostatic attraction between positively charged AgNPs and the negative charge carried by the bacterial cell walls.[8]

Iron oxide nanoparticles (IONPs) have played a significant role in MRI (magnetic resonance imaging) as contrast agents. Superparamagnetic iron oxide nanoparticles (SPIONs) have been extensively employed for their diagnostic visualisation of tumours and metastases. Intravenously injected SPIONs have demonstrated rapid uptake into the liver, thus, enabling the visualisation of lesions on the cancerous livers. SPIONs not only provide a visualisation for diagnosis but allows for the staging of the disease.[9]

Platinum nanoparticles (PtNPs) have been applied in several areas including glucose sensing, drug delivery and nanozymes. The development of glucose biosensors is crucial for the management and monitoring of patients with diabetes; PtNPs have enhanced the electrochemical performance to sense glucose, thus, providing high sensitivity and low detection limits. Recently, polyethylene glycol (PEG) modified PtNPs were immobilised on an indium tin oxide electrodes for glucose detection at 15 mM.[10]

For anticancer activity, mesoporous PtNPs were surfaced modified by PEG, loaded with the chemotherapy drug Doxorubicin, and assessed for their anticancer activity. The mesoporous structure of the PtNPs enabled the loading of more Doxorubicin via electrostatic absorption. Combined with laser irradiation, these modified PtNPs significantly improved the anticancer effect and killed up to 84% of the cancer cells.[11]

1.2.2 Electronics

As a result of their high electrical conductivity, metallic nanoparticles including gold, platinum, silver and palladium have been utilised as metallic inks for electronic devices.[12] Work by Im et al.[13] found printed gold films produced from AuNP inks experienced microcracks and pores from thermal induction, which subsequently led to poor integrity of the printed film. By functionalising the AuNPs with the alkanethiol octanethiol (OT) followed by 3-mercaptopropionate (3-MTP) as a cohesion enhancer to link together the AuNP-OTs. This functionalisation prevented microcracks and pores and improved electrical conductivity. Similarly, Sels et al.[14] demonstrated that functionalisation of PtNPs with dodecanethiol (DDT) provided stability to the PtNP inks in use for printing and fabrication of platinum films. The PtNP-DDT ink presented high conductivity when dispersed in a toluene/terpineol mix and demonstrated a resistive PtNP-DDT heater by inkjet printing.

1.2.3 Hydrogen fuel cells

Owing to the current climate crisis, much attention has been focused on fuel cells as an alternative renewable energy. With low carbon dioxide (CO_2) emissions, hydrogen fuel cells are

one of key renewable energies that can deliver a clean sustainable energy system; proton exchange membrane fuel cells (PEMFC) are promising candidates with their primary application in automobiles but also stationary and portable devices. PEMFC are ideal for automobiles as they operate at a low temperature range (60 - 120^{o}C) and use hydrogen and oxygen to produce electricity and water, Figure 1.2. The electricity generated would power the vehicle, while the water would leave the exhaust pipe.[15] Nanotechnology plays a pivotal role in PEMFC as platinum nanoparticles (PtNPs) are employed as catalysts due to their high catalytic activity amongst other transition metals; PtNPs of 3 - 5 nm supported on carbon black are situated on the anode and cathode of the PEMFC, where they catalyse the hydrogen oxidation reaction (HOR) and the oxygen reduction reaction (ORR), respectively, thus producing electricity and water. Challenges still remain in the commercialisation of PEMFC as their components are expensive (i.e. the platinum catalyst), poor cathodic reactions and degradation and aggregation of the catalyst.[16, 17]

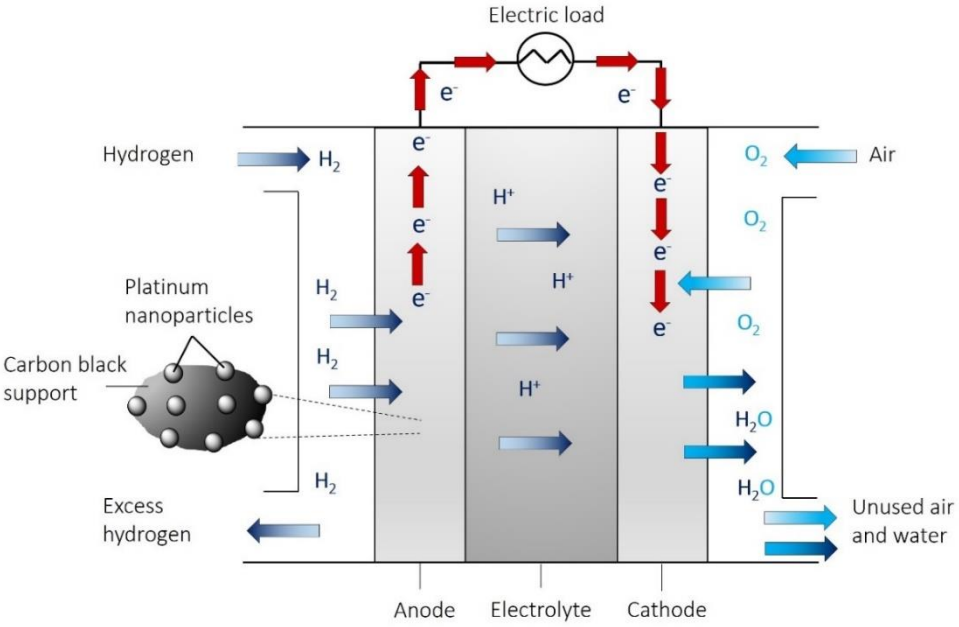

Figure 1.2 Platinum nanoparticles as catalysts for proton exchange membrane fuel cells. PtNPs of 3 – 5 nm on carbon black are located on the anode and cathode of the PEMFC and catalyse both hydrogen oxidation reaction (HOR) and the oxygen reduction reaction (ORR).

1.3 Synthesis and functionalised nanoparticles

1.3.1 Top down and bottom up

Metallic nanoparticles can be synthesised to have different physicochemical properties such as size, shape, and surface charge. Nanoparticle synthesis methods can be categorised into two main groups: 1) top-down approach and 2) bottom-up approach, as illustrated in Figure 1.3. Within these categories there are numerous methods that can be utilised for nanoparticle synthesis. Top-down approaches are destructive methods where the bulk material is broken down or decomposed into smaller units, which are then converted into nanoparticles. Top-down methods include laser ablation, chemical etching and mechanical milling to name a few. An advantage of top-down methods is their largescale production and low impact on the

environment. A limitation of these methods is that they require specialist equipment, can be energy demanding, can produce a broad particle distribution with varied morphologies, have high impurities and waste of raw materials.[18-20]

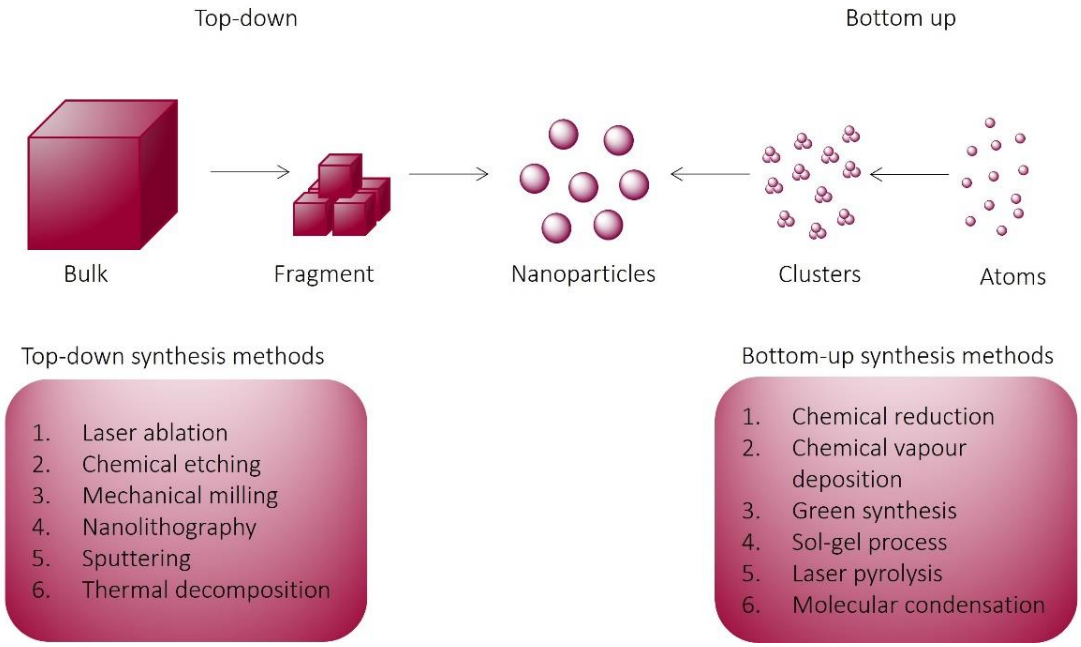

Figure 1.3 Illustration of top-down and bottom-up approaches for nanoparticle synthesis. Top-down approaches involve physical methods such as laser ablation or chemical etching. Bottom-down approaches use chemical synthesis methods such as chemical synthesis or sol-gel.

Conversely, bottom-up approaches involve producing nanoparticles starting from atoms, which then form clusters and finally nanoparticles. Bottom-up approaches use constructive methods for synthesising nanoparticles. Some of these methods are chemical reduction, green synthesis, chemical vapour deposition and sol-gel process. Bottom-up approaches can produce nanoparticles with narrow size distribution and consistent morphologies and can lead to large scale production. Unfortunately, the disadvantage of bottom-up methods is that they can be costly and requires the removal of unwanted by-products.[18-20]

1.3.2 Chemical reduction of metallic nanoparticles

Chemical reduction methods are frequently used for synthesising metallic nanoparticles such as gold, silver and platinum.[21-23] The synthesis methods are based on early works by Turkevich et al.[21] and later Frens,[24] where the method for synthesising gold nanoparticles (AuNPs) involved the reduction of the gold precursor chloroauric acid by sodium citrate. Sodium citrate served as both reducing and capping agents in these experiments. This initial work led the way for other modified synthesis methods for other metallic nanoparticles, in particular seed mediated synthesis. Seed mediated synthesis, is a nucleation process whereby the metallic seeds are utilised as a template to grow larger nanoparticles,[25, 26] as illustrated in Figure 1.4. Bigall et al.[27] adopted this approach to synthesise monodisperse platinum nanoparticles (PtNPs) of various sizes. First, platinum seeds were synthesised by the reduction of the platinum precursor chloroplatinic acid hexahydrate ($H_2PtCl_6.H_2O$) by the strong reducing agent sodium borohydride ($NaBH_4$). These platinum seeds were stabilised by sodium citrate. Using these platinum seeds, larger PtNPs were synthesised by a second reduction of $H_2PtCl_6.H_2O$ but with the milder reducing agent, L-ascorbic acid.

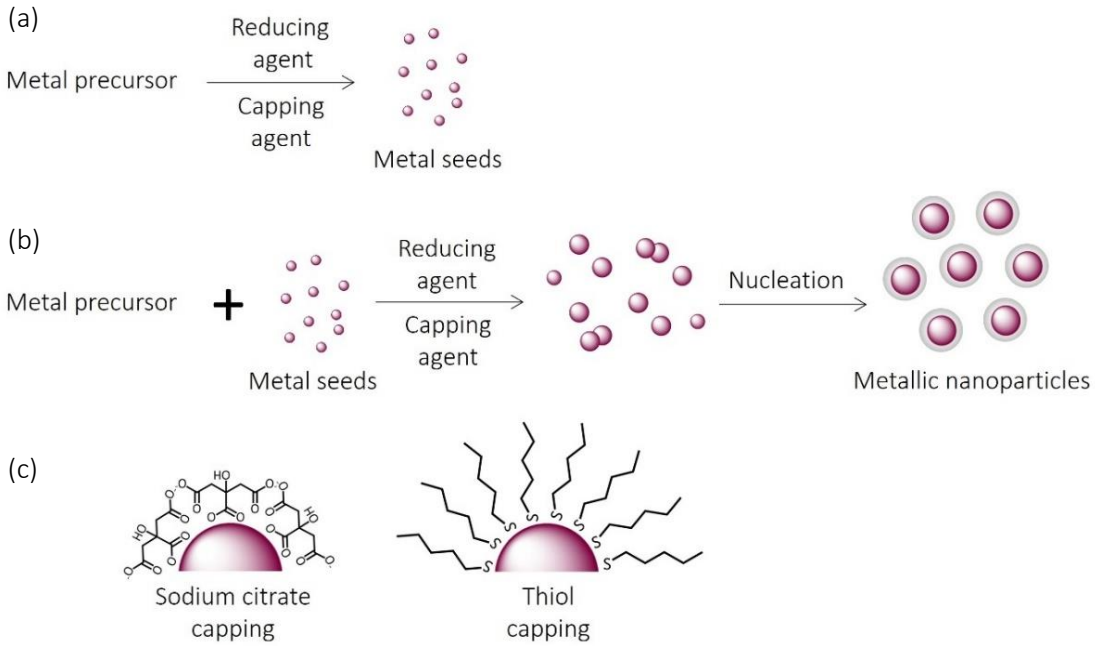

Figure 1.4 Seed mediated synthesis for metallic nanoparticles. (a) metallic seed synthesis, (b) metallic nanoparticle synthesis and (c) capping agents' sodium citrate and thiols.

The choice of reducing agents is imperative for successful synthesis. $NaBH_4$ is a strong reducing agent and facilitates the reduction of metallic precursors instantaneously, by contrast L-ascorbic acid is a milder reducing agent and works over a longer period of time. Capping agents play an equally significant role in metallic nanoparticle synthesis, namely, the capping agents influence the controlled growth of nanoparticles. The most common capping agent for metallic nanoparticles is sodium citrate. Citrate ions physisorb onto the nanoparticle surface to form an electric double layer (EDL) but are non-covalently bound. The citrate ion exhibits a negative charge from its carboxylic acid groups, this negative charge produces electrostatic repulsion between the neighbouring nanoparticles, thus, stabilising them.[21, 24, 28] Surfactants such as cetrimethylammonium bromide (CTAB) are also employed as capping agents for metallic nanoparticles. Similar to citrate ions, CTAB also physisorbs onto the nanoparticle surface but

forms a bilayer, the positive charge from the ammonium group creates electrostatic repulsion amongst the neighbouring nanoparticles.[29-31] Thus, capping agents not only protect the nanoparticle core but they can also provide functionality to the nanoparticle. Table 1.1 provides examples of common ligands used to functionalise metallic nanoparticles.

Table 1.1 Common ligands used to coat metallic and metal oxide nanoparticles.

Nanoparticle composition	Ligands
Metallic nanoparticles	Thiols (-SH) Amines (-NH_2) Carboxyl (-COOH) PEG (-CCO) PEG-thiols Citrate (-COOH Phosphines (-PR_3)
Metal oxide nanoparticles	Carboxyl (-COOH) Amines (-NH_2) Hydroxyl (-OH Phosphonyl (-$PO(OH)_2$)

1.3.3 Self-assembled monolayers by thiols

Self-assembled monolayers (SAMs) are described as the ordered assembly of organic molecules that have adsorbed onto a surface to create a 2D monolayer.[32] Early method development of SAMs was pioneered by Nuzzo and Allara,[33] their work demonstrated sulphur bonds on gold substrates by the adsorption of disulphides (R-S-S-R) in solution. Along with gold substrates, SAMs formation by alkanethiols have been observed on other noble metal surfaces including silver, copper and platinum films for wettability, corrosion studies and electronic devices.[34, 35] A typical SAM monomer unit comprises of three parts, the head group which directs the

process of self-assembly to the substrate, a tail or chain which is the spacer molecule and a functional group as illustrated in Figure 1.5 (a). The chain interacts with neighbouring chains via Van der Waals interactions to form a well-ordered SAM. The functional group determines it surface properties. In the case of alkanethiols, the mercapto group (SH) is the head group which forms a thiolate with a metal substrate, a spacer alkane chain and a functional head group such as carboxyl group (COOH) or an amino group (NH_2),[36] as shown in Figure 1.5 (b).

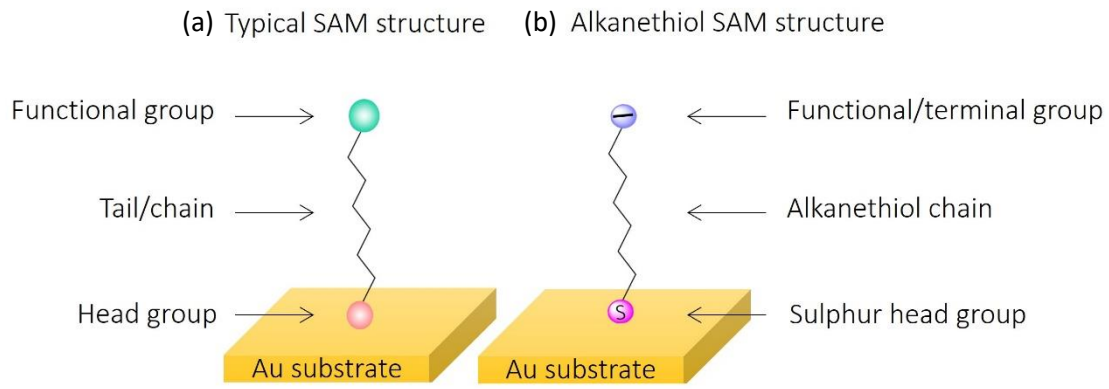

Figure 1.5 Self-assembled monolayer monomer structure on a gold substrate. (a) a typical SAM monomer exhibits a head group that binds to the substrate, a chain which is the spacer and a functional group. (b) an alkanethiol SAM monomer has a mercapto group which binds to the gold substrate, an alkanethiol chain and a functional group with a negative charge.

SAM formation by alkanethiols on gold surfaces is driven by the chemisorption of the thiol molecules onto the gold substrate to form a gold-thiol bond.[32] The mechanism by which this occurs is divided into 3 phases, the first of which is the rapid physisorption of the monomer alkanethiol units onto the gold substrate, followed by a slower of chemisorption where the gold-thiol bond is formed and the alkanethiols units become ordered,[37] as shown in Figure 1.6. In the physisorption phase, the monomer alkanethiol units are in a `lying down-position' where

they form Van de Waals interactions. As the surface coverage by the monomer units increases, the SAM alkanethiols undergo transition from the lying down position to the `standing up position.' In parallel with forming covalent bonds with the gold substrate, the thiol molecules and become densely packed.[36, 38]

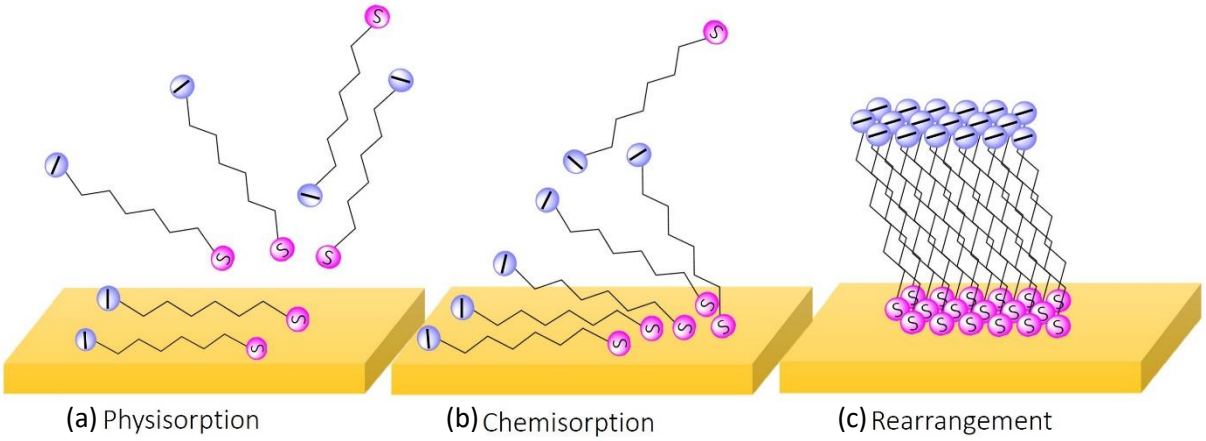

Figure 1.6 Phases of self-assembled monolayer formation by the alkanethiol 6-mercaptohexanoic acid (6-MHA) on a gold substrate. (a) Physisorption of 6-MHA, (b) chemisorption of 6-MHA and (c) rearrangement of 6-MHA.

Alkanethiols and disulphides form SAMs on curved surfaces i.e. nanoparticles, SAM formation on metallic nanoparticles enables them to become functionalised as well as stabilised.[39-41] There are two approaches that can be applied for functionalising metallic nanoparticles, first, the direct synthesis of the nanoparticle in the presence of the thiol. Second, post synthesis functionalisation via ligand exchange. These will be discussed in more detail in the next section.

1.3.4 Thiol functionalisation of nanoparticles in synthesis

Functionalisation of nanoparticles is largely dependent on the nature of the thiol compounds and their tolerance to the reducing conditions used in nanoparticle synthesis. 3- MTP is a water-soluble thiol compound, AuNPs functionalised by 3-MTP through the reduction of the gold precursor chloroauric acid by sodium citrate have resulted in AuNP-3-MTP of sizes ranging from 2.3 to 10 nm, this sizing was dependent on the ratio of the thiol:gold precursor.[42] More recently, Cerra et al.[43] synthesised AuNPs with 3-MPS for investigating the interaction mechanism between AuNP-3-MPS and melamine. The synthesis involved the reduction of the gold precursor tetrachloroauric acid by $NaBH_4$ with 3-MPS as the capping agent, this formed AuNP-3-MPS of 5-6 nm.

PtNPs have also been synthesised with an array of thiol compounds, early work by Yee et al.[44] describes the synthesis of thiol functionalised PtNPs with octandecanethiol (ODT) as a capping agent. As ODT is a hydrophobic thiol, synthesis was performed in tetrahydrofuran (THF) and reduced by lithium triethylborohydride (LiTEBH) to give a hydrophobic functionality to the PtNPs. Similar to the AuNPs functionalised by MTP and MPS, these functionalised PtNPs had small diameters with an average of 4 nm. Eklund et al.[45] continued by synthesising thiol functional PtNPs by employing two synthesis methods. For hydrophobic thiol compounds hexanethiol, 2-phenylethenthiol and dodecanethiol, PtNPs were synthesised following the method by Yee et al.[44] with THF and LiTEBH. By contrast, for the water-soluble thiols tiopronin, glutathione and mercaptoammonium, PtNPs were synthesised in a similar manner to AuNP-2-MPS, where $NaBH_4$ was used as a reducing agent. These thiol functionalised PtNPs had

diameters ranging from 2 to 3 nm. Collectively from these studies, it is apparent that the limitation of this approach is the size of the nanoparticles produced. Additionally, the size of the nanoparticles is dependent on the thiol:metal precursor ratio. Direct functionalisation of nanoparticle by thiols is a desirable method when nanoparticles of <5 nm are required. Conversely, to functionalise larger nanoparticles, a primary capping agent is required which can then be exchanged for a thiol compound.

1.3.5 Thiol functionalisation of nanoparticles by ligand exchange

Ligand exchange is a displacement method whereby existing capping agents are displaced enabling the functionalisation of the nanoparticles. This approach is favourable when the thiol of interest is not compatible with the reducing conditions in nanoparticle synthesis. Capping agents such as sodium citrate, CTAB and phosphines physisorb onto the nanoparticle surface and are non-covalently bound which renders them displaceable.[39] In a typical ligand exchange reaction with citrate capped AuNPs, AuNPs are incubated with free thiols in a large excess from 30 minutes up to 18 hours depending on the thiol chain length, with longer alkanethiols requiring longer incubation periods.[46] The non-covalently bound citrate ions are displaced off the AuNP surface by the thiol molecules; as the thiols form covalent bonds with gold surfaces, this displacement is driven by the gold-sulphur bond formation.[39, 41, 47] Stolarczyk and colleagues,[48] demonstrated a ligand exchange approach to examine the effect of the prostate cancer drug abiraterone on epithelial cells derived from prostate cancer (PTN-2). AuNPs were conjugated through ligand exchange with a thiolate form of abiraterone, thioabiraterone (S-AB) to form AuNP-S-AB. Initially, citrate capped AuNPs of 14.5 nm were synthesised using the

classic Turkevich method.[21] Post-synthesis, AuNPs were incubated with thiobiraterone for 4 hours to form AuNP-S-AB. Characterisation by nuclear magnetic resonance (NMR) and infrared spectroscopy (IR) confirmed the presence of thiobiraterone on the surface of the AuNPs; while thermogravimetric analysis (TGA) demonstrated a 40.9% surface coverage by thioabiraterone. Cell viability assays on PTN-2 cells indicated AuNP-S-AB was more biocompatible compared to thioabiraterone and abiraterone, thus, demonstrating a promising novel treatment for prostate cancer.

Chemisorption of some alkanethiols onto nanoparticle surfaces can also lead to nanoparticle aggregation. To circumvent this issue, Aslan and Perez,[49] used the non-ionic surfactant Tween20 to stabilise AuNPs prior to functionalisation by 11-mercaptoundecanoic acid (11-MUDA) and 16-mercaptohexadecanoic acid (16-MHDA). 20 nm citrate capped AuNPs underwent ligand exchange with Tween20 for 20 minutes to allow the physisorption of Tween20 and the displacement of the citrate ions off the AuNP surface. In subsquent experiments, AuNP-Tween20 were incubated with 11-MUDA and 16-MHDA. Characterisation by UV observed a shift in the absorbance of AuNP-16-MHDA suggesting a ligand exchange. However, it remains unclear if this is a viable method for ligand exchange as UV absorbance was the only characterisation method used; further surface analysis of AuNPs at the different ligand stages of ligand exhange is required. XPS would confirm if ligand exchange had taken place for both AuNP-11-MUDA and AuNP-16-MHDA.

Disulphides are favourable molecules for ligand exchange as they form well ordered SAMs by the two thiolates they form. Unlike the typical thiolate SAM formation discussed in section 1.3.3, the disulphide bond breaks allowing two thiolate bonds.[36, 50] Thioctic acid (TA) has been a common choice for functionalisation of metallic nanoparticles as an intermediate for further functionalisation by proteins and other thiols.[40, 51] Recent work published by Guzmàn-Soto et al.[52] reported the functionalisation of citrated AgNPs by TA, which were subsequently functionalised with human serum albumin (HSA) to form a stabile nanoparticle-protein hybrid. Covalent bonds were formed through the carboxylic functionality of AgNP-TA and the amides of HSA. Early investigations by Lin et al.[53] demonstrated the two step method whereby the functionalisation of citrated capped AuNPs by TA allows functionalisation by other thiol molecules. The displacement rate of citrate ions by TA is much slower compared with a typical thiol as the disulphide bond needs to be broken first and this does not occur with thiols, thus, there is opportunity for other thiols molecules to assemble and sterically stabilise the nanoparticle. Surprisingly, 80% of TA molecules are displaced from the AuNPs in this method.

1.3.6 Mechanism of ligand exchange on nanoparticles

Although these studies demonstrate methods and characterisations for ligand exchange, the mechanism of ligand exchange of citrate capped nanoparticles remains unclear. Work by Dinkel et al.[39] describes a `fast and slow' ligand exchange of citrate for 3-MPS on AuNPs using second-harmonic light scattering (SHS) and 2-photo fluorescence (2-PF). The addition of 3-MPS to AuNPs in solution observed a significant decrease in intensities of both SHS and 2-PF. This was assigned to displacement of the citrate ions and adsorption of 3-MPS onto the AuNP surface.

Surface coverage was correlated with intensity decrease; the eventual saturation of the decreased intensity was attributed to the chemisorption of 3-MPS. Displacement and adsorption were assigned to the fast phase as this occurred at less than one hundred seconds, while the chemisorption and coordination of 3-MPS relates to the slow phase which was completed at 23 minutes. Further analysis revealed that 3-MPS had displaced the citrate ions by up to 49%. This mechanism is similar to that presented on gold substrates.

Early work by Woehrle et al.[46] deduced a three-phase mechanism of ligand exchange with triphenylphosphine (PPh_3) stabilised AuNPs (AuNP-PPh_3) and ODT. Ligand exchange of PPh_3 for ODT was monitored by analysis using the ^{31}P NMR spectra. The authors describe the `fast phase' where PPh_3 was liberated from the AuNP surface as observed by an increase in PPh_3 in solution, while the free ODT decreased. In the second phase which was over a duration of sixty minutes, the concentration of PPh_3 increases and finally saturates, indicating that all the PPh_3 had been displaced. By contrast, the concentration of ODT continued to decrease, thus, indicating the thiol had chemisorbed onto the AuNP surface. In the final phase (from sixty minutes to seven hours) the NMR signal of ODT broadened out, suggesting that this was due to the rearrangement of the chemisorbed ODT. The increased reaction was likely due to the long alkanethiol chain length to allow rearrangement. It is important to consider that this mechanism applies to non-polar thiols in organic solvents, however, it could be potentially applicable for polar thiols in aqueous media. The mechanism of ligand exchange of non-covalent bound citrate ions and PPh3 on AuNPs are similar, both experience a fast phase with

physisorption of the thiol and displacement of the non-covalent bound ligand. This is followed by a slow phase where chemisorption and rearrangement of the thiol molecules occur.

1.4 Nanoparticles for biological interactions

1.4.1 Biocompatibility

Metallic nanoparticles have demonstrated promising applications in nanomedicine, such as drug delivery, the success of these applications are dependent on their biocompatibility. AuNPs have been extensively used in nanomedicine due to their biocompatibility. There is a plethora of research that focuses on the assessment on biocompatibility and toxicity of nanoparticles.[54] The cytotoxicity evaluation is carried out first followed by biocompatibility assessment. Regardless of a nanoparticle presenting no cytotoxic effects, the biocompatibility of the nanoparticles must still be assessed. For a nanoparticle to be considered biocompatible it must be compatible with living cells/tissue, without causing any toxicity, DNA damage, oxidative stress or immune response to the cells or tissues.[55] Despite in vitro and in vivo investigations, the cytotoxicity of metallic investigations can be contradictory. For example, AuNPs that were delivered orally and intraperitoneally presented a high cytotoxicity in comparison to those AuNPs that were delivered through intravenous injection.[56] The cytotoxicity and biocompatibility of metallic nanoparticles is governed by their physicochemical properties these include size, shape and surface charge, additionally other factors such as, concentration, formulation and cells/tissue type all need to be taken into consideration. The assessment method for both cytotoxicity and biocompatibility itself needs to be valid and independently verified.

1.4.1.1 Nanoparticle physicochemical properties and cytotoxicity

In a pilot study by Buchtelova et al.[57] poly(vinylpyrrolidone) (PVP) capped PtNPs of 10, 29 and 40 nm demonstrated high haemocompatibility. Cytotoxicity of these PtNP-PVP were assessed *in vitro* on three cancer cells lines: MDA-MB-231 (breast), LNCaP (prostate) and GI-ME-M (neuroblastoma). Marginal differences of these nanoparticles altered cell cytotoxicity. 10 nm PtNP-PVP presented the highest cytotoxicity in all the cell lines examined. Interestingly changes were observed in the cellular structures of these cell lines, however their cell viability was unaffected. High concentrations of reactive oxygen species were detected in cells lines that had previously been treated with 29 and 40 nm PtNP-PVP; consequently, PtNP-PVP-29 and PtNP-PVP-40 induced the expression protein and mRNA of metallothionein. Subnanosized PtNPs (less than 1 nm) were able to induce hepatotoxicity and nephrotoxicity both *in vivo and in vitro* in mouse models, however the toxicity could be reduce with larger PtNPs.

Nanoparticle shape can also influence cytotoxicity. Recent data published by Steckiewicz et al.[58] investigated how AuNPs of different morphologies impacted cytotoxicity. AuNPs with spherical, rod and star morphologies were examined for their potential cytotoxicity against the following cell lines: hFOB 1.19 (human foetal osteoblast), hTERT-HPNE (pancreatic duct cells) and MG-63 (osteosarcoma cells). Additionally, the impact of these various AuNPs on apoptosis was assessed by the expression of apoptosis specific proteins Bax and Bcl-2. Overall, the cancer cells investigated in this study were prone to the cytotoxic effects of AuNPs of different morphologies. MG-63 cells treated with AuNP rods and stars demonstrated an increased expression of Bax and conversely a decrease in Bcl-2 expression. Furthermore, these AuNPs

were able to absorb through the cell membrane and alter their ultrastructure. A possible explanation for this outcome is that the AuNP rods and stars had increased surface areas compared to the spherical AuNPs, thus, they were able to interact with the cell membrane to a higher degree. Despite, AuNPs stars presenting the highest anti-cancer potential, they proved to be the most cytotoxic AuNPs. By contrast, the spherical AuNPs had low cytotoxicity but also the lowest anti-cancer potential. It is clear from these findings that shape influences cytotoxicity.

In addition to size and shape, surface charge is another important physicochemical property that impacts on cell cytotoxicity. AuNPs were fabricated with (11-mercaptoundecyl)-N,N,N-trimethylammonium (11-MABr) and 11-mercaptoundecanoic acid (11-MUDA) to produce positively charged and negatively charged AuNPs, respectively. Positively charged AuNP-11-MABr were able to induce moderate cytotoxicity on erythrocytes in comparison to the negatively charged AuNP-11-MUDA. This cytotoxicity can be explained by the electrostatic interaction of the cell membrane and the positive charge of AuNP-11-MABr.[59] The evaluation of negatively charged PVP capped AuNPs and PtNPs had contradicting results. Both were assessed for their inhibition of matrix metalloproteases 1 (MMP-1) in the fibroblastic cell line L-929. At the same concentration, both AuNP-PVP and PtNP-PVP demonstrated inhibition of MMP-1, this is due to the chelation of Zn^{2+} from MMP-1 and the negative charges from the PVP on nanoparticle surface. Cells treated with various concentrations of AuNP-PVP presented no cytotoxic effects; however, PtNP-PVP at 100 and 400 µg/mL caused cytotoxicity. Assessment of other inflammatory markers by RT-PCR (real-time polymerase chain reaction) demonstrated no

changes in expression. This work demonstrates the potential of AuNP-PVP as an inhibitor for MMP-1 with compromising cell cytotoxicity. [60]

1.4.2 Protein corona

Protein corona is the phenomena whereby proteins spontaneously adsorb onto the nanoparticle surface when they are exposed to a biological environment.[61, 62] The collection of proteins that adsorbed onto the nanoparticles was termed `protein corona' and was conceived by Dawson and colleagues in 2007 which was a critical milestone.[63] However, early protein corona investigations began with Vroman, who found upon contact with biological milieu nanoparticles and other materials of a synthetic nature would become engulfed in resident proteins.[64, 65] The assembly of these proteins is the first interaction that nanoparticles undergo when exposed to biological environments. The events of protein corona provides nanoparticles with a new biological characteristics that influences its biodistribution, colloidal stability, interactions with other cells, clearance and toxicity.[62] To date, the proteomic profiling of protein coronas has provided valuable data on protein corona patterns, this has led to nanoparticles to be engineered with specific physicochemical properties that can selectively absorb proteins for diagnostics and therapeutics.

1.4.2.1 Protein corona formation

Owing to the dynamic nature of the protein corona process, the protein corona architecture is divided into two parts: `hard' corona and `soft' corona, as illustrated in Figure 1.7. These hard and soft coronas are dependent on the binding affinities of the proteins. Hard coronas which

are bound directly to the nanoparticle core are constituted to proteins that have high binding affinity. Their formation occurs within seconds to minutes on exposure to biological milieu, which translates to rapid formation of strongly bound protein-nanoparticle interactions with a low dissociation constant. Conversely, soft coronas are situated on the exterior surface of the nanoparticles, these are constituted to proteins with low binding affinities, and which take longer to form. The proteins here are weakly bound and are a result of protein-protein interaction with a high dissociation constant.[66] It has been reported that the dynamic process of protein corona occurs in three phases. First, proteins are irreversibly adsorbed on the nanoparticle surface to form the hard corona. In the second phase, these irreversibly bound proteins then interact with proteins to constitute the soft corona. Finally, in the third phase, proteins in the soft corona region experience reversible binding as they are loosely bound.[67]

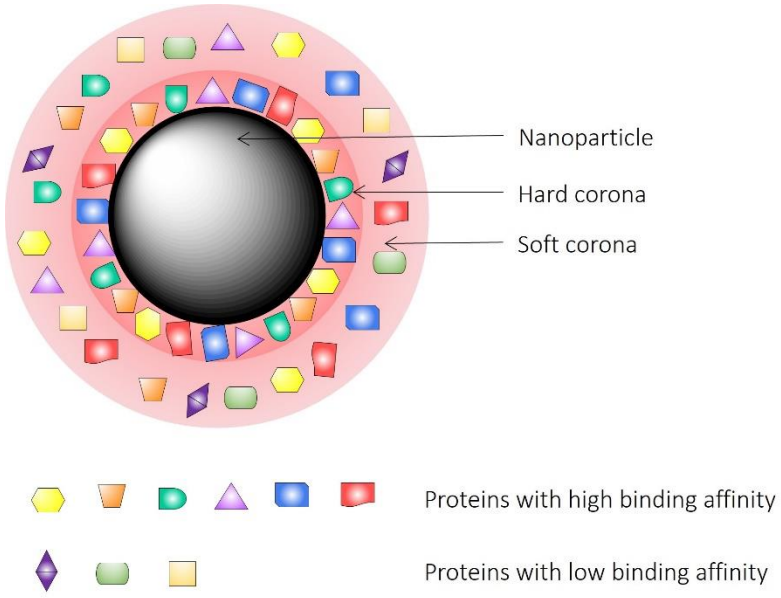

Figure 1.7 Protein corona. Proteins with a high binding affinity bind onto the nanoparticle surface first to form a hard corona, this is followed by proteins with a low binding affinity which form a soft corona.

1.4.2.2 Protein nanoparticle interactions

While protein corona is a dynamic process, protein nanoparticle interactions are complex, and there are several factors that influence the protein nanoparticle interaction. They include the physicochemical properties of the nanoparticles and the actual nature of the protein itself. The interaction between proteins and nanoparticles is facilitated by non-covalent interactions, in addition to protein binding affinity constants and the proteins thermodynamics. These non-covalent interactions include Van der Waals forces, electrostatic interactions, hydrophobic and hydrophilic interactions. It is important to note that these interactions are also influenced by the incubation/exposure time and the nature of the protein. i.e., its maintenance to keep its conformation.[62, 66]

1.4.2.3 Nanoparticle physicochemical properties and protein coronas

The influence of size on protein corona formation has frequently been investigated. Previous experiments by Dobrovolskaia et al.[68] focused on citrate capped AuNPs, their mass spectrometry data demonstrated protein corona formation when AuNPs of 30 and 50 nm were exposed to human plasma. More protein had adsorbed onto the 30 nm AuNPs compared to the 50 nm AuNPs. Lundqvist et al.[69] presented protein corona formation in 50 and 100 nm polystyrene nanoparticles (PSNP) which had been incubated with human plasma. The smaller PSNP observed a higher protein adsorption. Similar results were obtained with silica nanoparticles (SiNPs) and plasma.[70] Collectively these studies show that size is an important physicochemical property in protein corona formation. Furthermore, smaller nanoparticles

demonstrated higher protein adsorption, and this is likely due to smaller nanoparticles having larger surface areas compared with their large counter parts.

Another important physicochemical property is shape, the morphology of a nanoparticle can also influence protein adsorption. Titanium oxide nanoparticles (TiONPs) with varying morphologies that included nanorods, spheres and nanotubes all presented protein coronas when exposed to human plasma. Interestingly, specific proteins were exclusively found on the spherical TiONPs, indicating that the shape of the nanoparticles influenced which proteins adsorbed onto the surface.[71] García-Álvarez et al.[72] conducted an *in vivo* study whereby mice were administered with different morphologies and sizes of AuNPs, the recovered nanoparticles were analysed by gel electrophoresis and mass spectrometry. Their data observed protein corona formation with all the AuNPs, however the amount of protein adsorbed on the nanoparticle did not demonstrate the complex absorption dynamics of protein corona.

Surface charge is a key physicochemical property that can impact on protein corona formation. Experiments using positive, negative, and neutrally charged PSNPs of 50 and 100 nm demonstrated protein corona formation. Notably, the neutrally charged PSNPs of both sizes observed equal protein adsorption irrespective of size. Interestingly, both negatively and positively charged 50 nm PSNP showed a higher protein adsorption in comparison to the 100 nm PSNP with the same charges, which is in accordance with data reported by Dobrovolskaia

et al.[68, 69] These studies confirm that protein corona formation is not exclusively governed by one nanoparticle characteristic but rather all.

1.5 Health risk of nanoparticles

1.5.1 Nanoparticles

While nanotechnology is a rapidly emerging field, the health risks of various nanoparticles remain largely unknown. A collaborative study by Miller et al.[73] performed in healthy human volunteers demonstrated the translocation of AuNPs from the lungs into the bloodstream by acute inhalation. AuNPs of 5 nm and 30 nm were detected in blood and urine samples at 15 minutes and up to 24 hours using inductively coupled plasma mass spectrometry (ICP-MS). Unexpectedly, at a three month follow up, AuNPs were still detectable in the blood and urine. Of the two AuNPs sizes, 5 nm AuNPs were detected at high concentrations in both blood and urine. To further understand the fate of these AuNPs *in vivo*, the study was expanded into a murine model of atherosclerosis using apolipoprotein E ($ApoE^{-/-}$) deficient mice with a broader range of AuNPs from 2 to 200 nm. AuNPs of <10 nm were found at high concentrations in blood, liver and urine. Visualisation by transmission electron microscopy (TEM) revealed accumulation of AuNPs in areas of vascular inflammation. Though this study provides the link between translocation of inhaled nanoparticles into the circulatory system and sites of inflammation, the study did not address how the physicochemical properties of the nanoparticles enabled the translocation and what effect these may have on cells in the bloodstream.

PtNPs from PEMFC may pose a potential health risk, as previously discussed in section 1.2.3, the PtNPs can degrade within the PEMFC as result of their high voltages and acidic operating conditions. There are three mechanisms of degradation, carbon corrosion, platinum dissolution and migration and sintering,[74, 75] as illustrated in Figure 1.8. From carbon corrosion and platinum dissolution PtNPs can come off the carbon support and subsequently these PtNPs can enter the water supply of the PEMFC. In turn, the water would later come off the exhaust pipe and would emit the PtNPs into the atmosphere, thus, leaving them exposed to be inhaled. Which is similar to current nanoparticles coming off exhaust pipes from diesel vehicles. However, many studies focus on the catalytic performance of the PtNPs while their fate is ignored, thus, the fate of these nanoparticles out of the PEMFC remains unknown.

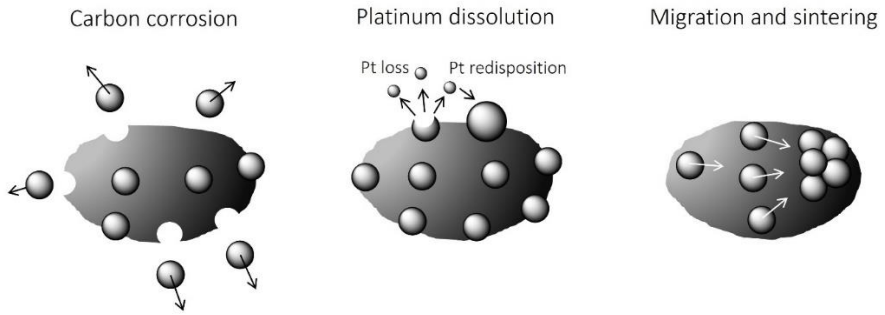

Figure 1.8. Degradation mechanism of platinum nanoparticles in proton exchange membrane fuel cells. (a) carbon corrosion, (b) platinum dissolution and (c) migration and sintering.

1.5.2 Diesel exhaust particles

Another type of nanoparticle that has been attributed to air pollution are diesel exhaust particles (DEP). They have been linked to cardiovascular and respiratory diseases both acutely and chronically.[76, 77] DEP are complex mixture of carbon, polycyclic hydrocarbons (PAHs), nitro-PAHs, sulphates, and platinum group metals mainly platinum, palladium and rhodium.[78]

Previous work by Solomon et al.[79] found that DEP were able to internalise in platelets as shown by electron microscopy analysis. Platelet aggregation was induced by direct physical interaction of DEP with human platelets *in vitro*. DEP induced platelet aggregation in mouse platelets at low concentrations *in vitro*, image analysis of the mouse lungs observed aggregated platelets and DEP at sites of aggregation. This work demonstrates a robust insight into how exposure to DEP can increase the risk of thrombotic events.

A previous study conducted by Lucking et al.[80] found a link between combustion-derived air pollution and thrombus formation. Healthy human volunteers were exposed to low concentrations of DEP and filtered air via inhalation in a controlled environment. Thrombosis formation and platelet activation was measured at two time intervals of 2 and 6 hours. Thrombosis formation was measured *ex vivo* and found to increase at both time points compared with filtered air. Post DEP exposure, flow cytometry was used to assess platelet function and found that exposure to low concentrations of DEPs was able to induce platelet activation. Overall exposure to DEP caused platelet activation which in turn led to increased thrombosis formation. While this investigation provides evidence between DEP and thrombosis formations, it also stipulates a greater understanding of how DEP exposure can affect those with pre-existing conditions, and how they are at increased risk of developing thrombotic related diseases.

1.6 Platelets

1.6.1 Platelets physiology

Platelets (thrombocytes) are small anucleate blood cells that have fragmented from megakaryocytes in the bone marrow.[81] They are central to a healthy vascular system and are primarily involved in haemostasis and thrombosis. The margination of platelets near vessel walls allows them to detect vascular injuries. In response to endothelial damage platelets are immediately recruited to form a haemostatic plug thereby preventing blood loss, see Figure 1.9. Formation of the haemostatic plug is dependent on the transformation of the platelets from their resting state to their activated state, upon activation they undergo a shape change transforming them to have projections on their cell membrane. Platelets express various surface receptors; binding of their respective ligands initiates intracellular signalling pathways which swiftly activate platelets. Healthy adults have approximately 150 – 400 x 10^9 platelets/L in their blood system with a typical life span of 8 - 9 days. Human platelets measure a diameter of 2 – 3 μm and display a biconvex discoid shape in their resting state.[82]

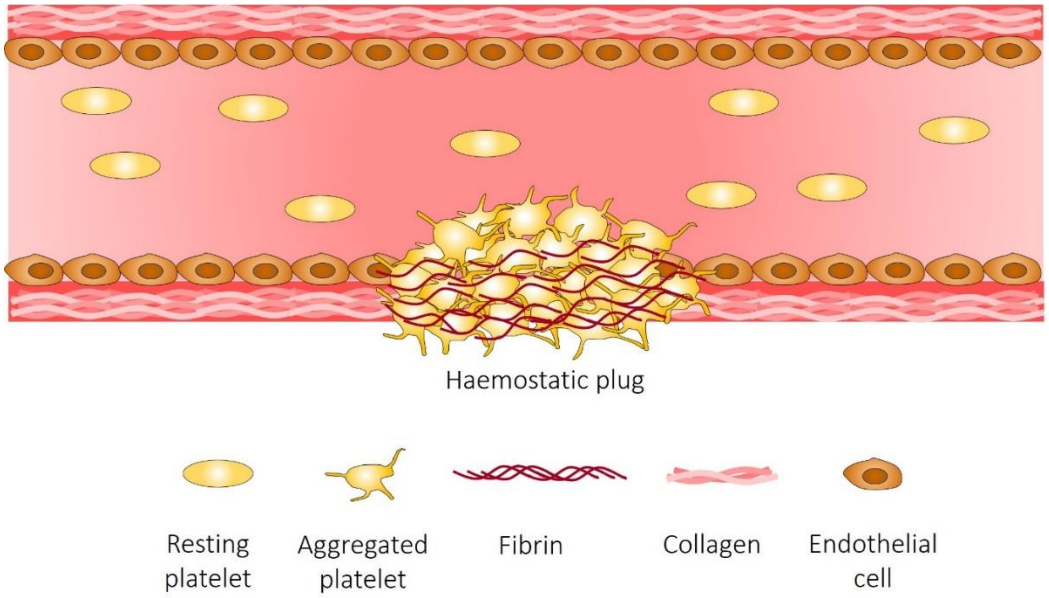

Figure 1.9 Haemostatic plug. At the site of vessel injury, platelets are recruited to exposed collagen and endothelial cells to form a haemostatic plug with fibrin. As the platelets become activated, they transform from their resting state and change shape, when they are fully aggregated, they form projections.

1.6.2 Platelet activation and aggregation

Platelet activation is a complex dynamic process that leads to platelet aggregation and formation of a haemostatic plug. At the onset of vascular injury, the subendothelium becomes exposed causing platelet adhesion to subendothelial collagen. The tethering of platelets to von Willebrand factor (VWF) brings subendothelial collagen into close proximity with glycoprotein VI (GPVI) the major platelet receptor for collagen. The interaction of both GPVI and integrin α2β1 by collagen and integrin αIIbβ3 to VWF and fibrinogen leads to platelet activation. These events leads to the confirmation change of the integrin α2β1 and αIIbβ3, leading inside out signalling and subsequently platelet adhesion.[83, 84] The binding of collagen to GPVI, which is linked to the FcR-γ chain, leads to the activation of a tyrosine kinase signalling cascade,

promoting the activation of PLC-gamma 2 and Ca^{2+} release. The activation of platelets triggers a morphological change whereby the discoid platelets become fully spread. The activation of GPVI causes the secretion of dense granules from the platelets, leading to the release of adenosine diphosphate (ADP). In addition, thromboxane A_2 is generated by the action of phospholipase A2. The two feedback agonists promote further activation of platelets which ultimately leads to platelet aggregation.[85] From this point, circulating platelets are then recruited, therefore, leading to the growth of the thrombosis. Thrombin produced via the activation of the coagulation cascades strengthens platelet activation. Furthermore, thrombin converts fibrinogen into fibrin, which stabilised the thrombosis and effectively occludes the site of injury.[86] Nevertheless, excessive activation of platelets can lead to thrombotic related diseases, the outcome of which can lead to events such as a stroke or heart attack. Charged molecules, specifically nanoparticles, can induce platelet activation and aggregation *in vitro* and induce vascular thrombosis.[87, 88]

1.6.3 Platelet-nanoparticle activation by nanoparticles

Numerous studies have reported platelet aggregation by nanoparticles, both metallic and non-metallic, see Table 1.2 and Table 1.3 and Figure 1.10. Many of these studies have investigated platelet aggregation in washed platelets to assess the direct effect of nanoparticles and have deduced different mechanisms of platelet activation which leads to their aggregation. Of the metallic nanoparticles, a large majority of the studies have primarily focused on AuNPs, AgNPs and IONPs due to their biocompatibility. Literature suggests that this activation of platelets is

governed by the physicochemical properties of the nanoparticles, these include size, shape and surface charge. These will be discussed in more detail.

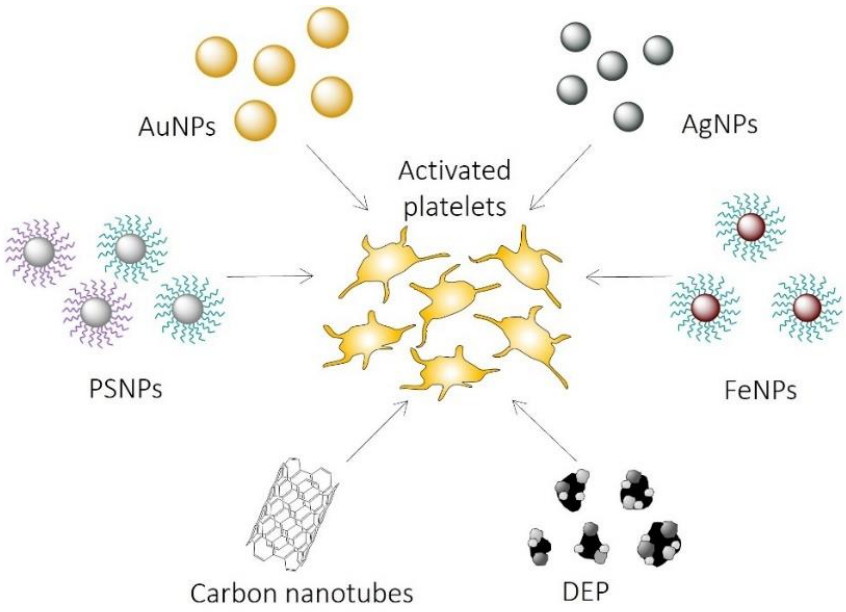

Figure 1.10 Activation of platelets by nanoparticles. Platelets have been shown to be activated by numerous nanoparticles of different materials, morphologies and size, these include gold, silver, carbon nanotubes and polystyrene nanoparticles.

Table 1.2 Metallic nanoparticle platelet interactions. This summary is from an opinion article co-written by the author of this thesis.[89] Platelet studies were performed in washed platelets (WP) and/or platelet-rich plasma (PRP) and assessed through light transmission aggregometry (LTA) or flow cytometry.

Nanoparticle	Size (nm)	Shape	Charge	Concentration	WP/PRP	Function	Proposed Mechanism (s)	Reference
Platinum	7 & 73	Spheres	Negative	log_{10} 1-4 cm^2/mL	WP	Activatory	Surface area and tyrosine kinases	90
Gold	18, 44, 55 & 68	Spheres	Negative	20 – 40 µM	WP	Activatory	Tyrosine kinases	91
Gold	30 & 50	Spheres	Negative	0.42 & 0.45 mg/mL	PRP	No effect	-	92
Gold	5, 10, 20, 30 & 60	Spheres	Negative	5 – 40 µM	PRP	No effect Inhibitory	- Size and functional group	68
Gold	12	Sphere	Negative	1.2 nM	PRP	No effect	-	93
	28, 45,63 & 85	Rods	Negative	1.2 nM	PRP	No effect		
Gold	27	Spheres	Negative	50 – 250 µg/mL	PRP	No effect	-	94
	25	Spheres	Positive	50 – 250 µg/mL	PRP	No effect	-	
Silver – PVP	20	Spheres	Negative	1 – 80 µg/mL	PRP	No effect	-	95
Silver – citrate	20	Spheres	Negative	1 – 80 µg/mL	PRP	No effect	-	
Silver	10 – 100	Spheres	Negative	50 – 250 µg/mL	WP	Activatory	GPIIb/IIIa/ calcium release	96
Silver	13	Spheres	Positive	50 µM	WP	Inhibitory	-	97
Silver	16	Spheres	Positive	5 µg/mL	PRP	No effect	-	98
Iron oxide – starch	45	Oval	-	160 µM	WP/PRP	No effect	-	99
Iron oxide – citrate	35	Spheres	-	160 µM	WP/PRP	Inhibitory	Charge	
Iron oxide – 5PAA	5 - 6	Spheres	Negative	8 – 1000 µg/mL	PRP	Activatory	Size and functional group	100
Iron oxide – 5HA	5 - 6	Spheres	Negative	8 – 1000 µg/mL	PRP	No effect	-	
Iron oxide – 5CS	5 - 6	Spheres	Positive	8 – 1000 µg/mL	PRP	No effect	-	
Iron oxide – 10PAA	10	Spheres	Negative	8 – 1000 µg/mL	PRP	Activatory	Size and functional group	
Iron oxide – 30PAA	30	Spheres	Negative	8 – 1000 µg/mL	PRP	No effect	-	

Table 1.3 Non-metallic nanoparticle platelet interactions. This summary is from an opinion article co-written by the author of this thesis.[89] Platelet studies were performed in WP and/or PRP and assessed through light transmission aggregometry (LTA) or flow cytometry.

Nanoparticle	Size (nm)	Shape	Charge	Concentration	WP/PRP	Function	Proposed Mechanism (s)	Reference
Polystyrene latex – amine	60	Spheres	Positive	12.5 – 100 µg/mL	PRP	Activatory	Functional group	[88]
Polystyrene latex – carboxyl	60		Negative	12.5 – 100 µg/mL	PRP	No effect	-	
Polystyrene latex – unmodified	60		Negative	12.5 – 100 µg/mL	PRP	No effect	-	
Polystyrene latex – amine	50 & 100	Spheres	Positive	8 – 60 µg/mL	WP/PRP	Activatory	Size and charge	[87]
Polystyrene latex – carboxyl	50 & 100	Spheres	Negative	8 – 60 µg/mL	WP/PRP	Activatory	Size and charge	
Polystyrene latex – unmodified	50 & 100	Spheres	Negative	8 – 60 µg/mL	WP/PRP	Activatory	Size and charge	
Polystyrene	25, 50, 119, 151 & 201	Spheres	Negative	$\log_{10}$ 1-3 cm^2/mL	WP	Activatory	Surface area and charge	[90]
Diesel exhaust particles	40 – 70	Agglomerates	-	0.2 – 12 µg/mL	WP	Activatory	Receptor dependent signalling	[79]
Diesel exhaust particles	35	-	-	5 – 50 µg/mL	WP	Activatory	Charge and tyrosine kinase	[101]
Single walled carbon nanotubes	-	Tubes	-	0.2 – 300 µg/mL	WP	Activatory	Receptor dependent signalling	[102]
Multi walled carbon nanotubes	-	Tubes	-	0.2 – 300 µg/mL	WP	Activatory	Receptor dependent signalling	
Single walled carbon nanotubes	1 – 2	Tubes	-	100 µg/mL	PRP	Activatory	Calcium influx	[103]
Multi walled carbon nanotubes	30, 60 & 100	Tubes	-	10 - 500 µg/mL	PRP	Activatory	Calcium influx	
Multi walled carbon nanotubes	1 – 2	Tubes	-	25 - 200 µg/mL	WP	Activatory	Receptor dependent signalling	[104]
PAMAM G4 – G6 amine	4.2 – 7.5	Spheres	Positive	1.6 – 100 µg/mL	PRP	Activatory	Functional group	[105]
PAMAM G3 – G6 carboxyl	3.5 – 7.6	Spheres	Negative	1.6 – 100 µg/mL	PRP	Activatory	- -	
PAMAM G3 – G6 hydroxyl	3 – 6.5	Spheres	Neutral	1.6 – 100 µg/mL	PRP	Activatory		

1.6.4 Platelet activation influence by nanoparticle size

Nanoparticle size is a critical factor of nanoparticle-platelet interactions. Platelet activation has been observed by nanoparticles of different sizes in washed platelets and platelet rich plasma preparations (PRP).[87, 90, 100] Previous work by Deb et al.[91] found that smaller AuNPs were able to induce platelet aggregation, while the larger AuNPs had no effect. A potential explanation for this is that smaller nanoparticles exhibit large surface areas compared to their larger counterparts. This was supported by work conducted by Zia et al.[90] where the surface area of PSNPs and PtNPs was a critical factor for platelet activation. Platelet activation was proportional to the surface area of the nanoparticles. This allows the nanoparticles to interact with the charged residues of the platelet receptors. Some studies were performed in PRP and observed no platelet aggregation by nanoparticles of varying sizes. This outcome is likely due to the formation of protein corona from proteins present in the platelet rich plasma.

1.6.5 Platelet activation influence by nanoparticle shape

Nanoparticle shape has also influenced platelet activation. Single walled carbon nanotubes (SWCNTs) and multiwalled carbon nanotubes (MWCNTs) are of tubular structures. Early studies by Radomski et al.[102] and Semberova et al.[103] found that SWCNTs and MWCNTs were able to induce platelet aggregations in both washed platelets and PRP preparations. Their proposed mechanisms involve receptor dependent signalling and calcium influx respectively. It could also be possible that SWCNTs and MWCNTs mimic molecular bridges in platelet-platelet interactions while spherically shaped nanoparticles are unable to support cell-cell communications. Additionally, platelet activation could have also been mediated through the

surface charges of the SWCNTs and MWCNTs interacting with the platelet receptors. While these studies did not show zeta potentials of these carbon nanotubes, other studies have reported that zeta potentials of -28 mV and -55 mV respectively.[106, 107]

1.6.6 Platelet activation influence by surface charge

An equally important physicochemical property is surface charge. Platelet activation has been observed by metallic nanoparticles that exhibit a negative charge and positive charge in washed platelets.[90, 91, 96, 99, 100] Investigations by Smyth et al.[87] found functionalised polystyrene latex nanoparticles (PLNPs) induce platelet activation. Carboxyl terminated PLNPs (cPLNPs) of 50 nm demonstrated the highest potency on platelet aggregation compared to amine terminated (aPLNPs) and unmodified PLNPs (uPLNPs) of 50 nm. Conversely, 100 nm uPLNPs were more potent compared to aPLNPs and cPLNPs. Work by Dobrovolskaia et al.[105] in polyamidoamine (PANAM) dendrimers showed positively charged PANAM dendrimers induced platelet aggregation in PRP in concentration dependent manner, while carboxyl and hydroxyl terminated PANAM dendrimers had no effect on platelet aggregation. In a comparison study between amine terminated PANAM and triazine dendrimers of similar sizes, the PANAM dendrimers where more potent in PRP aggregations. Additionally, large generations of dendrimers promote platelet aggregation.[108] These studies two identify both surface charge and size as two important physicochemical properties that mediate platelet activation.

1.6.7 Platelet surface receptors

Platelets express a range of surface receptors, the major platelet receptors are GPVI, C-type lectin 2 (CLEC-2), integrin αIIbβ3 (glycoprotein IIb/IIIa) and G protein-coupled receptors PAR1, PAR4, P2Y1 and P2Y12 as illustrated in Figure 1.11. As previously discussed, the interaction of the agonist and receptors leads to signalling events within the platelet, causing the platelet to change shape from the resting state into the aggregated state.[109] Various nanoparticles and have been shown to activate and aggregate platelets in vitro.[110] GPVI is the key signalling receptor for collagen Findings by Alshehri and colleagues,[101] showed that DEP were able to stimulate platelet activation through the GPVI receptor. Zia et al.[90] observed that platelet activation by PtNPs was mediated by passive agglutination and the activation of integrin αIIbβ3 via the same pathway as the DEP, potentially through the crosslinking of GPVI receptors.

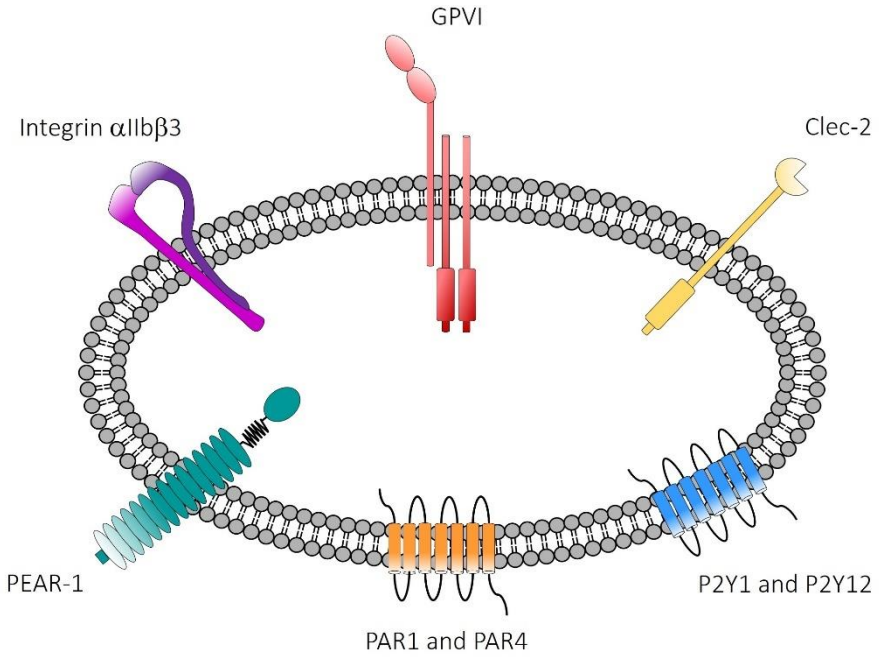

Figure 1.11 Platelet surface receptors. There are several main platelet receptors expressed on the surface of platelets that have differing structures, these include GPVI, integrin αIIbβ3, Clec-2, PEAR-1, and G protein-coupled receptors PAR1, PAR4, P2Y1 and P2Y12.

1.7 Concluding remarks

The application of nanotechnology is limitless, their applications play significant roles in medicine, biology, electronics, and hydrogen fuel cells. Nanomaterial physicochemical properties such as size and surface charge can be modified during synthesis or post synthesis. Surface modifications can enhance some the physicochemical properties proving beneficial in different applications. While these applications demonstrate the positive aspects of nanotechnology, the downside is that they could be a potential health risk. Degradation of PtNPs from PEMFC could lead to their release into the atmosphere, the fate of these PtNPs is unknown. Their physicochemical properties could potentially undergo modifications thus altering their size and surface chemistry and may pose a health risk if these PtNPs are inhaled and translocated from the lungs into the bloodstream. Various metallic nanoparticles and DEP have been shown to activate platelets *in vitro*. Excessive activation of platelets can be a causative factor for thrombotic diseases which in turn can consequently lead to undesirable events such as a stroke or a heart attack. PtNPs are of particular importance as they are the key catalyst for PEMFC, how the physicochemical properties of PtNPs can activate platelets is poorly understood and warrants further investigation.

1.8 Aims

This thesis aims to contribute to the growing knowledge of how the physicochemical properties of metallic nanoparticles influence human platelet activation. Platelet surface receptors exhibit charged residues that can interact with metallic nanoparticles. To address how the physicochemical properties of PtNPs can influence platelet activation and aggregation, an array

of PtNPs with different surface charges will be created. These will be used to investigate the interaction of PtNPs on platelet activation and aggregation. The aims of this PhD are as follows:

1. Synthesise and characterise monodispersed c-PtNPs with controlled sizes.
2. Functionalise c-PtNPs with carboxyl-terminated thiols and characterise to confirm whether the thiols have chemisorbed onto the PtNP surface.
3. Functionalise c-PtNPs with amino-terminated thiols and quaternary ammonium compounds and characterise to confirm whether the compounds have chemisorbed onto the PtNP surface.
4. Functionalise c-PtNPs with hydroxyl-terminated thiols and characterise to confirm whether the thiols have chemisorbed onto the PtNP surface.
5. Investigate how these functionalised PtNPs effect platelet activation and aggregation using physiological and biochemical analysis techniques. Examine how these functionalised PtNPs interact with plasma proteins.

1.9 Hypothesis

With the aim of synthesising c-PtNPs that will later be functionalised with a negative, positive and neutral charges using the ligand exchange method, we hypothesise that, *in vitro*, the functionalised PtNPs exhibiting a negative and positive charge will cause the human platelets to become activated leading to their aggregation. Conversely, the neutrally charged PtNPs will not have any effect on platelet aggregation. Overall, this study would provide insight on how charged PtNPs could potentially interact with platelets if they were to be inhaled and translocated into the bloodstream.

Chapter 2 Theory of Experimental Techniques

Abstract: *This chapter provides a general overview of the techniques used to assess the physicochemical properties of the platinum nanoparticles (PtNPs). Synthesised PtNPs were surface modified to create PtNPs that exhibit different surface charges. The techniques selected for the physicochemical characterisation were transmission electron microscopy, dynamic light scattering, zeta potential, gel electrophoresis and x-ray photoelectron spectroscopy. Following physicochemical characterisation, the interaction of these surface modified PtNPs with human platelets was assessed by the physiological and biochemical assays, light transmission aggregometry and western blotting. These techniques are outlined in Figure 2.1.*

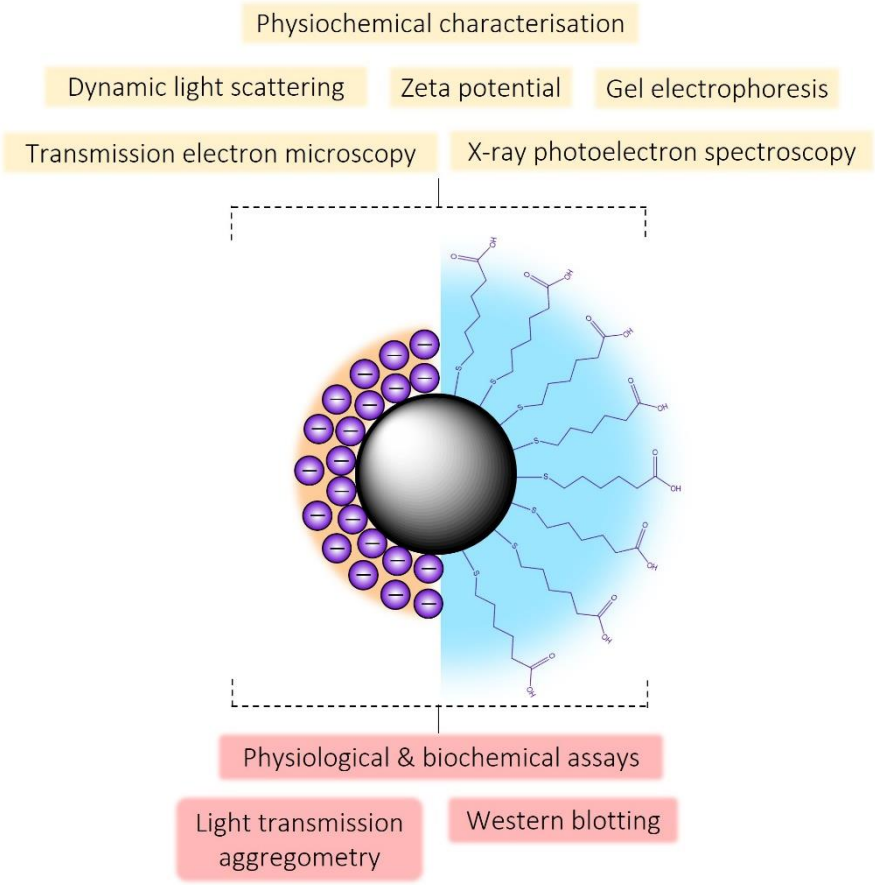

Figure 2.1 Overview of experimental techniques employed for the physicochemical characterisation of PtNPs and the physiological and biochemical assays used to assess the PtNP-platelet interactions.

2.1 Physicochemical characterisation

2.1.1 Transmission electron microscopy

Transmission electron microscopy (TEM) is an imaging technique that utilises a high energy beam of electrons to visualise a sample and produce high-resolution images; TEM carries an advantage over traditional light-based imaging techniques which are limited to the wavelength of light. In TEM, the wavelength of electrons is significantly smaller therefore high-resolution images are created. TEM is frequently used for the characterisation of nanoparticles and provides information on the particle size, morphology, composition, and in some instances the

crystalline structure.[111] TEM operates by an electron gun emitting a beam of electrons through the microscope's vacuum tube. Electromagnetic lenses are employed to focus the electrons into a fine beam, which then passes through the sample and impacts a fluorescent screen, this is illustrated in Figure 2.2. Areas where the sample is less dense the image will appear lighter as more electrons will pass through. Conversely, darker areas of the image represent areas where the sample is more dense and fewer electrons have transmitted through. There are a couple of considerations when employing TEM, first, the sample thickness, that is the amount of electron beam that can pass through the sample. Second, the sample material, heavier atoms scatter more electrons compared with lighter atoms. Metallic materials such as gold, platinum and silver have significantly high electron densities, thus, metallic nanoparticles are ideal for TEM imaging.[111, 112]

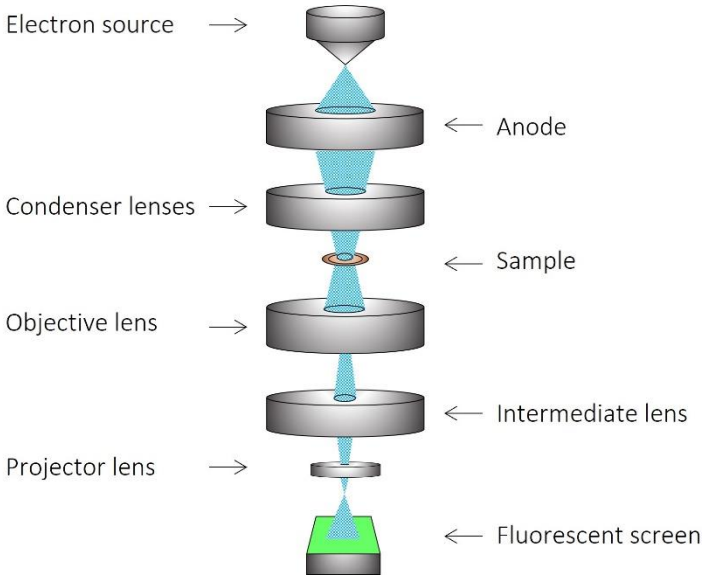

Figure 2.2 A typical transmission electron microscopy set up. The prepared TEM grid sample is placed into the instrument, a high energy beam of electrons is fired and then passed through a series of electromagnetic lenses, and the images are projected onto a fluorescent screen.

2.1.2 Dynamic light scattering

Dynamic light scattering (DLS) is a technique that measures the Brownian motion of particles in an aqueous environment and relates this to the particle size, thus, giving the hydrodynamic diameter. Brownian motion can be defined as the random movement of particles suspended in a solution; larger particles diffuse more slowly while smaller particles diffuse more rapidly.[113] The hydrodynamic diameter is determined by the translational diffusion coefficient using the Stoke-Einstein equation, see Equation 2.1.

Equation 2.1

In the Stoke-Einstein equation, d_H is the hydrodynamic diameter, D is the translational diffusion coefficient, k is the Boltzmann's constant, T is the absolute temperature and η is the viscosity. DLS functions by emitting a laser on colloidal particles which create a scattered light intensity. This scattered light intensity is measured over a period, the data is then correlated, and the hydrodynamic diameter calculated, Figure 2.3. It is important to note that DLS is a complementary technique to other size characterisation techniques mainly TEM, it not only provides the hydrodynamic diameter but also the aggregation state of the particles in solution. Monodispersed nanoparticles will have a hydrodynamic diameter similar or slightly larger than their TEM sizes. However, aggregated particles will have a higher hydrodynamic diameter compared to their TEM size. Although DLS is an inexpensive, quick and easy technique, a limitation of DLS is that it cannot distinguish between aggregated particles and large nanoparticles. An imaging method would be required to determine the state of the particles.[113-115]

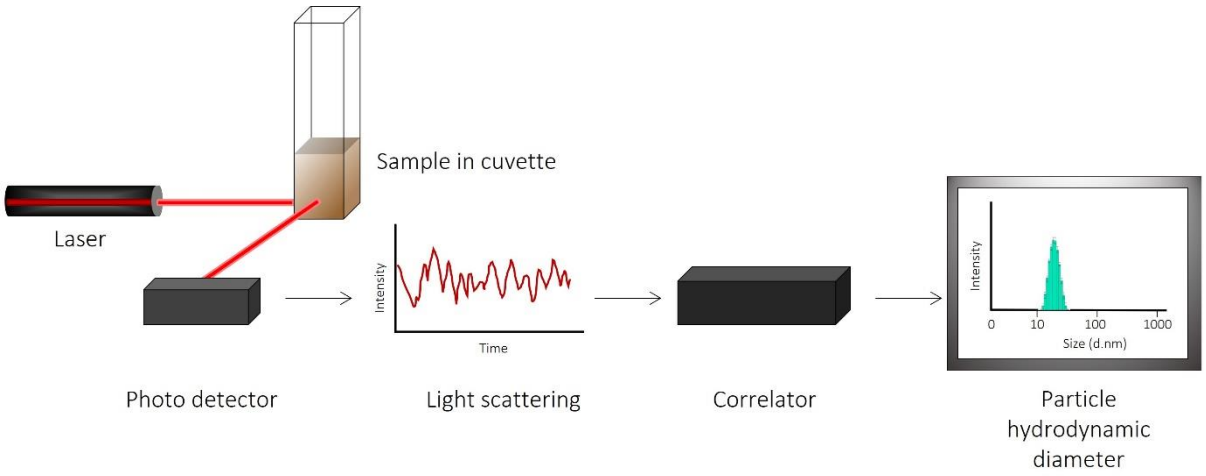

Figure 2.3 A dynamic light scattering set up. The helium laser hits the sample cuvette containing the colloidal particles and produces a scattered light intensity profile which then passes through a correlator creating a histogram of the data.

2.1.3 Zeta potential

A fundamental characterisation technique for determining the surface charge and colloidal stability of particles in solution is zeta potential.

2.1.3.1 Surface charge

Zeta potential is the electrical charge on the particle surface, it is a physical property exhibited by the particle in an aqueous solution. Nanoparticles are surrounded by two parallel layers collectively known as the electric double layer (EDL). The electric double layer comprises of the stern layer (inner region) where ions (positive or negative) are strongly bound and the slipping plane (diffuse region) where the ions are loosely bound. The slipping plane is the interface between the fluid and dispersion medium. The zeta potential itself is the potential difference from the surface of the particle to the edge of the slipping plane, as demonstrated in Figure

2.4. Furthermore, zeta potential can also determine if there has been a change in the surface chemistry.[115, 116]

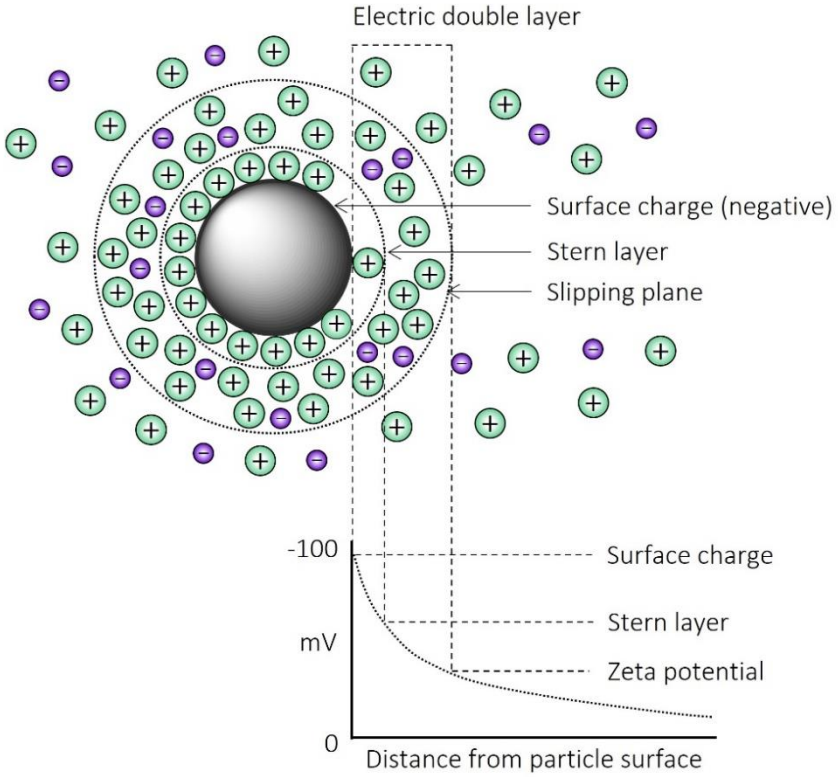

Figure 2.4 A zeta potential representation. Zeta potential measures the electric potential difference from the nanoparticle surface to the edge of the slipping plane which together make the EDL.

Zeta potential measurements are carried out in a folded capillary cell that has gold electrodes on either side. A helium neon laser is emitted and is divided creating an incident and reference beam (see Figure 2.5). The incident beam passed through an attenuator to adjust the intensity of light; this then passes through the centre of the sample. In the cell, an electric potential is applied to the sample causing the charged particles within the cell to migrate through the dispersion medium at a rate that is proportional to their zeta potential. Particles with high zeta potentials will move at a faster rate compared with particles with a low zeta potential. The

incident beam illuminates these particles which indirectly measures the particle speed through a frequency shift of scattered light, the scattered light is detected at 13° angle. The frequency shift is then converted to an electrophoretic mobility value, which is utilised to calculate the zeta potential.[116]

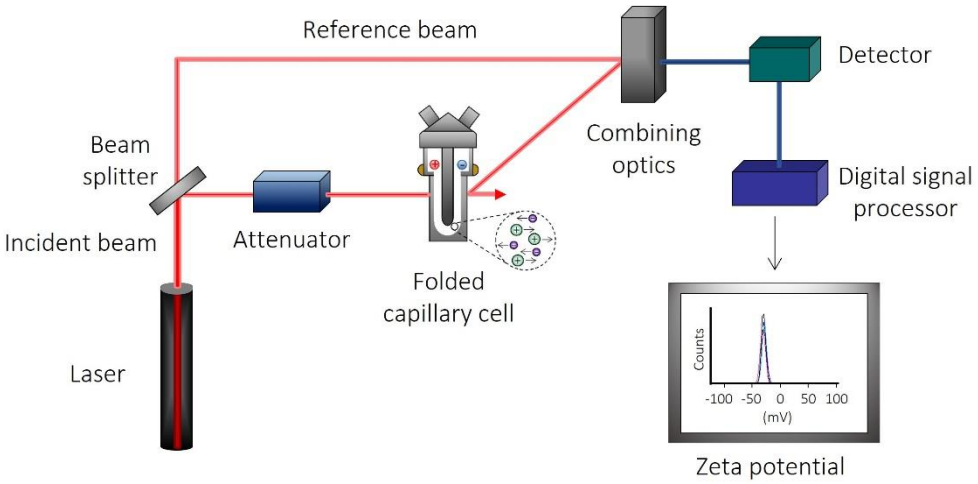

Figure 2.5 A typical zeta potential set up. Zeta potential is measured using a helium laser that splits into a reference and incident beam, the incident beam continues passing through the attenuator and then the folded capillary cell to enable zeta potential measurements. The optics of both beams are combined and pass to a detector which relays the data to the digital signal process to give the zeta potential data.

2.1.3.2 Colloidal stability

Zeta potential measurements are also indicative of colloidal stability. Based on the Derjaguin, Landau, Verwey and Overbeek (DLVO) theory, colloidal stability is determined by the combined attractive Van der Waals forces and the repulsive EDL forces that occur between moving particles due to Brownian motion.[117, 118] In a colloidal system where nanoparticles have a high repulsion, the nanoparticles will be stable and resist flocculation, however if there is low repulsion or if repulsion does not exist, flocculation or aggregation will occur. Zeta potential

measurements below -30 mV or above +30 mV suggest particles are stable.[115, 119] Figure 2.6 demonstrates the magnitude colloid stability for both negative and positively charge particles.

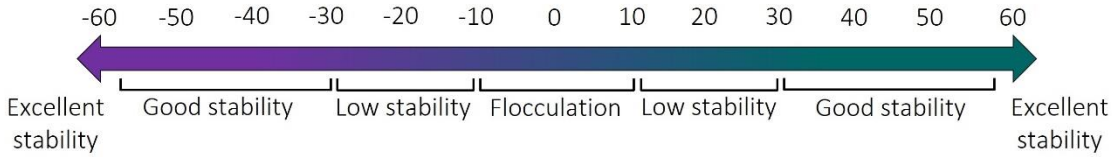

Figure 2.6 Zeta potential magnitude. Zeta potential values indicate colloidal stability of particles.

2.1.4 Gel electrophoresis

Gel electrophoresis is a common technique traditionally used for the separation of biomolecules, such as nucleic acids and proteins, based on their size and electrical charge. The technique utilises a gel matrix, either agarose or polyacrylamide, for separation. Samples are loaded into the gel matrix and an electric current is applied; this enables the migration of the biomolecules through the gel matrix as shown in Figure 2.7. Biomolecules with a positive charge will migrate towards a negatively charged electrode, conversely negatively charged biomolecules will migrate towards a positively charged electrode. Agarose is often used for the separation of nucleic acid while polyacrylamide is used for proteins, however polyacrylamide can be used for nucleic acid separation as it provides a better resolution. If we consider the similarity between metallic nanoparticles, nucleic acids and proteins all contain charged groups, thus a unique application of gel electrophoresis is the separation of metallic nanoparticles by their surface chemistry, size and shape. While this technique is qualitative, it is a relatively fast technique that can indicate a change in the surface chemistry from electrostatically stabilised to sterically stabilised nanoparticles.[120, 121]

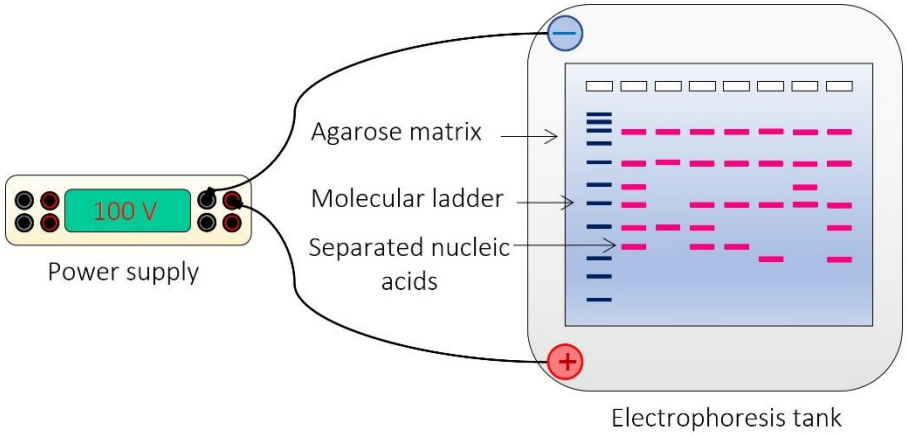

Figure 2.7 A gel electrophoresis set up. The agarose gel matrix and the voltage applied allow the separation of nucleic acids at different molecular weights.

2.1.5 X-ray photoelectron spectroscopy

Characterisation of functionalised nanoparticles in surface chemistry is a major challenge as techniques such DLS, zeta potential and gel electrophoresis are not highly sensitive and limited conclusions can be made from the data obtained, this can be overcome using X-ray photoelectron spectroscopy. XPS is a highly sensitive surface analysis technique that enables the identification of elements on a surface of up to 10 nm. The technique employs X-ray irradiation to cause ejection of photoelectrons from a sample and analyses the kinetic energies of the ejected photoelectrons to determine the elemental composition.[122] Figure 2.8 shows a basic XPS set up. An XPS set up operates by monochromatic X-ray produced form either a magnesium or aluminium proble be applied at a fixed angle to a sample that is situated in a vacuum chamber. The X-ray than causes the ejection of photoelectrons which are captured by the electron collection lens, these electrons are then detected by a hemispherical electron detector and analysed to generate an XPS spectra of the sample.

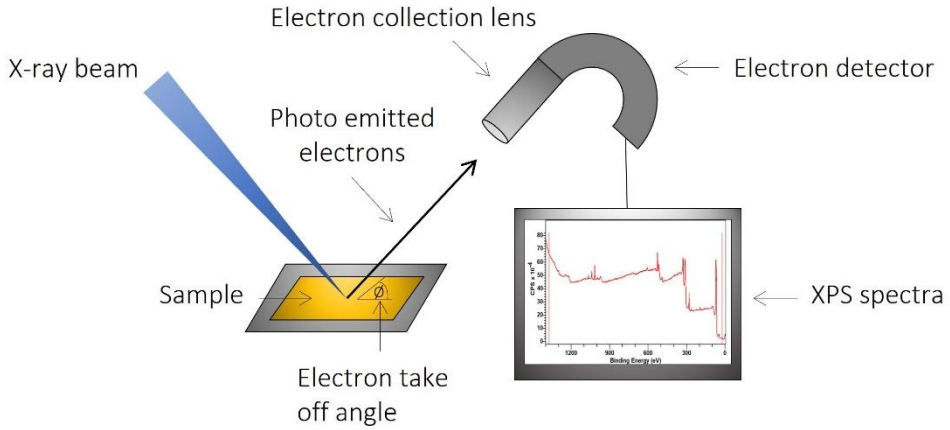

Figure 2.8 A typical X-ray photoelectron spectroscopy set up. A sample is positioned onto a platform within an ultra-high vacuum chamber. Monochromatic Kα X-rays produced from either magnesium or aluminium probes is directed onto the sample causing an ejection of photoelectrons. These photoelectrons are collected by the electron lens and detector to create an XPS spectra of the sample.

In the photoelectron process, when an electron is emitted subsequently a second electron from a higher energy level will move position to fill the vacancy causing a release of energy. There are two consequences for this energy, either by releasing an X-ray or release of another electron known as an auger electron,[122, 123] as illustrated in Figure 2.9. Using the kinetic energy (E_K) released from this process the binding energy of the electron can be calculated using equation 2.2:

Equation 2.2

In this equation, E_B is the binding energy, while hv is the photon energy from the X-ray, and W is the work function of the spectrometer. The binding energy of each atom vary depending on their environment, i.e., when alone or within a molecule, this will be reflected in the binding energies of the XPS spectra. Thus, an XPS spectra will comprise of peaks with characteristic binding energies for each atom and the different chemical environments within the sample.

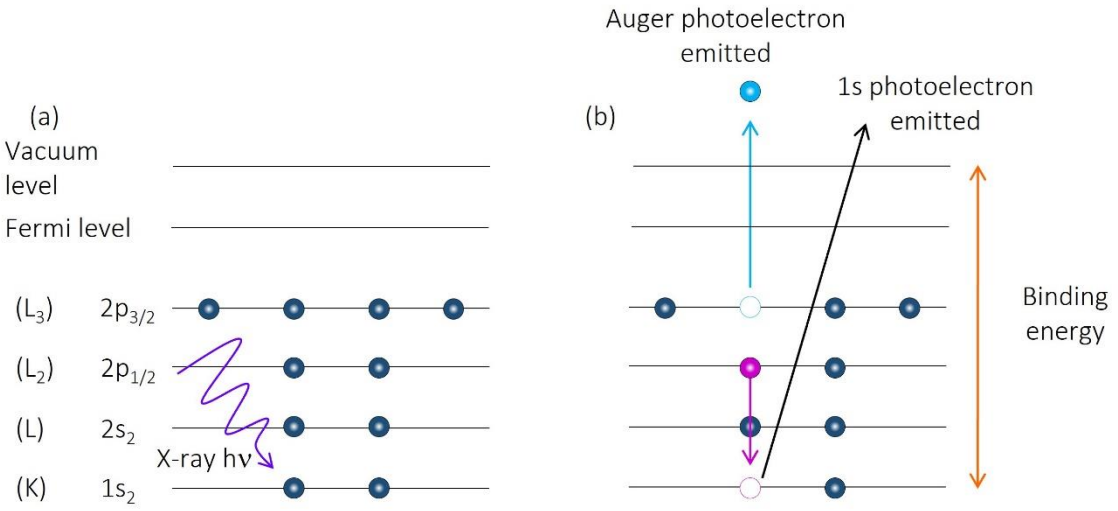

Figure 2.9 Photoelectron emission. (a) The sample is bombarded with an X-ray causing the emission of a photoelectron from 1s2 orbital. (b) An electron from a higher energy will occupy the vacancy generating an energy release. This energy will either be released as an X-ray or an Auger electron.

Binding energies will vary depending on several factors; electrons situated in orbitals further away from the nucleus will require less energy to eject them, therefore higher orbitals have lower binding energies. Electrons within different subshells i.e. s, p or d orbitals, will have different energies. Furthermore, binding energies are also dependent on the chemical environment of the atom, that is their chemical bonds, for example if we consider carbon (C-C) and carbonyl carbon (C=O) these two carbons will have different binding energies. With this information combined a material composition can be confirmed.[122, 123]

2.2 Physiological and biochemical assays

2.2.1 Light transmission aggregometry

Light transmission aggregometry (LTA) is a photometric technique used for assessing platelet function and is crucial for the diagnosis of patients with bleeding disorders. The original concept of LTA was described over 60 years ago and remains the gold standard for measuring platelet aggregation *in vitro*.[124] The method detects the changes in turbidity, caused by platelet aggregation, by measuring the variation in light transmission. In platelet biology, LTA measures the aggregation in either washed platelets or platelet-rich plasma (PRP) by measuring the light transmission in the presence of a platelet agonist over a time course, as illustrated in Figure 2.10. Both washed platelet suspensions and PRP start off almost opaque having 0% aggregation and allowing little light to pass through the sample, at this resting state platelets remain in their biconvex shape. Upon the addition of a platelet agonist e.g., collagen, the platelets start to transform and exhibit projections, during this phase the suspension starts to become clear increasing the light transmitting through the sample. As the platelets become completely aggregated there is a further increase in light transmission. This is demonstrated in the aggregation curve, where the extent of light transmission is proportional to the degree of platelet aggregation.[125]

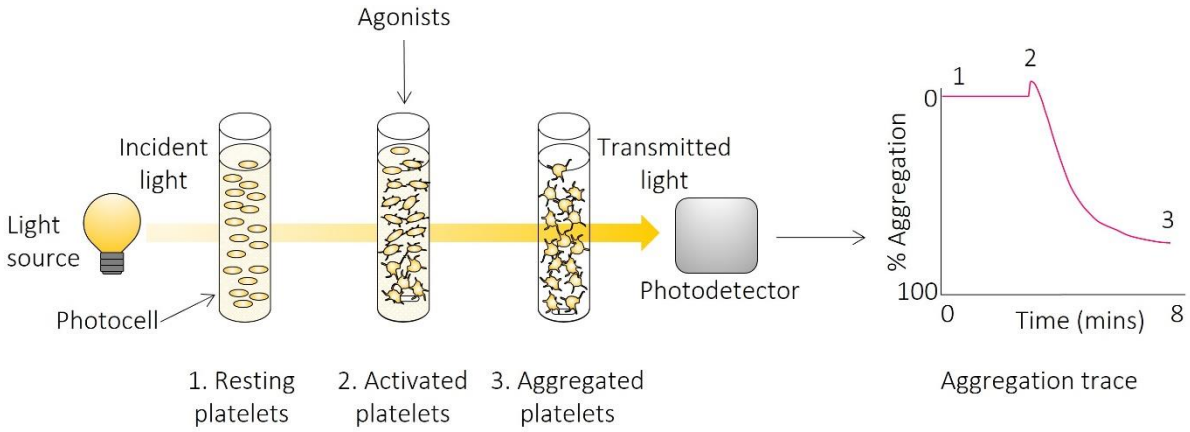

Figure 2.10 Light transmission aggregometry of platelets. An increased light transmission is observed as platelets activated and finally aggregated; this is demonstrated by the aggregation trace.

2.2.2 Western blotting

Western blotting is a biochemical technique routinely used for immunodetection of a protein(s) from a mixture of proteins, usually derived from tissue or cells. It is frequently used for examining target proteins and their isoforms, protein-protein interactions, nucleic acid-protein interactions, antibody characterisation, post-translational modifications, and signalling cascades.[126] There are 5 main steps in western blotting: (a) sample preparation, (b) gel electrophoresis, (c) electroblotting, (d) blocking and antibody incubation and (e) detection; this is illustrated in Figure 2.11. More in detail, samples are prepared by the extraction of proteins from either tissue or cells using lysis buffers containing detergents that breaks open cell membrane and conserves the protein of interest. As previously discussed, proteins can be separated by molecular weight using a polyacrylamide gel electrophoresis (PAGE). The polyacrylamide creates a porous structure which allow smaller proteins to migrate rapidly through the gel matrix compared with larger proteins therefore enabling the physical separation of the proteins. These separated proteins are then transferred to a solid support

either a nitrocellulose or polyvinylidene difluoride (PVDF) membrane by electroblotting. Here the gel matrix and membrane are sandwiched together with filter paper between two electrodes, a voltage is applied to the electrodes eluting the proteins from the gel matrix onto the membrane. After transfer, proteins will be immobilised on the membrane, to prevent non-specific binding the membrane is blocked to reduced high background signal. Primary antibodies specific to the protein of interest are incubated with the membrane, the membrane is then incubated with a secondary antibody that is specific to the primary antibody. For detection, the secondary antibody is conjugated with an enzyme or fluorescent molecule, which allows chemiluminescence or fluorescence for imaging the protein of interest either by X-ray film or digital imaging.[126, 127]

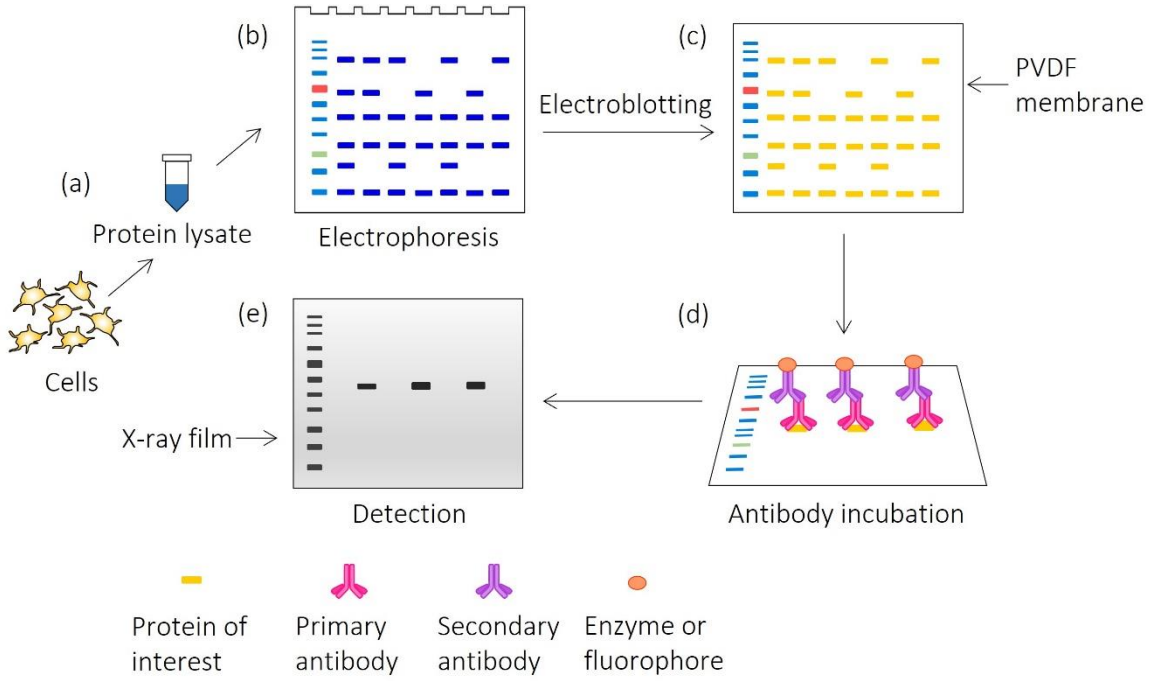

Figure 2.11 Western blotting overview. (a) Protein lysates are produced from cells ready for electrophoresis using lysis buffers, (b) proteins are separated by their molecular weight using electrophoresis, (c) separated proteins are transferred to a PVDF membrane by electroblotting, (d) the membrane is blocked and incubated with a primary antibody specific to the protein of interest followed by a secondary antibody conjugated to enzyme or fluorescent probe and (e) finally an X-ray film is exposed onto the PVDF membrane to detect the protein of interest.

Chapter 3 Materials and Methods

3.1 Materials & Chemicals

All chemicals were purchased from Sigma unless stated otherwise.

3.2 Platinum nanoparticle synthesis

3.2.1 Glassware preparation

Prior to synthesis all glassware was cleaned to prevent heterogenous nucleation occurring from metallic nanoparticles or dirt. Glassware was soaked overnight in the 1% Liquinox solution (anionic detergent) followed by thorough rinsing with tap water and complete drying. Aqua regia was prepared in a molar ratio of 3:1 of hydrochloric acid (Fisher Chemical 37%, Leicester UK) and nitric acid (Fisher Chemical 70%, Leicester UK). Synthesis glassware was then soaked in aqua regia for a minimum of 3 hours to ensure all traces of metal had dissolved. Aqua regia was neutralised by saturated sodium carbonate. Following neutralisation, all glassware was thoroughly rinsed with deionised water to remove all traces of the acids, then dried and covered with parafilm until synthesis to prevent flocculation sites during synthesis.

3.2.2 Chloroplatinic acid preparation

To ensure consistency in the PtNP synthesis reactions, chloroplatinic acid hexahydrate ($H_2PtCl_6.6H_2O$), (37.50% platinum basis) was prepared at a 1 M stock solution with dH_2O. 1.93 mL of degassed dH_2O was added directly into the $H_2PtCl_6.6H_2O$ stock bottle and left to stand

for a day before using. On each use of $H_2PtCl_6.6H_2O$, the stock bottle was purged with argon for 5 minutes to prevent oxidation of $H_2PtCl_6.6H_2O$.

3.2.3 Platinum seed synthesis

Pt seeds were synthesised by adding 3.6 mL of 3.86 mM $H_2PtCl_6.6H_2O$ to 46.6 mL of boiling dH_2O with continuous stirring. After 1 minute, 1.1 mL of 34 mM sodium citrate/2.38 mM citric acid was added to the reaction. After 30 seconds, 500 µL of 21 mM sodium borohydride ($NaBH_4$) /34 mM sodium citrate/2.38 mM citric acid was injected into the reaction. The reaction continued stirring at 100^oC for 10 minutes before cooling down to room temperature. Pt seed synthesis was performed on a 5x reaction scale.

3.2.4 Platinum nanoparticle synthesis

20 nm PtNP were synthesised using the Pt seeds as a template. Under inert conditions, 1 mL of Pt seed solution was added to 29 mL of dH_2O at room temperature. 45 µL of 0.035 M $H_2PtCl_6.6H_2O$ was added to the reaction followed by 500 µL of 34 mM sodium citrate/71 mM L-ascorbic acid. With continuous stirring the temperature was increased 10^oC/minute to boiling; the total reaction time was 30 minutes. Scaled up PtNP synthesis reactions were also performed on a 2x, 5x and 10x reaction scale. PtNPs were centrifuged at 10000 x g, the supernatant was discarded and the PtNPs were resuspended in 1.1 mM sodium citrate, this process was repeated twice. 60 nm PtNP were synthesised in same way as described above using an increased concentration of $H_2PtCl_6.6H_2O$ at 0.4 M to achieve nanoparticles of about 60 nm at the same reaction scales. In consequent synthesis reactions a new batch of

$H_2PtCl_6.6H_2O$ was used, however due to batch-to-batch variation to achieve 20 nm PtNP the concentration of $H_2PtCl_6.6H_2O$ was adjusted to 0.2 M.

3.3 Functionalisation of PtNP

All alkanethiols and PEGylated thiols used in this thesis are listed Table 3.1.

Table 3.1 Alkane and PEGylated thiols used for functionalisation experiments.

Thiol name	Alkane or PEGylated	Functional group charge
6-Mercaptohexanoic acid (6-MHA)	Alkane	Negative
8-Mercaptooctanoic acid (8-MOA)	Alkane	Negative
Thioctic acid (TA)	Alkane	Negative
O-(2-Carboxyethyl)-O'-(2-mercaptoethyl) heptaethylene glycol (2-MOHA)	PEGylated	Negative
Cysteamine hydrochloride (CSH)	Alkane	Positive
6-Amino-1-hexanethiol (6-AHT)	Alkane	Positive
11-Amino-1-undecanethiol hydrochloride (11-AUT)	Alkane	Positive
6-Mercaptohexanol (6-MCH)	Alkane	Neutral
2-{2-[2-(2-Mercaptoethoxy)ethoxyethoxy}ethanol (2-MEE)	PEGylated	Neutral
11-Mercaptoundecyl)hexa(ethylene glycol) (11-MUHEG)	PEGylated	Neutral

3.3.1 Solubility of alkanethiols

A fresh 2 mM stock of the desired alkanethiols from Table 3.1 were prepared in dH_2O and ethanol. Solubility was observed at 3 and 24 hours. After solvent solubility was assessed, alkanethiol solubility with PtNPs were assessed. Fresh 2 mM alkanethiol stocks were prepared in dH_2O and ethanol. 2 x 1 mL PtNP aliquots were prepared in clean glass vials per alkanethiol tested. 50 µl of 2 mM alkanethiol prepared in dH_2O was added to the first PtNP aliquot. 50 µl

of 2 mM alkanethiol prepared in ethanol was added to the second PtNP aliquot. Samples were left on an orbital shaker and solubility was observed at 3 and 24 hours.

3.3.2 Functionalisation of PtNPs by alkanethiols and pegylated thiols

Using the total surface area of a batch of 20 nm PtNPs, the alkanethiol footprint 0.214 nm^2 or the pegylated 0.35 nm^2 footprint and Avogadro's number, the number of alkanethiol molecules required for surface coverage was calculated, see Appendix for full calculations.[128, 129] For surface modification with alkanethiols, the total surface area of a 20 nm PtNP was calculated to be 1506.74 nm^2; with total surface area and the alkanethiol footprint, the number of alkanethiol molecules needed to coat each PtNP was 7040.83. Thus, using Avogadro's number, it was calculated that 5.9 µM of the alkanethiol was required for coverage. To ensure complete surface coverage, surface modifications were carried out in a 10x excess of alkanethiol. A fresh 2 mM alkanethiol stock was prepared on each day of the surface modification experiment. 6 x 1 mL PtNP aliquots were prepared in clean glass vials; 2 mM of alkanethiol was added to the aliquots in the volumes specified in Table 3.2. The reactions were left to incubate on an orbital shaker for 3 hours at room temperature. Samples were transferred to 1.5 mL tubes and then centrifuged at 10,000 x g for 10 minutes. Supernatants were discarded and each sample was resuspended in 1 mL of dH_2O and transferred into clean glass vials. The volumes and concentrations of the PEGylated thiols used for the functionalisation of the PtNPs are specified in Table 3.3.

Table 3.2 Final concentration and volume of alkanethiol added to coat platinum nanoparticles.

Final alkanethiol concentration (µM)	Volume of 2 mM alkanethiol (µL)
5	2.5
10	5
30	15
50	25
70	30
100	50

Table 3.3 Final concentration and volume of PEGylated thiols added to coat platinum nanoparticles.

Final PEG thiol concentration (µM)	Volume of 2 mM PEG thiol (µL)
3	1.5
5	2.5
10	5
30	15
50	25
70	35

3.3.3 Platinum nanoparticle synthesis with cetrimethylammonium bromide

Positively charged PtNPs were synthesised with the method described in section 3.2.4 with cetrimethylammonium bromide (CTAB, VWR, UK) as the capping agent and L-ascorbic acid as the reducing agent. Under the same conditions, 1 mL of platinum seed solution was added to 29 mL of deionised water at room temperature. 45 µL of 0.2 M $H_2PtCl_6.6H_2O$ was added to the reaction followed by 500 µL of 34 mM CTAB/71 mM L-ascorbic acid. Again, with continuous stirring the temperature was increased 10^{o}C/minute to boiling, giving a total reaction time of 30 minutes. CTAB capped PtNPs were centrifuged at 10000 x g, the supernatant was discarded and the PtNPs were resuspended in 1.1 mM CTAB.

3.3.4 Functionalisation of platinum nanoparticles with (6-aminohexyl)trimethylammonium bromide hydrobromide

Using total surface area of PtNP-CTAB, the approximated footprint of (6-aminohexyl)trimethylammonium bromide hydrobromide (6-ATA) was 0.145 nm^2 (derived from Chem3D by measuring the area), the concentration of 6-ATA required for surface coverage was calculated to 4.5 µM, see Appendix 11.2 for full calculations. For complete surface coverage, surface modifications were carried out in a 10x excess of 6-ATA. A fresh 2 mM 6-ATA stock was prepared on the day of the experiment. 6 x 1 mL PtNP aliquots were prepared in clean glass vials; 2 mM of 6-ATA was added to the aliquots in the volumes specified in Table 3.4. The reactions were left to incubate on an orbital shaker for 3 hours at room temperature. Samples were transferred to 1.5 mL tubes and then centrifuged at 10,000 x g for 10 minutes. Supernatants were discarded and each sample was resuspended in 1 mL of dH_2O and transferred into clean glass vials.

Table 3.4 Final concentration and volume of 6-ATA added to coat PtNP-CTAB.

Final 6-ATA concentration (µM)	Volume of 2 mM 6-ATA (µL)
3	1.5
5	2.5
10	5
30	15
50	25
70	35

3.3.5 Platinum nanoparticle synthesis with 2-diethylaminoethanethiol

2-Diethylaminoethanethiol (DEA) was used as the capping agent to synthesise positively charged PtNPs with sodium borohydride as the reducing agent. 0.48 mM $H_2PtCl_6.6H_2O$ was prepared in dH_2O at pH 2, 10 mL of 0.48 mM $H_2PtCl_6.6H_2O$ and 10 mL of 0.16 mM DEA was added to a reaction flask. The reaction was degassed with argon for 10 minutes. 10 mL of 2.4 mM $NaBH_4$ was added dropwise. The reaction was then left for 20 hours, aliquots of the reaction were characterised with and without centrifuging. PtNP-DEA were centrifuged at 10000 x g, supernatant was discarded, and PtNP-DEA were resuspended in dH_2O. The reaction was repeated with varying concentrations of DEA.

3.3.6 Platinum nanoparticle synthesis with 6-mercaptohexanol

Neutrally charged PtNPs were synthesised using the method previously used in section 3.2.4 with 6-mercaptohexanol (6-MCH) as the capping agent and L-ascorbic acid as the reducing agent. Due to the high cost of 6-MCH the reaction was scaled down from 30.55 mL to 10 mL. Under inert conditions, 327 µL of Pt seeds were added to 9.49 mL of dH_2O. 15 µL of 0.2 M $H_2PtCl_6.6H_2O$ was added to the reaction, along with 163.7 µL of 34 mM 6-MCH/71 mM L-ascorbic acid. Again, with continuous stirring the temperature was increased 10^oC/minute to boiling. The reaction was repeated under the same conditions with 21 mM $NaBH_4$ as a reducing agent and 6-MCH as a capping agent.

3.4 Nanoparticle characterisation

3.4.1 Transmission electron microscopy

TEM was performed at the Electron Microscopy Facility by Natalie Allcock at the University of Leicester, UK. Pt seeds were prepared for TEM imaging by diluting samples in 1:2 with dH_2O. For the PtNPs, 1 mL of PtNP solution was centrifuged at 10000 x g, the supernatant was discarded and the PtNPs were resuspended in 400 µL of deionised water. Samples were briefly sonicated and 10 µL of the PtNP suspension was applied to a freshly glow discharged (Quorum technologies, UK: Q150TES coating unit, 30 µA for 30 seconds) carbon film copper grid (Agar scientific, UK) for 20 minutes. Samples were blotted with filter paper and left to dry before imaging. TEM images were obtained using the JEOL JEM-1400 TEM with an accelerating voltage of 120kV; images were captured using a EMSIS Xarosa digital camera with Radius software. ImageJ software was used to measure the diameters of 200 individual nanoparticles to obtain the average PtNP diameter. The average diameters were then used to determine the frequency distribution and to calculate the surface area/mL of the PtNP.

3.4.2 Dynamic light scattering

DLS measurements were carried out using the Malvern Panalytical Zetasizer Nano ZS instrument (Malvern, UK) with Pt refractive index of 1.340 and absorption value 0.000. 1 mL of PtNPs were placed in a semi-micro cuvette (Fisherbrand, Leicester UK) with a 1 cm path length and placed into the Zetasizer, measurements were taken using a helium-neon laser at 633 nm and scattering detector at 173 degrees. 5 measurements were taken per sample and the average hydrodynamic diameter was reported in nm.

3.4.3 Zeta potential

Zeta potential measurements were also made using the same Malvern Panalytical Zetasizer Nano ZS instrument with the same refractive index and absorption values described for DLS measurements. 700 µL of PtNP was loaded into a folded capillary cell (Malvern Panalytical, DTS1070) using a 1 mL syringe. The cell was placed into the Zetasizer and measurements were taken using the red laser light at 633 nm, 5 measurements were taken per sample and the average zeta potential was reported in mV. All samples measured by zeta potential had pH measurements taken using a Inlab Semi Micro Probe (Mettler Toledo, Leicester UK).

3.4.4 Gel electrophoresis

PtNPs were surface modified using the lowest and highest concentrations specified in Table 3.2 and Table 3.3. Reactions were left to incubate for 3 hours at room temperature on an orbital shaker. A 1 % agarose gel was prepared by dissolving 0.5 g of agarose with 50 mL of 1x Tris-acetate-EDTA (TAE) buffer. The mixture was heated in a microwave for 1 -2 minutes at full power (950 W) and left to cool for 5 minutes. The agarose solution was poured into the electrophoresis cassette and left to solidify. Surface modification reactions were transferred to 1.5 mL tubes and centrifuged at 10000 x g for 10 minutes, the supernatant was discarded leaving the concentrated pellet. 1 µL of the surface modified PtNPs were premixed with 15 µL glycerol to assist depositing in the agarose gel wells. The solidified agarose gel was then submerged into 1x TAE buffer in the electrophoresis tank. The surface modified PtNPs were then deposited into each well and then run at 100 V for 30 – 40 minutes. Images were captured were taken with a standard smart phone.

3.4.5 X-Ray Photoelectron spectroscopy

3.4.5.1 XPS sample preparation

Copper discs (Alfa Aesar, UK) were used as a substrate for the XPS analysis of PtNPs alone and functionalised PtNPs. Copper discs were cleaned with chloroform and then ultrasonicated with isopropanol. Oxide reduction was performed by Abubakr Siddiq at the Birmingham Centre for Fuel Cell and Hydrogen Research, University of Birmingham, UK. The reduction procedure was carried out by placing copper discs in a Vecstar Split Tube Furnace and reduced with hydrogen and nitrogen gases at a flow rate of 50 mL/min, see Table 3.5 for program settings. Functionalised PtNPs were prepared as described in section 3.3.2, after centrifugation, supernatant was discarded, and the concentrated pellet was drop cast onto the copper discs with a glass pipette. Samples were left to dry and were wrapped in lint free tissue and foil and sent for XPS analysis.

Table 3.5 Vecstar Split Tube Furnace settings for oxide reduction.

Segment	Process
1	Ramp at 1°C/min to 300°C
2	Dwell 12 hours at 300°C
3	Ramp cool down at 2°C/min to 25°C

3.4.6 XPS Instrumentation and data analysis

XPS experiments were conducted by Dr Mark Issacs at the Harwell XPS EPSRC National Facility for XPS, Harwell, UK; data was acquired using Kratos Axis SUPRA system. The instrument used a monochromatic Al Kα X-ray source of 1486.69 eV at take-off angle of 90° to the surface plane. High resolution scans were acquired of Pt (4f), C (1s), O (1s), S (2p), Cu (2p) and Cu (LMM, Auger

parameter) with a pass energy of 20 eV at a step size of 0.1 eV. Peak fittings were conducted using the CasaXPS software version 2.3.25 all spectra were corrected to C (1s) at 284.6 eV and 285 eV for pegylated thiols.

3.5 Physiological and biochemical assays

3.5.1 Chemicals for platelet aggregation and western blotting

Reagents used in platelet aggregation and western blotting analysis are listed in Tables 3.6, 3.7, 3.8 and 3.9.

Table 3.6 Agonists used in platelet and platelet-rich plasma aggregations.

Agonist	Target Receptor	Concentration	Supplier
Thrombin	PAR1, PAR4	1 U/mL	Sigma, UK
Collagen related peptide (CRP)	GPVI	3 µg/mL	Dr Richard Farndale, University of Cambridge
PAR1 peptide (SFLLRN)	PAR1	50 µM	Alta Biosciences, Birmingham UK

Table 3.7 Inhibitors used in platelet aggregations and phosphorylation experiments.

Inhibitors	Target	Concentration	Solvent	Supplier
Prostacyclin (PGI_2)	Platelet inhibitor	1 µg/mL	Tris-buffer pH 9.1	Cayman Chemicals (Cambridge, UK
PP2	Src-family kinase inhibitor	20 µM	1% DMSO	TOCRIS (Abingdon, UK)
PRT-060318	Syk inhibitor	3 µM	1% DMSO	Caltag Medsystems (Buckingham, UK)
EGTA	Calcium chelator	1 mM	100 mM NaOH	Sigma, UK

Table 3.8 Primary antibodies used in Western blotting.

Antibody	Dilution	Molecular weight (kDa)	Supplier
Phosphotryrosine (4G10)	1:1000	-	Merck Millipore Abingdon, UK
Phospho Syk pY525/6	1:500	72	Cell Signalling, Leiden, The Netherlands
Phospho-LAT	1:500	37	Abcam, Cambridge, UK
α- tubulin	1:1000	50	Millipore/Sigma, UK
Syk 4D10	1:200	72	Insight Biotechnology, UK

Table 3.9 Secondary antibodies used in Western blotting.

Antibody	Dilution	Supplier
Anti-mouse-HRP	1:10000	Cytiva, Amersham, UK
Anti-rabbit-HRP	1:10000	Cytiva, Amersham, UK

3.5.2 Human washed platelet preparation

All platelet experiments were conducted at the Birmingham Platelet Research Laboratory, University of Birmingham UK. For blood donation by healthy volunteers' ethical approval was granted by Birmingham University Internal Ethical Review (ERN_11_0175). Blood was drawn from consenting healthy volunteers, free of anti-platelet drugs (minimum time of 10 days) in vacutainers containing 3.2% (w/v) sodium citrate on the day of the experiments for both preparations of washed platelets. Following blood collection, acid citrate dextrose (ACD) was added to the blood (1:10 v/v) as anticoagulant. The anticoagulated blood was centrifuged at 200 x g for 20 minutes at room temperature and to obtain the platelet rich plasma (PRP). The collected PRP was centrifuged in the presence of 10 µg/mL of prostacyclin (PGI_2) at 1000 x g for 10 minutes at room temperature, PGI_2 was added to inhibit platelet activation. The plasma was discarded leaving a platelet pellet, the pellet was re-suspended in Tyrodes-HEPES buffer (134 mM NaCl, 2.90 mM KCl, 0.34 mM Na_2HPO_4:$12H_2O$, 12 mM $NaHCO_3$, 20 mM HEPES, 1 mM $MgCl_2$ and 10 mM glucose, pH 7.3) with ACD (1:8 v/v). The platelets were centrifuged again in the

presence of 10 µg/mL PGI_2 at 1000 x g for 10 minutes at room temperature. The platelet pellet was re-suspended in Tyrodes-HEPES buffer and the washed platelets were quantified on the Coulter counter (Beckman Coulter Zcs counter, Beckman Coulter, High Wycombe, UK). The washed platelet concentration was adjusted with Tyrodes-HEPES buffer to 2 x 10^8 platelets/mL or 4 x 10^8 platelets/mL for platelet aggregation and biochemical analysis experiments respectively. Washed platelets were left to rest for 30 minutes before proceeding to experiments.

3.5.3 Human platelet rich plasma preparation

Human PRP was prepared in a similar manner to washed platelet, blood was collected in vacutainers with 3.2% (w/v) sodium citrate, however, no ACD was added to the blood. The blood was centrifuged at 200 x g for 20 minutes at room temperature. PRP was collected and retained into a separated tube ready for platelet aggregation experiments. The remaining blood was centrifuged at 1000 x g to obtained platelet poor plasma (PPP) which was later used a blank control for the LTA experiments.

3.5.4 Light transmission aggregometry

Platelet function was assessed by LTA using a Chrono-log 460-VS optical aggregometer (Labmedics, Manchester UK) at 37^{o}C. Aggregation tubes (with stir bars) containing 400 µL of washed platelet or PRP was pre-warmed for 2 minutes at 37^{o}C, then stirred for 1 minute at 1200 rpm before the addition of agonists. Aggregations were then recorded for 5 minutes, see Figure 3.1 for experiment timeline. Blank aggregation tubes either contained either Tyrodes-

HEPES buffer or PPP for experiments with washed platelets or PRP respectively. For platelet inhibitor aggregations, inhibitors were added to washed platelets 1 minute prior to agonist stimulations, aggregations were then recorded up to 5 minutes.

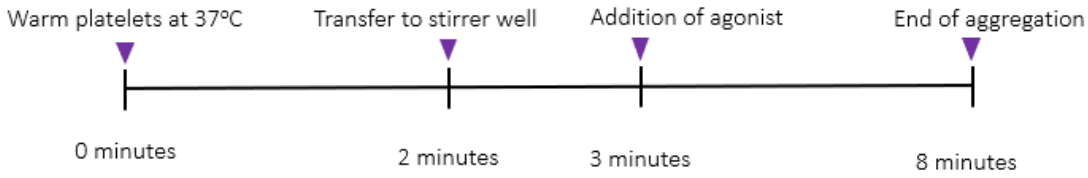

Figure 3.1 Aggregation stimulation timeline.

3.5.5 Protein phosphorylation

Washed platelets were pre-treated with (ethylene glycol-bis(β-aminoethyl ether)-N,N,N′,N′-tetraacetic acid) (EGTA) to prevent platelet aggregation; EGTA chelates to intracellular calcium which regulates platelet activation. Agonists were added under the same conditions described in section 8.6.4. For inhibitor experiments, inhibitors were added 5 minutes prior to agonist stimulations. Whole cell lysates (WCL) were prepared from these experiments by terminating experiments with 2X Laemmli sample buffer (4% SDS, 10% 2-mercaptoethanol, 20% glycerol and a trace of Brilliant Blue). Samples were then placed on ice and then stored at -20°C for western blotting. Baseline aggregations were performed in the absence of EGTA.

3.5.6 Western blotting

3.5.6.1 Sample preparation and electrophoresis

Prior to electrophoresis samples were thawed, heated at 100°C for 5 minutes, briefly vortexed and centrifuged. 4-12% gradient pre-cast sodium dodecyl sulphate polyacrylamide gel

electrophoresis (SDS-PAGE) gels were prepared in mini electrophoresis tanks (NuPAGE, ThermoFisher, UK) with 1X MOPS buffer (50 mM 3-(N-morpholino)propanesulphonic acid, 50 mM, 50 mM Tris base, 0.1% SDS and 1 mM EDTA, pH 7.7, (NuPAGE, ThermoFisher, UK)). 15 µL of WCL samples were loaded onto the gel alongside pre-stained molecular weight markers (New England Biolabs, UK). SDS-PAGE gels were initially run at 80 V until the samples had passed through the stacking gel, then separated on the remaining gel at 120 V for a further 40 minutes to 1 hour.

3.5.6.2 Membrane transfer, blocking and antibody incubation

SDS-PAGE gels were transferred to polyvinylidene fluoride (PVDF) membranes (Trans-Blot Turbo kit, LF PVDF Bio-Rad, UK). Membranes were incubated with 4% bovine serum albumin (BSA) in Tris-buffered saline with Tween (TBST; 20 mM Tris, 137 mM NaCl, pH 7.6, 0.2% Tween20) either for 1 hour at room temperature or overnight 4^{o}C to ensure blocking of non-specific protein binding sites. Membranes were incubated with desired primary antibody either at 1 hour at room temperature or overnight at 4^{o}C. Following primary antibody incubation, membranes were washed with TBST (3 x 10 minutes) and then incubated with the corresponding horseradish peroxidase (HRP) conjugated secondary antibody. Membranes were washed again with TBST (3 x 10 minutes).

3.5.6.3 Detection

Membranes were incubated with enhanced chemiluminescence (ECL) substrate (Pierce, ThermoFisher, UK) for 1 minute to enable detection of desired proteins. Excess ECL was

removed, and membranes were placed into plastic sleeves and secured into X-ray film processing cassette(s). Under darkroom conditions X-ray films (Amersham, UK) were exposed to membranes, films were processed in developer machine. Images were scanned and densitometry was performed using ImageJ software.

3.5.7 Protein corona

Utilising the method previously described in section 3.3.2 PtNPs were surface modified with the highest concentrations of alkane and pegylated thiols specified in Table 3.2 and Table 3.3. 6 x 2 mL PtNP aliquots were prepared in clean glass vials, 2 mM of alkanethiol and pegylated thiols were added to the PtNP aliquots. Samples were left to incubate for 3 hours at room temperature on an orbital shaker, following incubation reactions were centrifuged at 10,000 x g for 10 minutes. The supernatant for each reaction was discarded and the surface modified PtNPs were resuspended in 2 mL of dH_2O and then separated into 2 x 1 mL aliquots into clean glass vials. The duplicate aliquots were incubated with 1 mL of human plasma (TCS Biosciences Ltd, Buckingham UK) for 30 minutes at 37^{o}C. Samples were centrifuged at 10,000 x g for 10 minutes; supernatants were discarded, and samples were resuspended in 2 mL of PBS. The samples were characterised by DLS and zeta potential.

Chapter 4 Synthesis and Characterisation of Platinum Nanoparticles

Abstract: This chapter details the synthesis and characterisation of the core material used throughout this thesis, monodispersed platinum nanoparticles (PtNPs). In the first instance, platinum (Pt) seeds were synthesised; these platinum seeds were then utilised as a template to grow (PtNPs) of 20 and 60 nm on different reaction scales to examine if consistent sizes could be achieved. Of the two sizes synthesised, the 20 nm PtNPs were selected for reproducibility experiments by synthesising four large batches of PtNPs. XPS analysis of the 20 nm PtNPs revealed the presence of platinum, carbon and oxygen confirming the presence of the citrate ion capping on the PtNP surface. Finally, the physicochemical properties of these 20 nm PtNPs were assessed under physiological conditions and found to be unstable, warranting the need for sterically stabilised PtNPs for investigating platelet-PtNP interactions.

4.1 Introduction

Platinum nanoparticles (PtNPs) are widely employed for their catalytic properties in various applications including proton exchange membrane fuel cells, gas sensors, glucose sensors and bioimaging of cancer cells.[17, 130-133] The success of these applications is dependent on the physicochemical properties of the nanoparticle, such as size, shape, surface charge, composition and crystalline structure to name a few. Obtaining homogenous metallic nanoparticles of the same size and shape is challenging. A common synthesis method for colloidal metallic nanoparticles such as gold, silver and platinum are the chemical reduction of precursor metal salts by reducing agents.[22, 28, 134, 135] These methods are based on the early work of gold nanoparticles (AuNP) synthesis by Turkevich et al.[21] and later Frens in 1973,[24] where chloroauric acid was reduced to AuNPs by sodium citrate in an aqueous solution. In some methods, metallic seeds of the desired nanoparticles are first synthesised, these seeds act as template by providing a nucleation site for the nanoparticles to grow.[27, 28] Another key element of these chemical reduction methods are the capping agents; metallic nanoparticle synthesis regularly uses capping agents to stabilise the nanoparticles. They prevent nanoparticle aggregation absorbing onto the nanoparticle surface via physisorption or chemisorption creating repulsive forces between the nanoparticles, therefore stabilising the nanoparticle either electrostatically or sterically. In the case of AuNPs, sodium citrate is utilised as both reducing and capping agent simultaneously to allow controlled sizing of colloidal AuNPs.[21, 24, 28] Other common capping agents are thiols or polymers such as poly(vinylpyrrolidone) (PVP).[35, 45, 136]

4.1.1 Objectives:

1. Synthesise Pt seeds on different reaction scales, characterise the Pt seeds by TEM, DLS and zeta potential.

2. Synthesise monodispersed PtNPs of two controlled sizes, on four different reaction scales to examine if consistent sizes can be achieved. Characterise these PtNPs by TEM, DLS and zeta potential.

3. Synthesise four large batches PtNPs to assess reproducibility of PtNP synthesis reaction. Characterise these PtNPs by TEM, DLS zeta potential.

4. Confirm the presence of citrate ion capping on the PtNP surfacing using XPS analysis.

5. Examine the physicochemical properties of the PtNPs in a physiological buffer.

4.2 Results and Discussion

4.2.1 Synthesis of platinum seeds

Monodispersed PtNPs were synthesised using a seed mediated approach described by Bigall et al.[27] as illustrated in Figure 4.1. Pt seeds were first synthesised and used as a template to grow larger PtNPs. Pt seeds were synthesised by the reduction of the Pt precursor chloroplatinic acid hexahydrate ($H_2PtCl_6.6H_2O$, 3.86 mM) using the strong reducing agent sodium borohydride (21 mM) and capping agent sodium citrate/citric (34 mM/2.38 mM) acid at 100°C. Sodium borohydride instantaneously reduced the $H_2PtCl_6.6H_2O$ to Pt atoms, observed by the rapid colour change of the reaction from pale yellow to brown, see Figure 4.2 (a) & (b).

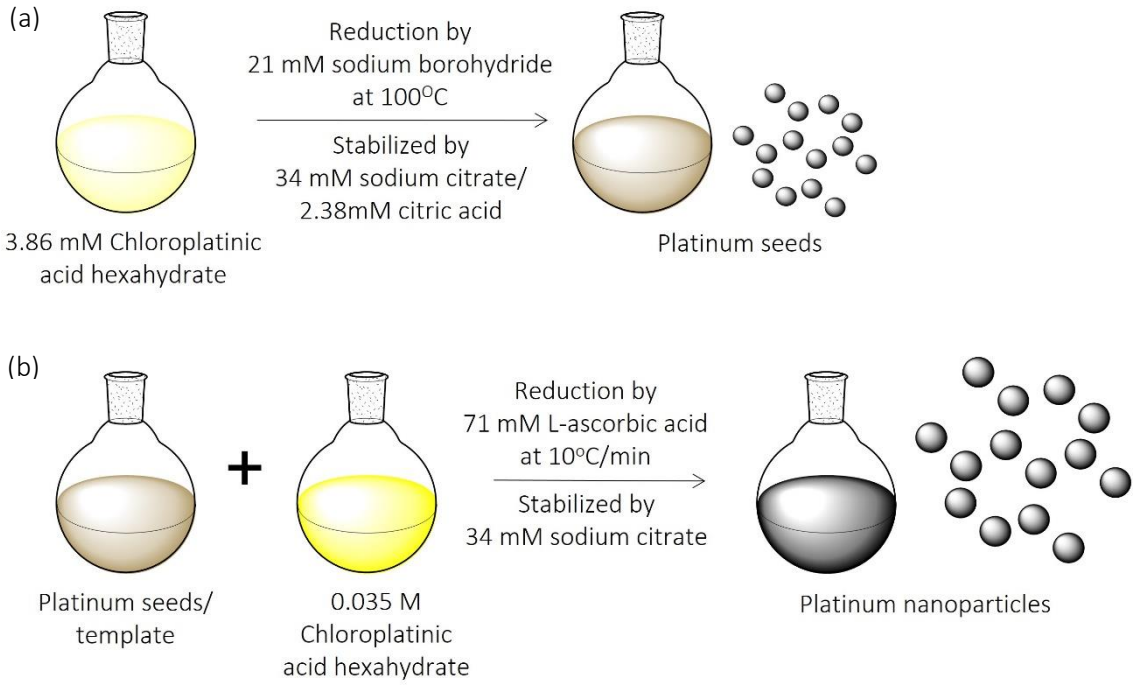

Figure 4.1 Overview of PtNP synthesis. (a) Pt seeds are synthesised by the reduction of ($H_2PtCl_6.6H_2O$) with sodium borohydride, (b) the Pt seeds are used as template to grow larger PtNPs using a milder reducing agent L-ascorbic acid.

$H_2PtCl_6.6H_2O$ was reduced to Pt atoms which flocculated into creating Pt seeds; the citrate ions from sodium citrate/citric acid stabilised the Pt seeds by physisorbing onto the surface and forming an electric double layer (EDL) of citrate ions around the Pt seeds. The negative charge carried by the citrate ions provides stability by creating electrostatic repulsion between neighbouring Pt seeds, therefore they are surrounded by a cloud of citrate ions that prevents their aggregation.[21, 24, 28] These Pt seeds were characterised by TEM, DLS and zeta potential see Figure 4.2 (c - g), this experiment was conducted once (n=1). The TEM size of the Pt seeds was obtained by measuring the diameters of 200 Pt seeds. Five DLS and zeta potential measurements were performed to obtain the mean for each sample, data is presented as mean.

TEM revealed the Pt seeds to be monodispersed exhibiting a spherical shape with an average diameter of 4.0 nm, this size was comparable to that obtained by Bigall et al.[27] DLS measurements demonstrated an average hydrodynamic diameter of 15.2 nm with a polydispersity index (PDI) of 0.220. The hydrodynamic diameter was significantly larger compared to the average TEM diameter. This was expected, the DLS technique measures the Brownian motion (or diffusion) of particles in solution and relates this to the particle size; DLS measures the particle size but also anything that is on the particle surface while in motion. Thus, the hydrodynamic diameter obtained by DLS is larger than TEM.[113, 115, 137]

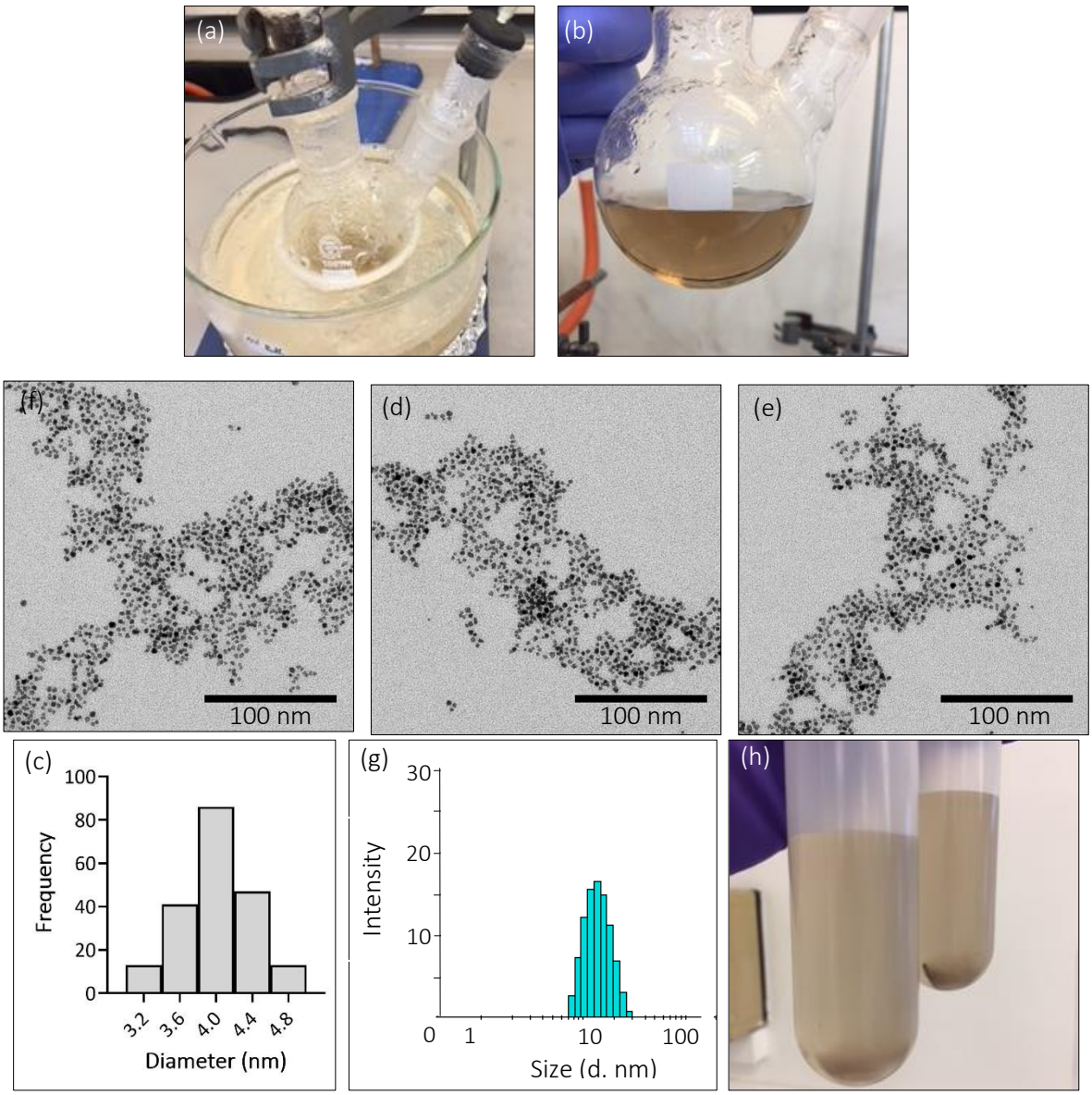

Figure 4.2 Pt seed characterisation of the 50 mL reaction. (a) synthesis of Pt seeds by the reduction of $H_2PtCl_6.6H_2O$, (b) Pt seeds after synthesis reaction, (c), (d) & (e) TEM images (f), particle size distribution from TEM, (g) particle size intensity by DLS, representative of 1 measurement (h) Pt seeds after centrifugation. Results presented from 1 synthesis reaction (n=1).

These Pt seeds had a zeta potential of -13.7 mV at pH 4.9, the negative charge was a result of the citrate ions capping the Pt seeds. Nanoparticles with zeta potentials below 30 mV or above -30 mV are considered to have low stability.[115, 138] While the zeta potential indicates Pt seeds have low stability, these seeds are indeed stable. There are factors that need to be considered when interpreting zeta potential data: (1) particle size, if the particle size is too small or too big, it can be out of the measurement range of the Zetasizer instrument, (2) surface coating, some surface coatings e.g., polyethylene glycol coated nanoparticles can give zeta potentials in low stability range as a result of their non-ionic nature but are actually sterically stable.[139]

The Pt seed synthesis method by Bigall et al.[27] did not describe a procedure for the removal of excess $H_2PtCl_6.6H_2O$ and sodium borohydride from the reaction. As it is unclear if excess $H_2PtCl_6.6H_2O$ and sodium borohydride will interfere with PtNP synthesis reaction, Pt seeds were centrifuged at 10000 x g to enable the removal of excess $H_2PtCl_6.6H_2O$ and sodium borohydride. However, due to their small size this was unsuccessful as not all the Pt seeds had spun down to the bottom of the tube as the reaction colour remained brown rather than colourless as demonstrated in Figure 4.2 (h), therefore the Pt seeds were used without centrifuging.

A large batch of Pt seeds were synthesised on a 5x reaction scale using the same method, as large quantities of Pt seeds were required for subsequent PtNP synthesis reactions. Again, these Pt seeds were characterised by TEM, DLS (Figure 4.3) and zeta potential. The Pt seed synthesis at 5x reaction scale had comparable data to that obtained on the 1x reaction scale. The average TEM and hydrodynamic diameters were 4.1 nm and 16.3 nm with a PDI of 0.430,

respectively, and the average zeta potential was -16.0 mV at pH 4.9. These data demonstrate that under the same conditions, Pt seeds could be effectively synthesised on different reaction scales with reproducible sizes. It was crucial to have consistent sizes between the two different reaction sizes, as large volumes of Pt seeds with uniform sizing are required as a template for PtNP synthesis reactions. Following the successful scaled up synthesis of the Pt seeds, these Pt seeds were utilised to synthesise PtNPs of 20 and 60 nm which would be later used in platelet experiments. In the next section the synthesis of 20 nm and 60 nm PtNPs will be discussed.

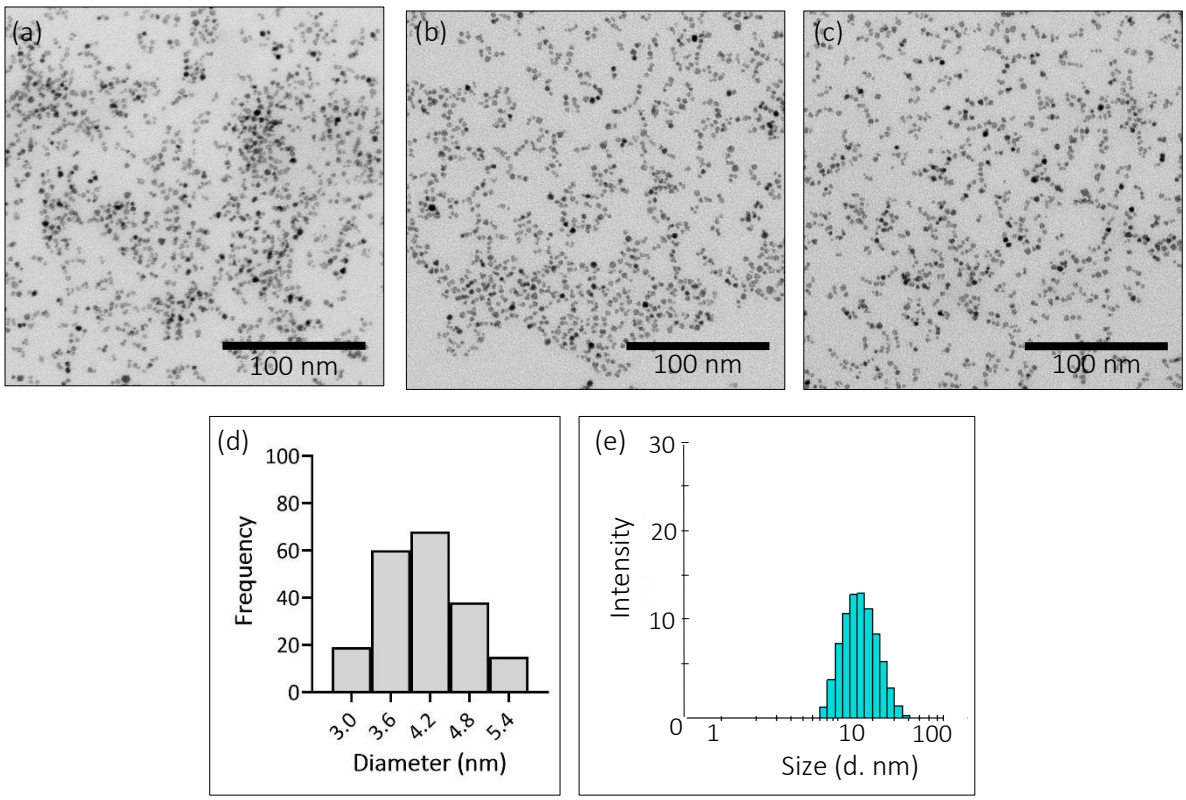

Figure 4.3 Pt seed synthesis characterisation of 5x reaction scale. (a) - (c) TEM images (d), particle size distribution and (e) particle size intensity by DLS, representative of 1 measurement. Results presented from 1 synthesis reaction (n=1).

4.2.2 Synthesis of 20 nm platinum nanoparticle

Citrate capped PtNPs were synthesised with 0.035 M $H_2PtCl_6.6H_2O$, using the Pt seeds as a template, larger PtNPs were grown with a temperature increment of 10°C/min to 100°C. Pt cations from the precursor were reduced onto the Pt seed surfaces, allowing growth into PtNPs. Growth was facilitated by the milder reducing agent, L-ascorbic acid (71 mM), that was used together with sodium citrate as a capping agent (34 mM). Similarly, to the Pt seeds, the citrate ions are physisorbed onto the PtNP surface to form the EDL once again; the negative charge from the citrate ions creates electrostatic repulsion between the neighbouring PtNPs therefore providing electrostatic stability. These citrate capped PtNPs will be referred to as c-PtNPs throughout unless stated otherwise.

These reactions were conducted on four different reaction scales to examine if consistent nanoparticle sizes could be achieved as subsequent experiments would require large quantities of c-PtNPs. From the synthesis method described by Bigall et al.[27] the PtNP synthesis had a total reaction volume of 30.6 mL, reaction scale 1x relates to this volume, larger reactions were scaled up 2x, 5x and 10x accordingly to this volume. For each reaction, excess $H_2PtCl_6.6H_2O$ and L-ascorbic acid were removed by washing the c-PtNPs by centrifugation and resuspending into 1.1 mM sodium citrate, as this was the final concentration of sodium citrate in the synthesis reaction. These c-PtNPs were characterised by TEM, DLS and zeta potential as shown in Figure 4.4. Five DLS and zeta potential measurements were taken 5 times to obtain the mean.

Figure 4.4 (a-d) illustrate monodispersed, spherical, and uniform c-PtNPs, the particle size distributions ranged from 15 - 30 nm. The average TEM diameters for 1x, 2x, 5x, and 10x reaction scales were 21.6, 22.9, 23.3 and 20.1 nm respectively. The average hydrodynamic diameters for 1x, 2x, 5x and 10x reactions were 32.3, 31.2, 32.4 and 29.6 nm with PDI of 0.218, 0.279, 0.254 and 0.252 respectively, see Figure 4.4 (j).

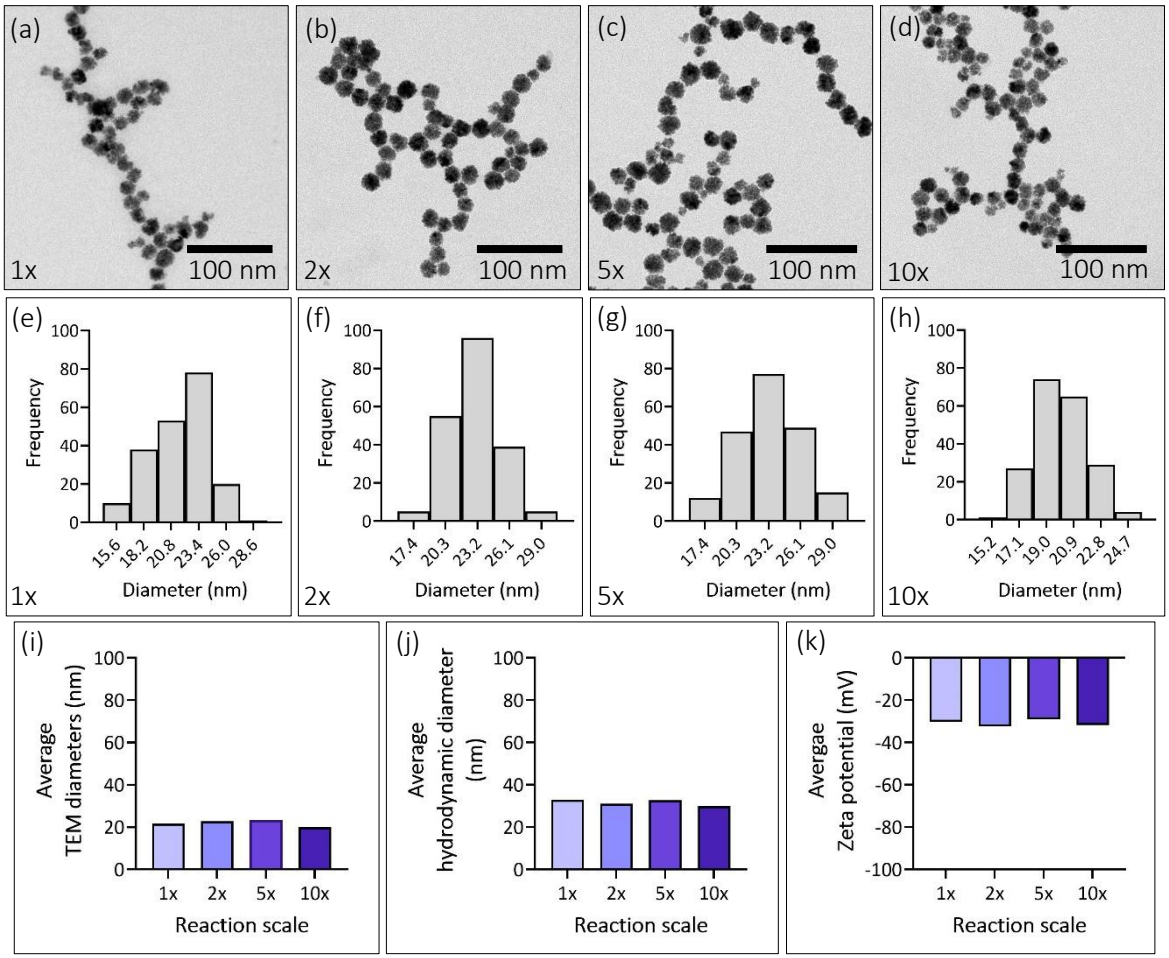

Figure 4.4 Characterisation of 20 nm c-PtNPs. (a-d) TEM images from each reaction scale, (e-h) particle size distribution from each reaction scale, (i) average diameters by TEM, (j) average hydrodynamic diameters & (k) average zeta potentials. Results presented from 1 synthesis reaction for each reaction scale (n=1).

Zeta potentials between these scaled up reactions were comparable ranging from -30 mV to -32 mV at pH 7 to 7.2, indicating good stability and a negative charge from the citrate ion capping. Using the average TEM diameters, the surface area was calculated for each reaction, see Table 4.1, for calculations see Appendix 11.1. The surface areas were comparable between the different reactions, these data demonstrate 20 nm c-PtNPs synthesis reactions can be scaled up at different reaction volumes to give stable negatively charged c-PtNPs with narrow size distributions, but more importantly controlled growth can be effectively achieved to give uniform PtNPs.

Table 4.1 20 nm c-PtNP scaled up reactions, volumes, diameters, and calculated surface areas/mL.

Reaction scale	Reaction volume (mL)	Average TEM diameter (nm)	Surface area (nm^2/mL)
1x	30.6	21.6	1.5×10^{14}
2x	61.2	22.9	1.4×10^{14}
5x	153	23.3	1.4×10^{14}
10x	306	20.1	1.6×10^{14}

4.2.3 Synthesis of 60 nm platinum nanoparticles

As the 20 nm c-PtNPs were successfully synthesised with good stability and a narrow particle size distribution, 60 nm c-PtNPs were synthesised following the same method with an increased concentration of 0.4 M $H_2PtCl_6.6H_2O$ Pt seeds were used as a template, while L-ascorbic acid (71 mM) and sodium citrate (34 mM) were used as a reducing and capping agent. Again, to demonstrate if consistent sizes could be achieved on a large scale, synthesis reactions were performed on different reaction scales as with the 20 nm c-PtNPs, these synthesis reactions were performed on a 1x, 2x, 5x and 10x. Excess $H_2PtCl_6.6H_2O$ and L-ascorbic acid were removed from each reaction by washing the c-PtNPs by centrifugation and resuspending into 1.1 mM

sodium citrate. The c-PtNPs were characterised by TEM, DLS and zeta potential as shown in Figure 4.5. Five DLS and zeta potential measurements were taken 5 times to obtain the mean.

The TEM images in Figure 4.5 (a-d) illustrate the c-PtNPs distribution synthesised using 0.4 M $H_2PtCl_6.6H_2O$ across different reaction scales, these c-PtNPs were large monodispersed with a spherical shape. Experiments conducted on the 1x, 2x, 5x, and 10x produced average nanoparticles sizes of 61.1, 70.3, 60.9 and 61.7 nm respectively, see Figure 4.5 (i). The average TEM sizes were comparable across the different scaled reactions. The large standard deviations were a result of broad particle size distribution. The particle size distribution of these reactions ranged from 30 to 110 nm as shown in Figure 4.5 (e-h). The sizes achieved were much greater than those observed by Bigall et al.[27] using the same concentration. This may be explained by the different brand of $H_2PtCl_6.6H_2O$ used in the reactions compared with the original method; the amount of Pt present in the precursor can vary from manufacturer to manufacturer.

The average hydrodynamic diameters of the c-PtNPs for 1x, 2x, 5x, and 10x reactions were 92.3, 102, 87.7 and 93 nm with PDI of 0.078, 0.049, 0.053 and 0.057 accordingly, see Figure 4.5 (j). Experiments at 1x, 5x, and 10x reaction scales had similar hydrodynamic diameters while 2x was slightly higher. The hydrodynamic diameters were greater than the average TEM diameters, again this was to be expected. Zeta potentials measurements of c-PtNPs were performed in 1.1 mM sodium citrate as this was the final concentration of sodium citrate in the synthesis reactions Figure 4.5 (k) shows the zeta potential of 1x, 2x, 5x, and 10x reaction scales

measured at -42.4, -42, -42.7 and -41.7 mV respectively with pH measuring between 7 – 7.2. This data demonstrates the c-PtNPs were negatively charged with a good stability.

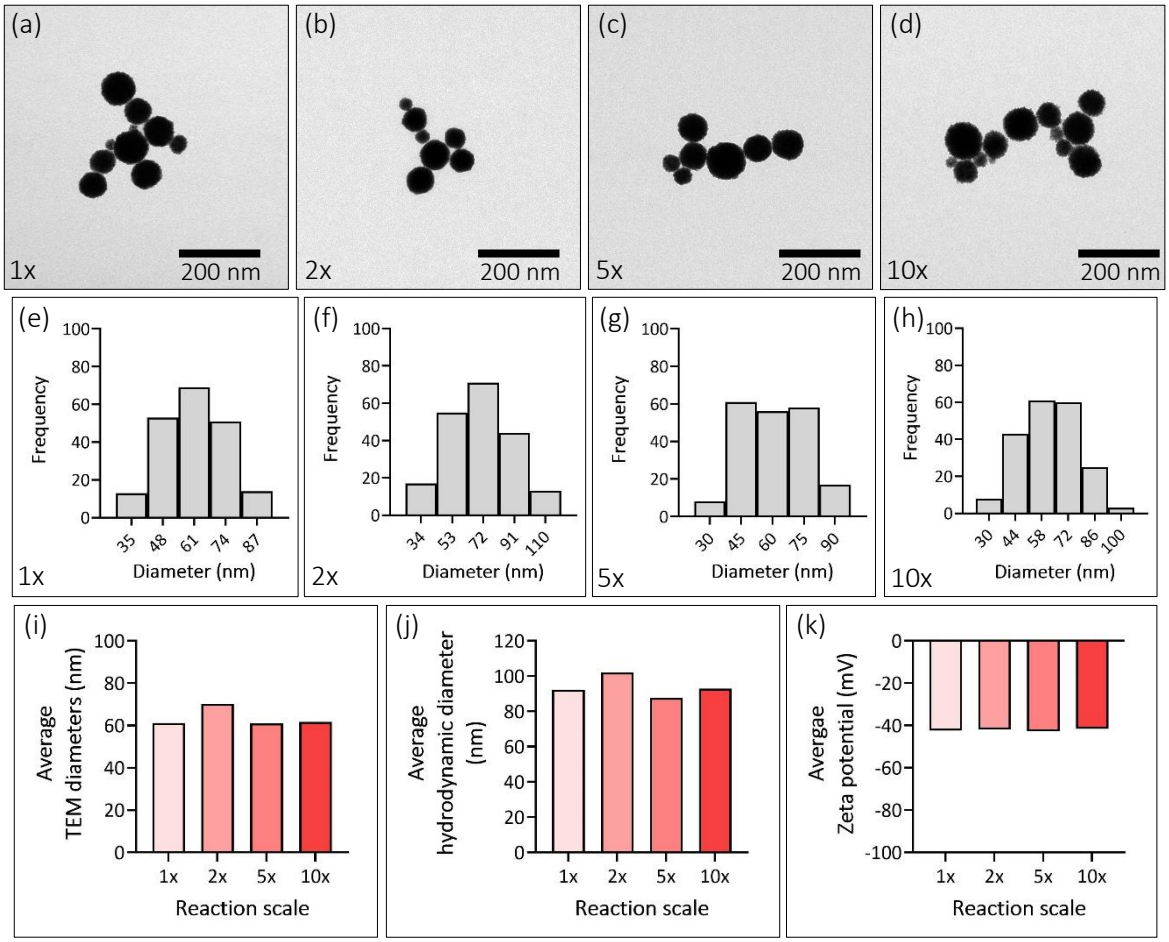

Figure 4.5 Characterisation of 60 nm c-PtNP. (a-d) TEM images from each reaction scale, (e-h) particle size distribution from each reaction scale, (i) average diameters by TEM, (j) average hydrodynamic diameters & (k) average zeta potentials. Results presented from 1 synthesis reaction for each reaction scale (n=1).

Utilising the average TEM diameters, the surface area of each reaction was calculated, see Table 4.2. The surface areas across all the reactions were similar except for 2x which had a smaller surface area; this is a result of 2x reaction having a slight larger average TEM diameter.

Along with the characterisation data, this data shows that large c-PtNPs were synthesised on different reaction scales with large particle distributions, overall, it was more difficult to control sizing of large PtNPs.

Table 4.2 60 nm c-PtNP scaled up reactions, volumes, diameters, and calculated surface areas/mL.

Reaction scale	Reaction volume (mL)	Average TEM diameter (nm)	Surface area (nm^2/mL)
1x	30.6	61.1	5.3×10^{14}
2x	61.2	70.3	4.6×10^{14}
5x	153	60.9	5.3×10^{14}
10x	306	61.7	5.3×10^{14}

20 and 60 nm c-PtNPs would be ideal for platelet experiments, as previous studies have demonstrated a size effect relationship on platelet activation, [90, 91, 140] however the 20 nm c-PtNPs were selected for platelet experiments, as they exhibited uniform sizes and narrow particle size distribution which was critical for subsequent experiments. Due to their large particle size distribution, 60 nm c-PtNPs were not taken forward for platelet experiments. Previous nanoparticle platelet experiments with metallic nanoparticles have primarily examined how size and shape effects platelet activation,[68, 90-93, 96] hence, as the focus of this PhD was to investigate how the surface charge of PtNPs can mediate platelet activation, the 20 nm c-PtNPs were best for platelet experiments. Although alternative methods were not tested, there are other possible approaches that could be tested to achieve larger c-PtNPs with narrow particle size distribution, either: (1) increase the concentration of both reducing and capping, (2) reduce volume of the Pt seeds or (3) increase template size i.e., start with a 20 nm template.[137, 141]

4.2.4 Reproducibility of 20 nm PtNP synthesis

The results in section 4.2.2 demonstrated c-PtNPs could be synthesised on different reaction scale to give uniform 20 nm c-PtNPs with good stability and narrow particle size distributions. To assess reproducibility of the 20 nm c-PtNPs synthesis reactions, four batches of 20 nm c-PtNPs were synthesised on the 10x reaction scale; all synthesis reactions were performed following the method described in section 4.2.2. The concentration of the precursor $H_2PtCl_6.6H_2O$ was adjusted to 0.2 M as new batch of $H_2PtCl_6.6H_2O$ was used for these synthesis reactions. Figure 3.6 illustrates the characterisation of these batches of 20 nm c-PtNPs by TEM, DLS and zeta potential.

TEM images shown in Figure 4.6 (a – d) revealed monodispersed, spherical, and uniform c-PtNPs. the average TEM diameters were similar across all from batches; batches A, B, C and D were 21.9, 22.6, 23.3 and 22.7 nm respectively. The particle size distribution between ranged from 18 to 25.6 nm as demonstrated in Figure 4.6 (e – f). These sizes were comparable to the previous data in section 4.2.2, where 20 nm c-PtNPs were synthesised on 10x reaction scales. The average hydrodynamic diameters amongst these batches were alike, for reactions A, B, C and D the hydrodynamic diameters were 37, 34, 35 and 36.4 nm with PDIs of 0.140, 0.125, 0.096 and 0.096 respectively. Zeta potentials measurements demonstrated good stability, all batches A, B, C & D exhibited zeta potentials of -44.6, -43.0, -43.6 and -41.6 mV, accordingly, these zeta potentials were comparable across the different batches. The average TEM diameters were used to calculate the surface area of each batch, see Table 4.3; these surface areas were equivalent across all four batches. Interestingly, the surface areas of these batches

were significantly larger compared to that previously obtained on the 10x reaction scale in section 4.2.2. Albeit the sizes of these c-PtNPs were similar to the previous data, this difference was a result of using an increased concentration of $H_2PtCl_6.6H_2O$ thus more particles were present in these reactions. Collectively, these data give confidence that 20 nm c-PtNPs can reproducibly be synthesised on a large reaction scale. These batches of 20 nm c-PtNPs were used for all experiments conducted in this thesis, unless acknowledged otherwise.

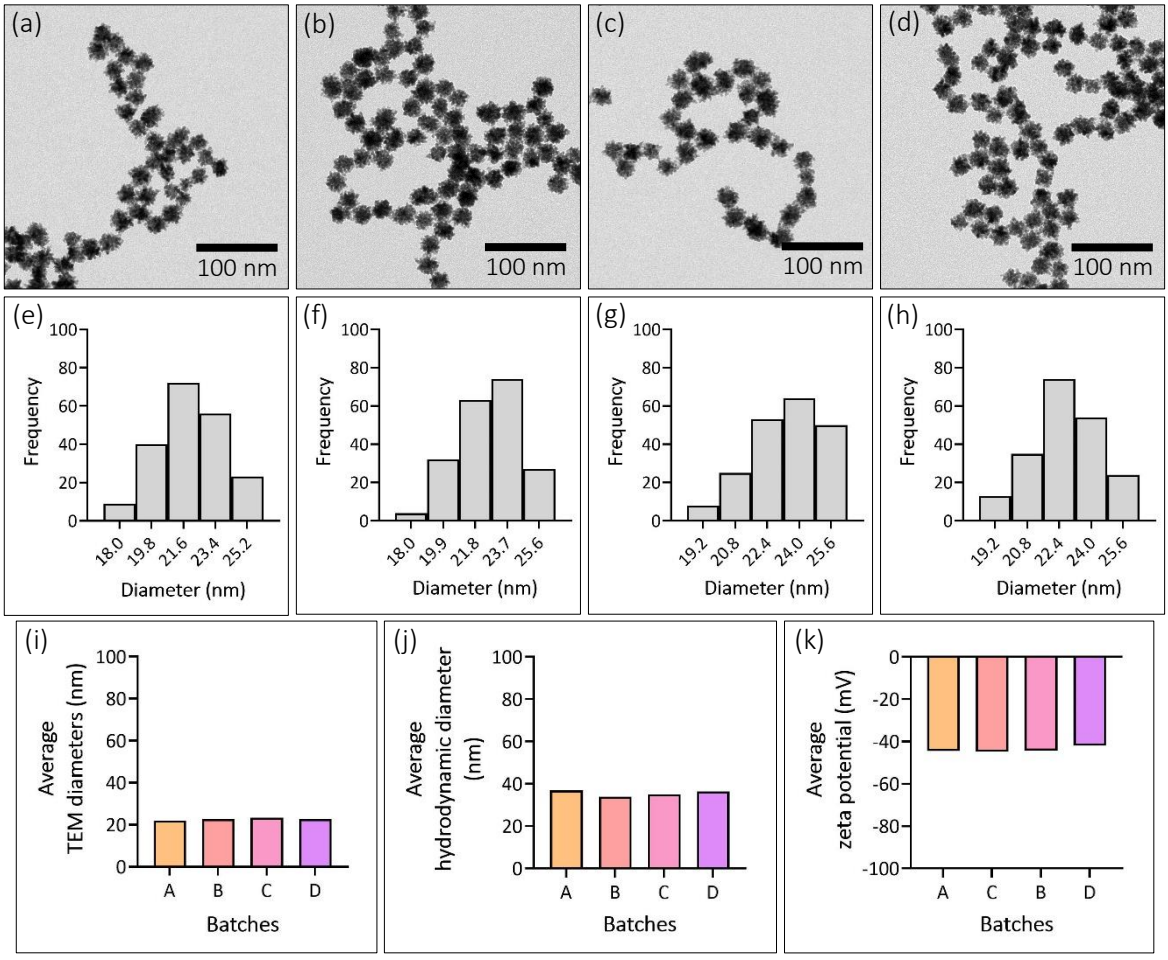

Figure 4.6 Characterisation of 20 c-PtNP synthesised from four batches. (a-d) TEM images from each reaction batch, (e-h) particle size distribution from each batch, (i) average diameters by TEM, (j) average hydrodynamic diameters & (k) average zeta potentials. Results presented from 4 synthesis reactions (n=1 per batch synthesised).

Table 4.3 20 nm c-PtNP synthesised from four batches, TEM diameters and calculated surface areas/mL.

Batch	Reaction scale	Average TEM diameter (nm)	Surface area (nm^2/mL)
A	10x	21.9	7.6×10^{14}
B	10x	22.6	7.3×10^{14}
C	10x	23.3	7.1×10^{14}
D	10x	22.7	7.3×10^{14}

4.2.5 XPS of 20 nm platinum nanoparticles

To confirm the presence of the citrate ion capping on the PtNP surface, c-PtNPs were analysed by XPS. A pilot XPS experiment using silicon wafers as substrate caused interference with the sulphur (2 p) peaks at starting at 163 eV, hence copper substrates were selected for all XPS experiments in this thesis as their main peaks starts from 933 eV. Prior to any XPS analysis of the c-PtNPs, all the copper substrates (discs) were subjected to an oxide reduction by hydrogen gas. A copper substrate was initially cleaned with chloroform and then ultrasonicated with isopropanol. Oxide reduction was performed by Abubakr Siddiq at the Birmingham Centre for Fuel Cell and Hydrogen Research at the University of Birmingham. The copper substrate was placed in a tube furnace and the oxide layer was reduced by hydrogen and nitrogen gases flowing over the copper substrate at a flow rate of 50 mL/min for 12 hours. To ensure the oxide layer had been effectively reduced, the reduced copper substrate was submitted for XPS analysis. Additionally, an oxidised (non-reduced) copper substrate was also submitted for XPS analysis for comparison. The XPS survey scan detected the presence of copper (Cu).

Examination of the high-resolution scans for both the oxidised and reduced blank copper substrate revealed a signal from Cu 2p orbitals, these are presented Figure 4.7. The high-

resolution scan of Cu 2p for the oxidised copper substrate exhibited two main peaks, Cu 2p $_{3/2}$ at 932.5 eV and Cu 2p $_{1/2}$ at 952.3 eV with a peak separation of 19.8 eV. However, both peaks revealed several CuO peaks as illustrated in Figure 4.7 (a). Conversely, the reduced blank copper substrate detected the two main peaks at Cu 2p $_{3/2}$ at 932.1 eV and Cu 2p $_{1/2}$ at 951.9 eV with a peak separation of 19.8 eV; two small CuO were also present with the two main peaks as shown in Figure 4.7 (b). This data corresponds with that obtained by Biesinger et al.[142] where the copper substrate was sputter cleaned to remove the oxide layer. From these XPS spectra it was clear that reduction by hydrogen and nitrogen gases effectively reduced the oxide layer on the copper substrate.

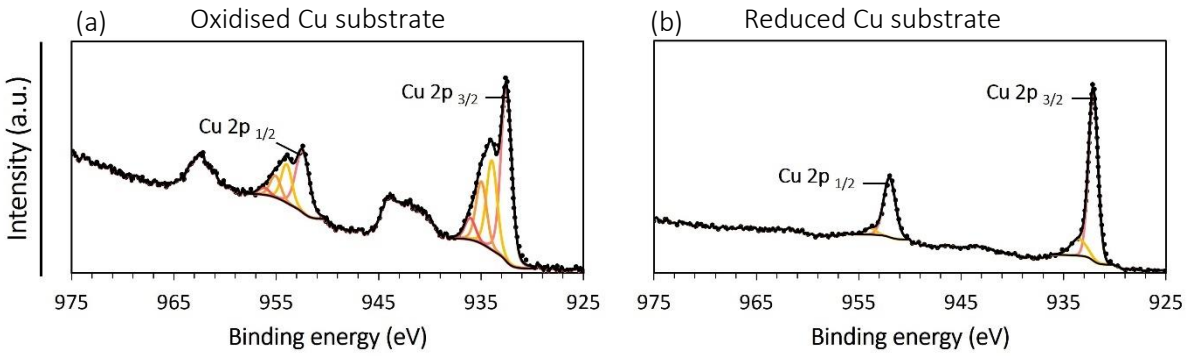

Figure 4.7 High-resolution XPS spectra of a copper substrate. (a) oxidised copper substrate and (b) reduced copper substrate using hydrogen and nitrogen gases.

As oxide reduction on the copper substrate was effective, c-PtNPs were further characterised by XPS. An aliquot of 20 nm c-PtNPs was concentrated by centrifugation, the supernatant was discarded and concentrated c-PtNPs were drop cast onto copper substrate, dried and submitted for XPS. For comparison, a clean blank copper substrate was also submitted for XPS analysis. Two measurements per sample were performed for each sample in this thesis. The

XPS survey scan detected the presence of platinum (Pt), carbon (C), oxygen (O) and copper (Cu) elements.

A common artefact of XPS is adventitious carbon and oxygen contamination. When analysing peaks for carbon and oxygen from high-resolution scans XPS, adventitious carbon and oxygen must be taken into consideration; although the XPS technique is performed under a vacuum, samples exposed to air will normally have a thin layer of contamination by carbon.[143] The presence of adventitious carbon and oxygen does not permit the quantification of carbon and oxygen elemental ratios. For this reason, the high-resolution scans of carbon and oxygen will be used to identify the species present of the surface of the c-PtNPs. Adventitious carbon is frequently used for charge correction of high-resolution scans, all scans in this thesis unless stated otherwise was charge corrected to 284.8 eV. All peaks were fitted using the CasaXPS software version 3.2.25 for all XPS analysis throughout this thesis.

Investigation of the high-resolution scans for the blank copper disc (substrate) and PtNPs on the copper substrate revealed the signals from Pt 4f, Cu 2p, C 1s, and O 1s and orbitals, these are presented Figure 4.8. The high-resolution scan of Pt 4f for the copper substrate did not detect the presence of Pt 4f, this was to be expected as no c-PtNPs were present on the copper substrate. However, three Cu 3p peaks were detected, Cu $3p_{3/2}$ at 75.1 eV, CuO at 75.6 eV and Cu $3p_{1/2}$ at 77.5 eV, see Figure 4.8 (a). Cu 3p has a spectral overlap with Pt 4f as their binding energies are similar, thus Cu 3p was detected in the high-resolution scan of Pt-4f. A recent study by Khalakhan et al.[144] demonstrated the Cu 3p/Pt 4f spectral overlap from the XPS analysis of

Pt-Cu bimetallic alloys. These Cu 3p peaks are attributed to the copper substrate. By contrast, the high-resolution scan of Pt 4f for the c-PtNPs on the copper substrate detected the Pt 4f signal, see Figure 4.8 (b). Pt 4f exhibits an asymmetric doublet peak, Pt $4f_{7/2}$ at 70.9 eV and Pt $4f_{5/2}$ at 74.2 eV with a separation of 3.33 eV, these two main peaks are characteristic of platinum metal and are similar to those in literature.[145, 146] The high-resolution scans also presented broad peaks of PtO at 73.2 eV and CuO at 76.5 eV. The Pt 4f, PtO and CuO peaks are attributed to the PtNPs on the copper substrate.

Figure 4.8 (c) and (d) illustrate the high-resolution scan of Cu 2p for the copper substrate and the c-PtNPs on the copper substrate. In both samples, Cu 2p were presented as doublet peaks, the copper substrate detected Cu $2p_{3/2}$ at 932.5 eV and Cu $2p_{1/2}$ at 952.4 eV with a peak separation of 19.9 eV. PtNPs on the copper substrate also detected a doublet peak with comparable binding energies to the copper substrate only; Cu $2p_{3/2}$ and Cu $2p_{1/2}$ were observed at 932.4 eV and 952.3 eV with a separation of 19.9 eV. These binding energies correspond to those in literature.[146, 147]. Additionally, the PtNPs on the copper substrate detected CuO peaks within the Cu 2p peaks, CuO at 934.9 eV and 954.5 eV. As Cu 2p has a multitude of species with similar binding energies,[147] only the two main large peaks of Cu 2p and CuO will be reported. Cu 2p in both samples are ascribed to the copper substrate.

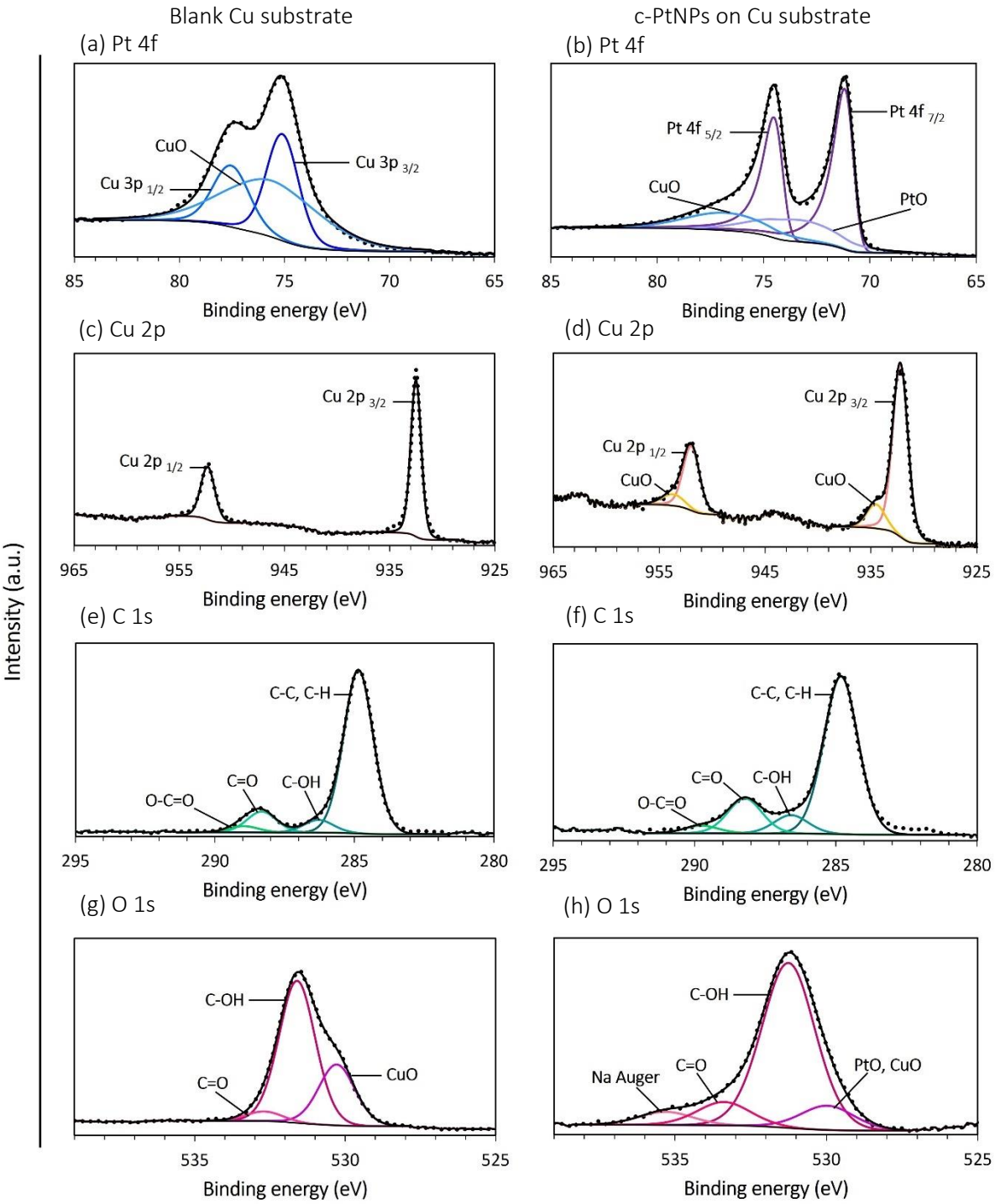

Figure 4.8 High-resolution XPS spectra of a copper substrate and c-PtNPs on a copper substrate. (a) Pt 4f - Cu substrate, (b) Pt 4f – c-PtNPs on Cu substrate, (c) Cu 2p - Cu substrate, (d) Cu 2p – c-PtNPs on Cu substrate, (e) C 1s - Cu substrate, (f) C 1s – c-PtNPs on Cu substrate, (g) O 1s - Cu substrate and (h) O 1s – c-PtNPs on Cu substrate (n=1).

Examination of the high-resolution scans of C 1s for the copper substrate and the c-PtNPs on the copper substrate are demonstrated in Figure 4.8 (e) and (f) respectively. The copper substrate revealed four carbon species, C-C, C-H at 284.8 eV followed by C-OH at 286.4 eV, C=O at 288.4 eV and O-C=O at 289.3 eV. Interestingly, C-C, C-H, C-OH and O-C=O are found in the citrate ion structure, see Figure 4.9. These carbon species are also attributed to adventitious carbon contamination as no c-PtNPs were present on the copper substrate. The high-resolution scans of C 1s for the PtNPs on the copper substrate also revealed the same for carbon species, C-C, C-H at 284.8 eV preceded by C-OH at 286.6 eV, C=O at 288.2 eV and finally O-C=O at 289.6 eV. The O-C=O specie had a slightly larger peak; this likely due to the presence of the carboxylic acid group from the citrate ions capping the PtNPs, however they are also attributed to adventitious carbon contamination as these species were present on the blank copper substrate.

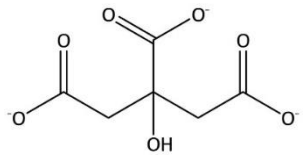

Figure 4.9 Structure of citrate ion with different carbon and oxygen species.

Deconvolution of the high-resolution scan of O 1s for the copper substrate detected three oxygen species, CuO at 530.3 eV, C-OH at 531.6 eV and C=O at 532.7 eV, see Figure 4.8 (g). Although, the oxide layer had been reduced by hydrogen gas, these oxygen species were detected due to adventitious oxygen contamination. C-OH and C=O are attributed to adventitious oxygen while CuO is attributed to the blank copper substrate. The high-resolution scan of O 1s for the PtNPs copper substrate detected the same three oxygen species, CuO at

530 eV, C-OH at 531.3 eV and C=O at 535.3 eV, as shown in Figure 4.8 (h). These oxygen species had comparable binding energies to those found on the blank copper substrate. The presence of these oxygen species in both samples confirms contamination by adventitious oxygen. Additionally, a sodium (Na) Auger peak was also detected in the high-resolution scan of O 1s for the PtNP on the copper substrate; this was a result of sodium citrate used as a capping agent on the PtNPs. The Na Auger peak confirms the presence of citrate capped PtNPs in this sample as the Na Auger peak was not present on the blank copper substrate.

Collectively, the XPS analysis of the copper substrate alone confirms the absence of c-PtNPs, the presence of copper and contamination by adventitious carbon and oxygen contamination. XPS analysis of the c-PtNPs on the copper substrate was confirmed by the presence of platinum and copper species. The citrate ion capping was verified by presence of carbon and oxygen species. The next step is now to understand how these 20 nm c-PtNPs interact with platelet physiological buffer.

4.2.6 Interaction of platinum nanoparticles with platelet physiological buffer

Before any PtNP platelet experiments could be conducted with the 20 nm c-PtNPs; it was crucial to understand how the physicochemical properties of the c-PtNPs may change when interacting with the platelet physiological buffer Tyrodes-HEPES. This interaction was assessed by DLS and zeta potential, 20 nm c-PtNPs were exposed to Tyrodes-HEPES and along with phosphate buffered saline (PBS). PBS was selected as it commonly used as a physiological buffer. Control samples included 20 nm c-PtNPs resuspended in 1.1 mM sodium citrate and

dH_20. The experiment was repeated across three batches of 20 nm c-PtNPs, five DLS and zeta potential measurements were performed to obtain the mean for each sample, data is presented as mean ± SD.

The exposure of 20 nm c-PtNPs to Tyrodes-HEPES and PBS caused the nanoparticles to aggregate; the average hydrodynamic diameters of c-PtNPs in 1.1 mM sodium citrate increased from 36.4 ± 0.4 nm to 2221.2 ± 245.2 nm and 3183.6 ± 581.2 nm respectively, as shown in Figure 4.10 (a). Aggregation was caused by the high ionic salt concentrations in both Tyrodes-HEPES and PBS, see Table 4.4 and Table 4.5 for salt concentrations. The citrate ion capping provides electrostatic stability for the PtNP core, yet the interaction between the PtNP core and citrate ions is relatively weak as citrate ions are non-covalently bound. Under physiological conditions the electrostatic forces between the c-PtNPs and citrate ions is disrupted by the high ionic salt concentrations and induce irreversibly aggregation triggering them to precipitate out of solution as shown in Figure 4.10 (c) and (d). Previous studies with metallic nanoparticles also observed nanoparticle aggregation from high ionic salt concentrations. Additionally, these studies demonstrated that nanoparticle aggregation was governed by the strength of the ionic solution. [137, 148]

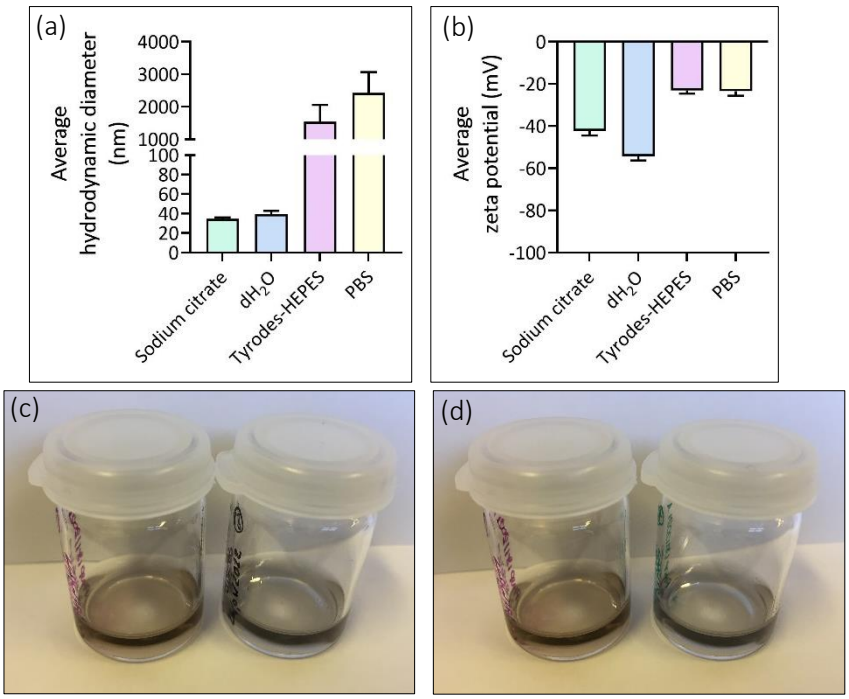

Figure 4.10 c-PtNP physiological buffer interactions. (a) hydrodynamic diameters and (b) zeta potentials & (c) c-PtNPs in Tyrodes-HEPES buffer and (d) c-PtNPs in PBS. Results presented from 3 experiments (n=3) and presented as mean ± SD.

Table 4.4 Components of Tyrodes-HEPES buffer.

Compound	Concentration (mM)
Sodium chloride	134
Potassium chloride	2.9
Sodium phosphate	0.34
Sodium bicarbonate	12
HEPES	20
Magnesium chloride	1
Glucose	5

Table 4.5 Components of 1x PBS.

Compound	Concentration (mM)
Sodium chloride	137
Potassium chloride	2.7
Sodium phosphate	10
Potassium phosphate	1.8

Zeta potential of c-PtNPs were demonstrated in Figure 4.10 (b), c-PtNPs in 1.1 mM sodium citrate and dH_2O exhibited zeta potentials of -43.76 ± 1 and -56.0 ± 2.1 mV respectively, demonstrating good stability; this stability significantly increased to -22.3 ± 1.3 mV in Tyrodes-HEPES buffer and -22.3 ± 1.3 mV in PBS. The high salt concentration in both buffers compresses the citrate ion capping leading to a low stability. Interestingly, the zeta potential of c-PtNPs in dH_2O indicated good stability; this was owing to the loss of citrate ion capping during the centrifugation and resuspension process causing some aggregation. A caveat of zeta potential is that the technique cannot distinguish between measuring monodispersed particles and aggregates, hence some aggregates can exhibit good stability. Collectively, this data demonstrates that the c-PtNPs need steric stabilisation to investigate PtNP platelet interactions.

4.3 Conclusion

The preparation of monodispersed c-PtNPs was successfully carried out using a seed mediated synthesis. Pt seeds were reproducibly synthesised on 2 different reactions scales, using these Pt seeds, electrostatically stabilised negatively charged c-PtNPs of 20 nm and 60 nm were synthesised on 4 different reaction scales with reproducible sizes. 20 nm c-PtNPs had good stability with a narrow particle size distribution range, again this was shown across all reaction scales. The 60 nm c-PtNPs had good stability albeit a broad particle size distribution range, this was demonstrated across all reaction scales. Large quantities of the 20 nm c-PtNPs were synthesised with reproducible sizing. High-resolution XPS scan of the 20 nm c-PtNPs revealed the elemental composition attributing to both platinum and the citrate ion capping. In the physiological buffers Tyrodes-HEPES and PBS, the 20 nm c-PtNPs were unstable and

aggregated; to utilise these c-PtNPs for later platelet studies, the c-PtNPs will need to undergo steric stabilisation.

Chapter 5 Functionalisation of Platinum Nanoparticles with Negatively Charged Thiol Compounds

Abstract: *This chapter examines the functionalisation of 20 nm citrate capped platinum nanoparticles (c-PtNPs) synthesised in Chapter 4. Owing to their citrate ion capping, these c-PtNPs were negatively charged but lacking a stable covalent bond, thus making them unsuitable for platelets studies. To enable platelet investigations, PtNPs were sterically stabilised/functionalised with thiols via a ligand exchange method. First, three carboxyl-terminated alkanethiols, 6-mercaptohexanoic acid (6-MHA), 8-mercaptooctanoic acid (8-MOA) and thioctic acid (TA), were investigated for functionalising 20 nm c-PtNPs. Utilising various surface characterisation techniques, it was confirmed their functionalisation with the alkanethiol molecules to produce sterically stable negatively charged 20 nm PtNPs via ligand exchange. In addition to previous alkanethiols, a polyethylene glycol (PEG) thiol O-(2-carboxyethyl)-O'-(2-mercaptoethyl) heptaethylene glycol (2-MOHA) was also investigated for functionalising c-PtNPs using the same method. The surface characterisation techniques confirmed that 20 nm functionalised PtNPs possessed negatively stable charges. This study is the first to report the functionalisation of c-PtNPs by alkane and pegylated thiols 6-MHA, 8-MOA, TA and 2-MOHA to create sterically stable negatively charged nanoparticles.*

5.1 Introduction

Nanoparticles have been extensively used in a wide variety of applications including biomedicine, sensing, electronics and energy. These applications are dependent on the functionalisation/synthesis of the nanoparticle, chemical reduction methods are often employed to synthesise metallic nanoparticles, as they enable controlled sizes. Capping agents such as sodium citrate provide nanoparticles with a negative charge,[21, 22, 90] and electrostatic stabilisation which in turn prevents their aggregation. Sterically stabilised nanoparticles can be achieved by modifying the surface of the nanoparticles with ligand molecules; the nature of ligand can influence the functionality, solubility, and colloidal stability of the nanoparticle. Thiol linkage is frequently used to functionalise/stabilise nanoparticles during synthesis or post-synthesis via ligand exchange methods.[42, 46, 149] Thiol molecules can suppress nanoparticle aggregation by chemisorbing onto the nanoparticle surface via covalent interactions to form a self-assembled monolayer (SAM).[150] The functional head group can bear groups such as carboxylic acid, amine, or hydroxyl that that enable hydrophobic and hydrophilic moieties, thus providing repulsive forces between neighbouring nanoparticles and enabling functionalisation and stabilisation at the same time.[40, 49, 151] Previous studies have primarily focused on the functionalisation of AuNPs by negatively charged and hydrophobic alkanethiols.[42, 46, 49] By contrast, there has only been one report on the functionalisation of PtNPs by the negatively charged alkanethiol 3-mercapto-1-propanesulfonic acid (3-MPS) with the hydrophobic alkanethiols to form a mixed SAM on PtNPs.[152] Nonetheless, SAM formation by 3-MPS is limited as short-chain alkanethiol such as 3-MPS do not form well-ordered SAMs.[153] Thus, with an increasing number of applications using PtNPs, [10, 11, 17, 18, 154] the functionalisation of PtNPs by negatively charged alkanethiols and PEGylated thiols warrants further investigation.

5.1.1 Objectives

1. Functionalise 20 nm c-PtNPs with 6-MHA. Characterise by DLS, zeta potential, gel electrophoresis and XPS.

2. Functionalise 20 nm c-PtNPs with 8-MOA. Characterise by DLS, zeta potential, gel electrophoresis and XPS.

3. Functionalise 20 nm c-PtNPs with TA. Characterise by DLS, zeta potential, gel electrophoresis and XPS.

4. Functionalise 20 nm c-PtNPs with 2-MOHA. Characterise by DLS, zeta potential, gel electrophoresis and XPS.

5.2 Results and Discussion

5.2.1 Solubility of alkanethiols

In the previous chapter, it was demonstrated that 20 nm c-PtNPs were electrostatically stabilised through the physisorption of citrate ions onto the PtNP surface. It was revealed, that under physiological conditions these c-PtNPs were unstable and aggregated immediately. To enable the PtNPs to withstand such conditions, capping the PtNPs with alkanethiol molecules via chemisorption methods were investigated. Herein, we explored different alkanethiol compounds to make the sterically stable negatively charged PtNPs. Three negatively charged alkanethiols compounds, 6-MHA, 8-MOA and TA were selected for sterically stabilising the c-PtNPs, their structures are illustrated in Figure 5.1.

(a) 6-mercaptohexanoic acid

(b) 8-mercaptooctanoic acid

(c) Thioctic acid

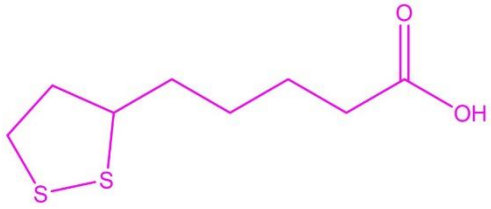

Figure 5.1 Negatively charged carboxyl-terminated alkanethiols. (a) 6-mercaptohexanoic acid (6-MHA), (b) 8-mercaptooctanoic acid (8-MOA) and (c) thioctic acid (TA).

These alkanethiol compounds exhibit a terminal carboxylic acid (COOH) functional group, while 6-MHA and 8-MOA are more similar in structure as both have a mercapto group (SH) head

group. 6-MHA has a 6-carbon alkane chain while 8-MOA has an 8-carbon alkane chain. To assess if there was a difference by a slight increase in the alkanethiol chain length 6-MHA and 8-MOA were selected, an increase in alkanethiol chain length enables well-ordered SAM formation via Van der Waals interactions.[155] Like 6-MHA; TA also has a 6-carbon alkane chain but more interestingly it has a disulphide group (R-S-S-R), thus allowing two sulphur-metal bonds to form on the nanoparticle surface. These alkanethiols have medium alkane chain lengths, a caveat of using long chain alkanethiols (≥ 9 carbons) is their non-polar tendency and their water solubility decreases.[156] As c-PtNPs were synthesised in aqueous solution and will be tested under physiological conditions, it is essential that the surface modifying compounds are water soluble.

Prior to thiol exchange, the solubility of 6-MHA, 8-MOA and TA was tested by preparing the alkanethiols in dH_2O and ethanol, their solubility was observed at 3 hours and 24 hours. Both 6-MHA and 8-MOA were soluble in dH_2O and ethanol at 3 and 24 hours; TA was only soluble in ethanol. Based on this observation, all 3 alkanethiols were prepared in ethanol for functionalisation experiments. The next part of this chapter will focus of the functionalisation of PtNPs by 6-MHA, 8-MOA and TA.

5.2.2 Functionalisation of 20 nm platinum nanoparticles by 6-mercaptohexanoic acid

Based on previous functionalisation methods with AuNPs [46, 49] 20 nm c-PtNPs were functionalised with 6-MHA by ligand exchange. In this method, a ligand exchange occurs between the citrate ion capping of the nanoparticles and the alkanethiol molecule. Citrate ions are non-covalently bound to the nanoparticle surface and can be easily displaced by thiol

molecules to form a strong covalent interaction, thus forming a SAM providing steric stabilisation and functionality.[39] Figure 5.2 illustrates the ligand exchange of citrate ions with 6-MHA to create sterically stable negatively charged PtNP. The concentration of 6-MHA required for surface coverage was calculated to be 5.9 µM, using the alkanethiol footprint 0.214 nm^2,[128] see Appendix 11.2 for calculations. c-PtNPs surface modified by 6-MHA will be referred to as PtNP-6-MHA throughout this thesis.

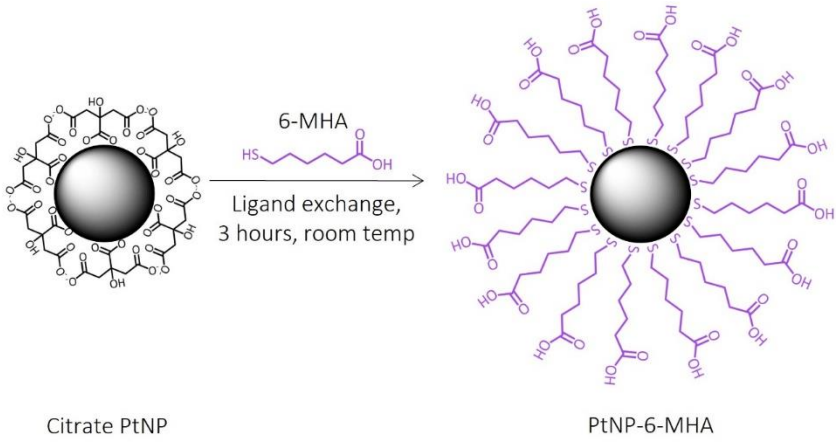

Figure 5.2 Ligand exchange of citrate ions on the 20 nm c-PtNP by 6-MHA. Note figure not to scale.

20 nm c-PtNPs were incubated with 6-MHA at concentrations ranging from 5 – 100 µM for 3 hours at room temperature. Excess 6-MHA and citrate ions were removed by centrifugation at 10000 x g for 10 minutes. The supernatant was discarded, and the PtNP-6-MHA were resuspended in dH_2O and then characterised by DLS, zeta potential and pH. Although pH is not a characterisation technique per say, they were reported as zeta potential measurements are dependent on pH, hence they were reported throughout this thesis. The control samples included 20 nm c-PtNPs in 1.1 mM sodium citrate and dH_2O (referred to as the dH_2O control). The c-PtNPs control was selected to assess if there was a difference between the capping

agents, dH_2O was used as a control as all PtNP-6-MHA were resuspended in dH_2O. For gel electrophoresis, 20 nm PtNPs were surface modified with 5 µM and 100 µM 6-MHA only following the method above up to the discarding step as concentrated functionalised PtNPs were required for this technique. Unconcentrated nanoparticles would not be visible on the agarose gel. Gel electrophoresis was only used qualitatively manner. 1 µL of concentrated 5 µM and 100 µM PtNP-6-MHA were then premixed with 15 µL glycerol and separated on a 1% agarose gel submerged in Tris-acetate-EDTA (TAE) buffer and concentrated c-PtNPs were used as a control. For full procedure see materials and methods section. DLS and zeta potential experiments were repeated across three batches of 20 nm PtNPs, five DLS and zeta potential measurements were performed to obtain the mean for each sample, data is presented as mean ± standard deviation (SD).

Figure 5.3 (a) demonstrates the hydrodynamic diameters of PtNP-6-MHA, the c-PtNPs control and dH_2O controls were similar at 30.9 ± 1.0 and 31.4 ± 1.1 nm respectively. The PtNP-6-MHA had comparable hydrodynamic diameters to the control samples, their hydrodynamic diameters ranged from 29.7 to 31.9 nm. There were no differences amongst the different concentrations of 6-MHA used. Looking at the zeta potentials in Figure 5.3 (b) the c-PtNPs control and dH_2O controls exhibited negative charges of -32.9 ± 3.7 and -37.2 ± 3.6 mV respectively; the zeta potential of PtNP-6-MHA exhibited negative charges, ranging from -19.3 to -34.6 mV. Interestingly, as the concentration of 6-MHA increased, the zeta potential increased, indicating low stability. This trend suggests a ligand exchange between the citrate ions and 6-MHA has taken place on the PtNP surface.

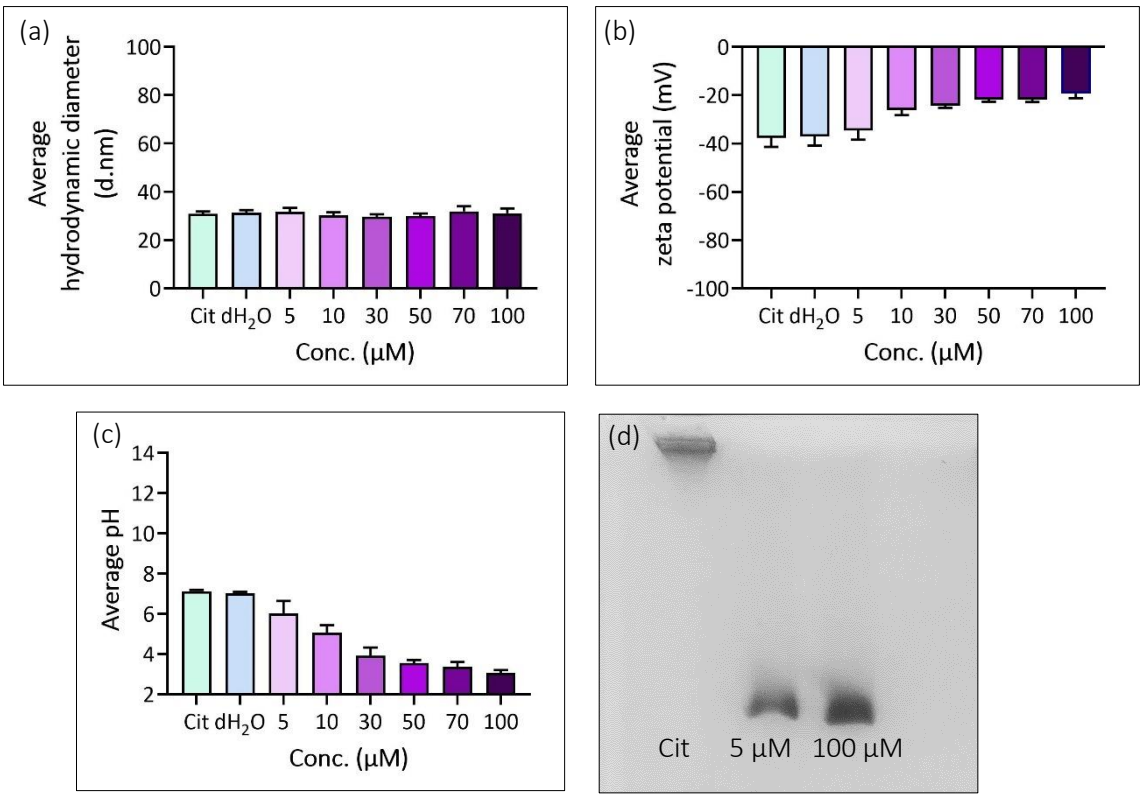

Figure 5.3 Characterisation of PtNP-6-MHA. (a) hydrodynamic diameters, (b) zeta potentials (c) pH and (d) gel electrophoresis. Results (except electrophoresis) are representative of 3 experiments (n=3) and presented as mean ± SD.

Additionally, the pH of PtNP-6-MHA solutions after purification decreased with increasing concentrations of 6-MHA from pH 6.9 to 3.7; the pH of the citrate control and dH_2O controls remained in the neutral range at pH 7.2 and 7.1 respectively, as shown in Figure 5.3 (c). Thus, indicating a ligand exchange has occurred. The decrease in pH could be as result of 6-MHA having a lower pH than the sodium citrate, therefore, as the concentration of 6-MHA increased the pH decreased. Furthermore, the decrease in pH suggests a change in the protonation equilibrium of 6-MHA. It is presumed, at high acidic conditions the COOH group of 6-MHA is deprotonated and negatively charged; by contrast in low acidic conditions the COOH group

would be in a protonated state and positively charged. This fact is related to the increase in zeta potential as a decrease in pH is observed, which is in accordance with literature.[157]

Gel electrophoresis was also used to assess ligand exchange; this technique was only used qualitatively. 5 μM and 100 μM of PtNP-6-MHA were selected for gel electrophoresis to examine if there was a difference in surface coverage in comparison to the c-PtNPs. The 20 nm c-PtNPs control sample aggregated within the well see Figure 5.3 (d). Due to their electrostatic stabilisation by citrate ions, these c-PtNPs are unprotected from the TAE buffer and the applied charge. Conversely, both 5 μM and 100 μM PtNP-6-MHA migrated through the agarose gel as they had become sterically stable with a negative charge. 5 μM PtNP-6-MHA had a fainter band compared with 100 μM PtNP-6-MHA which had a denser band; one reason for this difference could be that at the lower concentration, fewer 6-MHA molecules had bound to the PtNP surface, hence only a fewer c-PtNPs had become sterically stable and were able to migrate the through the agarose gel. At 100 μM of 6-MHA, more PtNPs had become sterically stabilised, therefore more sterically stable PtNP-6-MHA migrated through the agarose gel. This data further supports that a ligand exchange has occurred between 6-MHA and the citrate ions on the PtNP surface. Although, the zeta potential, pH and gel electrophoresis data provide evidence of ligand exchange of the citrate ions for 6-MHA, further investigation is required to confirm the platinum-thiol bond, therefore the next step is to conduct XPS analysis of 20 nm PtNP-6-MHA.

5.2.3 XPS of 20 nm PtNP-6-MHA

To further confirm if 6-MHA had bound onto the PtNP surface, XPS was employed to assess the elemental composition of PtNP-6-MHA. 6-MHA was selected as a control sample, the control sample was prepared by directly drop casting 6-MHA onto the copper substrate and air dried. Following the method described in 5.2.2, c-PtNPs were surface modified with 100 µM of 6-MHA for 3 hours at room temperature. 100 µM 6-MHA was used for XPS analysis as this concentration demonstrated the greatest increase in zeta potential as shown in Figure 5.3 (b). The excess 6-MHA and citrate ions were removed by centrifuging the sample at 10000 x g for 10 minutes, the supernatant was then discarded, and the concentrated PtNP-6-MHA were drop cast onto copper disc (substrate), air dried and submitted for XPS analysis.

Survey scans of the control sample 6-MHA detected the presence of copper (Cu), carbon (C), oxygen (O) and sulphur (S), while PtNP-6-MHA detected platinum (Pt) in addition to Cu, C, O and S. Examination of the high-resolution scans of 6-MHA detected signals from Pt 4f, Cu 2p, C 1s, O 1s and S p orbitals, these are presented in Figure 5.4. These high-resolution scans were charge corrected to the adventitious carbon peak at 284.8 eV. As previously discussed in section 4.2.5, contamination by adventitious carbon and oxygen are common artefacts found in XPS and are presented in high-resolution scans, therefore the high-resolutions scans will only be used to determine the species present on the surface of modified PtNPs.

As expected, the high-resolution scans of 6-MHA did not detect a signal for Pt 4f as no c-PtNPs were present on the copper substrate, see Figure 5.4 (a). However, three Cu 3p peaks were detected, Cu 3p $_{3/2}$ at 74.9 eV, CuO at 75.4 eV and Cu 3p $_{1/2}$ at 77.4 eV. These peaks were comparable to those obtained on the blank copper substrate in section 3.2.5. Cu 3p and Pt 4f have similar binding energies, thus there is a spectral overlap, this has been previously reported in the XPS analysis of Pt-Cu bimetallic alloys.[144] Investigation of the high-resolution scans of PtNP-6-MHA detected Pt 4f as typical asymmetric doublet peak, Pt 4f $_{7/2}$ at 71.1 eV and Pt 4f $_{5/2}$ at 74.4 eV with a separation of 3.33 eV, see Figure 5.4 (b). These peaks are attributed to the c-PtNPs and are characteristic of platinum metals and PtNPs.[145, 146, 158] In addition, the spectral overlap of Cu 3p $_{3/2}$ and Pt 4f $_{5/2}$ is clearly evident. Again, three peaks of Cu 3p were detected, Cu 3p $_{3/2}$ at 74.9 eV, CuO at 75.4 eV and Cu 3p $_{1/2}$ at 77.3 eV, which had similar binding energies to those found in the 6-MHA control sample. Cu 3p is attributed to the copper substrate.

Examination of the high-resolution scans Cu 2p for both 6-MHA and PtNP-6-MHA are illustrated in Figure 5.4 (c) & (d). Cu 2p revealed a doublet peak in both samples, 6-MHA exhibited Cu 2p $_{3/2}$ at 932.7 eV preceded by Cu 2p $_{1/2}$ at 952.5 eV, while PtNP-6-MHA exhibited Cu 2p $_{3/2}$ at 932.7 eV and Cu 2p $_{1/2}$ at 952.6 eV. Both 6-MHA and PtNP-6-MHA had a separation of 19.8 eV, these spectra were almost identical and the peaks found were in accordance with literature.[146, 147] Like Cu 3p, Cu 2p is also attributed to the copper substrate used in XPS analysis.

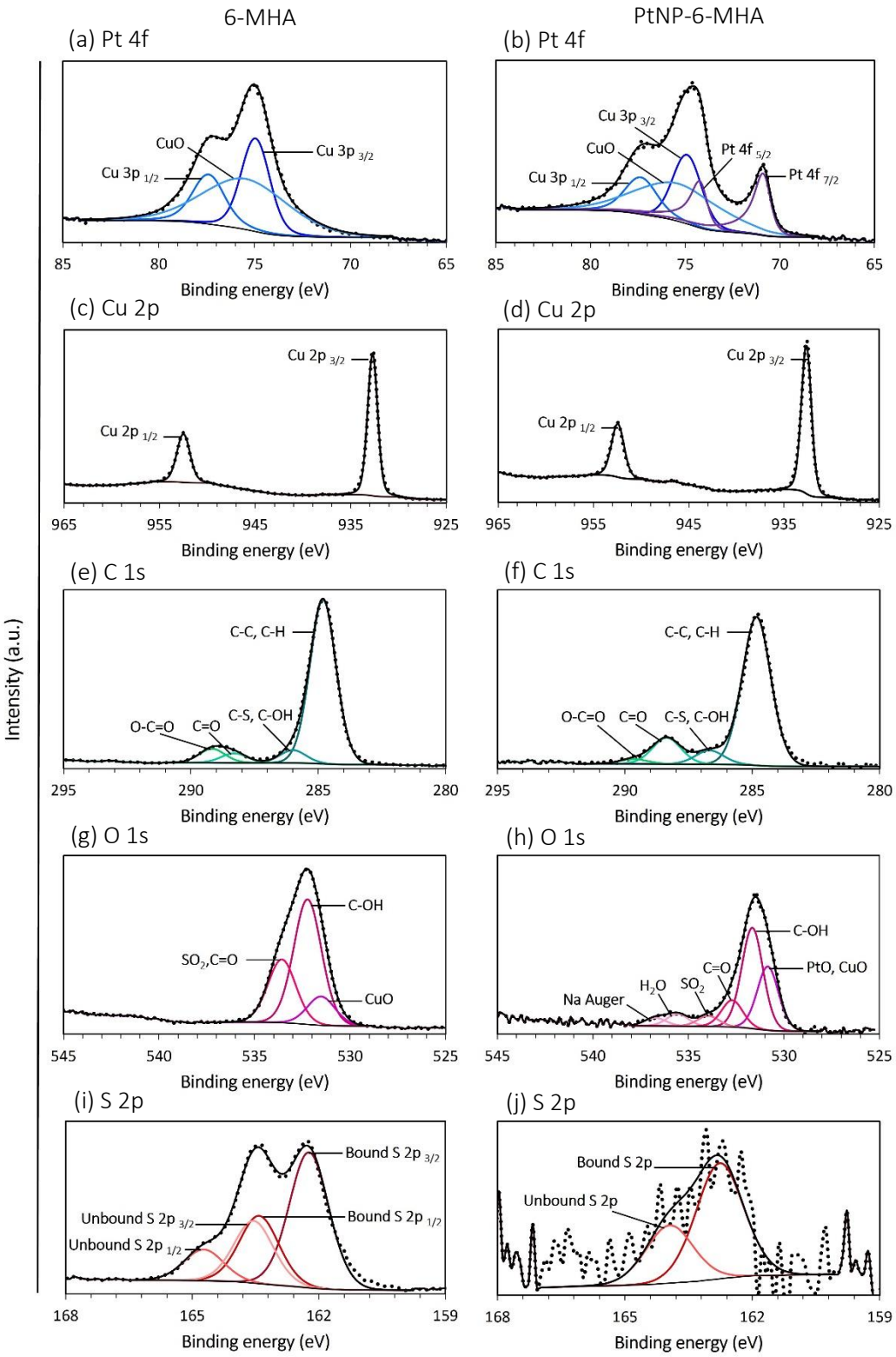

Figure 5.4 High resolution XPS spectra of 6-MHA and PtNP-6-MHA on a copper substrate. (a) Pt 4f - 6-MHA, (b) Pt 4f - PtNP-6-MHA, (c) Cu 2p - 6-MHA, (d) Cu 2p – PtNP-6-MHA, (e) C 1s – 6-MHA, (f) C 1s – PtNP-6-MHA, (g) O 1s – 6-MHA, (h) O 1s – PtNP-6-MHA (i) S 2p – 6-MHA and (j) S 2p – PtNP-6-MHA (n=1).

Interpretation of the C 1s high resolution scans for 6-MHA revealed five carbon species as presented in Figure 5.4 (e). C-C, C-H at 284.8 eV corresponds to the main alkanethiol chain of 6-MHA however adventitious carbon is also presented 284.8 eV; this was previously observed in the XPS of the blank copper substrate in section 3.2.5. The next peaks were C-S, C-OH at 285.9 eV, C=O at 287.9 eV and O-C=O at 289.2 eV. C-S is attributed to the carbon-thiol bond of the 6-MHA, while C-OH, C=O and O-C=O are attributed to the COOH group of 6-MHA but also to adventitious carbon. The high-resolution scan of C 1s for PtNP-6-MHA also detected five species, C-C, C-H at 284.7 eV, this was proceeded by smaller peaks, C-S, C-OH at 286.8 eV, C=O at 288.3 eV and O-C=O at 289.7 eV. The C-C, C-H peak relates to the alkanethiol chain and adventitious carbon, C-S corresponds to presence of the thiol and C-OH, C=O and O-C=O correspond to the COOH group of 6-MHA and but again also adventitious carbon. Interestingly, the C=O peak was more pronounced suggesting more oxidation of the sample. The carbon species in both 6-MHA and PtNP-6-MHA are in accordance with literature.[146, 159]

Deconvolution of the high-resolution scans of O 1s for 6-MHA found three chemical species, CuO at 531.5 eV, followed by C-OH at 532.2 eV and SO_2,C=O at 533.6 eV, these binding energies are those found in literature.[146] CuO corresponds to the copper substrate, both C-OH and C=O species correspond with COOH group, nonetheless these two species were present on the blank copper substrate (see section 4.2.5), thus confirming adventitious oxygen contamination. SO_2 is attributed to oxidised sulphur from 6-MHA. The examination of the O 1s high-resolution scans of PtNP-6-MHA found six oxygen species, PtO and CuO at 530.8 eV, which ascribes to the PtNPs and the copper substrate. Next, C-O at 531.7 eV, C=O at 532.7 eV, again C-O and C=O

relate to adventitious oxygen and the COOH group of PtNP-6-MHA. These peaks were preceded by SO_2 at 534 eV, H_2O at 535.6 eV and a sodium (Na) Auger peak at 536.9 eV; SO_2 corresponds with the oxidised sulphur. A possible explanation for the presence of the H_2O and Na Auger peaks is that not all the citrate ions had been displaced by 6-MHA on the PtNP surface, dH_2O was used to prepare the sodium citrate, thus the H_2O and Na Auger peaks were detected.

The high-resolution scans of S 2p for 6-MHA on the copper substrate observed two integrated doublets with a 2:1 area ratio, with a separation of 1.18 eV, as illustrated in Figure 5.4 (i). Bound S $2p_{3/2}$ and S $2p_{1/2}$ were present at 162.2 eV and 163.4 eV respectively, demonstrating a copper-thiol bond. The second doublet was present at 163.5 eV and 164.7 eV and is ascribed to the unbound thiol, these data were similar to those obtained using gold surfaces.[160] Sulphur binding to the copper substrate was expected, early studies investigated SAM formation by various alkanethiols on copper substrates for their wetting properties and for their ability to inhibit corrosion of the underlying copper substrate.[34, 161, 162] The unbound thiol could possibly due to physisorbed 6-MHA. Conversely, the high-resolution scans of S 2p for PtNP-6-MHA displayed high background with one S 2p doublet with a 2:1 area ratio, with a separation of 1.18 eV was observed, see Figure 5.4 (j). Bound S 2p was present at 162.4 eV while the unbound S 2p ½ was present at 163.7 eV. The difference of S 2p peaks is due to the sample preparation, 6-MHA was directly deposited onto the copper substrate without incubation and rinsing, by contrast PtNPs were first incubated for 3 hours with 6-MHA, thus, allowing more time for a platinum-thiol bound to form, then centrifuged to remove excess 6-MHA and citrate ions and then deposited on the copper substrate.

The % of bound and unbound S 2p was derived from the area of the peak fittings from the CasaXPS software from two scans, this is shown Table 5.1. The bound and unbound S 2 p of 6-MHA on the copper substrate was 65.5% and 34.5% respectively, confirming 6-MHA had bound to the copper substrate. The unbound S 2p could be due to bond formation between the mercapto groups of 6-MHA and or the physisorption of 6-MHA on the copper substrate. In the PtNP-6-MHA, the % of bound and unbound S 2p was 66.7% and 33.3% respectively, this was comparable to 6-MHA on the copper substrate. Again, the unbound S 2p is likely due to the physisorption of 6-MHA on the c-PtNPs.

Table 5.1 - % of bound and unbound S 2 p in 6-MHA and PtNP-6-MHA.

	6-MHA	PtNP-6-MHA
% of S 2p bound	65.5	66.7
% of S 2p unbound	34.5	33.3

This XPS data demonstrated PtNP-6-MHA were present on the copper substrate. However, the carbon and oxygen species, attributed to the structure 6-MHA in both high-resolution scans of 6-MHA and PtNP-6-MHA, were masked by adventitious carbon and oxygen. Na Auger peaks indicated citrate ions were still present on the PtNP surface after ligand exchange, thus, PtNP-6-MHA was only partially functionalised by 6-MHA via chemisorption. Partial functionalisation has previously been observed with the ligand exchange of citrate ions on AuNPs for 3-MPS.[39]

5.2.4 Functionalisation of 20 nm platinum nanoparticles with 8-mercaptooctanoic acid

Using the same chemisorption method described in section 5.2.2, 20 nm c-PtNPs were surface modified by the 8-MOA, the ligand exchange is illustrated in Figure 5.5. The same alkanethiol footprint of 0.214 nm^2 was utilised for the surface coverage calculations for 8-MOA, hence the concentrations used to functionalise the c-PtNPs are the same as 6-MHA. c-PtNPs functionalised by 8-MOA will be referred to as PtNP-8-MOA throughout this thesis.

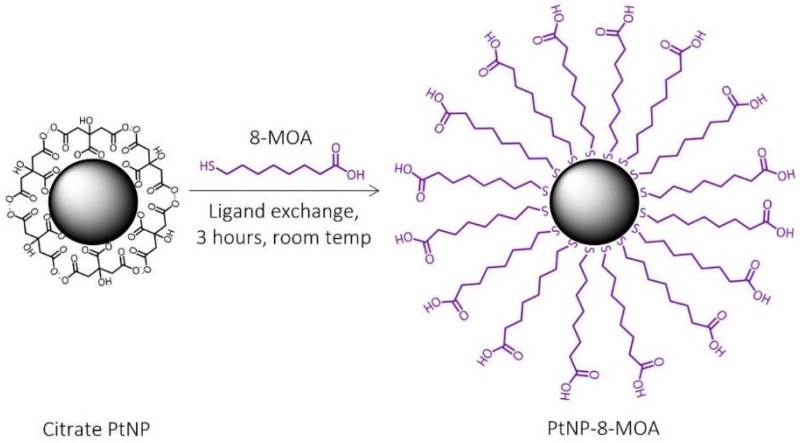

Figure 5.5 Ligand exchange of citrate ions on the 20 nm c-PtNP by 8-MOA. Note figure not to scale.

In brief, 20 nm c-PtNPs were incubated with 8-MOA for with concentrations from 5 – 100 µM for 3 hours at room temperature. Excess 8-MOA and citrate ions were removed by centrifugation at 10000 x g for 10 minutes. The supernatant was discarded, and the PtNP-8-MOA were resuspended in dH_2O and then characterised by DLS, zeta potential and pH. Again, the 20 nm c-PtNPs in 1.1 mM sodium citrate and dH_2O were utilised as control samples. For gel electrophoresis characterisation, 20 nm c-PtNPs were surface modified with 5 µM and 100 µM 8-MOA only following the method above, until the discarding step. 1 µL of concentrated 5 µM and 100 µM PtNP-8-MOA were then premixed with 15 µL glycerol and separated on a 1% agarose gel submerged in TAE buffer and concentrated c-PtNPs were used as a control. PtNP-

8-MOA were characterised by DLS, zeta potential and gel electrophoresis. All DLS and zeta potential experiments were repeated across three batches of 20 nm c-PtNPs, five DLS and zeta potential measurements were performed to obtain the mean for each sample, data is presented as mean ± SD.

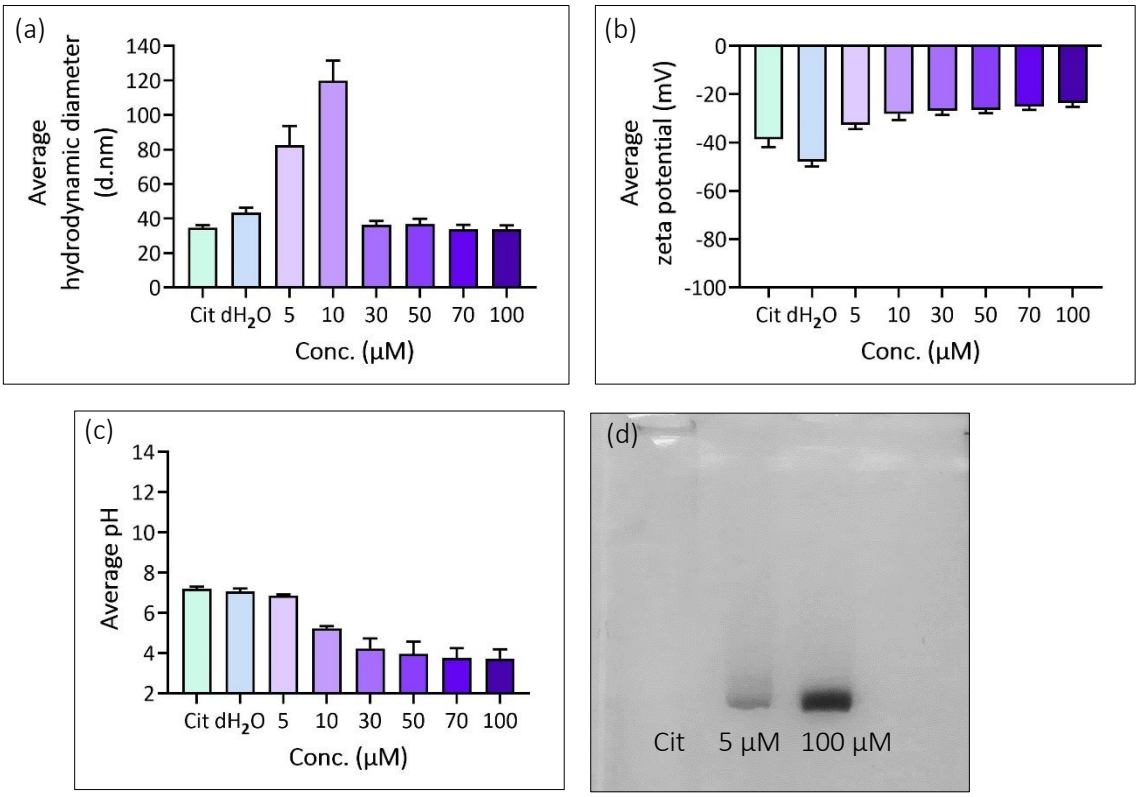

Figure 5.6 Characterisation of PtNP-8-MOA, (a) hydrodynamic diameters, (b) zeta potentials (c) pH and (d) gel electrophoresis. Results (except electrophoresis) are representative of 3 experiments (n=3) and presented as mean ± SD.

Figure 5.6 (a) displays the hydrodynamic diameter of PtNP-8-MOA, the citrate and dH_2O control had hydrodynamic diameters of 34.7 ± 1.4 nm and 43.3 ± 2.9 nm respectively. The hydrodynamic diameters of PtNP-8-MOA increased at 5 µM and 10 µM of 8-MOA, while the remaining concentrations 30 to 100 µM had similar hydrodynamic diameters ranging from 33.7

to 36.8 nm. It is unclear why 5 µM and 10 µM 8-MOA gave larger hydrodynamic diameters of 82.4 ± 11.2 and 119.8 ± 11.8 nm respectively, this was previously not observed with 6-MHA. A possible explanation could be that c-PtNPs have aggregated during the ligand exchange process. As the citrate ions are being displaced by 8-MOA, the c-PtNPs surface can be exposed if there are not enough thiol molecules to bind to the PtNP surface, forming aggregates with neighbouring nanoparticles. Thus, when the nanoparticles form aggregates, they exhibit larger hydrodynamic diameters compared with individual nanoparticles. Moreover, these aggregates are not necessarily spherical in shape, the DLS technique measures everything on the particle surface and it assumes all particles measured are spherical. Therefore, the hydrodynamic diameter of these particles appears larger than expected.

The zeta potential of PtNP-8-MOA demonstrated a negative charge which ranged from -24.5 to -32.6 mV, in comparison to the citrate and dH_2O controls which had zeta potentials of -38.6 ± 3.2 mV and -47.9 ± 2 mV respectively. The reduced zeta potential of dH_2O control sample is due to the loss of the citrate ion capping during the resuspension step in dH_2O, therefore some of the c-PtNPs aggregate forming a larger particle which the Zetasizer instrument translates to large stable nanoparticle. The zeta potential of PtNP-8-MOA followed a similar trend to that of PtNP-6-MHA, as the concentration of 8-MOA increased the zeta potential of PtNP-8-MOA shown in Figure 5.6 (b), suggesting a ligand exchange had occurred between the citrate ions and 8-MOA. Albeit the increase in zeta potential indicates low stability, it is indicative of more 8-MOA molecules binding to the PtNP surface, therefore more citrate ion capping has been exchanged for 8-MOA. Ligand exchange was further supported by the change in pH of purified

surface modified PtNPs solutions after the procedure, see Figure 5.6 (c). The increasing concentration of 8-MOA decreased the pH from pH 6.9 to pH 3.7, indicating more 8-MOA had bound to the PtNP surface as it was indicated in the previous section. Similar to 6-MHA, the decrease in pH could be due to 8-MOA having a lower pH than the sodium citrate, thus, as the concentration of 8-MOA increased the pH decreased. The decrease also indicates a change in the protonation equilibrium of 8-MOA; at high acidic conditions the COOH group of 8-MOA would be deprotonated and negatively charged. At low acidic conditions the COOH group would stay protonated and positively charged. Again, this fact is corresponds to the increase in zeta potential as a decrease in pH is observed, which is in accordance with literature.[157]

Figure 5.6 (d) shows the gel electrophoresis of PtNP-8-MOA, the 20 nm c-PtNPs control sample once again aggregated due to its citrate ion capping; 5 µM and 100 µM PtNP-8-MOA migrated through the sample, confirming a thiol exchange had taken place. 5 µM PtNP-8-MOA appeared as faint band, by contrast 100 µM PtNP-8-MOA appeared as a darker band, indicating more 8-MOA had bound to the PtNPs. Thus, making the PtNPs more sterically stable, in turn more PtNP-8-MOA migrated through the agarose gel. These gel electrophoresis results support a ligand exchange has taken place. Together, the DLS, zeta potential, pH and gel electrophoresis data provided evidence that 8-MOA has chemisorbed onto the PtNP surface. To confirm if 8-MOA has bound to the c-PtNPs to form a thiol bond, XPS analysis was performed on 8-MOA and PtNP-8-MOA.

5.2.5 XPS of 20 nm PtNP-8-MOA

XPS was used to investigate the elemental composition of 8-MOA and PtNP-8-MOA. 8-MOA was used a control sample and was prepared by directly drop casting onto the copper substrate and air dried. Following the method described in section 5.2.2, PtNP-8-MOA was prepared by surface modifying c-PtNPs with 100 µM of 8-MOA for 3 hours at room temperature; the excess 8-MOA and citrate ions were removed by centrifuging the sample at 10000 x g for 10 minutes. The supernatant was discarded, and the concentrated PtNP-8-MOA were drop cast onto copper substrate, air dried and submitted for XPS analysis.

Survey scans of 8-MOA and PtNP-8-MOA revealed the presence of Pt, Cu, C, O and S elements. Investigation of high-resolution scans of Pt 4f found for 8-MOA detected no signal from the Pt 4f orbital as no c-PtNPs was present in the sample, however three Cu 3p species were detected, Cu $3p_{3/2}$ at 74.9 eV, CuO at 75.3 eV and Cu $3p_{1/2}$ at 77.3 eV as shown in Figure 5.7 (a). This was to be expected as Cu 3p and Pt 4f have similar binding energies.[144] Although Cu 3p was previously found in the blank copper substrate (section 4.2.5), 6-MHA and PtNP-6-MHA, Cu 3p was not detected in the high-resolution scans of Pt 4f for PtNP-8-MOA as illustrated Figure 5.7 (b). Potentially more PtNP-8-MOA had covered the surface of the copper substrate. The asymmetric peaks of Pt 4f were detected, Pt $4f_{7/2}$ at 70.8 eV and Pt $4f_{5/2}$ at 74.2 eV, with a separation of 3.33 eV. These binding energies are in accordance with those found in literature.[145, 146, 158] The presence of Pt 4f is ascribed to the PtNPs.

The high-resolution scans of Cu 2p for 8-MOA and PtNP-8-MOA displayed the typical doublet peaks, see Figure 5.7 (c) & (d); 8-MOA presented Cu $2p_{3/2}$ 932.5 eV and Cu $2p_{1/2}$ 952.4 eV. PtNP-8-MOA found Cu 2p at comparable binding energies, Cu $2p_{3/2}$ 932.1 eV and Cu $2p_{1/2}$ 954 eV. Both 8-MOA and PtNP-8-MOA had a separation of 19.9 eV. CuO peaks were also detected in each of the main two Cu 2p peaks of PtNP-8-MOA, CuO at 933.7 eV and 954.2 eV, indicating some oxidation. Both Cu 2p peaks in 8-MOA and PtNP-8-MOA are attributed to the copper substrate and are similar to those in literature.[146, 147]

Interpretation of the high-resolution scans of C 1s for 8-MOA revealed five carbon species, see Figure 5.7 (e), a large C-C, C-H peak at 284.8 eV followed by smaller peaks, C-S, C-OH at 286.7 eV, C=O at 288.4 eV and 289.9 eV, these binding energies are agreement with literature.[146, 159] C-C, C-H ascribes to the alkanethiol chain and adventitious carbon, while C-S relates to the presence carbon-thiol bond on the alkanethiol chain, C-OH, C=O and O-C=O are attributed to the COOH group of 8-MOA and adventitious carbon as these peaks were found on the blank copper substrate (section 4.2.5). Examination of the high-resolution C 1s scans of PtNP-8-MOA also displayed the same four carbon species with similar binding energies. C-C, C-H was found 284.8 eV, C-S at 286.7 eV, C=O at 288.4 eV and O-C=O 289.9 eV, again these binding energies are agreement with literature.[146, 159] C-C, C-H relates to the alkanethiol chain and adventitious carbon, while C-S is due to the carbon-thiol bond on the alkanethiol chain. C-OH, C=O and O-C=O are attributed to the carboxylic acid group of 8-MOA and adventitious carbon.

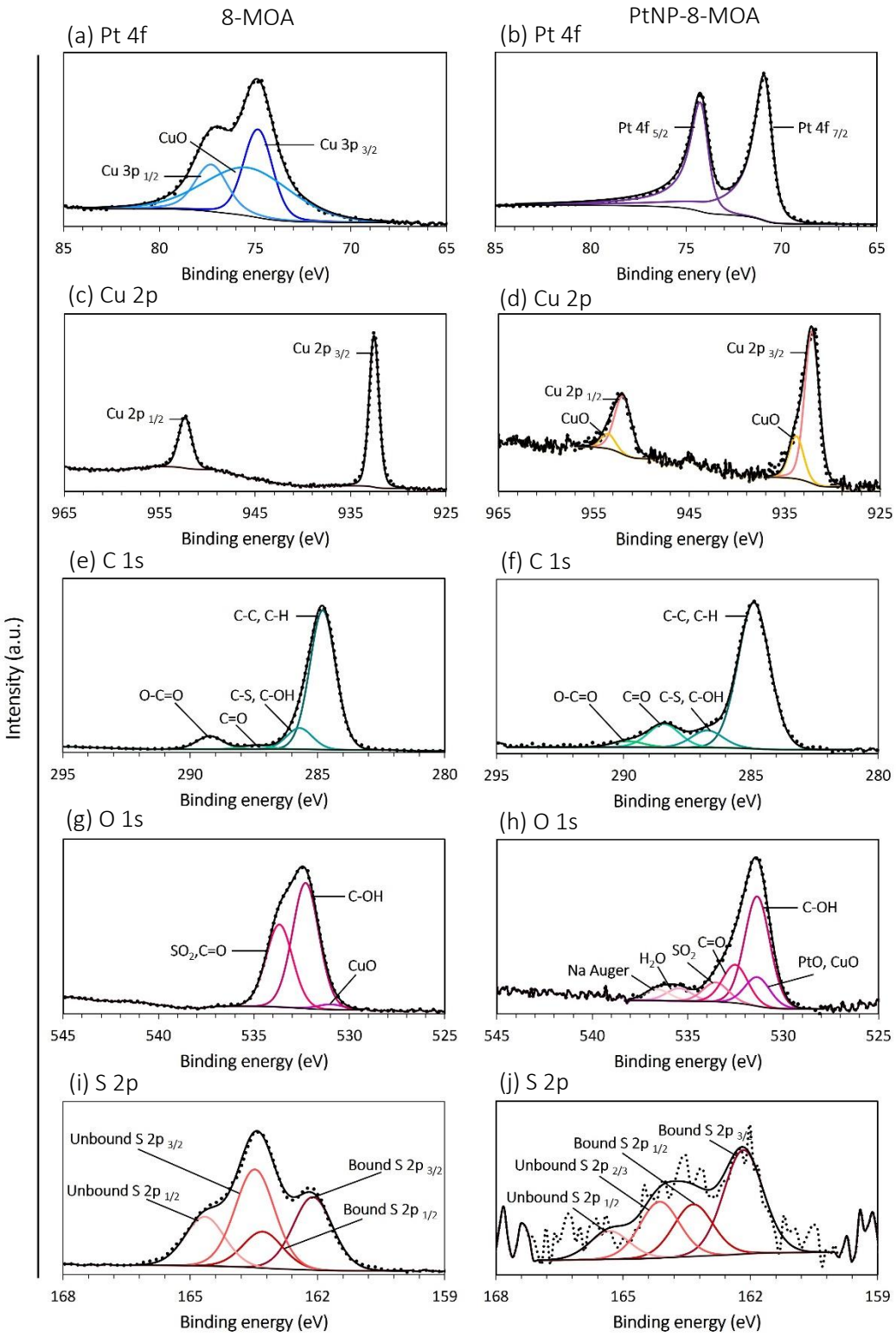

Figure 5.7 High resolution XPS spectra of 8-MOA and PtNP-8-MOA on a copper substrate. (a) Pt 4f - 8-MOA, (b) Pt 4f - PtNP-8-MOA, (c) Cu 2p - 8-MOA, (d) Cu 2p – PtNP-8-MOA, (e) C 1s – 8-MOA, (f) C 1sPtNP-8-MOA, (g) O 1s – 8-MOA, (h) O 1s – PtNP-8-MOA, (i) S 2p – 8-MOA and (j) S 2p – PtNP-8-MOA (n=1).

The examination of O 1s high resolution scans revealed three chemical species, as displayed in Figure 5.7 (g), CuO at 531 eV, C-OH at 532.3 eV and SO_2, C=O at 533.6 eV. CuO corresponds to the copper substrate, while C-OH and C=O correspond with the COOH group of 8-MOA, however these two species were found on the blank copper substrate, thus these peaks are also attributed to adventitious oxygen contamination. The high-resolution scans of PtNP-8-MOA revealed six oxygen species, the metal oxide peaks (PtO, CuO) were overlayed with and C-OH at 531.4 eV; both metal oxide species attributed to the PtNPs and the copper substrate. These were preceded by C=O at 532.5 eV, SO_2 at 533.5 eV and H_2O at 535.5 eV and a Na Auger peak at 536.6 eV. Again, C-OH and C=O are attributed to both COOH and adventitious oxygen and the carboxylic acid group of 8-MOA. The H_2O and Na Auger peaks attributed to the citrate ion capping, indicating citrate ions were still present on the surface of PtNP-8-MOA.

Investigation of the high-resolution scans of S 2p of 8-MOA and PtNP-8-MOA, revealed the presence of two intercalated doublets with 2:1 area ratio and 1.18 eV separations, these peaks correspond with bound and unbound S 2p, as shown in Figure 5.7 (i) and (j). As observed with 6-MHA, 8-MOA also formed a sulphur-copper bond, the bound S 2p species were S $2p_{3/2}$ at 162 eV and S $2p_{1/2}$ at 163.2 eV and the unbound species were S $2p_{3/2}$ at 163.5 eV and S $2p_{1/2}$ at 164.6 eV. SAM formation by alkanethiols thiols on copper substrates have previously demonstrated the copper-thiol bond.[34, 161, 162] The examination of PtNP-8-MOA high resolution scans had comparable S 2p peaks to that of 8-MOA. Two bound S 2p peaks were detected at 162.2 eV and 163.3 eV, while the unbound S 2p peaks were detected at 164.1 and 165.3 eV. Both 8-MOA and PtNP-8-MOA revealed S 2p species that were similar to those found on gold

substrates.[160] Using the areas from the peak fitting using CasaXPS, the % of bound and unbound S 2p was calculated and shown in Table 5.2.

Table 5.2 - % of bound and unbound S 2p in 8-MOA and PtNP-8-MOA.

	8-MOA	PtNP-8-MOA
% S 2p bound	38.4	65.7
%S 2p unbound	61.6	33.4

The % of S 2p bound and unbound from 8-MOA on the copper substrate was 38.4% and 61.6% respectively. Conversely, PtNP-8-MOA had 65.7% bound S 2p and 33.4% unbound. A possible explanation for this difference is the preparation of both samples; 8-MOA was drop cast on the copper substrate and was air dried immediately, therefore, only a few 8-MOA molecules were chemisorbed onto the copper substrate. PtNP-8-MOA was prepared by incubating PtNPs with 8-MOA for 3 hours, hence more 8-MOA molecules were able form a platinum-thiol bound. The unbound sulphur of 8-MOA is likely due to physisorption on the copper substrate. In the case of PtNP-8-MOA, citrate ions were still present on the PtNP surface this was confirmed by the Na Auger peak. Herein, this XPS data revealed that PtNPs were present on the copper substrate. Carbon and oxygen species ascribed to the structure of 8-MOA were detected in both 8-MOA and PtNP-8-MOA samples but could not be distinguished from adventitious carbon and oxygen. Comparison of sulphur species for 8-MOA and PtNP-8-MOA demonstrated 65.7% of 8-MOA has bound to the PtNP surface via chemisorption to give a platinum-thiol bound. Similar to PtNP-6-MHA, PtNP-8-MOA was partially functionalised by 8-MOA.

5.2.6 Functionalisation of platinum nanoparticles with Thioctic acid

TA was used to functionalise the 20 nm c-PtNPs, see Figure 5.8 overall for ligand exchange. The alkanethiol footprint of 0.214 nm^2 could not be applied for the TA surface coverage calculations as the TA molecule exhibits a disulphide bond (R-S-S-R). The TA footprint of 0.428 nm^2 was approximated using Chem3D by calculating the area of the molecule; using this footprint the concentration of TA required for surface coverage was calculated to 2.9 µM, see Appendix 11.2 for calculations. c-PtNPs surface modified by TA will be referred to as PtNP-TA throughout this thesis.

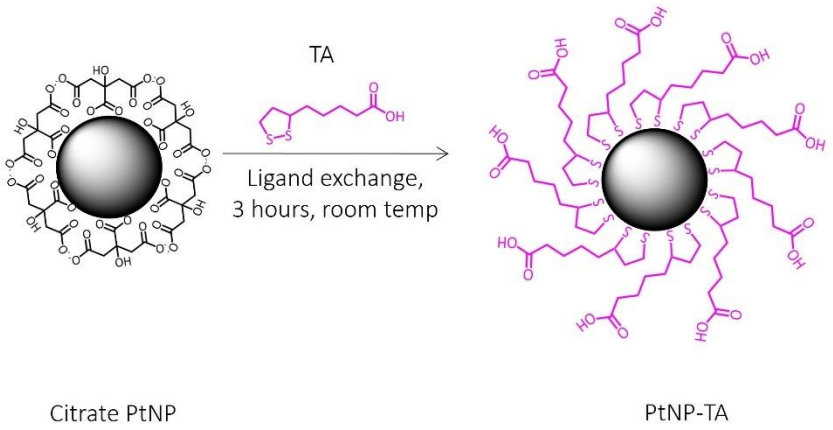

Figure 5.8 Ligand exchange of citrate ions on the 20 nm c-PtNP by TA. Note figure not to scale.

Following the method previously used in section 5.2.2, 20 nm c-PtNPs were incubated with TA at concentrations from 2 – 70 µM for 3 hours at room temperature. Excess TA and citrate ions were removed by centrifugation at 10000 x g for 10 minutes. The supernatant was discarded, and the PtNP-TA were resuspended in dH_2O and then characterised by DLS zeta potential and pH. As before, 20 nm c-PtNPs in 1.1 mM sodium citrate and dH_2O were selected as controls to assess if there was a difference between the capping agents, dH_2O was as a control as all PtNP-TA were resuspended in dH_2O. For gel electrophoresis characterisation, 20 nm PtNPs were

surface modified with 2 µM and 70 µM TA following the method above, until the discarding step. 1 µL of concentrated 2 µM and 70 µM PtNP-TA were then premixed with 15 µL glycerol and separated on a 1% agarose gel submerged in TAE buffer and concentrated PtNP were used as a control. All DLS and zeta potential experiments were repeated across three batches of 20 nm PtNPs. Five DLS and zeta potential measurements were performed to obtain the mean for each sample, data is presented as mean ± SD.

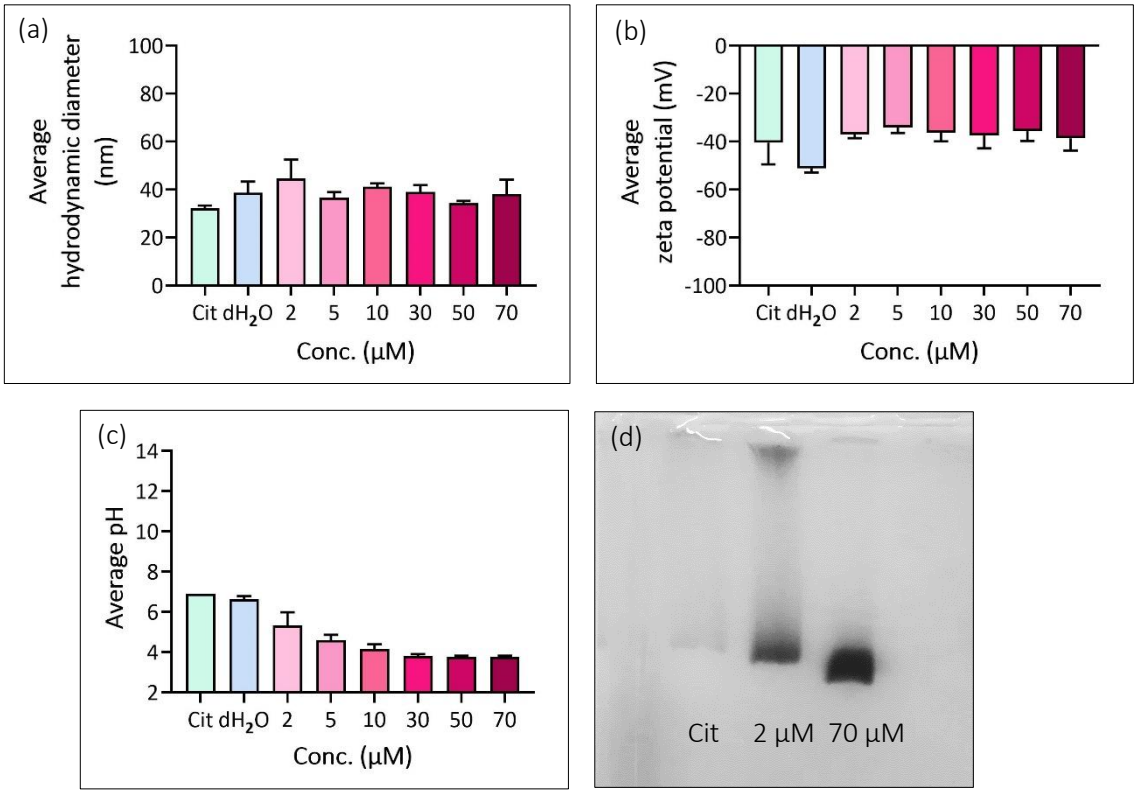

Figure 5.9 Characterisation of PtNP-TA. (a) hydrodynamic diameters, (b) zeta potentials (c) pH and (d) gel electrophoresis. Results (except electrophoresis) are representative of 3 experiments (n=3) and presented as mean ± SD.

The hydrodynamic dynamic of PtNP-TA is shown in Figure 5.9 (a). As before, controls samples in citrate and dH_2O demonstrated hydrodynamic diameters of 32.2 ± 1.2 and 38.6 ± 4.8 nm

respectively. The hydrodynamic diameters of PtNP-TA were similar across the different concentrations ranging from 34.4 to 44.7 nm. These results were comparable those obtained with PtNP-6-MHA where no differences in hydrodynamic diameters were observed. Zeta potentials are displayed in Figure 5.9 (c), the control samples in citrate and dH_2O exhibited zeta potentials of -40.5 ± 9.0 and -51.1 ± 1.8 mV. Compared with the control samples, there was an increase in the zeta potential in the PtNP-TA samples ranging from -34.1 to -38.6 mV, indicating good stability. However, no difference in zeta potentials was observed between the PtNP-TA samples, this was not the case with PtNP-6-MHA and PtNP-8-MOA. A possible explanation for this for these results, is that more TA molecules were bound to the PtNP surface. As TA exhibits a R-S-S-R group, two sulphur atoms are available to form two covalent bonds with the PtNPs. Consequently, more citrate ions would be displaced by the TA molecules, therefore, the nanoparticle surface would be exposed allowing more TA molecules to bind onto the c-PtNPs compared with 6-MHA and 8-MOA, which was reflected by the zeta potential.

Ligand exchange was further supported by the change in pH of purified PtNPs solutions after exchange, see Figure 5.9 (c). The c-PtNPs and dH_2O controls had pH's of 6.9 and 6.6 respectively, by contrast the pH of PtNP-TA decreased with increasing concentrations of TA from pH 6.9 to 3.8. Presumably, TA has a lower pH than sodium citrate, thus, the pH of PtNP-TA decreased. Additionally, the decrease in pH indicates a change in the protonation equilibrium of TA. At low acidic conditions (low TA concentration), the COOH group of TA would remain protonated and positively charged. By contrast, at high acidic conditions the COOH group would be protonated and negatively charged.

Gel electrophoresis of PtNP-TA is shown in Figure 5.9 (d). 2 µM and 70 µM of TA were selected for gel electrophoresis to assess if there was a difference in surface coverage. The c-PtNPs control sample aggregated as the electrostatic stabilisation of PtNP by citrate ions did not withstand the TAE buffer environment. Both 2 µM and 70 µM PtNP-TA migrated through the agarose gel, the 2 µM PtNP-TA had a fainter band in comparison to 70 µM PtNP-TA which had a denser band. At 2 µM of TA fewer molecules were available to bind to the c-PtNPs surface, therefore fewer PtNP were sterically stabilised by TA, in turn fewer PtNP-TA were able to migrate through the agarose gel. By contrast, at 70 µM more TA molecules were bound to the c-PtNPs surface, hence more PtNP had become sterically stabilised and able were to migrate through the agarose gel. This data further implies that a ligand exchange has occurred. Collectively, the zeta potential, pH and gel electrophoresis data suggest TA has chemisorbed onto the PtNP surface, however further investigation by XPS is required to confirm the platinum-thiol bond.

5.2.7 XPS of 20 nm PtNP-TA

XPS was used to investigate the elemental composition of TA and PtNP-TA. TA was used as a control sample and was prepared by directly drop casting onto the copper substrate and air dried. Following the method described in 5.2.2, PtNP-TA was prepared by surface modifying c-PtNPs with 70 µM of TA for 3 hours at room temperature; the excess TA and citrate ions were removed by centrifuging the sample at 10000 x g for 10 minutes. The supernatant was discarded, and the concentrated PtNP-TA were drop cast onto copper substrate, air dried and submitted for XPS analysis.

The survey scans of TA and PtNP-TA detected the Pt, Cu, C, O and S elements. Examination of the high-resolution scans of Pt 4f for TA did not detect Pt 4f peaks, as no c-PtNPs were present on the samples. As expected, three Cu 3p species were found, Cu 3p $_{3/2}$ at 75 eV, CuO at 75.5 eV and Cu 3p $_{1/2}$ at 77.4 eV , see Figure 5.10 (a) & (b); as mentioned before the Cu 3p species were due to the binding energies of Pt 4f and Cu 3p overlapping.[144] The high resolution scans of PtNP-TA detected two Pt 4f species, Pt 4f at 70.9 eV and Pt 4f at 74.2 eV, with a separation of 3.33 eV. These Pt 4f peaks are attributed to the PtNPs. Additionally, three Cu 3p species were detected, Cu 3p $_{3/2}$ at 74.9 eV, CuO 75.4 at eV and Cu 3p $_{1/2}$ 77.3 at eV. For both TA and PtNP-TA, Cu 3p is attributed to the copper substrate.

The high-resolution scans Cu 2p for TA and PtNP-TA are displayed in Figure 5.10 (c) & (d). Both samples revealed a Cu 2p doublet peak, TA exhibited Cu 2p $_{3/2}$ at 932.7 eV followed by Cu 2p $_{1/2}$ at 952.6 eV with a separation of 19.9 eV. PtNP-TA exhibited identical binding energies to TA alone, Cu 2p $_{3/2}$ at 932.7 eV and Cu 2p $_{1/2}$ at 952.6 eV with a separation of 19.9 eV; these peaks are in accordance with those found in accordance with literature.[146] Like Cu 3p, Cu 2p is also attributed to the copper substrate use in XPS analysis.

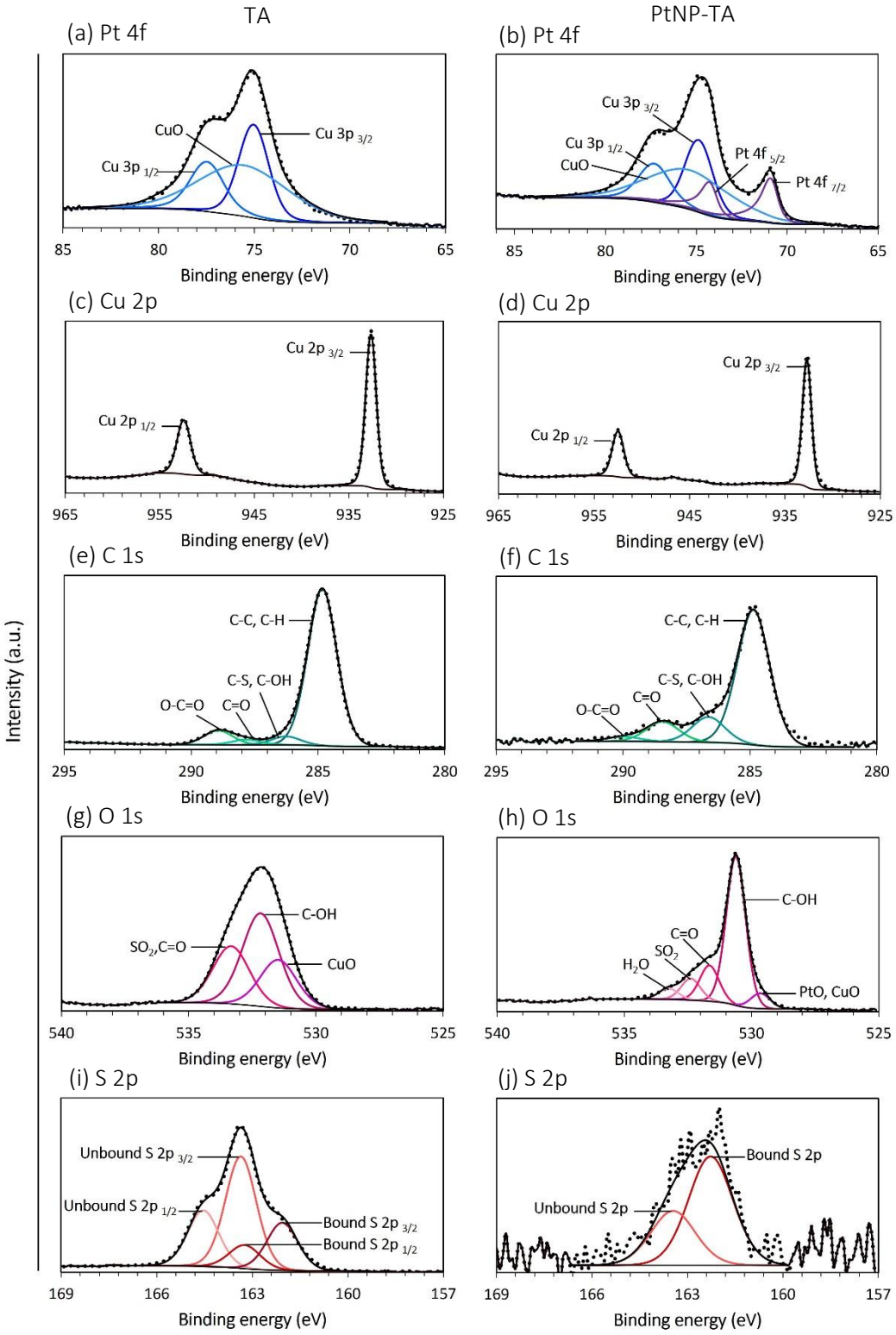

Figure 5.10 High resolution XPS spectra of TA and PtNP-TA on a copper substrate. (a) Pt 4f - TA, (b) Pt 4f - PtNP-TA, (c) Cu 2p - TA, (d) Cu 2p – PtNP-TA, (e) C 1s – TA, (f) C 1s – PtNP-TA, (g) O 1s – TA, (h) O 1s – PtNP-TA (i) S 2p – TA and (j) S 2p – PtNP-TA, (n=1).

Next, the high-resolution scans of C 1s for TA were examined. Five carbon species, C-C, C-H at 284.8 eV followed by C-S, C-OH at 286.3 eV, C=O at 287.8 eV and O-C=O at 288.9 eV as shown in Figure 5.10 (e). C-C, C-H is attributed to the alkane-disulphide and adventitious carbon. C-S correspond to the presence of carbon-thiol bond on the alkane-disulphide chain. The remaining species C-OH, C=O and O-C=O are ascribed to the COOH group of TA and adventitious carbon. Adventitious carbon peaks were found on the blank copper substrate in section 4.2.5. The high-resolution C 1s scans of PtNP-TA also displayed the same five carbon species with similar binding energies, Figure 5.10 (f). C-C, C-H was found 284.9 eV, C-S at 286.3 eV, C=O at 288.4 eV and O-C=O 290 eV. C-C, C-H relates to the alkane-disulphide chain and adventitious carbon, while C-S is due to the carbon-thiol bond on the alkane-disulphide chain. C-OH, C=O and O-C=O are attributed to the carboxylic acid group of TA and adventitious carbon. The carbon species observed in TA and PtNP-TA are in accordance with those in literature.[146, 159]

Figure 5.10 (g) & (h) illustrates the high-resolution spectra of O 1s for TA and PtNP-TA. Deconvolution of the high-resolution peaks of O 1s for TA revealed three oxygen species, CuO at 531.5 eV, SO_2, C-OH at 532.2 eV and C=O at 533.3 eV. CuO is attributed to the copper substrate, C-OH and C=O are attributed with the COOH group of TA and adventitious oxygen contamination. By contrast, five oxygen species were detected from the high-resolution O 1s scans of PtNP-TA. The metal oxide PtO, CuO were found at 529.3 eV, preceded by C-OH at 530.5 eV, C=O at 531.6 eV, SO_2 at 532.4 eV and H_2O at 533.5 eV. Again, C-OH and C=O are attributed to both COOH and adventitious oxygen and the carboxylic acid group of TA. Interestingly there was no Na Auger peak detected indicating the citrate ions had been exchanged for TA

molecules. This was further support by the increase of the bound S 2 p peak shown in Figure 5.10 (j).

Investigation of the high-resolution scans of S 2p for TA revealed two intercalated doublet peaks with a 2:1 area ratio, with a separation of 1.18 eV as shown in Figure 4.10 (i). The bound S 2p peaks were detected at 162.1 eV and 163.3 eV and the unbound S 2p peaks were detected at 163.4 eV and 164.5 eV, this result was comparable to those observed on gold surfaces.[160] Thiol binding to the copper substrate was anticipated with TA as both 6-MHA and 8-MOA demonstrated a copper-thiol bond. Previous studies investigating SAM formation by alkanethiols on copper substrates for wettability properties and inhibition of corrosion also observed thiols binding to copper.[34, 161, 162] The unbound S 2p is likely due to physisorbed TA on the copper substrate. PtNP-TA revealed one doublet with a 2:1 area ratio, with a separation of 1.18 eV, bound at 162.2 eV and 163.4 eV as illustrated in Figure 5.10 (j). Comparing both high-resolution scans, it is clearly evident that more TA molecules were bound to the PtNPs. The % of bound and unbound S 2p was derived from the area of the peak fittings from CasaXPS from two scans, see Table 5.3.

Table 5.3 % of bound and unbound S 2 p in TA and PtNP-TA.

	TA	PtNP-TA
% of S 2p bound	23.6	66.7
% of S 2p unbound	76.4	33.3

XPS analysis of TA demonstrated 23.6% of bound S 2p on the copper substrate and 76.4% of unbound S 2p. In comparison to TA, the % of bound S 2p increased to 66.7 % in the PtNP-TA sample, this increase can be explained by sample preparation. TA was directly drop cast on the copper substrate and was air dried, while the PtNP-TA was prepared by incubating the PtNPs with TA for 3 hours, then removing the excess TA, followed by drop casting on the copper substrate. Furthermore, TA exhibits a disulphide bond, allowing two platinum-sulphur bonds to form, with an incubation period of 3 hours the PtNPs were able to form more platinum-sulphur bonds via covalent interactions and displaced the citrate ions. This was reflected by the absence of the Na Auger peak in the O 1s high resolution scan in Figure 5.10 (h). Contrarily, both PtNP-6-MHA and PtNP-8-MOA detected Na Auger peaks in their O 1s high resolution scans. Remarkably, PtNP-TA had a comparable % of bound S 2p to 8-MOA at 65.7%, this could be explained by 8-MOA exhibiting a longer alkanethiol chain than TA. 8-MOA would form more Van der Waals interactions between the alkanethiol chains allowing more dense packing of the SAM. TA can form two sulphide bonds with metallic surface,[51] therefore more TA molecules are able to bind to the PtNP surface. These XPS results found PtNPs were present on the copper substrate, carbon and oxygen species ascribe to the structure of TA in both TA and PtNP-TA samples, however they also correspond with adventitious carbon and oxygen. The sulphur XPS spectra of TA and PtNP-TA confirms TA has bound to the PtNP surface via chemisorption, thus a platinum-sulphur bond was formed. Lasty, this is the first report of PtNP functionalised by TA.

5.2.8 Functionalisation of PtNP with O-(2-carboxyethyl)-O'-(2-mercaptoethyl)heptaethylene glycol

Although three carboxyl-terminated alkanethiols with medium alkane chains have been used to functionalise c-PtNPs s to give sterically stable negatively charged PtNPs, it would be ideal to have a long chain alkanethiol to functionalise the c-PtNPs for comparison. Long chain alkanethiols provide more stability by forming well-ordered SAMs owing to Van der Waals forces.[163, 164] A limitation of using long chain alkanethiols is their non-polar tendencies,[156] to overcome this boundary PEG molecules can be utilised. As PEGylated molecules are hydrophilic, they enhance the water solubility of the overall nanoparticle.[165, 166] PEGylated thiols have previously been employed to stabilise and functionalise metallic nanoparticles.[167, 168] The PEG-thiol compound O-(2-carboxyethyl)-O'-(2-mercaptoethyl)heptaethylene glycol (2-MOHA) was selected for functionalising PtNPs as it exhibits a terminal COOH functional group as well as the -C-O-C PEG group, its structure is shown in Figure 5.11.

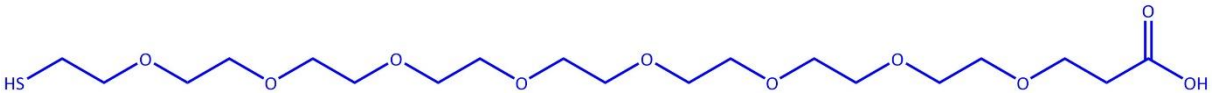

Figure 5.11 Structure of O-(2-carboxyethyl)-O'-(2-mercaptoethyl)heptaethylene glycol (2-MOHA).

Following the method described in section 5.2.2, c-PtNPs were surface modified by 2-MOHA, the overall ligand exchange is illustrated in Figure 5.12. The concentration of 2-MOHA required for surface coverage was determined using the PEGylated thiol footprint of 0.35 nm^2 from literature. [169] Using the PEGylated thiol footprint, the concentration of 2-MOHA for surface coverage was calculated to 3.9 µM, see Appendix 11.2 for calculations. 20 nm c-PtNPs were incubated with 2-MOHA from 2 – 70 µM for 3 hours at room temperature. Excess 2-MOHA and citrate ions were removed by centrifugation at 10000 x g for 10 minutes. The supernatant was

discarded, and the 2-MOHA were resuspended in dH_2O and then characterised by DLS, zeta potential and pH. The control samples included 20 nm c-PtNPs in 1.1 mM sodium citrate and dH_2O. Again, the c-PtNPs was selected to assess if there was a difference between the capping agents, while dH_2O was as a control as all PtNP-2-MOHA were resuspended in dH_2O. For gel electrophoresis characterisation, 20 nm c-PtNPs were surface modified with 3 µM and 70 µM of 2-MOHA only following the method above, until the discarding step. 1 µL of concentrated 3 µM and 70 µM PtNP-2-MOHA were then premixed with 15 µL glycerol and separated on a 1% agarose gel submerged in TAE buffer and concentrated PtNP were used as a control. DLS and zeta potential experiments were repeated across three batches of 20 nm c-PtNPs, five DLS and zeta potential measurements were performed to obtain the mean for each sample, data is presented as mean ± SD.

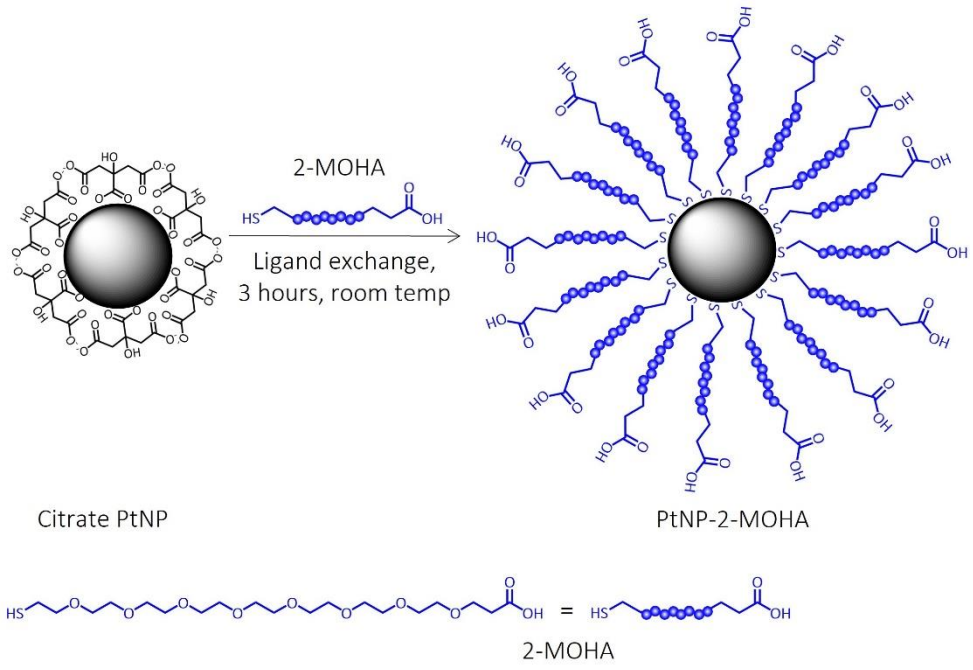

Figure 5.12 Ligand exchange of citrate ions on the 20 nm c-PtNP by 2-MOHA. Note figure not to scale.

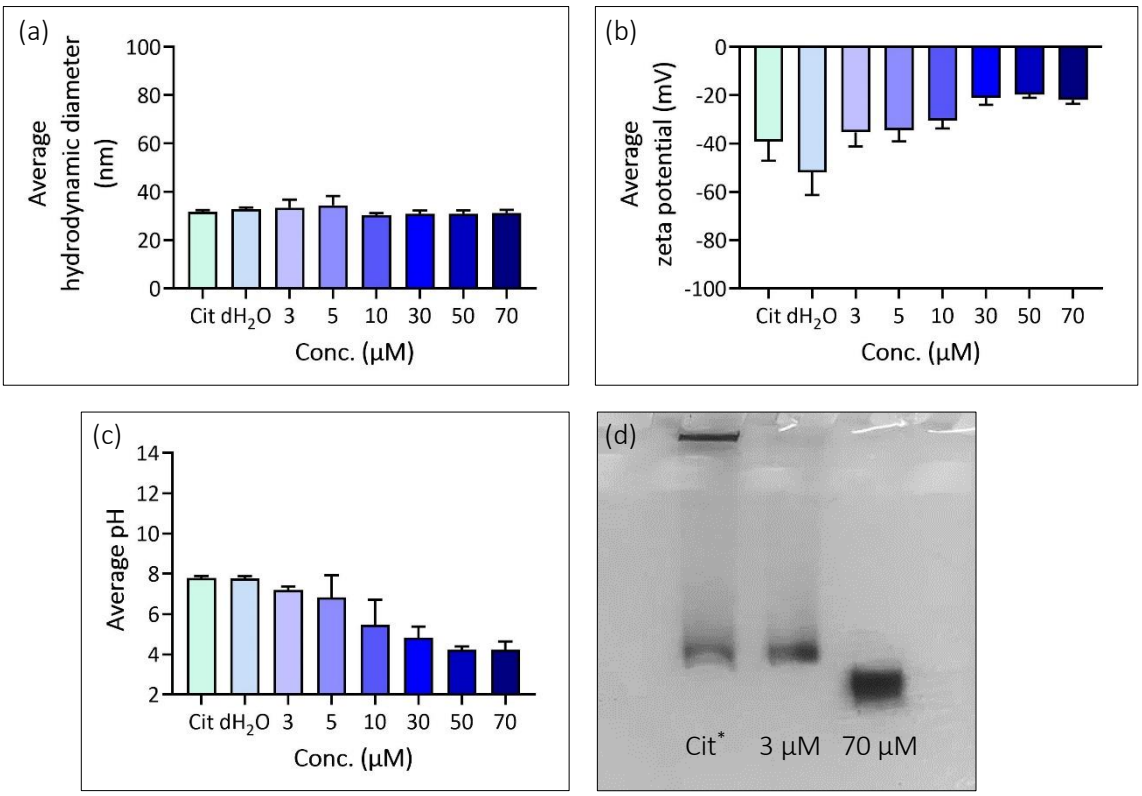

*Figure 5.13 Characterisation of PtNP-2-MOHA. (a) hydrodynamic diameters, (b) zeta potentials (c) pH and (d) gel electrophoresis. Results (except electrophoresis) are representative of 3 experiments (n=3) and presented as mean ± SD. Note *: overspill*

Figure 5.13 (a) demonstrates the hydrodynamic diameters of PtNP-2-MOHA, the c-PtNPs and dH_2O controls had similar hydrodynamic diameters of 31.1 ± 1.3 nm and 32.5 ± 0.8 nm respectively. The hydrodynamic diameters of PtNP-2-MOHA ranged from 30.8 to 36.7 nm, which were comparable to the control samples. Following the DLS the measurements, the zeta potentials of PtNP-2-MOHA were examined. The c-PtNPs and dH_2O controls had zeta potentials of -44.3 ± 3.0 and -55.6 ± 9.4 mV, the zeta potentials of PtNP-2-MOHA increased with increasing concentrations of 2-MOHA from -19.8 to -36.6 mV as shown in Figure 5.13 (b) indicating a ligand exchange has occurred. This trend was also observed with PtNP-6-MHA and PtNP-8-MOA. As

2-MOHA is PEGylated molecule, the zeta potential was expected to be close to 0 mV in the range of -2.7 to -4.6 mV.[170] This difference could be due to citrate ions still present on the PtNP surface, thus the zeta potential of PtNP-2-MOHA appear in the same range. XPS analysis would confirm if there were still citrate ions and 2-MOHA were both present on the PtNP surface.

Ligand exchange was further supported by pH measurements of purified surface modified PtNPs solutions after reaction, see Figure 5.13 (c), the pH of PtNP-2-MOHA decreased with increasing concentrations of 2-MOHA. As more 2-MOHA molecules bind to the surface of the c-PtNPs, the environment becomes more acid, thus a decrease in pH is observed. Furthermore, the decrease in pH indicates the COOH group has a different protonation behaviour; the decrease in pH was observed with PtNP-6-MHA, PtNP-8-MOA and PtNP-TA. The gel electrophoresis of PtNP-2-MOHA in Figure 5.13 (c) further confirmed the ligand exchange. PtNPs exchanged with 3 µM and 70 µM of MOHA were selected for gel electrophoresis to assess if there was a difference in surface coverage. The c-PtNPs aggregated in the well due to their electrostatic stabilisation by the citrate ions, however, a small amount of control PtNPs migrated through the gel as demonstrated by the faint band, this is a result of an overspill from 3 µM PtNP-2-MOHA sample into the control well. Both 3 µM and 70 µM PtNP-2-MOHA migrated through the agarose gel, the 3 µM PtNP-2-MOHA had a faint band, indicating fewer 2-MOHA molecules had bound to the PtNP surface, therefore fewer molecules had migrated through the agarose gel. In comparison, the 70 µM PtNP-2-MOHA had a denser band as more 2-MOHA molecules had bound to the PtNP surface, hence more c-PtNPs had become sterically stabilised and able were to migrate through the agarose gel. Collectively, the DLS, zeta

potential, pH and gel electrophoresis data indicate a ligand exchange has occur. Next, to confirm 2-MOHA has bound to the PtNP, the platinum-sulphur bond was investigated by XPS.

5.2.9 XPS of 20 nm PtNP-2-MOHA

XPS was employed to investigate the elemental composition of 2-MOHA and PtNP-2-MOHA. 2-MOHA was used a control sample and was prepared by directly drop casting onto the copper substrate and air dried. Following the method described in 5.2.2, PtNP-2-MOHA was prepared by surface modifying c-PtNPs with 70 µM of 2-MOHA for 3 hours at room temperature; the excess 2-MOHA and citrate ions were removed by centrifuging the sample at 10000 x g for 10 minutes. The supernatant was discarded, and the concentrated PtNP-2-MOHA were drop cast onto copper substrate, air dried and submitted for XPS analysis. 2-MOHA and PtNP-2-MOHA were charged corrected to 285 eV rather than 284.8 eV as polymers generally have their aliphatic component at 285 eV. Additionally, this allows comparison with polymer handbook.[171]

Survey scans of both 2-MOHA and PtNP-2-MOHA revealed the presence of Pt, Cu, C, O and S elements. The high-resolution scan of 2-MOHA detected no signal for Pt 4f as presented in Figure 5.14 (a), however as result of overlaying binding energies with Pt 4f, three Cu 3p peaks were detected, Cu $3p_{3/2}$ at 73.8 eV, CuO at 74.2 eV and Cu $3p_{1/2}$ at 76.2 eV. By contrast, the high-resolution scan of PtNP-2-MOHA detected both Pt 4f and Cu 3p, Figure 5.14 (b). The asymmetric peaks of Pt 4f were observed, Pt $4f_{7/2}$ at 71 eV and Pt $4f_{5/2}$ at 74.3 eV with a separation of 3.33 eV. Three Cu 3p peaks were observed, Cu $3p_{3/2}$ at 74.7 eV, CuO at 75.2 eV

and Cu 3p $_{1/2}$ at 77.1 eV. Cu 3p is attributed to copper substrate in both samples. The Pt 4f and Cu 3p were similar to those found in literature.[144]

The high resolutions scans of Cu 2p for 2-MOHA detected two Cu 2p peaks, Cu 2p $_{3/2}$ at 932.7 eV and Cu 2p $_{1/2}$ at 952.6 eV as shown in Figure 5.14 (c). These Cu 2p peaks were comparable to those detected in the high-resolution scans for PtNP-2-MOHA see Figure 5.14 (d). Cu 2p $_{3/2}$ was detected at 932.7 eV and Cu 2p $_{1/2}$ at 952.6 eV. Both samples had separations of 19.9 eV, these binding energies are in accordance with literature.[146] Additionally, PtNP-2-MOHA exhibited two CuO peaks at 934.5 eV and 954.8 eV. Cu 2p peaks from 2-MOHA and PtNP-2-MOHA are attributed to the copper substrate.

The examination of the high-resolution of C 1s for 2-MOHA detected six carbon species, as shown in Figure 5.14 (e); C-C, C-H at 285 eV preceded by C-S, C-OH, C-O-C at 286.3 eV, C=O at 287.8 eV and O-C=O at 289.1 eV, these binding energies, correspond with those in literature[146, 172] All species correspond with the structure of 2-MOHA, C-C, C-H and C-S ascribes to the PEGylated thiol chain and the carbon-thiol bond respectively. C-O-C is attributed to polar regions of the PEG thiol, while C-OH, C=O and O-C=O correspond with carboxyl functional head group. However, C-C, C-H, C-OH, C=O and O-C=O are also attributed to adventitious carbon contamination. The same six carbon species were detected in the high-resolution scan of PtNP-2-MOHA. C-C, C-H was detected at 285 eV, C-S, C-OH, C-O-C at 286.5 eV, C=O at 288.3 eV and O-C=O at 289.4 eV. All species correlate with structure of 2-MOHA, nonetheless, C-C, C-H, C-OH, C=O and O-C=O are attributed to adventitious carbon contamination as all four species

were detected on the blank copper substrate in section 4.2.5, thus, carbon species of 2-MOHA are masked by adventitious carbon.

Examination of the high-resolution scans of O 1s for 2-MOHA revealed three oxygen species, CuO at 530.5 eV, C-O-C at 532.2 eV and SO_2, C=O at 533.4 eV, see Figure 5.14 (g). CuO corresponds to the copper substrate and C-O-C is attributed to the PEGylated thiol. SO_2 corresponds to sulphur atom from the thiol, while C=O is attributed to COOH and adventitious oxygen. These peaks correspond to those in literature.[146] The high-resolution scans of O 1s for PtNP-2-MOHA detected five oxygen species, Figure 5.14 (h), PtO, CuO at 530.7 eV preceded by C-O-C at 531.6 eV, SO_2, C=O at 533.6 eV and a Na Auger peak at 535.8 eV. PtO and CuO are attributed to the PtNPs and copper substrate; C-O-C is attributed to the PEGylated thiol. SO_2 ascribes to sulphur atom of the thiol, C=O is again attributed to COOH and adventitious oxygen. The Na Auger peaks indicates the presence of citrate ions on the PtNP surface which was previously observed with PtNP-6-MHA and PtNP-8-MOA.

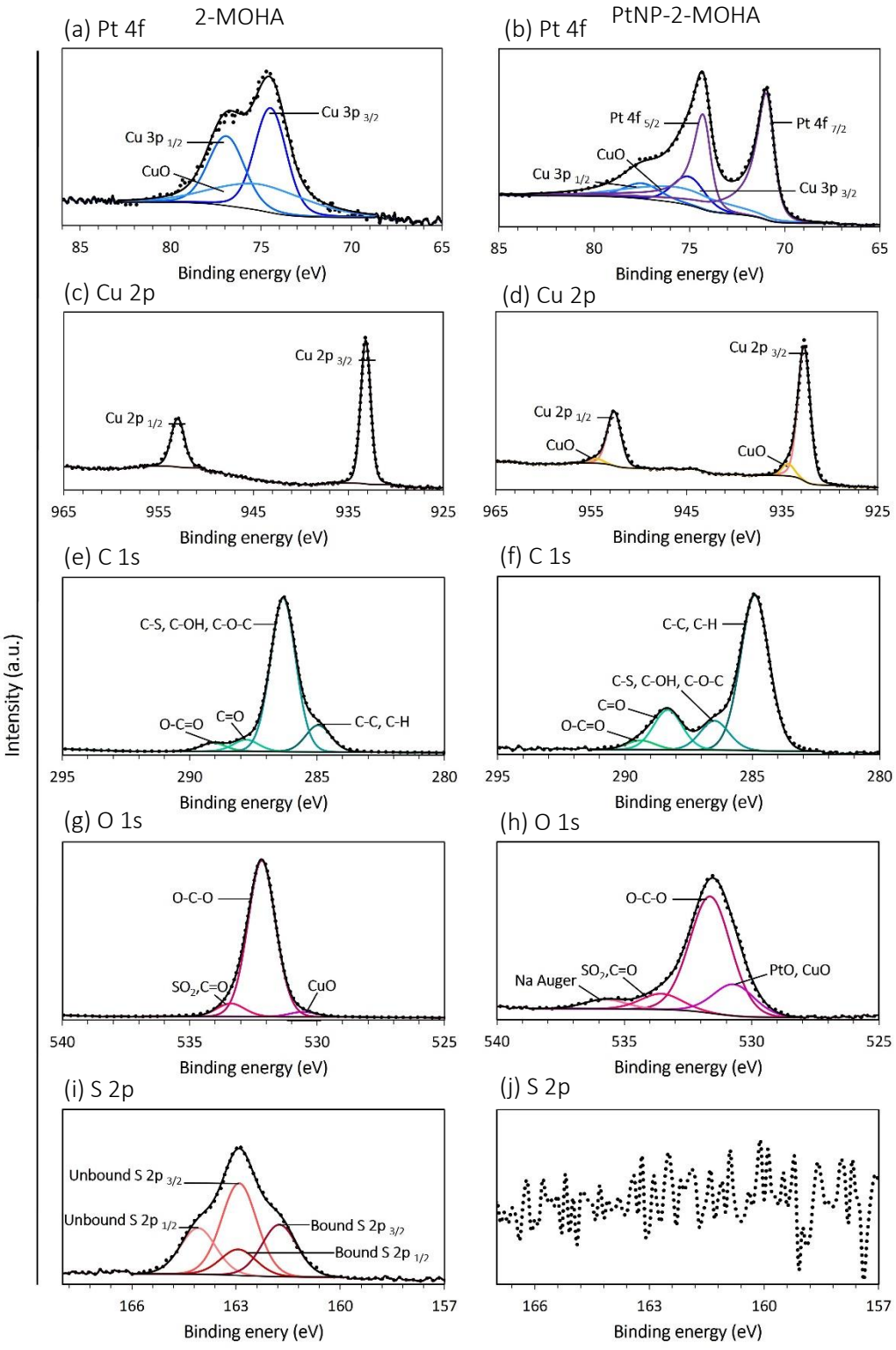

Figure 5.14 High resolution XPS spectra of 2-MOHA and PtNP-2-MOHA on a copper substrate. (a) Pt 4f – 2-MOHA, (b) Pt 4f - PtNP-2-MOHA, (c) Cu 2p - 2-MOHA, (d) Cu 2p – PtNP-2-MOHA, (e) C 1s – 2-MOHA, (f) C 1s – PtNP-2-MOHA, (g) O 1s – 2-MOHA, (h) O 1s – PtNP-2-MOHA, (i) S 2p – 2-MOHA and (j) S 2p – PtNP-2-MOHA, (n=1).

Interpretation of the high-resolution scans of S 2p for 2-MOHA demonstrated two intercalated doublets with 2:1 area ratio with a separation of 1.18 eV as illustrated in Figure 5.14 (i). Bound S 2p was observed at 160.9 eV and 162.1 eV and the unbound S 2p were observed at 162.1 eV and 163.3 eV, these binding energies are similar to those in literature.[160] The bound S 2p is ascribed to the copper-thiol bound, thus, 2-MOHA had chemisorbed onto the copper substrate, while the unbound S 2p suggests 2-MOHA physisorbed onto the copper substrate. The copper-thiol bond was previously observed in early investigations of SAM formations of copper substrates in wettability and corrosion studies.[34, 161, 162] Bound and unbound S 2p species were not detected in high-resolution scan of S 2p for PtNP-2-MOHA, see Figure 5.14 (j), it is unlikely 2-MOHA has not bound to the PtNP surface, a possible explanation for this occurrence amount of S 2p was too low to be detected. If there was not sufficient ligand exchange between the citrate ions and 2-MOHA on the PtNP surface the XPS may not be to detect the S 2p signal, this was reflected by the zeta potential which indicated citrate ions were still present on the PtNP surface. Moreover, as each 2-MOHA molecule only has one sulphur atom, it can be difficult to detect S 2p; this was evident by the low signal to noise ratios found in all the XPS high-resolution scans for PtNP-6-MHA, PtNP-8-MOA, PtNP-TA.

These XPS data confirms the PtNPs were present on the copper substrate, carbon and oxygen species attributed to 2-MOHA, however they could all be attributed to adventitious carbon and oxygen. High-resolutions scans of 2-MOHA revealed that 2-MOHA had chemisorbed onto the copper substrate forming a thiolate, conversely, S 2p signal on the PtNP was too low to be detected by XPS, indicating ligand exchange was not sufficient.

5.3 Conclusion

In the current study, 20 nm c-PtNPs were partially functionalised by the carboxyl-terminated alkanethiols 6-MHA, 8-MOA, TA via a chemisorption approach. For PtNP-6-MHA, PtNP-TA and PtNP-2-MOHA, characterisation by DLS did not show changes in hydrodynamic diameters for each of these functionalised PtNPs. Interestingly, at low thiol concentrations both PtNP-8-MOA and PtNP-2-MOHA exhibited increased hydrodynamic diameters indicating nanoparticle aggregation during ligand exchange. The zeta potential and pH demonstrated the citrate ions capping the PtNPs were ligand exchanged for PtNP-6-MHA, PtNP-TA, PtNP-8-MOA, thus creating sterically stable negatively charged PtNPs. By contrast the zeta potential of PtNP-2-MOHA did reflect the zeta potential expected from PEGylated nanoparticles. XPS analysis confirmed the platinum-thiol bond in PtNP-6-MHA, PtNP-8-MOA, PtNP-TA but PtNP-2-MOHA. Gel electrophoresis demonstrated the largest physical differences between citrate capped PtNPs and functionalised PtNPs, further confirming ligand exchange between the citrate ion capping on the PtNP surface and the thiol molecules. Importantly, this is the first study to report the partial functionalisation of PtNPs by 6-MHA, 8-MOA and TA by ligand exchange.

5.4 Further work

Though ligand exchange was performed at 3 hours, extending the incubation time with alkane and PEGylated thiols at the maximum concentration of 100 µM and 70 µM respectively would potentially characterising the ligand exchange at different incubations time would provide insight on how the surface charge changes along with the % of bound thiol on the PtNP surface. allow more chemisorption on to the PtNP surface. Characterising ligand exchange at different

incubations time would ascertain how the surface charge changes the % of bound thiol on the PtNP surface. Additionally, the functionalised PtNP in this chapter could also be examined for stability by assessing the hydrodynamic diameter and zeta potential over several weeks and months.

Chapter 6 Synthesis and Functionalisation of Positively Charged Platinum Nanoparticles

Abstract: *This chapter describes the functionalisation and synthesis approaches used to create sterically stable positively charged PtNPs. Preliminary experiments of 20 nm c-PtNPs in the presence of amino-terminated alkanethiols resulted in aggregation of PtNPs. Two alternative methods were assessed for creating positively charged PtNPs. First, the cationic surfactant cetrimethylammonium bromide (CTAB) was employed as a capping agent to synthesise positively charged PtNP; to make PtNP-CTAB sterically stable, the CTAB capping was ligand exchanged for the quaternary ammonium compound (6-aminohexyl)trimethylammonium bromide hydrobromide (6-ATA). In the second approach, positively charged PtNPs were synthesised using the amino-terminated alkanethiol 2-diethylaminoethanethiol hydrochloride (DEA). Both methods resulted in positively charged PtNPs, albeit the stability of these nanoparticles were short-lived and hence excluded from platelet functional studies.*

6.1 Introduction

Positively charged nanoparticles many been used in a variety of applications in biomedicine. Previous work by Cao et al.[173] synthesised positively charged AuNPs with the alkanethiol cysteamine hydrochloride (CSH) for the colorimetric detection of heparin based on the optical properties of AuNPs. The positive charge exhibited by these AuNPs electrostatically interacted with the negatively-charge heparin molecule causing their the AuNPs to aggregate; in turn this led to the colour change of the AuNP solution from red to blue, where blue indicated the AuNPs in an aggregated state. Experiments by Stewart et al. [174] demonstrated the synthesis of positively charged AgNPs by the reduction hydroxylamine hydrochloride followed by functionalisation by thiocholine. These functionalised AgNPs served as a surface enhancer for Raman spectroscopy (SERS) substrates, thus, allowing for the recognition of anionics targets. While most studies have focused on AuNPs and AgNPs. However, a limitation of using thiols to functional metallic nanoparticles is the results in small sized nanoparticles. Cationic surfactants such as CTAB have frequently been utilised for synthesising AuNPs, AgNPs and PtNPs. [29, 175-178] The use of cationic surfactants enables the growth of larger nanoparticles in comparison to thiols. Furthermore, they protect the nanoparticle core by adsorbing onto the surface, the positive charge from cationic surfactant creates electrostatic repulsion between neighbouring nanoparticles and prevents their aggregation. Similar to citrate ions, cationic surfactants only provide electrostatic stabilisation, therefore, nanoparticles need to undergo ligand exchange with alkanethiols to create sterically stable nanoparticles. However, few studies have focused on creating sterically stable positively charged PtNPs via ligand exchange with thiols, thus this warrants further investigation.

6.1.1 Objectives

1. Assess the solubility of positively charged amino-terminated alkanethiols with PtNPs.

2. Synthesise monodispersed positively charged PtNPs with a cationic surfactant and characterise by TEM, DLS and zeta potential.

3. Assess if the positively charged PtNPs capped with a cationic surfactant can be surface modified with a quaternary ammonia compound to produce sterically stable positively charged PtNPs and characterise by DLS and zeta potential.

4. Synthesise sterically stable positively charged PtNPs with an alkanethiol as a capping agent, characterise these PtNPs by TEM, DLS and zeta potential.

6.2 Results and Discussion

6.2.1 Solubility of positively charged alkanethiols

In Chapter 4, 20 nm c-PtNPs were synthesised with good stability and narrow particle distribution, these were used to functionalise the PtNPs to exhibit a positive charge. Three positively charged alkanethiols compounds were selected for functionalising the c-PtNPs, CSH, 6-amino-1-hexanethiol (6-AHT) and 11-amino-1-undecanethiol hydrochloride (11-AUT), see Figure 6.1. All three alkanethiols possess an amino (NH_2) terminated functional group and a mercapto group (SH) head group. They differ by their alkane chain length, CSH has a 2-carbon alkane chain, while 6-AHT and 11-AUT have a 6-carbon and 11-carbon alkane chain, respectively.

(a) Cysteamine hydrochloride

(b) 6-amino-1-hexanethiol

(c) 11-amino-1-undecanethiol hydrochloride

Figure 6.1 Amino terminated alkanethiols. (a) cysteamine hydrochloride, (b) 6-amino-1-hexamethiol and (c) 11-amino-1-undecanethiol hydrochloride

Before thiol exchange, the solubility of all 3 alkanethiols was tested by preparing each thiol in dH_2O or ethanol, followed by directly adding directly to 20 nm c-PtNPs aliquots at a final concentration of 100 µM and observation at 3 and 24 hours. All 3 alkanethiols were soluble in

dH_2O and ethanol, however, the addition of these thiols caused the c-PtNPs to immediately aggregate. One possible explanation for aggregation could be due to both SH and NH_2 groups simultaneously binding to the c-PtNPs surface as illustrated in Figure 6.2. The NH_2 group is positively charged and is known to have a high binding affinity to platinum group complexes; a common example of the platinum-amino complex is the chemotherapy drug Cisplatin. [179, 180] Together with the SH group also binding to the PtNP this could explain why aggregation occurred.

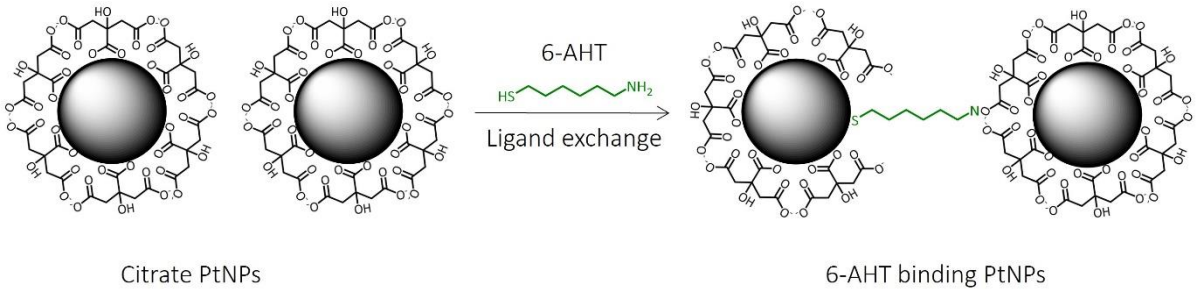

Figure 6.2 Simultaneous binding of 6-AHT to 20 nm c-PtNPs.

Additionally, these c-PtNPs were surrounded with a cloud of citrate ions for electrostatic stabilisation; the negative charge from the citrate ions are able to electrostatically interact with the positively charged NH_2 groups of the alkanethiols, providing a second mechanism of aggregation. However, as this solubility experiment was purely qualitative, to confirm the PtNPs had aggregated, the DLS of the 20 nm c-PtNPs was measured before and after a 3-hour incubation with one of the alkanethiols. 100 µM 6-AHT was selected for this experiment as it has a medium alkane chain length and 100 µM would be the maximum concentration used for ligand exchange experiments, these results are illustrated in Figure 6.3.

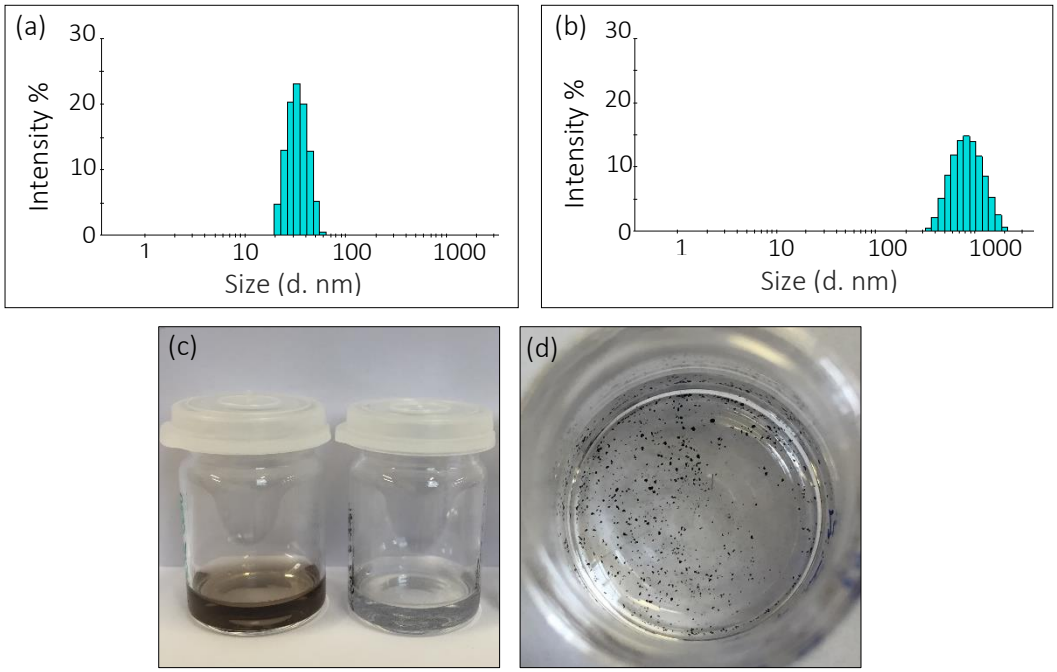

Figure 6.3 c-PtNP with 6-AHT. (a) c-PtNP particle size distribution, (b) c-PtNP with 6-AHT particle size distribution, (c) c-PtNPs (left vial), c-PtNPs with 6-AHT (right vial), (d) c-PtNP aggregation by 6-AHT. Results are from 1 experiment (n=1).

In the literature, 6-AHT has been reported to form self-assembled monolayers (SAMs) on gold electrode surfaces,[181] but not on metallic nanoparticles. In our case, the addition of 6-AHT caused the c-PtNPs to aggregate. The hydrodynamic diameter of 20 nm c-PtNPs was 31.9 nm, and upon the addition of 6-AHT this significantly increased to 625.4 nm, see Figure 6.3 (a) & (b). This is supported by the images in Figure 6.3 (c) & (d). c-PtNPs alone are a brown solution with which became clear on addition of 6-AHT with visible aggregates. These results show that addition of amino terminated alkanethiols cause the c-PtNPs to aggregate. As a similar result was seen with all three alkane thiols, alkanethiol chain length has no effect on causing this instability. Therefore, amino terminated alkanethiols were considered unsuitable compounds for functionalising c-PtNPs into positively charged sterically stable PtNPs.

To create sterically stable positively charged PtNPs two further approaches were assessed: (1) synthesis with a cationic surfactant, followed by a ligand exchange with a quaternary ammonium compound, (2) synthesis with a positively charged alkanethiol. In the next section, the synthesis of positively charged PtNPs with a cationic surfactant will be discussed.

6.2.2 Synthesis of positively charged platinum nanoparticles with a cationic surfactant

The cationic surfactant CTAB has been employed as a capping agent for gold, silver and platinum nanoparticles.[29, 175-178] CTAB is an amphiphilic quaternary ammonium compound consisting of a positively charged hydrophilic functional group from the ammonium and neutral hydrophobic tail made of a 16-carbon alkane chain, see Figure 6.4. The high toxicity of CTAB prevents nanoparticles capped with CTAB to be directly tested in biological applications, as it well established that CTAB dissolves cell membranes (hence it is used in DNA isolation protocols).[182-184] Thus, nanoparticles capped with CTAB would require a surface modification with an alternative compound to reduce toxicity and stabilise the nanoparticle. A benefit of CTAB is that it is non covalently bound to nanoparticle surface during synthesis and can subsequently be ligand exchanged for another compound that can covalently bond to the nanoparticle surface.[185]

Figure 6.4 Structure of cetrimethylammonium bromide (CTAB).

In a pilot experiment, CTAB capped PtNPs (PtNP-CTAB) were synthesised using same the seed mediated synthesis method described in section 4.2.4, with a modification of 34 mM sodium citrate replaced by 34 mM CTAB. Pt seeds remained as the template to grow the PtNPs, 0.2 M $H_2PtCl_6.6H_2O$ remained as the precursor with 71 mM L-ascorbic acid as the reducing agent. Growth was controlled by L-ascorbic acid and a temperature increment of 10°C/min to 100°C. It has been proposed that CTAB adsorbs onto the nanoparticle surface forming a bilayer.[29-31] The positive charge carried by the quaternary ammonia group of CTAB creates stability by causing electrostatic repulsion amongst neighbouring nanoparticles; this repulsion therefore prevents the nanoparticles from aggregation.[29, 186] The addition of CTAB caused the reaction to go first go cloudy and then to black, with the black colour change indicating that $H_2PtCl_6.6H_2O$ had been reduced to Pt, see Figure 6.5 (a) & (b). The reaction was centrifuged at 10000 x g and resuspended in 1.1 mM CTAB to remove excess $H_2PtCl_6.6H_2O$ and L-ascorbic acid.

A control synthesis reaction also was performed directly after the PtNP-CTAB synthesis using 34 mM sodium citrate as a capping agent and the same working solutions of 0.2 M $H_2PtCl_6.6H_2O$ and 71 mM L-ascorbic acid to confirm the $H_2PtCl_6.6H_2O$ and L-ascorbic acid were working as expected. These PtNPs, were also centrifuged 10000 x g and resuspended in 1.1 mM sodium citrate to remove excess $H_2PtCl_6.6H_2O$ and L-ascorbic acid. PtNP-CTAB and c-PtNPs were characterised by TEM, DLS and zeta potential. The TEM size of both sets of PtNP was obtained by measuring 200 diameters. Five DLS and zeta potential measurements were 5 times performed to obtain the mean. Figure 6.5 (c) to (h) displays the TEM images and particle distribution. Figure 6.6 shows the DLS and zeta potential measurements, which were performed with 1.1 mM CTAB and dH_2O as these were the solvents used for resuspending the

PtNP-CTAB. Both PtNP synthesis reactions with CTAB and citrate were conducted once as the experiment was a pilot.

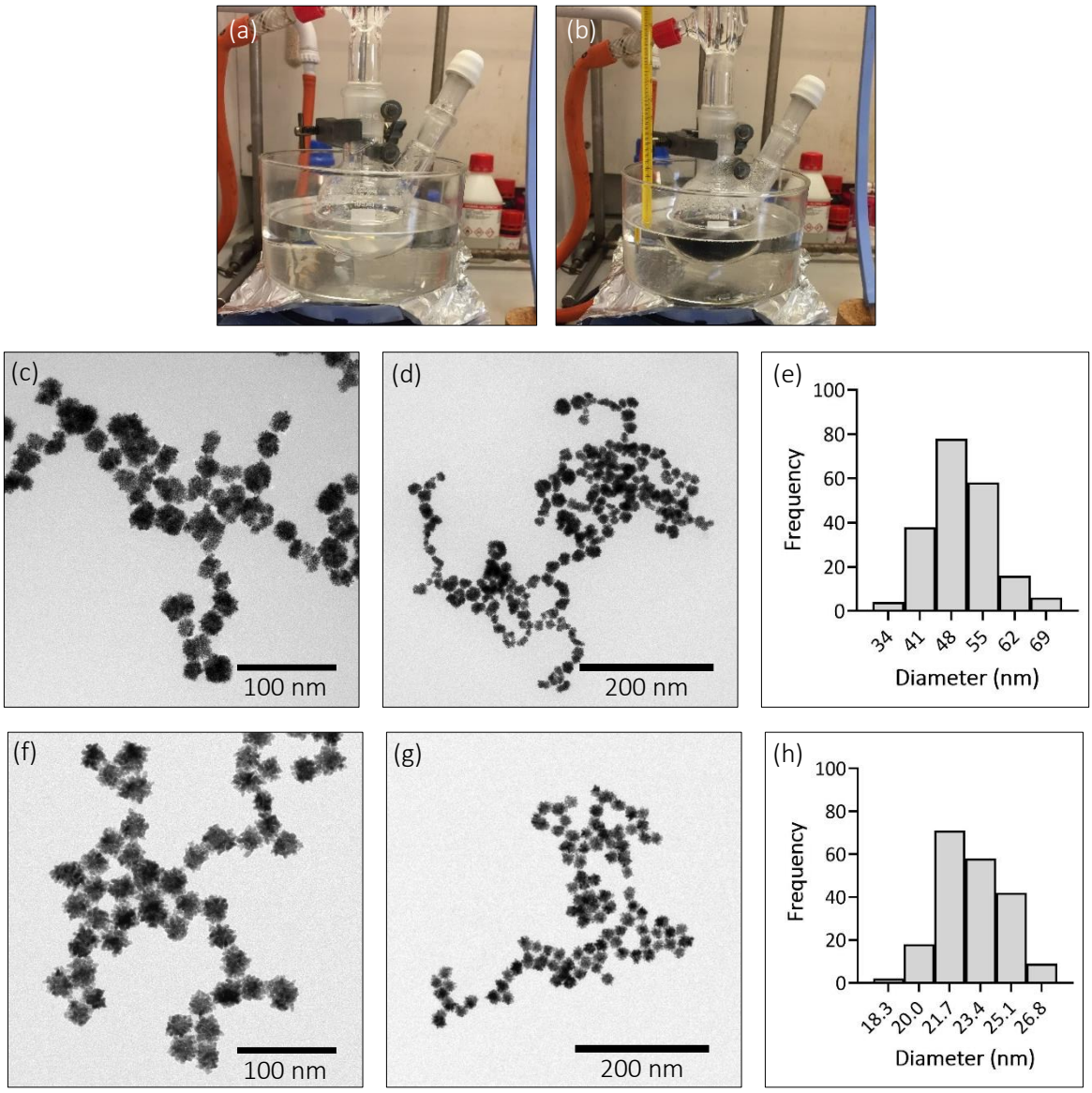

Figure 6.5 Synthesis and characterisation of PtNP-CTAB and c-PtNPs. (a) addition of CTAB, (b) reduction of $H_2PtCl_6.6H_2O$, (c & d) TEM images of PtNP-CTAB, (e) particle size distribution of PtNP-CTAB, (f & g) TEM images of citrate PtNPs, (h) particle size distribution of citrate PtNPs. Results are from 1 experiment (n=1).

The results in Figure 6.5 (c) & (d) demonstrated that PtNP-CTAB had a large particle distribution. This could be due to CTAB not having as good size control as citrate ions have for the negatively charged PtNPs which exhibit a uniform shape. Recent work by Wei et al.[187] demonstrated that gold nanorods (AuNRs) could be synthesised with a control shape using low concentrations of CTAB, therefore CTAB may be better suited for control size of nanorods than spherical nanoparticles.

Additionally, the negative charge carried by the Pt seed and L-ascorbic acid could be potentially binding to the positively charged functional group of CTAB during synthesis and affect the nanoparticle growth. The PtNP-CTAB had an average TEM diameter of 50.2 nm and the particle size distribution ranged from 34 to 69 nm, as shown in Figure 6.5 (e). The control experiment with 34 mM sodium citrate as a capping agent demonstrated PtNPs with a more uniform size (Figure 6.5 (f) & (g)), the average TEM diameter was 22.9 nm with a particle size distribution of 18.6 to 26.8 nm, as shown in Figure 6.5 (h). This size and particle distribution was similar to the sizes obtained in sections 4.2.2 and 4.2.4 using sodium citrate as a capping agent.

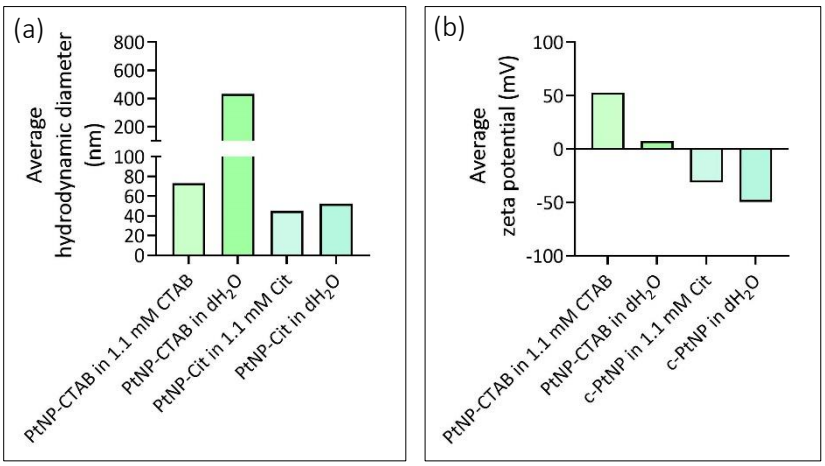

Figure 6.6 PtNP-CTAB and c-PtNP characterisation by DLS and zeta potential. (a) average hydrodynamic diameters & (b) average zeta potentials. Results are respresentitive of 1 experiment (n=1).

Looking at the hydrodynamic diameter in Figure 6.6 (a), PtNP-CTAB centrifuged and resuspended in 1.1 mM CTAB had an average hydrodynamic diameter of 73.2 nm, this significantly increased to 433.2 nm when the PtNP-CTAB was centrifuged and resuspend in dH_2O. These data suggest CTAB capping was lost during the centrifugation and resuspension step of PtNP-CTAB into dH_2O, hence they aggregated. As CTAB is non-covalently bound to the nanoparticle surface it can be easily displaced, He et al.[188] showed the removal of CTAB on AuNRs by centrifugation: without a capping agent the AuNRs aggregated and required a thiol or polymer for stabilisation. The loss of the CTAB capping was supported by the zeta potential data, PtNP-CTAB had a zeta potential of 52.7 mV at pH 7.9 when the resuspended in 1.1 mM CTAB (Figure 6.6 (b)), indicating good stability, but this was reduced to 7.7 mV at pH 6 by the centrifugation and resuspension step into dH_2O, further supporting the CTAB capping had come off the nanoparticle surface.

In the control experiment with sodium citrate, the hydrodynamic diameter of c-PtNP was 45.1 nm, this slightly increased when the c-PtNP were centrifuged and resuspended in dH_2O to 52.1 nm. This difference indicates the citrate ion capping was still present on the c-PtNP surface but that some of the PtNPs had aggregated, hence the hydrodynamic diameter increased. A limitation of the DLS technique is that it is unable to distinguish between monodispersed nanoparticles and aggregated nanoparticles. The zeta potential of these c-PtNPs were -31 mV at pH 7.1 in 1.1 mM sodium citrate, while in dH_2O the zeta potential decreased to -49.5 mV at pH 7.2; the pH's were similar in both cases. Although the zeta potential of the c-PtNPs resuspended in dH_2O indicates good stability they are likely to have aggregated. As with the DLS measurements, the zeta potential technique cannot distinguish between measuring the monodispersed particles and aggregates, hence some aggregates can exhibit good stability.

Interestingly, both PtNP-CTAB and c-PtNP were synthesised with the same concentration of $H_2PtCl_6.6H_2O$ and L-ascorbic acid from the same stock solutions, yet at the same concentration of 34 mM, CTAB gave PtNPs with varied sizing while the citrate allowed controlled uniform sizes as demonstrated by TEM and hydrodynamic diameters. This difference can be explained by the nature of different capping agents, CTAB is amphiphilic and carries a positive charge from the NR_4^+ functional group, and a has 16-carbon alkane chain, which forms an intercalated bilayer on the nanoparticle surface; [29,30,31] By contrast citrate ions are negatively charged arising from their three COOH groups, and much smaller in size compared to CTAB, they known to physisorb onto the nanoparticle surface, thus, the small size of citrate ions allows controlled sizes of PtNPs. [21,24,28] These data establish that positively charged PtNPs can be synthesised using the

cationic surfactant CTAB, however size control and stability are still challenging; citrate ions as a capping agent produces negatively charged c-PtNPs with good, controlled sizes, stability, and narrow particle distribution. Nonetheless, it's important to remember that these two capping agents, have different functional groups and structures.

6.2.3 Functionalisation of platinum nanoparticles with (6-aminohexyl)trimethylammonium bromide hydrobromide

Although the PtNP-CTAB did not exhibit a uniform shape, they were utilised to examine if they could be functionalised by ligand exchange to create sterically stable positively charged PtNPs. As previously found in section 6.2.1, amino-terminated alkanethiols were unsuitable for functionalising PtNPs. An ideal compound would be (6-mercaptohexyl)trimethylammonium bromide (6-MTAB) shown in Figure 6.7. 6-MTAB comprises of an SH group, a 6-carbon alkane chain, and an ammonium (NR_4^+) functional group that carries positive charge.

Figure 6.7 Structure of (6-mercaptohexyl)trimethylammonium bromide (6-MTAB).

Although the NR_4^+ carries a positive charge it is unable to form a bond, as the $-NR_4^+$ is protonated, the non-bonding electrons are unavailable to interact, unlike amino-terminated alkanethiols where the non-bonding electrons of NH_2 are available. Moreover, the methyl (CH_3) groups of the NR_4^+ would sterically prevent the N^+ from binding to the PtNP core, thus, only SH would bind the PtNP core. Unfortunately, the 6-MTAB compound was not commercially

available; an alternative compound was the quaternary ammonium 6-ATA, as illustrated in Figure 6.8. 6-ATA consists of an NH_2, 6 carbon hydrocarbon chain and an ammonium group NH_3^+. 6-ATA was selected for functionalising the PtNP as -NH_2 have shown to form complexes with platinum.[179, 180] In this instance NH_2 would be the head group binding to the PtNP core while the NH_3^+ would be the functional group.

Figure 6.8 Structure of (6-aminohexyl)trimethylammonium bromide hydrobromide (6-ATA).

Utilising the average TEM diameter of 50.2 nm, the surface area of the PtNP-CTAB was calculated to 3.28 X 10^{15} nm^2/mL; using the approximated footprint of 6-ATA 0.145 nm^2 (derived from Chem3D by measuring the area), the concentration of 6-ATA required for surface coverage was calculated to 4.5 µM. To ensure full surface coverage, PtNP-CTAB were surface modified with concentrations of 6-ATA ranging from 3 to 70 µM for 3 hours at room temperature; the overall ligand exchange is illustrated in Figure 6.9. Excess 6-ATA and CTAB were removed by centrifuging the samples at 10000 x g. The supernatant was discarded and resuspended and in dH_2O and then characterised by DLS, zeta potential and pH, as shown below Figure 6.10. Five DLS and zeta potential measurements were 5 times performed to obtain the mean. PtNP-CTAB were used as a control and referred to as CTAB in Figure 5.9 to demonstrate the surface coating of the PtNP.

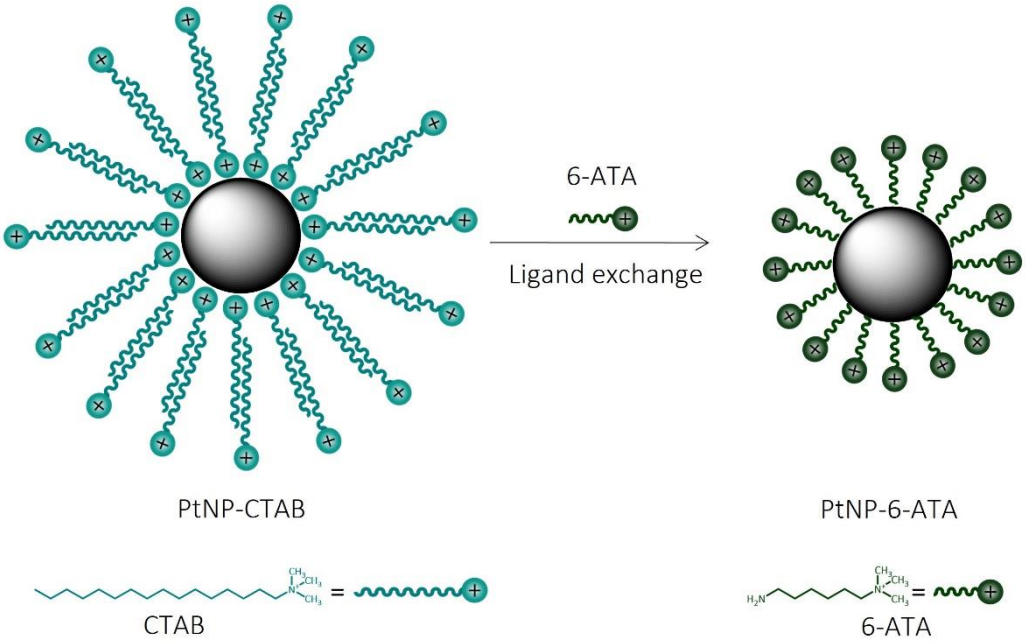

Figure 6.9 PtNP-CTAB ligand exchange with 6-ATA. Note figure not to scale.

The average hydrodynamic diameters did not change from the PtNP-CTAB of 75 nm to PtNP-6-ATA that ranged between 70.9 to 76.9 nm as shown in Figure 6.10 (a). Although CTAB and 6-ATA have two different alkane chain lengths, the DLS technique is not sensitive enough to detect these changes. Interestingly, the zeta potential decreased from 46.2 mV to between 14.9 and 23.9 mV with the 6-ATA surface coating (Figure 6.10 (b)); demonstrating low stability and suggesting less molecules were present on the PtNP surface, hence less charge. Interestingly, between 3 – 10 µM of 6-ATA a decreasing trend was observed in the zeta potential; however, at the higher concentrations of 30 – 70 µM the zeta potentials began to increase, indicating more 6-ATA molecules were present on the PtNP surface, thus an increased surface charge.

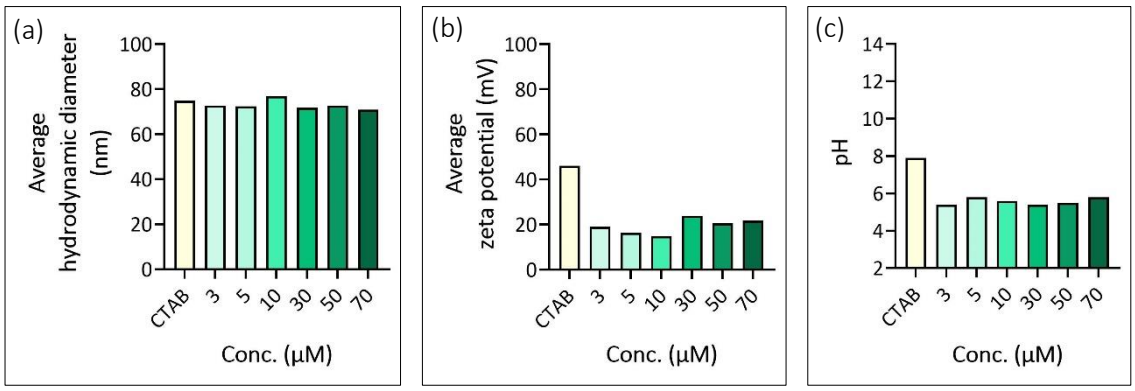

Figure 6.10 6-ATA characterisation by (a) DLS (b) zeta potential and (c) pH. Results are respresentitive of 1 experiment (n=1).

The pH measurements in Figure 6.10 (c) showed the pH of PtNP-CTAB decreased from pH 7.9 to a range of 5.4 to 5.8 between PtNP-6-ATA samples indicating that the CTAB capping had been ligand exchanged for 6-ATA. The zeta potential also indicated that CTAB had been exchanged for 6-ATA, however further investigation was required; specifically, XPS would be required to confirm if CTAB had been exchanged for 6-ATA on the PtNP surface by observing the platinum-nitrogen bond. Unfortunately, a day after the reaction, all PtNP-6-ATA had aggregated to the bottom of the glass vial, leaving a clear solution, see Figure 6.11.

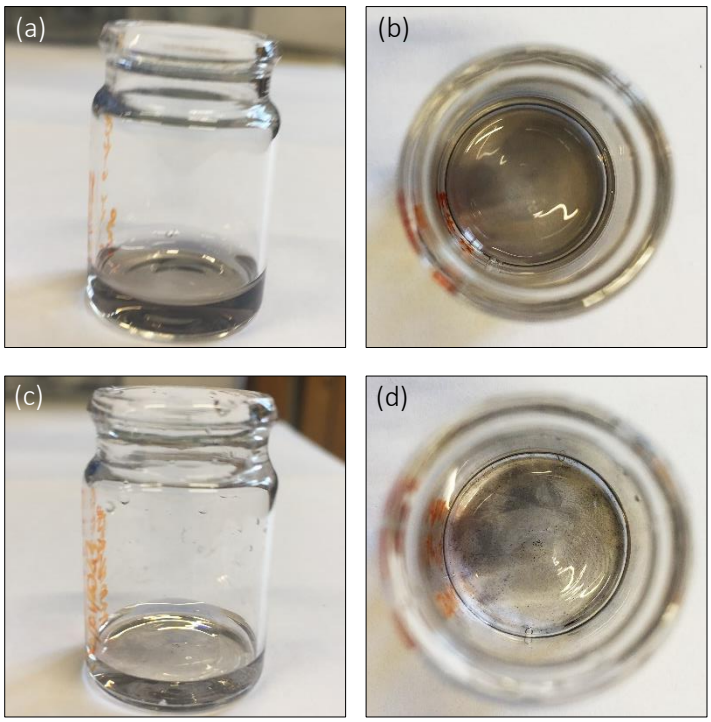

Figure 6.11 PtNP surface modified with 70 µM 6-ATA. (a & b) PtNP + 70 µM 6-ATA post surface modification and (c & d) PtNP + 70 µM 6-ATA day after surface modification. Results are representative of 1 experiment (n=1).

Collectively, this data confirms the quaternary ammonium compound 6-ATA is unstable on the PtNP surface, however why 6-ATA is unstable on the PtNP surface remains unclear. There are no reports of 6-ATA functionalising platinum or other metallic surfaces. A possible explanation is there was not enough 6-ATA bound to the PtNP or the amino-platinum was not as strong enough to keep the 6-ATA molecule bound to the PtNP surface, leaving the PtNP unprotected, such that they precipitated out of solution. A previous study by Wand et al.[189] found amine functionalised PtNPs to have weak bond in comparison to thiol functionalised PtNPs. Furthermore, the amino-functionalised PtNPs aggregated, which was what we observed in our experiments.

Since, the ligand exchange between PtNP-CTAB for 6-ATA was unsuccessful, the next step was to synthesise positively charged PtNPs with an alkanethiol as a capping agent, thereby forming a covalent bond between the PtNP and thiol molecule.

6.2.4 Synthesis of positively charged PtNP with 2-diethylaminoethanethiol hydrochloride

In the second approach, positively charged PtNPs were synthesised following a method described by Testa et al.[190] whereby the alkanethiol 2-diethylaminoethanethiol hydrochloride (DEA) was used as a capping agent to synthesis positively charged PtNPs. DEA was selected as a capping agent as it is hydrophilic and was previously reported to stabilise both AuNPs and PtNPs. [190, 191] DEA is a short chain alkanethiol with only 2 carbons on the alkane chain, a SH group and a NH_3^+, as shown in Figure 6.12.

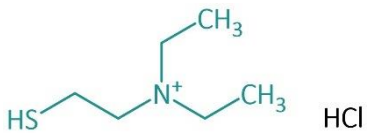

Figure 6.12 Structure of 2-diethylaminoethanethiol hydrochloride (DEA).

In this experiment, PtNPs capped with DEA (referred to as PtNP-DEA) were synthesised by reduction of $H_2PtCl_6.6H_2O$ with the strong reducing agent sodium borohydride at room temperature for 20 hours, the overall reaction is illustrated in the schematic in Figure 6.13. As specified by Testa et al.[190] $H_2PtCl_6.6H_2O$, DEA, and sodium borohydride were prepared in molar ratios of 1:0.33:0.5, respectively, see Table 6.1 for ratios and concentrations; with the precursor prepared in dH_2O specifically at pH 2 (reaction A) as specified by Testa et al.[190] Initially, $H_2PtCl_6.6H_2O$ and DEA were combined and degassed by argon, followed by the dropwise addition of sodium borohydride. To examine how the role of pH affects PtNP synthesis method,

a parallel experiment was conducted, where $H_2PtCl_6.6H_2O$ was prepared in just dH_2O, i.e., a neutral pH (reaction B) Figure 6.14 (a) & (b). These PtNP-DEA were characterised by TEM, DLS and zeta potential, see Figure 6.14 and Figure 6.15. The TEM size of the PtNP-DEA was obtained by measuring the diameters of 200 PtNP-DEA. Five DLS and zeta potential measurements were 5 times performed to obtain the mean. DLS and zeta potential measurements were performed directly from the synthesis reaction and after centrifuging and resuspending in dH_2O.

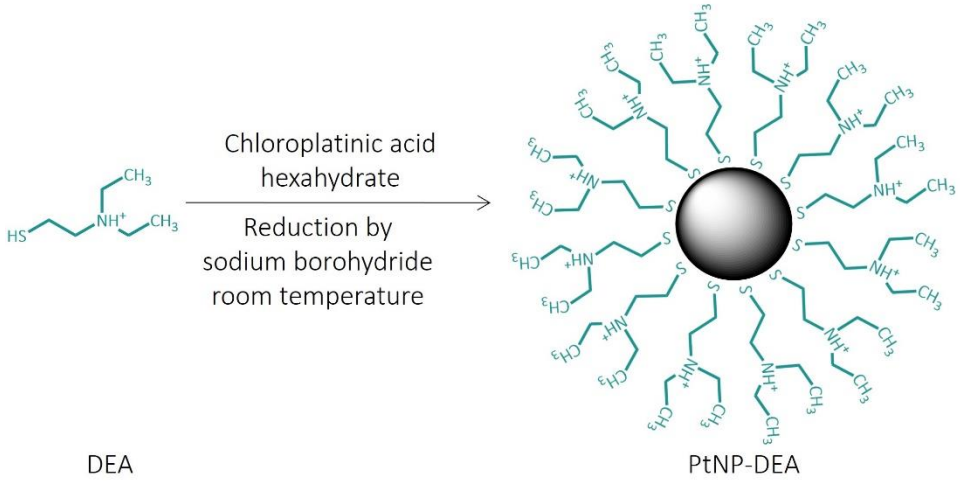

Figure 6.13 Schematic of synthesis of positively charged PtNPs by reduction of sodium borohydride with DEA as a capping agent. Note figure not to scale.

Table 6.1 PtNP-DEA synthesis reaction ratios of precursor, capping and reducing agent.

	$H_2PtCl_6.6H_2O$	DEA	$NaBH_4$
Ratio	1	0.33	5
Concentration (mM)	0.48	0.16	2.4

Figure 6.14 (a) & (b) show reactions A and B before the addition of the strong reducing agent sodium borohydride and after 20 hours. The dropwise addition of sodium borohydride caused both reactions to slowly change colour from a pale-yellow to a black/brown solution, indicating the sodium borohydride had reduced the $H_2PtCl_6.6H_2O$ to platinum. The TEM images in Figure

6.14 (c) & (d) of reaction A showed spherical PtNP-DEA of varied sizes with a large particle size distribution, see Figure 6.14 (e).

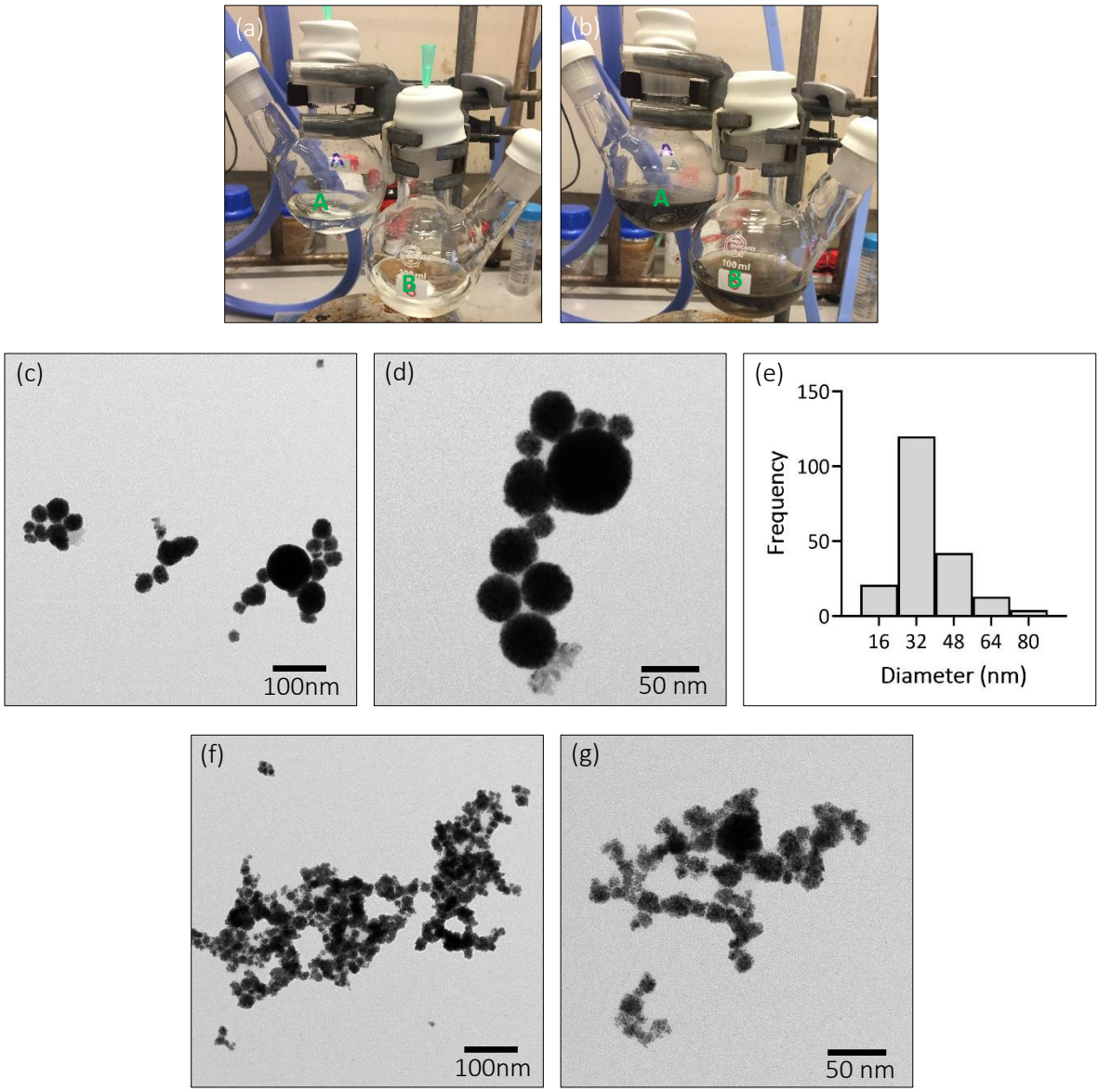

Figure 6.14 Synthesis of positively charged PtNPs with DEA as a capping agent. (a) reaction A with $H_2PtCl_6.6H_2O$ prepared in dH_2O at pH 2 and reaction B $H_2PtCl_6.6H_2O$ prepared in just dH_2O, (b) reactions A and B after 20 hours, (c) & (d) TEM images of reaction A, (e) frequency distribution of reaction A and (f) & (g) TEM images of reaction B. Results are representative of 1 experiment (n=1).

In contrast, the TEM images of reaction B shown in Figure 6.14 (f) & (g) display large agglomerates of PtNP-DEA with a non-spherical shape, this indicates the DEA was unable to adsorb on the PtNP surface. As result, the individual nanoparticles could not be distinguished, and the nanoparticle diameters could not be measured hence no particle size distribution was displayed. The TEM images of both reactions A & B revealed that PtNP-DEA synthesis was highly dependent on acidic conditions at pH 2.

How pH affects PtNP-DEA synthesis is not fully understood, it is thought that the highly acidic conditions enable protonation of the ammonium group. Therefore, the highly charged DEA exhibits a greater surface charge and repels deprotonated DEA molecules on the nanoparticle surface, thereby maintaining the colloidal stability of PtNP-DEA. Experiments by Venditti et al.[192] using AuNP-DEA, hypothesised that at pH 2 the protonated DEA is chemisorbed on the nanoparticle surface as result of the highly charged DEA. Conversely, at pH 7 where there is a mixture of protonated and deprotonated DEA on the nanoparticle surface, the deprotonated DEA is physisorbed and as there is less charge coming from the protonated DEA molecule this leads to nanoparticle aggregation. This theory supports the results obtained in our experiments, at pH 2 spherical PtNP-DEA were observed as shown in Figure 6.14 (c) & (d) while PtNP-DEA aggregates were observed at the higher pH, Figure 6.14 (f) & (g).

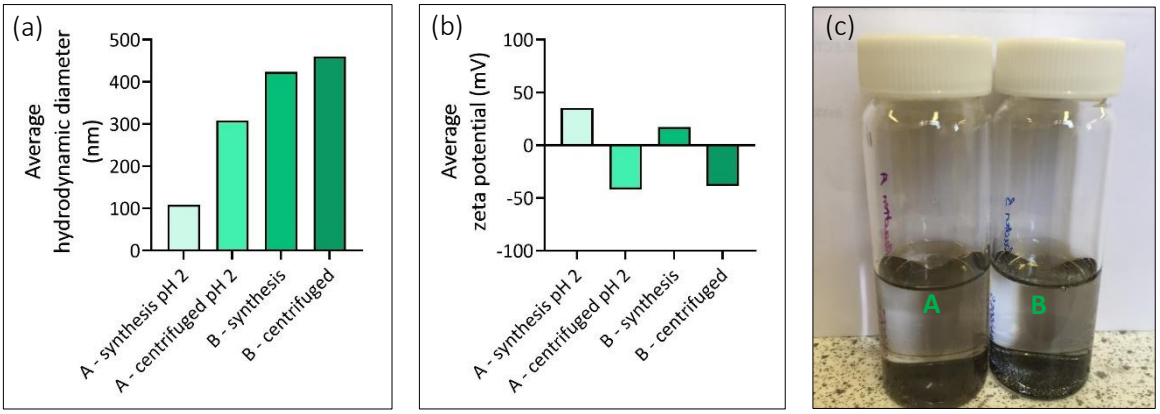

Figure 6.15 PtNP-DEA synthesis and characterisation by (a) DLS, (b) zeta potential and (c) reaction A and B the day after synthesis. Results are representative of 1 experiment (n=1).

Figure 6.15 (a) demonstrates the hydrodynamic diameters of reactions A & B after synthesis and after centrifugation. The hydrodynamic reaction A after synthesis was 109 nm, however after centrifugation this significantly increased to 309 nm suggesting the PtNP-DEA had aggregated. Reaction B showed a hydrodynamic diameter of 423.7 nm after synthesis, this was expected as the TEM data in Figure 6.14 (f) & (g) showed large agglomerates; after centrifugation the hydrodynamic diameter only slightly increased to 460.3 nm.

The zeta potential of the PtNP-DEA from reaction A were 35.2 mV after synthesis indicating good stability however this was reduced to -41.9 mV (Figure 6.15 (b)) after centrifugation, demonstrating the PtNP-DEA had become unstable and DEA capping was lost during the centrifugation step. The aggregation of PtNP-DEA suggests that the DEA had oxidised, XPS analysis would be required to confirm this. Though reaction B showed PtNP-DEA agglomerates, the zeta potential was still measured after synthesis and was 17.2 mV suggesting some DEA

was present on the PtNP surface. Again, the DEA capping was also lost after centrifugation as the zeta reduced to -38.9 mV.

The data from these experiments demonstrate pH 2 is crucial for creating monodispersed positively charged PtNP with a DEA capping. Experiments conducted by Testa et al.[190] claimed the PtNP-DEA to be stable, however the stability of these PtNP-DEA was lost after centrifugation. As previously discussed, this aggregation could be due to the oxidation of thiol. Nonetheless, DEA was an unstable capping agent, this could be due to 2 possible factors: (1) both SH and NH groups were both forming bonds with PtNP core, Figure 6.16 illustrates a hypothetical arrangement of DEA on the PtNP surface but note the actual orientation of DEA on the PtNP surface is unknown, investigation by XPS could confirm the presence of the platinum-sulphur and platinum-nitrogen bonds but not the orientation. (2) Successful SAM formation is dependent on the hydrocarbon chain lengths, longer alkanethiol can sufficiently pack onto noble metal surfaces, [156] as DEA is a short alkanethiol, it could be that it was not sufficiently packed onto the PtNPs. The combination of these two factors makes DEA an unstable capping agent, if the NH group of DEA is bound to the PtNP core, this would sterically hinder the SAM formation with the SH group binding to the PtNP surface.

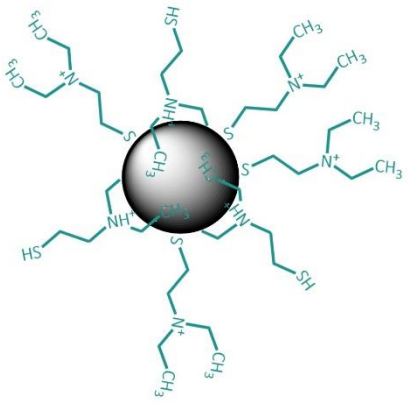

Figure 6.16 Hypothetical arrangement of DEA on the PtNP surface, not to scale.

6.3 Conclusion

6-AHT was confirmed to be an unsuitable compound for functionalising citrate capped PtNPs. Positively charged PtNPs were created using 2 different methodologies. The first method employed cationic surfactant CTAB to synthesise positively charged PtNPs; characterisation revealed the PtNP-CTAB to be positively charged with good stability, however their shape was non-uniform. These PtNP-CTAB were taken forward by surface modifying via ligand exchange with 6-ATA, however stability was significantly reduced. The second method utilised 2-DEA as a capping agent to synthesise positively charged PtNPs, it was evident that PtNP synthesis at pH 2 was a vital factor to achieve spherical nanoparticles, more importantly it indicated surface coverage was a function of pH. Unfortunately, though positively charged PtNP were created via these 2 different methods, both methods resulted in unstable positively charged PtNPs. For this reason, they were not included in later functional platelet studies.

6.3.1 Further work

Though short chain alkanethiols were utilised in these experiments, they do not sufficiently pack onto the nanoparticle surface as well as long chain alkanethiols. An alternative alkanethiol thiol that could be used as a capping agent could be (11-mercaptoundecyl)-N,N,N-trimethylammonium bromide (11-MABr), see Figure 6.17 for structure. 11-MABr is analogous to 6-MTAB, with a SH head group and NR_4^+ group, the main difference is the spacer molecule which has an 11-carbon alkane chain. The $-CH_3$ groups of the ammonium group would sterically prevent the N^+ from binding to the PtNP core.

Figure 6.17 Structure of (11-mercaptoundecyl)-N,N,N-trimethylammonium bromide (11-MABr).

A second alternative compound is the polymer polyethyleneimine (PEI), see Figure 6.18 for its structure. PEI is a synthetic cationic polymer with repeating units of the amine group spaced by 2 carbon atoms, PEI can be either linear or branched with differing molecular weights. Using PEI would be advantageous over 11-MABr as it exhibits several NH_2 groups, thus it has multiple valences available to bind the nanoparticle surface. Previous work by Nagao et al.[193] used PEI is to synthesise positively charged PtNPs to exhibit a positive charge with different morphologies. The use of PEI has also been extended to other metallic nanoparticles, experiments conducted by Sharonova et al.[194] demonstrated positively charged AgNPs of 70 ± 20 nm with a zeta potential of 55 mV demonstrating good stability with PEI as the capping agent.

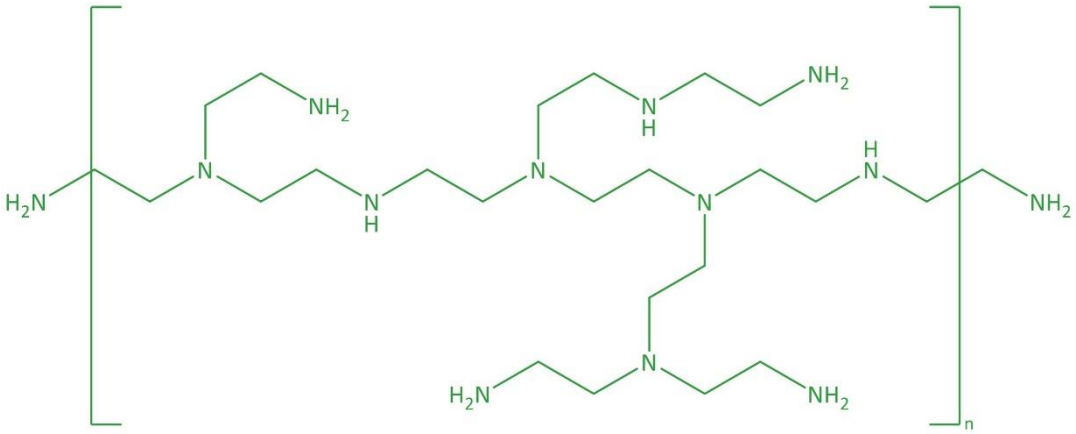

Figure 6.18 Structure of polyethyleneimine (PEI).

Chapter 7 Functionalisation of Platinum Nanoparticles with Neutrally Charged Thiol Compounds

Abstract: This chapter examines the functionalisation and synthesis approaches used to create sterically stable neutrally charged PtNPs to be later utilised in platelet investigations. 20 nm c-PtNPs synthesised in Chapter 4 were assessed for functionalisation with the neutrally charged alkanethiol 6-mercaptohexanol (6-MCH) via ligand exchange. Various surface characterisation techniques confirmed 6-MCH was unable to ligand exchange with the citrate ions capping the PtNP surface. In a second approach, 6-MCH was employed as a capping agent to synthesise neutrally charged PtNPs, unfortunately this approach was unsuccessful. In a third approach, the neutrally charged PEGylated thiols 2-[2-[2-(2-mercaptoethoxy)ethoxy]ethoxy]ethanol (2-MEE) and 11-(mercaptoundecyl)hexa(ethylene glycol) (11-MUHEG) were used to functionalise the 20 nm c-PtNP via the ligand exchange method. Using various surface characterisation techniques, it was successfully confirmed their functionalisation with the PEGylated thiol molecules to produce sterically stable neutrally charged 20 nm PtNPs via ligand exchange. This study is the first to report the functionalisation of PtNPs by the PEGylated thiols 2-MEE and 11-MUHEG.

7.1 Introduction

Thiols molecules are common ligands that have been frequently used to functionalise nanoparticles, this has been this has been established either chemisorption methods by ligand exchange post-synthesis or during synthesis.[42, 46, 49] Thiol molecules can chemisorb onto the nanoparticle surface to form self-assembled monolayers (SAMs).[150] Although several studies have reported SAM formation on PtNPs by the hydrophobic alkanethiols octandecanethiol, 1-decanethiol (DT) and 1-dodecanethiol (DTT), their applications are limited and unsuitable for biological studies, as hazardous reagents such as tetrahydrofuran and lithium triethylborohydride are utilised to synthesis them.[45, 195-197] Alternatively, neutrally charged thiols which do not require hazardous reagents could be used to synthesis/functionalise neutrally charged nanoparticles. Neutrally charged nanoparticles such as polymeric, lipid and metallic nanoparticles are favourable in drug delivery as they can circulate in the bloodstream without electrostatically interacting with cell membranes or membrane proteins.[198] Of the metallic nanoparticles, it is predominately gold nanoparticles that have been functionalised with a neutral charge.[199-201] To date, there are currently no studies reporting the functionalisation of PtNPs by neutrally charged alkanethiols and PEGylated thiols and warrants further investigations.

7.1.1 Objectives

1. Functionalise 20 nm c-PtNPs with 6-mercaptohexanol. Characterise by DLS and zeta potential.

2. Synthesise neutrally charged 20 nm PtNPs with 6-mercaptohexanol. Characterise by DLS and zeta potential.

3. Functionalise 20 nm c-PtNPs with 2-[2-[2-(2-mercaptoethoxy)ethoxyethoxy}ethanol. Characterise by DLS, zeta potential, gel electrophoresis and XPS.

4. Functionalise 20 nm c-PtNPs with 11-(169mercaptoundecyl)hexa(ethylene glycol). Characterise by DLS, zeta potential, gel electrophoresis and XPS.

7.2 Results and Discussion

7.2.1 Functionalisation of 20 nm platinum nanoparticles by 6-mercaptohexanol

In Chapter 4, carboxyl-terminated alkane and PEGylated thiols were used to functionalise the 20 nm c-PtNP via ligand exchange to create to sterically stable negatively charged PtNPs. Following the same ligand exchange method, 20 nm c-PtNPs (synthesised in Chapter 3) were functionalised by hydroxyl-terminated alkane and PEGylated thiols to produce neutrally charged PtNPs. The neutrally charged alkanethiol 6-mercaptohexanol (6-MCH) was selected of functionalising the c-PtNP as it is analogous to 6-mercaptohexanoic and water soluble. 6-MCH exhibits a terminal hydroxyl group (OH) functional group, a mercapto group (SH) and a 6-carbon alkane chain, as illustrated in Figure 7.1.

Figure 7.1 Structure of 6-mercaptohexanol (6-MCH).

Using the method described in section 4.2.2, 20 nm c-PtNPs were functionalised by ligand exchange where the citrate ions capping the PtNPs were exchanged for a thiol molecule. Citrate ions are non-covalently bound to the nanoparticle surface and provide electrostatic stabilisation for the core nanoparticle. As the citrate ions are non-covalently bound, they can be displaced by thiol molecules to form strong covalent bonds, therefore forming a SAM and providing steric stabilisation in addition to functionality.[46, 49] Figure 7.2 illustrates the overall ligand exchange to produce neutrally charged PtNPs. The concentration of 6-MCH required for surface coverage was calculated using the alkanethiol footprint of 0.214 nm^2 from literature,[128] see Appendix 11.2 for calculations. c-PtNP surface modified by 6-MCH will be referred to as PtNP-6-MCH throughout this thesis.

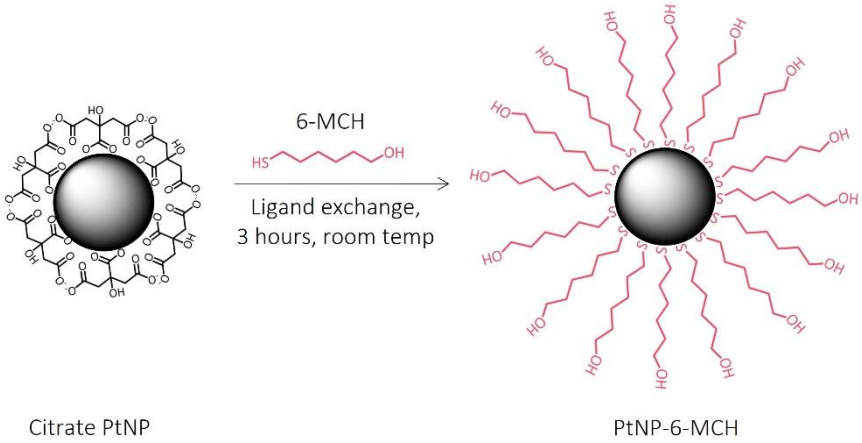

Figure 7.2 Ligand exchange of citrate ions on 20 nm c-PtNP by 6-MCH. Note figure not to scale.

20 nm c-PtNPs were incubated with 6-MCH at concentrations from 5 – 100 µM for 3 hours at room temperature. Excess 6-MCH and citrate ions were removed by centrifugation at 10000 x g for 10 minutes. The supernatant was discarded, and the PtNP-6-MCH were resuspended in dH_2O and then characterised by DLS, zeta potential and pH. Though pH is not a characterisation technique per say, they were reported as zeta potential measurements are dependent on pH; changes in pH of the nanoparticle solution can occur indicate when a ligand exchange has occurred. The control samples were 20 nm c-PtNPs in 1.1 mM sodium citrate and dH_2O (referred to as the dH_2O control). c-PtNPs was chosen as a control to assess if there was a difference between the capping agents, the dH_2O control was selected as all PtNP-6-MCH samples were resuspended in dH_2O. DLS and zeta potential were repeated across three batches of 20 nm, Figure 7.3 represents the characterisation of PtNP-6-MCH. Five DLS and zeta potential measurements were performed to obtain the mean for each sample, data is presented as mean ± SD.

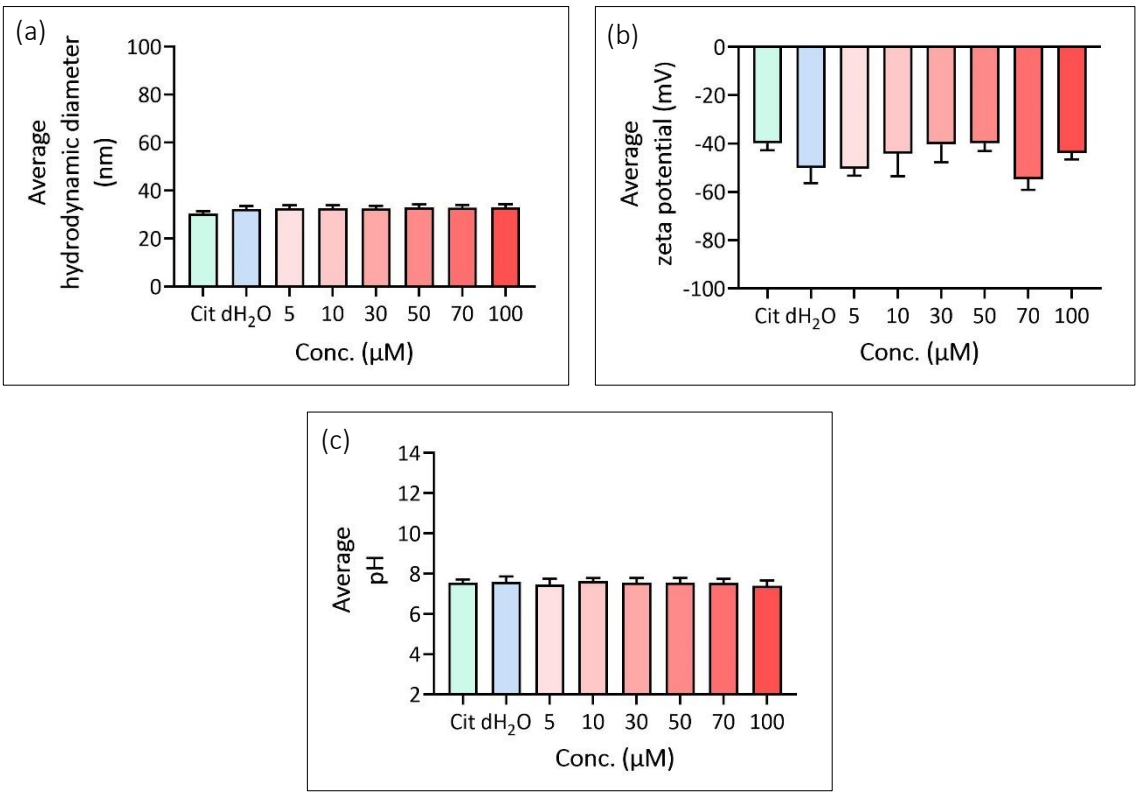

Figure 7.3 Characterisation of PtNP-6-MCH. (a) hydrodynamic diameters, (b) zeta potentials and (c) pH. Results are representative of 3 experiments (n=3) and presented as mean ± SD.

Figure 7.3 (a) represents the hydrodynamic diameters of PtNP-6-MCH, the c-PtNPs and dH_2O controls had hydrodynamic diameters of 30.3 ± 1.1 nm and 32.4 ± 1.2 nm respectively. The PtNP-6-MCH had comparable hydrodynamic diameters to the control samples, these hydrodynamic diameters ranged from 32.5 to 33.1 nm. With increasing concentrations of 6-MCH no differences in hydrodynamic diameter were observed. The zeta potentials of PtNP-6-MCH ranged from -39.9 to -54.8 mV as shown in Figure 7.3 (b); no differences were observed between the PtNP-6-MCH samples. These zeta potentials were comparable to the citrate and dH_2O controls which had zeta potentials of -39.9 ± 3 mV and -50.1 mV ± 6.2 mV respectively, this data indicates no ligand exchange has taken place. The pH of PtNP-6-MCH also demonstrated no difference between the PtNP-6-MCH samples compared the citrate and dH_2O

control samples. Both control samples exhibited pH of 7.6, the pH PtNP-6-MCH ranged from pH 7.4 to pH 7.6, this suggests ligand exchange had not taken place. As the zeta potential and pH data indicated no ligand exchange had occurred, further characterisation by gel electrophoresis and XPS was not undertaken.

It is unclear why 6-MCH was unable to undergo ligand exchange with citrate ions, citrate ions are non-covalently bound with metallic nanoparticle surface and should be displaced by thiol molecules to form a covalent metal-thiol bond. This was previously observed with alkane and PEGylated thiols in Chapter 5. The mechanism of ligand exchange by 6-MCH on metallic nanoparticles remains unknown. Previous literature depicts 6-MCH as a blocker or spacer molecule on AuNPs. Work by Bi et al.[202] describes the bi-functionalisation of citrate capped AuNPs by the negatively charged alkanethiol 11-mercaptoundecanoic acid (11-MUA) and 6-MCH for the colourimetric detection of heavy metal ions. Here, 6-MCH was utilised as a blocker to prevent non-specific binding of macromolecules. The bi-functionalisation of 11-MUA/6-MCH involved the ligand exchange of the citrate ions from the AuNP surface. In this instance, 11-MUA would be able to displace the citrate ions from the AuNP surface, thus allowing opportunity for 6-MCH to then bind to the AuNP surface, thus providing bifunctionality. In a more recent study by Lai et al.[203] 6-MCH was utilised as a spacer molecule for AuNPs conjugated with thiolated DNA. Citrate capped AuNP were first conjugated with thiolated DNA. Characterisation by TEM and UV absorbance demonstrated successful conjugation, the AuNP-DNA conjugate was mixed with 6-MCH to allow spacing on the AuNP surface. In the studies described, 6-MCH is utilised in the presence of a charged ligand rather than 6-MCH alone.

Previously, AuNPs have been directly functionalised with 6-MCH in synthesis to use for subsequent functionalisation with other ligands. 1.5 nm AuNP-6-MCH were prepared by the reduction of tetrachloroaurate with an excess of tetraoctylammonium bromide in a water toluene mixture with sodium borohydride.[204] However, a limitation of this method is the size of the AuNPs are very small and the reagents used in synthesis are harmful. To ascertain, if PtNPs can be directly functionalised with 6-MCH, PtNP will be synthesised with 6-MCH as the capping agent following the methods used in chapter 4.

7.2.2 Platinum nanoparticle synthesis with 6-mercaptohexnol

To assess if 6-MCH can chemisorb onto the PtNP surface in the absence of citrate ions, PtNPs were synthesised with 6-MCH as the capping agent. In this preliminary experiment, PtNPs were synthesised following the same seed mediated synthesis method described in section 4.2.4, with a modification of 34 mM sodium citrate was replaced by 34 mM 6-MCH, see Figure 7.4.

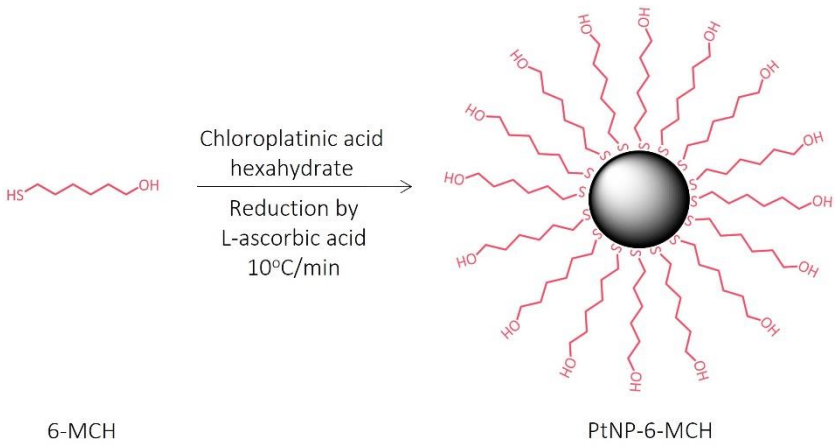

Figure 7.4 Schematic of synthesis of neutrally charged PtNPs with 6-MCH as a capping agent. Note Figure to scale.

Pt seeds from chapter 4 were used as the template to grow PtNPs, 0.2 M $H_2PtCl_6.6H_2O$ remained as the precursor with 71 mM L-ascorbic acid as the reducing agent. PtNP growth was controlled by L-ascorbic acid and a temperature increment of 10°C/min to 100°C. The reduction of $H_2PtCl_6.6H_2O$ performed in section 4.2.4 was observed by a change in reaction colour from yellow to a brown/black. However, in this case, the addition of L-ascorbic acid did not cause the $H_2PtCl_6.6H_2O$ to reduce to platinum, the reaction turned cloudy as shown in Figure 7.5 (a).

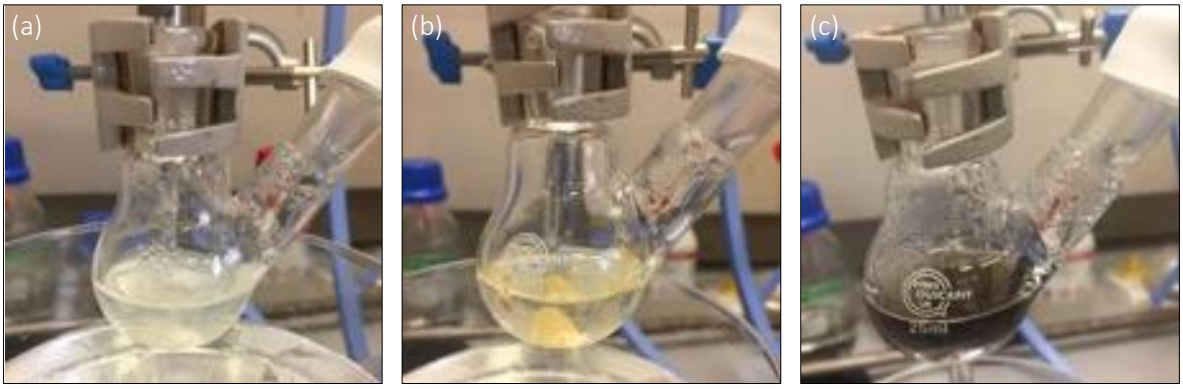

Figure 7.5 Synthesis of PtNP with 6-MCH as a capping agent. (a) with L-ascorbic acid, (b) with sodium borohydride and (c) with sodium citrate and L-ascorbic acid. Results are from 1 experiment (n=1).

As L-ascorbic acid is a mild reducing agent, the experiment was repeated under the same conditions using the stronger reducing agent sodium borohydride at the same concentration of 71 mM. Unfortunately, the $H_2PtCl_6.6H_2O$ failed to reduce to platinum as no colour change was observed, see Figure 7.5 (b). To confirm if the precursor and reducing reagents were working, a control synthesis reaction using 34 mM sodium citrate as the capping agent was performed. As previously used in Chapter 4, Pt seeds were used the template to grow the c-PtNPs, the same working solutions of 0.2 M $H_2PtCl_6.6H_2O$ and 71 mM L-ascorbic acid were used. PtNP growth was controlled by L-ascorbic acid and a temperature increment of 10°C/min

to 100°C. As expected, the $H_2PtCl_6.6H_2O$ reduced to platinum, this was demonstrated by the colour change of the reaction from a yellow colour to brown/black as shown in Figure 7.5 (c). The data suggests 6-MCH is blocking the reduction of $H_2PtCl_6.6H_2O$ to platinum, however the mechanism remains unknown. The non-reduction of these reactions is likely be due to the neutral charge of 6-MCH; if we compare 6-MCH to the common capping agent sodium citrate, the citrate ions exhibit three carboxylic acid groups and is able to physisorb onto the PtNP surface. Mudunkotuwa et al.[205] reported that deprotonated citric acid absorbs onto the surface of titanium oxide nanoparticles. It could be that for 6-MCH to adsorb onto the PtNP surface it needs to be in a deprotonated state. Thus, the protonation state of the capping agent not only aids absorption but is fundamental for functionalising the nanoparticle surfaces. These findings suggest that 6-MCH is an unsuitable capping agent for PtNPs. An alternative molecule that could be used to functionalise the PtNPs with a neutral charge would be a PEGylated thiol with a OH group functional head group. As PEGylated molecules are comprised of both polar and non-polar regions. The next section with examine the functionalisation of 20 nm PtNPs by neutrally charged PEGylated thiols.

7.2.3 Functionalisation of 20 nm PtNP with 2-[2-[2-(2-mercaptoethoxy)ethoxy]ethoxy]ethanol

Although the functionalisation of PtNP by 6-MCH was unsuccessful via ligand exchange and synthesis, to achieve neutrally charged PtNP, functionalisation was assessed using the PEGylated thiol 2-[2-[2-(2-mercaptoethoxy)ethoxy]ethoxy]ethanol (2-MEE), see Figure 7.6 for its structure. 2-MEE consists of SH group, OH functional head group and three PEG units (C-C-O). PtNP surface modified by 2-MEE will be referred to as PtNP-2-MEE throughout this thesis.

Figure 7.6 Structure of 2-[2-[2-(2-mercaptoethoxy)ethoxy]ethoxy]ethanol (2-MEE).

Using the method described in section 4.2.2, c-PtNPs were surface modified by 2-MEE, the overall ligand exchange is illustrated in Figure 7.7. The PEGylated thiol footprint of 0.35 nm^2 from literature[169] was used to determine the concentration of 2-MEE required for surface coverage which was 3.5 µM, see Appendix 11.2 for calculations.

20 nm c-PtNPs were incubated with 2-MEE at concentrations from 3 – 70 µM for 3 hours at room temperature. Excess 2-MEE and citrate ions were removed by centrifugation at 10000 x g for 10 minutes. The supernatant was discarded, and PtNP-2-MEE were resuspended in dH_2O and then characterised by DLS and zeta potential. pH was reported as zeta potential measurements are dependent on pH. Once again, c-PtNPs was selected as a control to assess if there was a difference between the capping agents, dH_2O (referred to as the dH_2O control) as all PtNP-2-MEE were resuspended in dH_2O.

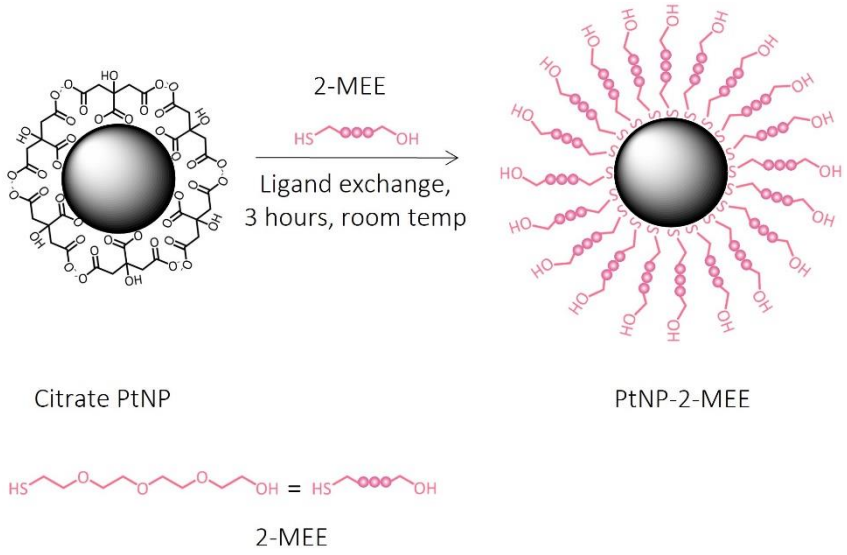

Figure 7.7 Ligand exchange of citrate ions on 20 nm c-PtNP by 2-[2-[2-(2-mercaptoethoxy)ethoxy]ethoxy]ethanol.

For gel electrophoresis, 20 nm c-PtNPs were surface modified with 3 µM and 70 µM 2-MEE only up to the discarding step as concentrated functionalised PtNPs were required for this technique. Unconcentrated nanoparticles would not be visible on the agarose gel. 1 µL of concentrated 3 µM and 70 µM PtNP-2-MEE were then premixed with 15 µL glycerol and separated on a 1% agarose gel submerged in Tris-acetate-EDTA (TAE) buffer, concentrated PtNP were used as a control. Gel electrophoresis was only used qualitatively manner. All DLS, zeta potential and pH experiments were repeated across three batches of 20 nm c-PtNPs, five DLS and zeta potential measurements were performed to obtain the mean for each sample, data is presented as mean ± SD.

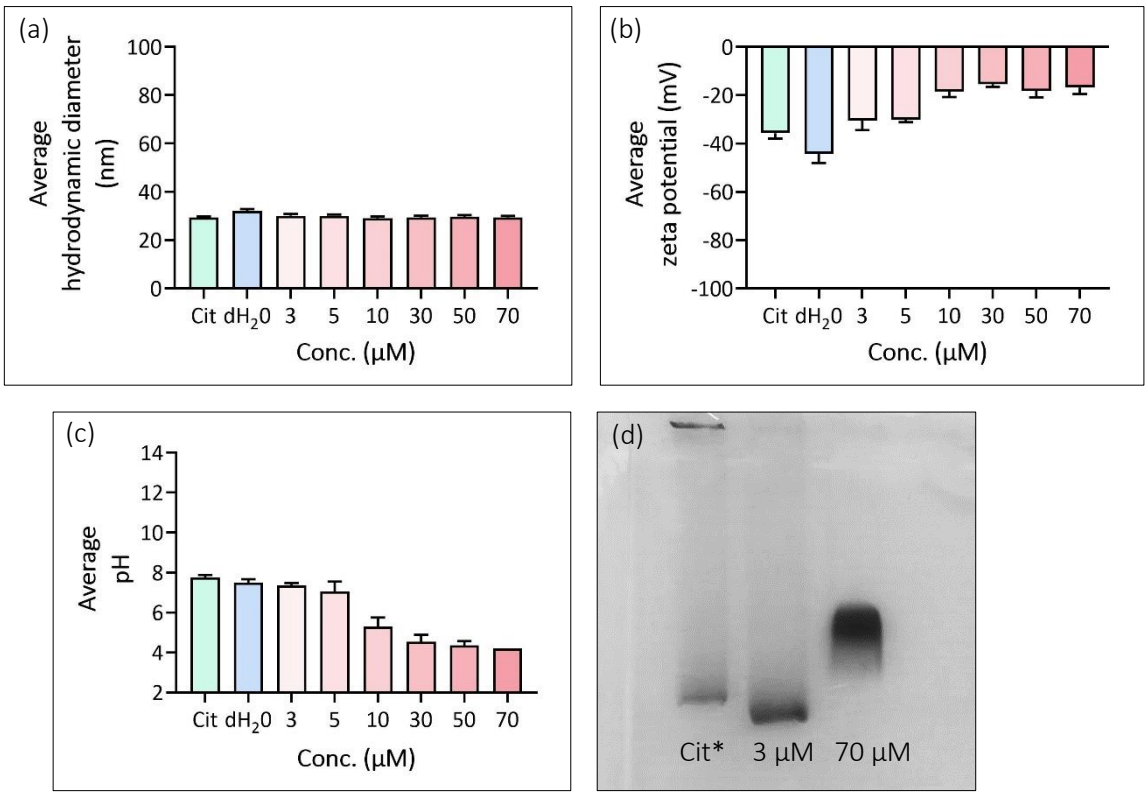

*Figure 7.8 Characterisation of PtNP-2-MEE. (a) hydrodynamic diameters, (b) zeta potentials (c) pH and (d) gel electrophoresis. Results (except electrophoresis) are representative of 3 experiments (n=3) and presented as mean ± SD. Note *: overspill*

The hydrodynamic diameters of PtNP-2-MEE are displayed in Figure 7.8 (a). The c-PtNP and dH_2O controls had hydrodynamic diameters of 29.4 ± 0.4 and 32.1 ± 0.8 nm respectively. PtNP-2-MEE had comparable hydrodynamic diameters to the control samples ranging from 29.4 to 30.1 nm. There was no difference in hydrodynamic diameters amongst the different PtNP-2-MEE samples. The zeta potentials of PtNP-2-MEE are shown in Figure 7.8 (b), as expected the citrate control and dH_2O control exhibited negatives charge of -35.7 ± 2.2 and -44.3 ± 3.7 mV respectively. As the concentration of 2-MEE increased, the zeta potential increased, indicating more 2-MEE molecules has bound to the PtNP surface. This trend was previously observed in Chapter 5 with PtNP-6-MHA, PtNP-8-MOA, PtNP-TA and PtNP-2-MOHA. Although, the

functional head group of 2-MEE is neutrally charged, the zeta potential of PtNP-2-MEE demonstrated negative charges, ranging from -15.4 to -30.4 mV; PEGylated nanoparticles have been shown to exhibit zeta potentials close to 0 mV in the range of -2.7 to -4.6 mV.[121] It is likely there are still citrate ions present on the surface of PtNP-2-MEE, hence, the zeta potential of PtNP-2-MEE does not fall into the same range. XPS analysis would be required to verify the presence of the citrate ions on the PtNP surface.

Ligand exchange was further supported by the pH of PtNP-2-MEE as shown in Figure 7.8 (c). The pH of PtNP-2-MEE decreased with increasing concentrations of 2-MEE from pH 7.4 to 4.2; the pH of the citrate control and dH_2O controls remained in the neutral range at pH 7.8 and 7.5 respectively, therefore, demonstrating ligand exchange had taken place. The decrease in pH could possibly be due to 2-MEE having a lower pH than the sodium citrate, thus, as the concentration of 2-MEE increased the pH decreased.

In addition, gel electrophoresis of PtNP-2-MEE also confirmed ligand exchange as shown in Figure 6.8 (d). 3 µM and 70 µM of 2-MEE were selected for gel electrophoresis to examine if there was a difference in surface coverage. As the c-PtNPs are only electrostatically stabilised they were not protected to withstand the TAE buffer, hence they aggregated in the well. Unfortunately, a small amount of the c-PtNP migrated through the gel, this was due to an overspill from the neighbouring well with 3 µM PtNP-2-MEE. 3 µM and 70 µM PtNP-2-MEE migrated through the agarose gel, 3 µM PtNP-2-MEE had a faint band indicating fewer 2-MEE molecules had bound to the PtNP surface. Conversely, 70 µM PtNP-2-MEE had a denser band

demonstrating more 2-MEE molecules had bound to the PtNP surface. Interestingly, 70 µM PtNP-2-MEE did not migrate to the same distance compared with 3 µM PtNP-2-MEE. Gel electrophoresis separates molecules/particles based on charge; in this instance, 2-MEE possess a neutral charge from the OH group and only a partial charge from the PEG units, therefore at higher concentrations of 2-MEE, more OH and PEG units were present on the PtNP surface, thus less charge, therefore at 70 µM PtNP-2-MEE was unable to migrate to the same distance as 3 µM PtNP-2-MEE. Altogether, the DLS, zeta potential, pH and gel electrophoresis data indicate a ligand exchange has occur. Next, to confirm 2-MEE has bound to the PtNP surface, the platinum-thiol bond was investigated by XPS.

7.2.4 XPS of 20 nm PtNP-2-MEE

To confirm if the 2-MEE had bound to the PtNP surface, XPS was performed to assess the elemental composition of PtNP-2-MEE. 2-MEE was selected as control sample, the control sample was prepared by directly drop casting 2-MEE onto the copper substrate and air dried. Following the method described in 5.2.2, c-PtNPs were surface modified with 70 µM of 2-MEE for 3 hours at room temperature. 70 µM 2-MEE was used for XPS analysis as this concentration demonstrated the greatest increase in zeta potential as displayed in Figure 7.8 (b). The excess 2-MEE and citrate ions were removed by centrifuging the sample at 10000 x g for 10 minutes, the supernatant was discarded, and the concentrated PtNP-2-MEE were drop cast onto the copper substrate, air dried and submitted for XPS analysis. 2-MEE and PtNP-2-MEE were charged corrected to 285 eV rather than 284.8 eV as polymers generally have their aliphatic component at 285 eV. Additionally, this allows comparison with polymer handbook.[171] As

previously discussed in section 4.2.5, common artefacts of XPS are contamination by adventitious carbon and oxygen contamination which are found in high-resolution scans, thus the high-resolutions scan only be used to identify species on the surface of the PtNPs.

Surveys scans of the control sample of 2-MEE and PtNP-2-MEE detected the presence of platinum (Pt), copper (Cu), carbon (C), oxygen (O) and sulphur (S). Examination of the high-resolution scans of 2-MEE and PtNP-2-MEE detected signals from Pt 4f, Cu 2p, C 1s, O 1s and S 2p orbitals, these are presented in Figure 7.9. As no PtNPs were present on the copper substrate, the high-resolutions scans of 2-MEE did not detect a signal for Pt 4f shown in Figure 7.9 (a). However, three Cu 3p peaks were detected, Cu $3p_{3/2}$ at 74.9 eV, CuO at 75.4 eV and Cu $3p_{1/2}$ at 77.4 eV, these peaks were also present on the blank copper substrate in section 4.2.5. XPS experiments in Chapter 5 also detected Cu 3p on the copper substrates with thiol directly deposited. Cu 3p and Pt 4f have similar binding energies as they have a spectral overlap; this was observed in the XPS analysis of Pt-Cu bimetallic alloys.[144] Additionally, this spectral overlap was observed in XPS experiments in Chapter 5 with PtNP-6-MHA, PtNP-TA and PtNP-2-MOHA. The high-resolution scans of PtNP-2-MEE detected the Pt 4f signal. Pt 4f was presented as an asymmetric peak, Pt $4f_{7/2}$ at 71 eV and Pt $4f_{5/2}$ at 74.3 eV, with a separation of 3.33 eV, these binding energies were comparable to those in literature.[144, 146] A CuO peak was also detected at 74.5 eV, see Figure 7.9 (b). Pt 4f ascribes to the PtNPs and CuO ascribes to the copper substrate.

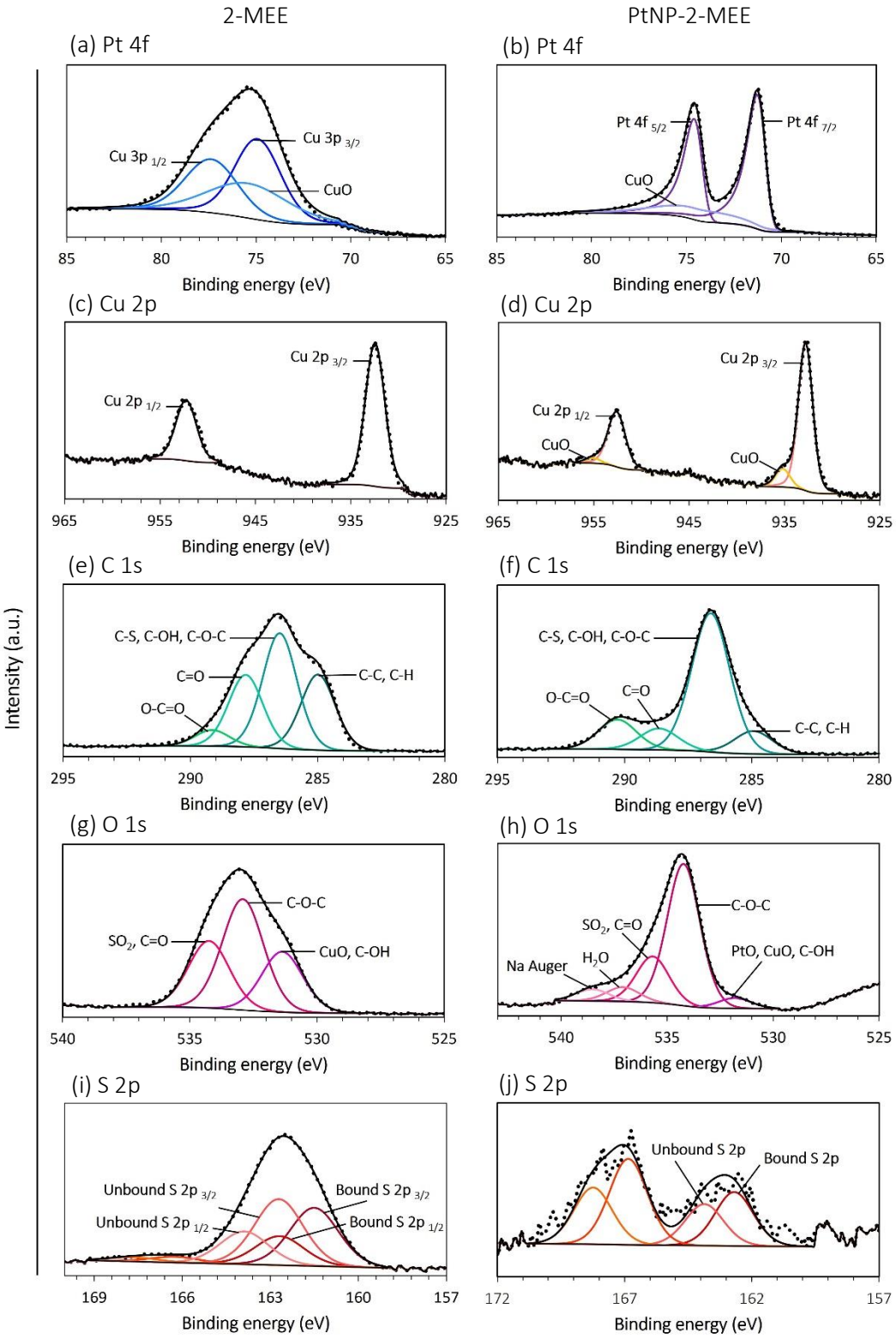

Figure 7.9 High resolution XPS spectra of 2-MEE and PtNP-2-MEE on a copper substrate. (a) Pt 4f –2-MEE, (b) Pt 4f - PtNP-2-MEE, (c) Cu 2p - 2-MEE, (d) Cu 2p – PtNP-2-MEE, (e) C 1s – 2-MEE, (f) C 1s – PtNP-2-MEE, (g) O 1s – 2-MEE, (h) O 1s – PtNP-2-MEE, (i) S 2p – 2-MEE and (j) S 2p – PtNP-2-MEE, (n=1).

The high-resolutions scans of Cu 2p for 2-MEE detected two Cu 2p peaks, Cu $2p_{3/2}$ at 932.5 eV and Cu $2p_{1/2}$ at 952.3 at eV with a separation of 19.8 eV, as illustrated in Figure 7.9 (c). Comparable binding energies were observed in the Cu 2p high-resolution scans of PtNP-2-MEE as shown in Figure 7.9 (d); Cu $2p_{3/2}$ at 932.8 eV and Cu $2p_{1/2}$ at 952.6 eV with a separation of 19.8 eV. Within the Cu 2p peaks, CuO peaks were also detected with at 935.2 eV and 955 eV. The binding energies of Cu 2p peak from both 2-MEE and PtNP-2-MEE accordance with literature,[146, 147] and are attributed to the copper substrate.

Deconvolution of the high-resolution scan of C 1s for 2-MEE revealed six carbon species as shown in Figure 7.9 (e); C-C, C-H at 285 eV, this was preceded by C-S, C-OH, C-O-C at 286.5 eV, C=O at 288 eV and O-C=O 289 eV. C-C, C-H, C-O-C and C-S ascribes to the PEGylated thiol chain and the carbon-thiol bond respectively, while C-OH ascribed to the hydroxyl functional head group. These carbon species have similar binding energies to those in literature.[146, 159, 171] The carbon species C-C, C-H, C-OH, C=O and O-C=O are also attributed to adventitious carbon contamination as these carbon species were also detected on the blank copper substrate in section 4.2.5. The high-resolution scan of C 1s for PtNP-2-MEE also revealed the same six carbon species, as shown in Figure 7.9 (f), C-C, C-H at 285 eV, followed by C-S, C-OH, C-O-C at 286.7 eV, C=O at 288.7 eV and O-C=O 290.4 eV. Again, these species carbon have similar binding energies to those in literature.[146, 159, 171] These binding energies were comparable to those detected in 2-MEE. The carbon species C-C, C-H, C-O-C and C-S are attributed to the PEG thiol chain and the carbon-thiol bond respectively and C-OH is attributed to the hydroxyl functional head group. The C-C, C-H, C-OH, C=O and O-C=O carbon species are presumed to be

a result of the citrate ion capping of the PtNPs and adventitious carbon. This suggests citrate ions were still present on the PtNP surface, this was confirmed by the Na Auger peak in Figure 7.9 (f). Furthermore, these carbon species were also detected on the blank copper substrate on the copper substrate in section 4.2.5, thus these species are result of both citrate ions and adventitious carbon.

Examination of the high-resolution scans of O 1s for 2-MEE detected five oxygen species, CuO, C-OH at 532.5.7 eV, C-O-C at 531.4 eV and SO_2, C=O at 535.6 eV, as illustrated in Figure 7.9 (g). CuO ascribes to the copper substrate, C-OH and C-O-C are attributed to the PEGylated thiol. SO_2 corresponds to an oxidised sulphur specie from the thiol, see Figure 7.9 (i). The remaining oxygen species C=O is attributed to adventitious oxygen contamination. These peaks correspond to those in literature.[146] The high-resolution scans of O 1s for PtNP-2-MEE detected seven oxygen species, see Figure 7.9 (h). PtO, CuO and C-OH at 531.1 eV preceded by C-O-C at 533.1 eV, SO_2, C=O at 534.3 eV, H_2O at 536.1 eV and a Na Auger peak at 537.6 eV. These oxygen species have comparable binding energies to those found in literature.[145, 146] PtO and CuO are attributed to the PtNPs and copper substrate; C-OH and C-O-C corresponds to the PEGylated thiol. SO_2 ascribes to oxidised sulphur specie from the thiol, see Figure 7.9 (j). Again, C=O is attributed to adventitious oxygen contamination, however a Na Auger peaks indicates the presence of citrate ions from the PtNPs. Citrate ions possess C=O in their carboxylic acid groups, thus the C=O is a result of both citrate ions still present on the PtNP surface and adventitious oxygen.

Upon examination, the high-resolution scan of S 2p for PtNP-2-MEE revealed two integrated doublets with a 2:1 area ratio, with a separation of 1.18 eV as presented in Figure 7.9 (i). The first doublet observed bound S $2p_{3/2}$ at 161.5 eV and S $2p_{1/2}$ 162.7 eV demonstrating a thiol-copper bond. Unbound S 2p was detected at S $2p_{3/2}$ at 162.7 eV and S $2p_{1/2}$ at 163.9 eV and these data were similar to those obtained using gold surfaces.[160] The bound sulphur is ascribed to the platinum-thiol bond, while unbound sulphur is likely a result of physisorbed 2-MEE; sulphur binding to the copper substrate was observed in chapter 4 with 6-MHA, 8-MOA, TA and 2-MOHA. Additionally, SAM formation by alkanethiols on copper substrates for corrosion and wettability studies also observed copper-thiol binding. [34, 161, 162] Two small sulphur oxide species were found at 166.3 eV and 167.7 eV.

The high-resolution scan of S 2p presented in Figure 7.9 (j) demonstrates a low signal to noise ratio, therefore, was fitted with one doublet peak with a 2:1 area ratio as shown in Figure 7.9 (j). Single doublet fitting of S 2p have previously been presented by Castner[160], where thiols and disulphides were investigated on gold substrates using XPS. Bound S $2p_{3/2}$ was detected at 162.7 eV while the unbound S $2p_{1/2}$ was detected 163.9 eV. The bound sulphur is ascribed to the platinum-thiol bond, while unbound is likely due to physisorbed 2-MEE. However, two large sulphur oxide species were also detected at 166.9 eV and 168.2 eV. A possible explanation for these sulphur oxide species is that oxide although 2-MEE and PtNP-2-MEE were prepared and submitted for XPS at the same, they were not subjected to XPS within a short time of its preparation, therefore, the samples may be oxidised. Furthermore, prior to sample deposition, all copper substrates used for XPS analysis were treated with hydrogen gas to reduce oxide

layer, see chapter 3, Materials and Methods section 3.4.5.1. The % of bound and unbound S 2p was derived from the area of the peak fittings using the CasaXPS software from two scans, this is presented in Table 7.1. The % of bound and unbound S 2p for 2-MEE on the copper substrate was 39.6% and 55.6% respectively, thus, 2-MEE had bound to the copper substrate via chemisorption. Conversely, PtNP-2-MEE had 26.5% the unbound S 2p and 16.3% bound S 2p, therefore demonstrating 2-MEE had chemisorbed onto the PtNP surface. The % of bound S 2p decreased compared to PtNP-8-MOA and PtNP-TA in chapter where an increase in bound S 2p was observed. This difference is due to the presence of the two sulphur oxide species. Furthermore, the % of bound and unbound S 2p could be disputed as not reliable as the high-resolution scan of S 2p for PtNP-2-MEE demonstrates a low signal to noise ratio, thus, the % of bound sulphur in this sample does not reliably reflect the % of bound and unbound S 2p.

Table 7.1 -% of bound and unbound S 2p in 2-MEE and PtNP-2-MEE.

	2-MEE	PtNP-2-MEE
% of S 2p bound	39.6	26.5
% of S 2p unbound	55.6	16.3

This XPS data confirms the PtNPs were present on the copper substrate, the presence of carbon and oxygen species attributed to the structure 2-MEE in both samples, however these were masked by the presence adventitious carbon and oxygen. The sulphur XPS spectra of 2-MEE confirmed a copper-thiol bond via chemisorption of 2-MEE onto the copper substrate. Though the XPS spectra of PtNP-2-MEE demonstrates a platinum-thiol, the S 2p XPS shows a low signal to noise ratio, additionally, there are two sulphur oxide species detected. Furthermore, the presence of the Na Auger peak indicated citrate ions were still present on the PtNP surface,

which supports the zeta potential data where the surface charge of PtNP-2-MEE was not near neutral, therefore, PtNP-2-MEE is only partially functionalised. This data supports previous data reported by Dinkel et al.[39] where the ligand exchange of citrate capped AuNPs for 3-MPS was found to be a 49% displacement. Thus, this study reports the partial functionalisation 2-MEE on c-PtNPs.

7.2.5 PtNP functionalisation with 11-(Mercaptoundecyl)hexa(ethylene glycol)

In addition to 2-MEE, 20 nm c-PtNPs were also functionalised with the neutrally charged PEGylated thiol 11-(Mercaptoundecyl)hexa(ethylene glycol) (11-MUHEG). 11-MUHEG was selected to assess if there was any difference using longer PEGylated thiols molecule. The structure of 11-MUHEG is illustrated in Figure 7.10, 11-MUHEG exhibits a terminal hydroxyl group (-OH) functional group, a mercapto group (-SH), an 11-carbon alkane chain and eight PEG units (-C-C-O). PtNP surface modified by 11-MUHEG will be referred to as PtNP-11-MUHEG throughout this thesis.

Figure 7.10 Structure of 11-(mercaptoundecyl)hexa(ethylene glycol) (11-MUHEG).

Following the method described in section 5.2.2, 20 nm c-PtNPs were functionalised by ligand exchange where the citrate ion capping of the PtNPs are exchanged for 11-MUHEG, the overall ligand exchange is displayed in Figure 7.11. The concentration of 11-MUHEG required for surface coverage was determined using the PEGylated thiol footprint of 0.35 nm^2 from literature,[169] which was 3.5 µM, see Appendix 11.2 for calculations.

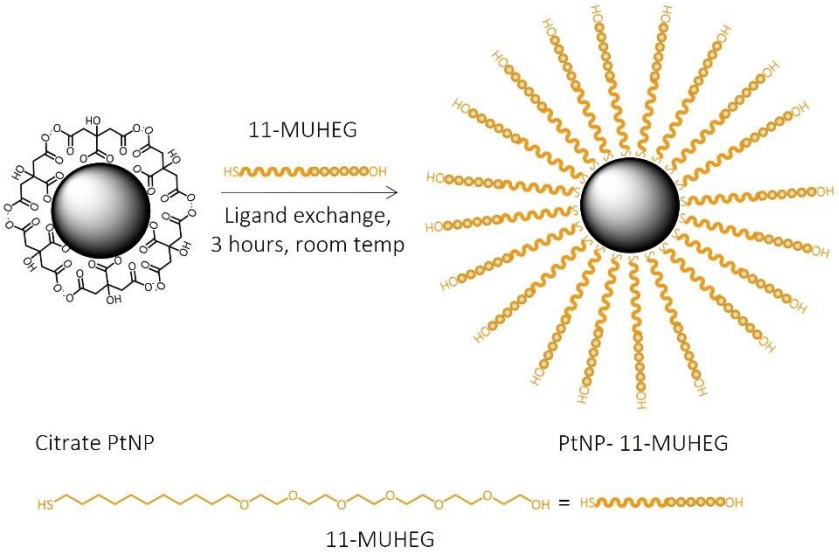

Figure 7.11 Ligand exchange of citrate ions on 20 nm c-PtNPs by 11-MUHEG. Note figure not to scale.

For gel electrophoresis, 20 nm c-PtNPs were surface modified with 3 µM and 70 µM 11-MUHEG following the method above up to the discarding step. 1 µL of concentrated 3 µM and 70 µM PtNP-11-MUHEG were then premixed with 15 µL glycerol and separated on a 1% agarose gel submerged in TAE buffer and concentrated c-PtNPs were used as a control. The DLS, zeta potential and pH experiments were repeated across three batches of 20 nm c-PtNPs. Five DLS and zeta potential measurements were performed to obtain the mean for each sample, data is presented as mean ± SD.

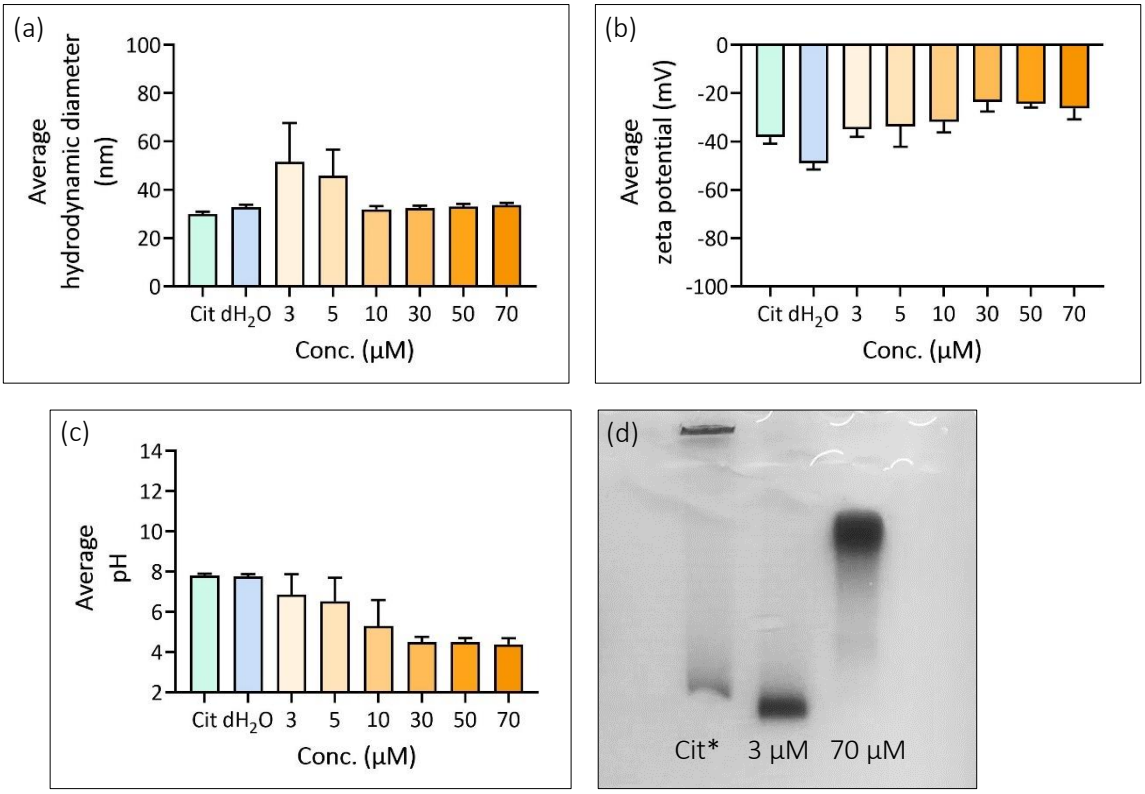

*Figure 7.12 Characterisation of PtNP-11-MUHEG. (a) hydrodynamic diameters, (b) zeta potentials (c) pH and (d) gel electrophoresis. Results (except electrophoresis) are representative of 3 experiments (n=3) and presented as mean ± SD. Note *: overspill*

Figure 7.12 (a) displays the hydrodynamic diameters of PtNP-11-MUHEG, the citrate and dH_2O controls had hydrodynamic diameters of 30.1 ± 0.9 and 32.9 ± 1.0 nm respectively. The hydrodynamic diameters of PtNP-11-MUHEG increased at 3 µM and 5 µM of 11-MUHEG to 51.6 ± 16.1 nm and 45.9 ± 10.8 nm respectively. However, the remaining concentrations had similar hydrodynamic diameters ranging from 32 to 33.7 nm. This increase in hydrodynamic diameter was previously observed with 5 µM and 10 µM PtNP-8-MOA in section 5.2.4. This increase in hydrodynamic diameter could be a result of the PtNP aggregating during ligand exchange, when the citrate ions are being displaced by 11-MUHEG the PtNP core surface is exposed, aggregates can form with neighbouring nanoparticles if the thiol molecule does not

bind to PtNP surface. These aggregates give large hydrodynamic diameters compared with individual nanoparticles, furthermore they may project a non-spherical shape and the DLS technique assumes all particles measured are spherical. Thus, the hydrodynamic diameter of these particles will appear larger than expected.

The zeta potentials of PtNP-11-MUHEG are demonstrated in Figure 7.12 (b), the c-PtNPs and dH_2O control which had zeta potentials of -38.2 ± 2.7 mV and -48.9 ± 2.6 mV respectively. The zeta potential of PtNP-11-MUHEG followed a similar trend to that of PtNP-2-MEE; The concentration of 11-MUHEG increased the zeta potential of PtNP-11-MUHEG from -35 to -23.6 mV, thus indicating a ligand exchange has occurred between the citrate ions and 11-MUHEG. Albeit the functional head group is neutrally charged, the zeta potential of PtNP-11-MUHEG exhibits a negative charge. Normally PEGylated nanoparticles exhibit zeta potentials in the range of -2.7 to -4.6 mV.[121] This difference suggests there are still citrate ions present on the surface of the PtNPs with 11-MUHEG, therefore, this would explain why the zeta potential of PtNP-11-MUHEG does not fall into the same range as other PEGylated molecules on nanoparticles. XPS analysis would be required to verify the presence of the citrate ions on the PtNP surface.

Additionally, ligand exchange was taking place was also confirmed by the pH of the PtNP-11-MUHEG solutions after purification, see Figure 7.12 (c). The pH of PtNP-11-MUHEG decreased with increasing concentrations of 11-MUHEG from pH 6.9 to 4.4 in comparison to the pH of the citrate control and dH_2O control which both remained at pH 7.8. This difference in pH could

possibly be due to 11-MUHEG having a lower pH than the sodium citrate, therefore, as the concentration of 11-MUHEG increased the pH decreased.

Gel electrophoresis of PtNP-11-MUHEG further confirmed ligand exchange had taken place, as presented in Figure 7.12 (d). 3 µM and 70 µM of 11-MUHEG were selected for gel electrophoresis to examine if there was a difference in surface coverage. The c-PtNPs control aggregated in the well due to their electro stabilisation by the citrate ions. The c-PtNPs also shows a faint band migrated through the agarose gel; this is due to a small overspill from the neighbouring well with 3 µM PtNP-11-MUHEG. Both 3 µM and 70 µM PtNP-11-MUHEG migrated through the agarose gel. 3 µM PtNP-11-MUHEG had a smaller dark band, indicating fewer 2-MUHEG molecules had bound to the PtNP surface compared with 70 µM PtNP-11-MUHEG which had a larger dark band. Thus, at 70 µM 11-MUHEG more molecules of 11-MUHEG had bound to the PtNP surface. As observed with 70 µM PtNP-2-MEE, 70 µM PtNP-11-MUHEG also did not migrate to the same distance compared with 3 µM PtNP-11-MUHEG. As 11-MUHEG exhibits a neutral charge from the OH group and only a partial charge from the PEG units, at higher concentrations of 11-MUHEG, more OH and PEG units present on the PtNP surface. Hence, less charge was present from 70 µM 11-MUHEG and effected the migration on the agarose gel. Collectively, the DLS, zeta potential, pH and gel electrophoresis data indicate a ligand exchange has occur. Next, to confirm 11-MUHEG has bound to the PtNP, the platinum-thiol bond was investigated by XPS.

7.2.6 XPS of 20 nm PtNP-11-MUHEG

To confirm if 11-MUHEG had bound to the PtNP surface, XPS was performed to examine the elemental composition of PtNP-11-MUHEG. 11-MUHEG was selected as control sample, the control sample was prepared by directly drop casting 11-MUHEG onto the copper substrate and air dried. Following the method described in 5.2.2, 20 nm c-PtNPs were surface modified with 70 µM of 11-MUHEG for 3 hours at room temperature. 70 µM 11-MUHEG was used for XPS analysis as this concentration demonstrated the greatest increase in zeta potential as displayed in Figure 7.12 (b). The excess 11-MUHEG and citrate ions were removed by centrifuging the sample at 10000 x g for 10 minutes, the supernatant was discarded, and the concentrated PtNP-11-MUHEG were drop cast onto the copper substrate, air dried and submitted for XPS analysis. 11-MUHEG and PtNP-11-MUHEG were charge corrected to 285 eV to enable comparison with the polymer handbook.[171] As adventitious carbon and oxygen contamination are common artefacts of XPS found in high-resolution scans, the high-resolutions scan only be used to identify species on the surface of the PtNPs.

Survey scans of 11-MUHEG and PtNP-11-MUHEG detected the presence of Pt, Cu, C, O and S elements. Investigation of the high-resolution scans of 11-MUHEG and PtNP-11-MUHEG detected signals from Pt 4f, Cu 2p, C 1s, O 1s and S 2p orbitals, these are presented in Figure 6.13. As expected, the high-resolution scans of Pt 4f for 11-MUHEG did not detect the presence of Pt 4f. Three Cu 3p peaks were detected, Cu $3p_{3/2}$ at 74.3 eV, Cu $3p_{1/2}$ at 75.6 eV and CuO at 75.6 eV, see Figure 7.13 (a). Previously in section 3.2.5, Cu 3p peaks ascribed to the blank copper substrate were detected in the Pt 4f region , as they have similar binding energies.[144]

PtNP-11-MUHEG exhibited the typical asymmetric doublet peak attributed to the PtNPs, Pt 4f $_{7/2}$ at 70.9 eV and Pt 4f $_{5/2}$ at 74.2 eV with a separation of 3.33 eV as shown in Figure 7.13 (b). These peaks are characteristic for platinum and are comparable to those in literature.[146] [145] CuO peak attributed to the copper substrate was present at 74.6 eV.

The high-resolution scans of Cu 2p for both 11-MUHEG and PtNP-11-MUHEG are illustrated in Figure 7.13 (c) and (d) respectively. 11-MUHEG exhibited a doublet peak, Cu 2p $_{3/2}$ at 931.7 eV and Cu 2p $_{1/2}$ at 951.5 eV, these peaks had a separation of 19.8 eV. CuO was also detected within the doublet peak, at 933. eV and 952.8 eV. PtNP-11-MUHEG also presented a doublet with comparable binding energies, Cu 2p $_{3/2}$ at 932 eV and Cu 2p $_{1/2}$ 951.8 eV with a separation of 19.8 eV. Again, CuO was also detected within the Cu 2p peaks at 935 eV and 954.1 eV. The Cu 2p and CuO peaks are attributed to the copper substrate.

Examination of the high-resolution scans of C 1s for 11-MUHEG revealed six carbon species as demonstrated in Figure 7.13 (e); C-C, C-H at 285 eV, preceded by C-S, C-OH, C-O-C at 286.5 eV, C=O at 287.8 eV and O-C=O 289 eV. The C-C, C-H, C-O-C and C-S species are attributed to the PEGylated thiol chain and the carbon-thiol bond respectively, while C-OH ascribes to the hydroxyl functional head group. C-C, C-H, C-OH, C=O and O-C=O are also detected on the blank copper substrate in section 3.2.5; hence these species are also attributed adventitious carbon. The same six species were presented in the high-resolution scans of C 1s for PtNP-11-MUHEG see Figure 7.13 (f). As follows, C-C, C-H at 285 eV, followed by C-S, C-OH, C-O-C at 286.8 eV, C=O at 288.8 eV and O-C=O 290.4 eV. These carbon species had comparable binding energies

to those detected in 11-MUHEG. C-C, C-H, C-O-C and C-S attributed to the PEGylated thiol chain and the carbon-thiol bond respectively and C-OH is attributed to the hydroxyl functional head group. However, the C-C, C-H, C-OH, C=O and O-C=O species correspond with adventitious carbon contamination. The carbon species present in 11-MUHEG and PtNP-11-MUHEG are comparable to those in literature.[146, 159, 171]

Devolution of the high-resolution scans of O 1s for 11-MUHEG revealed five oxygen species, CuO, C-OH at 531 eV, 533.1 eV and C-O-C, C=O, SO_2 at 534.5 eV, as shown in Figure 6.13 (g). CuO is attributed to the copper substrate, C-OH and C-O-C are attributed to the PEGylated thiol, and SO_2 corresponds to an oxidised sulphur species from the thiol. The oxygen specie C=O is attributed to adventitious oxygen contamination. These oxygen peaks are comparable to those reported in literature.[146] The high-resolution scans of O 1s for PtNP-11-MUHEG detected seven oxygen species, see Figure 7.13 (h); PtO, CuO and C-OH at 530.1 eV preceded by C-O-C at 533.2 eV, SO_2, C=O at 534.9 eV, H_2O at 536.7 eV and a Na Auger peak at 537.9 eV. PtO and CuO are attributed to the PtNPs and copper substrate; C-OH and C-O-C corresponds to the PEGylated thiol. SO_2 ascribes to oxidised sulphur species from the thiol. Again, C=O is attributed to adventitious oxygen contamination, however a Na Auger peaks indicates the presence of citrate ions from the PtNPs. Citrate ions possess C=O in their carboxylic acid groups, thus the C=O is a result of both citrate ions still present on the PtNP surface and adventitious oxygen.

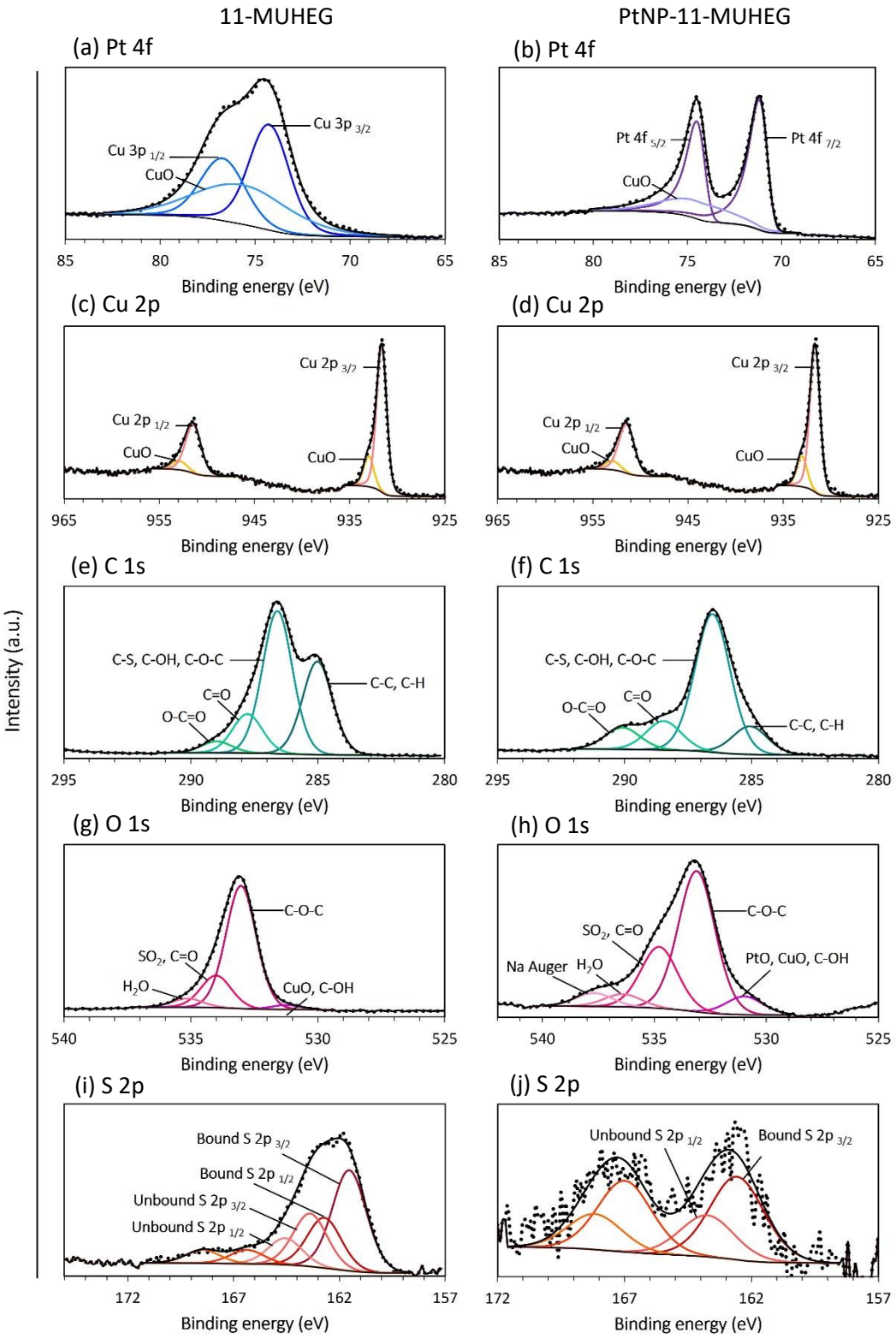

Figure 7.13 High resolution XPS spectra of 11-MUHEG and PtNP-11-MUHEG on a copper substrate. (a) Pt 4f –11-MUHEG, (b) Pt 4f - PtNP-11-MUHEG, (c) Cu 2p - 11-MUHEG, (d) Cu 2p – PtNP-11-MUHEG, (e) C 1s – 11-MUHEG (f) C 1s – PtNP-11-MUHEG, (g) O 1s – 11-MUHEG, (h) O 1s – PtNP-11-MUHEG, (i) S 2p – 11-MUHEG and (j) S 2p – PtNP-11-MUHEG, (n=1).

Interpretation of the high-resolution scans of S 2p for 11-MUHEG observed two intercalated doublets with a 2:1 area ratio, with a separation of 1.18 eV, as illustrated in Figure 7.13 (i). Bound S 2p was present at 161.5 eV and 162.7 eV, while the unbound S 2p was present at 163.4 eV and 164.6 eV, these binding energies are in accordance with literature.[146, 160] The bound sulphur is ascribed to the copper-thiol bond, while unbound is likely due to physisorbed 11-MUHEG. The copper-thiol bond was also observed with 2-MEE, 6-MHA, 8-MOA and TA, furthermore these results are similar to those in early work investigation SAM formation by alkanethiols on copper substrates for wettability and corrosion studies.[34, 161, 162] Additionally, two sulphur oxide species at 166.4 eV and 168.4 eV, these are likely due to the oxidation of the sample. The high-resolution scan of S 2p for PtNP-11-MUHEG revealed a single doublet peak with a 2:1 area ratio, with a separation of 1.18 eV, as shown in Figure 7.13 (j). This was similar to the high-resolution scan of S 2p for PtNP-2-MEE, as there was a low signal to noise ratio and sulphur oxide species only one doublet could be fitted. Bound S 2p was detected at 161.1 eV and unbound S 2p was detected at 164.7 eV, these binding energies are in accordance with literature.[146, 160] The bound S 2p is attributed to the platinum-thiol, therefore 11-MUHEG bound to the surface of the PtNPs via chemisorption, while the unbound S 2p suggests 11-MUHEG physisorbed onto the surface. Two sulphur oxide species were also detected 166.9 eV and 168.2 eV, these sulphur oxide species are similar to those found in literature.[145, 160, 206] The presence of these sulphur oxide species is likely due to the oxidation of samples. Both 11-MUHEG and PtNP-11-MUHEG were prepared and submitted for XPS at the same, they were not subjected to XPS within a short time of its preparation, hence the samples may be oxidised, and sulphur oxide species were detected in the high-resolution scan for 11-MUHEG and PtNP-11-MUHEG. As previously mentioned, prior to sample deposition, all copper substrates used

for XPS analysis were treated with hydrogen gas to reduce oxide layer, see chapter 3, Materials and Methods section 3.4.5.1.

Although sulphur oxide species were detected in both 11-MUHEG and PtNP-11-MUHEG, the % bound and unbound S 2p was calculated. The % of bound and unbound S 2p was obtained from the area of the peak fittings using the CasaXPS software from two scans, this is presented in Table 7.2. The % of bound and unbound S 2p for 11-MUHEG on the copper substrate was 59.9% and 30.6% respectively, thus, 11-MUHEG had bound to the copper substrate via chemisorption forming a copper-thiol bound. Contrarily, in the PtNP-11-MUHEG sample, % of bound S 2p decreased to 33.9% and the unbound further decreased to 17%, as observed with PtNP-2-MEE. A possible explanation for the decrease in bound S 2p is the oxidation of the sample which is evident by the sulphur oxide species at higher binding energies. Although, some this data indicates some 11-MUHEG has bound to the PtNP, the low signal to noise ratio does not give confidence that this the true % of bound S 2p.

Table 7.2 -% of bound and unbound S 2p in 11-MUHEG and PtNP-11-MUHEG.

	11-MUHEG	PtNP-11-MUHEG
% of S 2p bound	59.9	33.9
% of S 2p unbound	30.6	17

These XPS data confirm the PtNP were present on the copper substrate, carbon and oxygen species attributing to 11-MUHEG were detected but also masked due to the presence adventitious carbon and oxygen. The sulphur XPS spectra of 11-MUHEG and PtNP-11-MUHEG

supports that 11-MUHEG has bound to the PtNP surface via chemisorption, thus a platinum-thiol bond was formed via covalent interactions. However, the Na Auger peak indicated citrate ions were still present on the PtNP surface, which is also supported by the zeta potential data in Figure 7.12 (b). Thus, this study demonstrates the partial functionalisation of c-PtNPs by 11-MUHEG. Partial functionalisation of citrated capped AuNPs have previously been reported with 3-MPS via the ligand exchange method.[39]

7.3 Conclusion

The present study demonstrated that the hydroxyl-terminated neutrally charged alkanethiol 6-MCH was unable to functionalise 20 nm c-PtNPs by ligand exchange or nanoparticle synthesis, potentially due to the lack of deprotonation of the 6-MCH molecule. 20 nm c-PtNPs were partially functionalised by the hydroxyl-terminated neutrally charged PEGylated thiols 2-MEE and 11-MUHEG via ligand exchange. DLS did not show changes in hydrodynamic diameter for PtNP-2-MEE, while PtNP-11-MUHEG demonstrated some aggregated nanoparticles. The zeta potential and pH demonstrated ligand exchange had taken place in both PtNP-2-MEE and PtNP-11-MUHEG, but was not completely displaced, thus, some citrate ions remained on the PtNP surface. Gel electrophoresis demonstrated the largest physical differences between c-PtNPs and PtNP-2-MEE and PtNP-11-MUHEG, this additionally supported a ligand exchange had taken place between the citrate and the PEGylated thiol molecules. The XPS analysis confirmed the platinum-thiol bound in both PtNP-2-MEE and PtNP-11-MUHEG, but some citrate was still present on the surface of the PtNP. Moreover, the presence of the oxidised sulphur species in both samples does not give confidence the amount of thiol bound on the PtNP surface. Finally,

this study is the first to report the partially functionalisation of c-PtNPs by PEGylated thiols 2-MEE and 11-MUHEG via ligand exchange.

7.4 Further work

Despite 6-MCH not demonstrating ligand exchange by DLS and zeta potential, XPS would demonstrate if any 6-MCH had bound to the PtNP surface by assessing the platinum-thiol bound. Gel electrophoresis would also confirm if a ligand exchange had occurred; if no ligand exchange took place the PtNPs would aggregate in the wells. While ligand exchange was performed at 3 hours with 2-MEE and 11-MUHEG, extending the incubation time with these PEGylated thiols would potentially allowing more displacement of citrate ions and chemisorption onto the PtNP surface. By characterising the ligand exchange by at different incubations time would provide insight on how the surface charge changes along with the % of bound thiol on the PtNP surface. Finally, both PtNP-2-MEE and PtNP-11-MUHEG could also be assessed for stability by measuring the hydrodynamic diameter and zeta potential over several weeks and months.

Chapter 8 Platinum Nanoparticle Human Platelet Interactions

Abstract: This chapter examines the effect of the platinum nanoparticles (PtNPs) functionalised with a negative charge and neutral charge on human platelets. To investigate whether the functionalised PtNPs are suitable for platelet investigations, their hydrodynamic diameter and surface charge was assessed directly in the platelet physiological buffer with Tyrodes-HEPES buffer. PtNPs functionalised by the alkanethiols were found to be unstable in Tyrodes-HEPES buffer resulting in increased hydrodynamic diameters and surface charges. Conversely, PtNPs functionalised by PEGylated thiols O-(2-carboxyethyl)-O'-(2-mercaptoethyl) heptaethylene glycol (2-MOHA), 2-[2-[2-(2-mercaptoethoxy)ethoxyethoxy}ethanol (2-MEE), and 11-(mercaptoundecyl)hexa(ethylene glycol) (11-MUHEG) were found to be stable in Tyrodes-HEPES buffer. c-PtNPs (negatively charged), PtNP-2-MOHA (negatively charged) and PtNP-11-MUHEG (neutrally charged) were assessed for platelet function by light transmission aggregometry (LTA). PtNPs stimulated platelet aggregation in washed platelets, however, PtNP-2-MOHA and PtNP-11-MUHEG did not stimulate platelet aggregation. Platelet activation by the PtNPs was found not to be mediated through the platelet surface receptor glycoprotein VI (GPVI). The mechanism of platelet activation could not be fully elucidated. PtNPs also did not stimulate platelet aggregation in platelet rich plasma (PRP), presumably due to plasma binding to the PtNPs. Pre-incubation of PtNPs (including functionalised PtNPs) with commercial human mixed plasma demonstrated an increase in hydrodynamic diameters and zeta potentials, thus, indicating the formation of a protein corona.

8.1 Introduction

Nanoparticles can be engineered to exhibit different physicochemical properties such as size, shape, and surface charge to enable a plethora of applications.[207-210] PtNPs are of particular importance, they demonstrate high catalytic properties and are utilised in catalytic converters, they are also the main catalyst for proton exchange membrane fuel cells (PEMFC) in automotives.[17, 78] However, their degradation may pose a health risk if they come off the PEMFC and are able gain access to the blood stream via inhalation.[16, 73, 211] Once in the blood stream, they can encounter the complex environment of plasma proteins and blood cells, which include platelets. Platelets are crucial for vascular health, their primary role is to maintain haemostasis and thrombosis; nevertheless, excessive activation of platelets, which results in their aggregation, can be instrumental for thrombotic diseases which in turn can lead to a stroke or heart attack. Various nanoparticles including gold, silver, platinum, polystyrene, and diesel exhaust particles (DEP) have all been shown to stimulate platelet aggregation in isolated human platelets.[79, 87, 90, 91, 96, 101, 140] A common physicochemical property between these nanoparticles is surface charge, nanoparticles exhibiting different surface charges (negative and positive) have been shown to mediated platelet aggregation to varying degrees.[87, 105, 212] How these different surface charges on the nanoparticles surface interact with platelet surface receptors is poorly understood. Attention should be drawn specifically to PtNPs as they have imperative roles in catalytic converters and PEMFC,[17, 78] which could pose potential health risk. To date, only one study has investigated the effects of PtNPs on human platelets. Zia et al.[90] demonstrated platelet activation by PtNPs (citrated) was dependent on their surface area and not size of the nanoparticles. The effect of surface charge on PtNPs has not been investigated

and warrants further investigation to elucidate how different surface charges can mediate platelet activation which results in platelet aggregation.

8.1.1 Objectives:

1. Examine the functionalised PtNPs (negatively charged and neutrally charged) with Tyrodes-HEPES buffer. Characterise by DLS and zeta potential.

2. Assess platelet aggregation using human washed platelets with functionalised PtNPs using LTA.

3. Investigate the mechanism of platelet activation by inhibitory studies using LTA and western blotting.

4. Assess platelet aggregation in platelet rich plasma with functionalised PtNPs using LTA.

5. Examine protein corona of functionalised PtNPs with human plasma. Characterise by DLS and zeta potential.

8.2 Results and Discussion

8.2.1 Interaction of functionalised 20 nm platinum nanoparticles in Tyrodes-HEPES buffer

In chapter 4, DLS and zeta potential confirmed that the electrostatically stabilised negatively charged 20 nm c-PtNP aggregated when exposed to the platelet physiological buffer Tyrodes-HEPES. To render these 20 nm c-PtNPs suitable for platelet experiments, they were functionalised/stabilised by alkane and PEGylated thiols to create sterically stable negatively charged PtNPs (carboxyl terminated, chapter 5) and neutrally PtNPs (hydroxyl terminated, charged chapter 7) see Table 8.1. Although XPS confirmed the presence of citrate ions on the PtNP surface after ligand exchange, these functionalised PtNPs were still utilised. By exhibiting different surface charges either negative or neutral, the effect of surface charge of 20 nm PtNP on platelet activation and aggregation can be investigated. Positively charged PtNPs (chapter 6) were not included as the functionalisation and synthesis methods produced unstable nanoparticles.

Table 8.1 Functionalised platinum nanoparticles.

Functionalised PtNP	Thiol name	Alkane or PEGylated thiol	Functional group	Surface charge	Zeta Potential (mV)
PtNP-6-MHA	6-mercaptohexanoic acid (6-MHA)	Alkane	COOH	Negative	-21.8
PtNP-8-MOA	8-mercaptooctanoic acid (8-MOA)	Alkane	COOH	Negative	-17
PtNP-TA	Thioctic acid (TA)	Alkane	COOH	Negative	-27.3
PtNP-2-MOHA	O-(2-carboxyethyl)-O'-(2-mercaptoethyl) heptaethylene glycol (2-MOHA)	PEGylated	COOH	Negative	-21.1
PtNP-2-MEE	2-[2-[2-(2-Mercaptoethoxy)ethoxyethoxy}ethanol (2-MEE)	PEGylated	OH	Negative	-23
PtNP-11-MUHEG	11-(Mercaptoundecyl)hexa(ethylene glycol) (11-MUHEG)	PEGylated	OH	Negative	-23.1

Prior to platelet function testing, the hydrodynamic diameter and surface charge of these functionalised PtNPs were examined in Tyrodes-HEPES buffer (see Table 3.4 in section 3.2.7 for its chemical constituents). Tyrodes-HEPES buffer is crucial for platelets ex vivo as the buffer enables osmotic buffering to the platelets. The DLS and zeta potential of the functionalised PtNPs (in dH_2O) were measured before and after exposure to the platelet physiological buffer Tyrodes-HEPES, as shown in Figure 8.1. As previously mentioned, although pH is not a characterisation technique per say, they were reported as zeta potential measurements are dependent on pH; changes in the pH of the nanoparticle solution can determine changes in the nanoparticle environment. 20 nm c-PtNP in 1.1 mM sodium citrate were used as control sample. For this experiment DLS and zeta potential measurements were performed once as the high salt concentration from the Tyrodes-HEPES buffer degraded the electrodes on the capillary cells used for zeta potential measurements. Five DLS and zeta potential measurements were performed to obtain the mean for each sample, data is presented as mean.

Figure 8.1 (a) demonstrates the hydrodynamic diameter of functionalised PtNPs, as expected the citrate coated PtNPs aggregated upon exposure to Tyrodes-HEPES buffer. The hydrodynamic diameter increased from 31.3 nm to 593.8 nm, this was similar to data previously obtained in section 4.2.6. During PtNP synthesis, the citrate ions physisorb onto the nanoparticle surface to form the electric double layer (EDL). The citrate ions in the Stern layer (inner layer) are strongly bound in comparison to those in the slipping layer (outer layer). These citrate ions are non-covalently bound to the PtNPs surface, though interaction is relatively weak, when exposed to Tyrodes-HEPES buffer, the electrostatic forces between the core PtNP

and citrate ions are disrupted by the high ionic salt concentrations and induces irreversible aggregation, thus, the aggregates exhibit large hydrodynamic diameters.

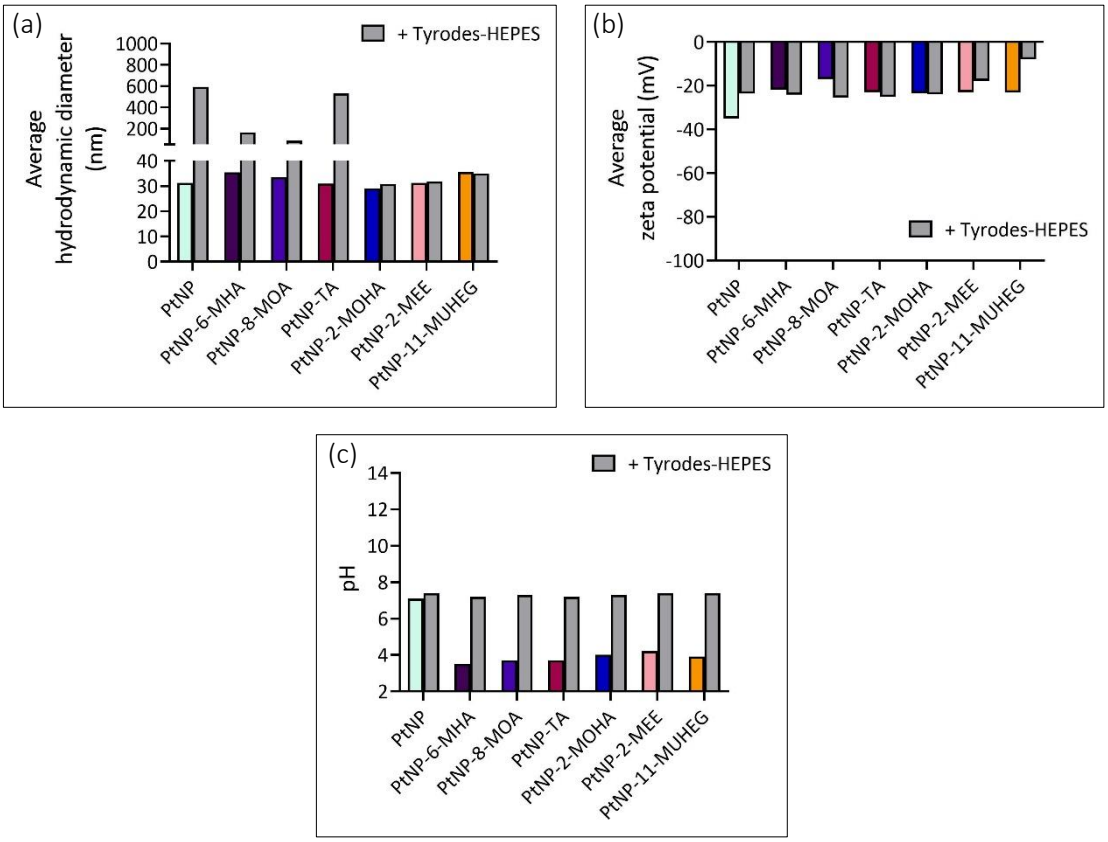

Figure 8.1 Functionalised PtNP with Tyrodes-HEPES buffer. (a) hydrodynamic diameters with Tyrodes-HEPES buffer, (b) zeta potentials with Tyrodes-HEPES buffer and (c) pH with Tyrodes-HEPES buffer. Results presented from 1 experiment (n=1).

Under exposure to the Tyrodes-HEPES buffer, the hydrodynamic diameters of PtNP-6-MHA, PtNP-8-MOA and PtNP-TA also increased. A possible explanation for this result is that the citrate ions that are still present on the surface of these functionalised PtNPs have been disrupted by the high salt concentration of the Tyrodes-HEPES buffer. The non covalently bound citrate ions would be displaced leaving the PtNP core exposed and prone to aggregation, hence, these

functionalised PtNPs aggregated. Interestingly, after exposure to Tyrodes-HEPES buffer the hydrodynamic diameters of PtNP-2-MOHA, PtNP-2-MEE and PtNP-11-MUHEG remained the same. This was expected as these PtNPs were functionalised by PEGylated thiols, PEG molecules are hydrophilic polymers that provide steric stability and can withstand high salt concentrations.[167, 168, 213]

The zeta potentials of the functionalised PtNPs before and after exposure to Tyrodes-HEPES buffer is presented in Figure 8.1 (b). As expected, the citrated PtNPs demonstrated an increase in zeta potential from -38.9 mV to -23.5 mV; this was comparable to the previous results in chapter 3, section 3.2.6. Additionally, previous work by Zia et al.[90] reported changes in zeta potential of PtNPs after exposure to Tyrodes buffer, PtNPs of 7 and 73 nm had zeta potentials of -59.3 and -52.3 mV in water respectively. In Tyrodes-HEPES buffer their zeta potentials increased to -20.8 and -22.4 mV. This difference is due the high ionic salt concentration of the Tyrodes-HEPEs buffer, as the citrate ions are non-covalently bound, high salt buffers can displace the citrate ions on the PtNP surface, therefore, reducing the citrate ions surrounding the PtNP surface, thus, leading to an increased the zeta potential.

Interestingly, of the functionalised PtNPs, PtNP-6-MHA, PtNP-TA and PtNP-2-MOHA had comparable zeta potentials before and after exposure to Tyrodes-HEPES buffer. A possible explanation for this occurrence could be that more thiol molecules had chemisorbed on the PtNP surface and the negatively charge from the carboxylic acid functional head group of these thiol molecules have created repulsive forces with the negatively charged ions from the

Tyrodes-HEPES. For PtNP-8-MOA the zeta potential decreased from -17 mV to -25.4 mV. In this instance, there could be more citrate ions present on the PtNP surface; these citrate ions were displaced by the Tyrodes-HEPES buffer, leading to aggregation, and therefore increasing the hydrodynamic diameter and a decrease in zeta potential.

By contrast, the zeta potential of the PtNPs functionalised by the neutrally charged PEGylated thiols 2-MEE and 11-MUHEG showed an increase in zeta potential in Tyrodes-HEPES buffer from -23 mV to -17.7 mV and -23.1 to -8 mV respectively. From the XPS analysis in chapter 7, it was confirmed that citrate ions were still present on the PtNPs after ligand exchange. When these neutrally charged PtNPs were exposed to the Tyrodes-HEPES buffer, the remain citrate ions on the PtNP surface were disrupted, this leads to a displacement of citrate ions, therefore the surface charge is reduced, this translates to an increased zeta potential.

The pH of the functionalised PtNPs are displayed in Figure 8.1 (c). The citrated PtNPs suspended in 1.1 mM sodium citrate buffer exhibited a pH of 7.1, in Tyrodes-HEPES buffer, the pH increased to pH 7.3 as the Tyrodes-HEPES buffer itself has a pH of 7.3. The pH of the PtNPs functionalised by negatively charged and neutrally charged thiols demonstrated a reduced pH in the acidic range after ligand exchange. The pH of all the functionalised PtNPs increased to physiological range pH 7.2 – 7.4 when measured in Tyrodes-HEPES buffer. From the results presented in Figure 8.1, the hydrodynamic diameters of the PtNPs functionalised by PEGylated thiols were able to withstand the high ionic salt concentration of the Tyrodes-HEPES buffer. PtNP-2-MOHA and PtNP-11-MUHEG were selected for platelet investigations as PtNP-2-MOHA

was negatively charged and PtNP-11-MUHEG was neutrally charged. Additionally, they had similar chain lengths, see Figure 8.2 for their chemical structures. A 10 mL aliquot of 20 nm PtNPs, PtNP-2-MOHA and PtNP-11-MUHEG were concentrated to 100 µL by centrifugation at 10000 x g to give a stock concentration of 5.9 mg/mL and final concentration of 59.2 µg/mL in the subsequent platelet experiments, Appendix 11.3.

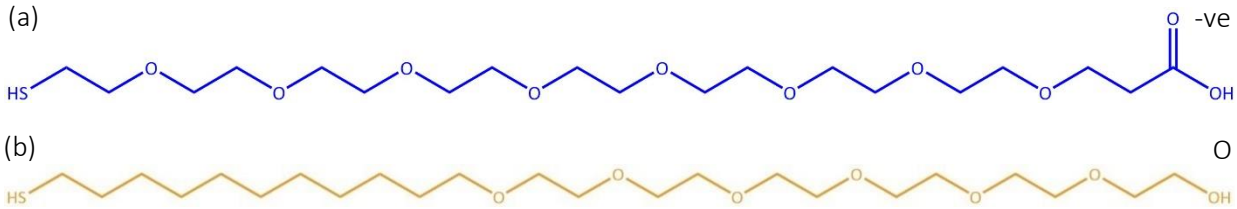

Figure 8.2 Structure of PEGylated thiols used to functionalise PtNPs. (a) O-(2-carboxyethyl)-O'-(2-mercaptoethyl) heptaethylene glycol (2-MOHA) and (b) 11-mercaptoundecyl)hexa(ethylene glycol) (11-MUHEG).

8.2.2 Human platelet aggregations with functionalised platinum nanoparticles

Platelet function was examined with PtNP-2-MOHA (negatively charged) and PtNP-11-MUHEG (neutrally charged) using conventional LTA on human isolated washed platelets. 20 nm c-PtNPs were used as controls, capping agent controls included sodium citrate, 2-MOHA and 11-MUHEG alone. Washed platelets were prepared from fresh whole blood donated by healthy volunteers on each day of the experiments. Whole blood was collected with 3.2% (w/v) sodium citrate, the anticoagulant acid citrate dextrose (ACD) was added to the blood in a 1:10 v/v ratio and centrifuged at 200 x g for 20 minutes at room temperature to obtain the platelet rich plasma (PRP). The PRP was centrifuged in the presence of 10 µg/mL prostacyclin (PGI_2) at 1000 x g for 10 minutes at room temperature. PGI_2 inhibits platelet activation, hence, it was added during centrifugation. The plasma was discarded leaving a platelet pellet; the pellet was re-

suspended in Tyrodes-HEPES buffer with ACD at a 1:8 v/v ratio. The platelets were centrifuged for a further 10 minutes at room temperature at 1000 x g with 10 µg/mL PGI_2. The supernatant was discarded, and the remaining platelet pellet was re-suspended in Tyrodes-HEPES buffer. These washed platelets were quantified on a Coulter counter and platelet concentration was adjusted with Tyrodes-HEPES buffer to either 2 x 10^8 platelets/mL for platelet aggregations or 4 x 10^8 platelets/mL for biochemical analysis by western blotting.

Platelet function was assessed by LTA, washed platelets were pre-warmed for 2 minutes at 37^oC in aggregation tubes with stir bars, platelets were then stirred for 1 minute at 1200 rpm before the addition of agonists/nanoparticles. Aggregations were then recorded for 5 minutes. The % aggregation was determined by measuring the height difference of the aggregation trace against the baseline and then calculating the % difference. Experiments were performed using 3 human donors, data was expressed as mean ± standard error of the mean (SEM). Platelet aggregation data was analysed using a one-way ANOVA with Bonferroni's post-hoc test or a Student T-test, a P value less than 0.05 was considered significant.

Initial platelet function was assessed with the control platelet agonist thrombin at final concentration 1U/mL. Thrombin is a serine protease that primarily catalyses fibrinogen to fibrin.[214] Additionally, thrombin activates platelets through the protease activated receptors (PAR1) and PAR4, thus it was used to assess platelet function.[214] Stimulation of washed platelets by 1 U/mL of thrombin gave 80.8 ± 5.4% aggregation as illustrated in Figure 8.3 (a), demonstrating the platelets had a strong response to thrombin.

Prior to stimulation by the c-PtNP, the baseline on the aggregometer was adjusted as c-PtNPs can absorb light from the aggregometer during measurements. Upon stimulation by the control c-PtNPs, an increase in light transmission was observed, demonstrating the platelets had aggregated, as shown in Figure 8.2 (b). By increasing the concentration of c-PtNP in a dose-dependent manner, more c-PtNP were available to interact with the platelets, thus, the % of platelet aggregation increased in a dose-dependent manner. At the highest concentration of 59.2 μg/mL of c-PtNPs the washed platelets aggregated to an average of 58.8 ± 14.3%. When interpreting this data, it is important to consider that c-PtNPs can absorb light from the aggregometer which can then be deflected, if this is the case, the aggregation observed may not be a true reflection of platelet aggregation by c-PtNPs. Previous experiments by Zia et al. 2018,[1] also observed platelet aggregation in washed platelets by c-PtNPs of 7 and 73 nm; an important finding of this study was that platelet aggregation was governed by the surface area of the nanoparticles. Additionally, these results are similar to those by Alshehri et al. 2015,[101] whereby aggregation was induced by DEP in dose-dependent manner in washed platelets. The concentration of DEP were similar to those used in this experiment. To assess if the citrate capping alone could cause aggregation, 11 μM of sodium citrate was tested on the washed platelets. This concentration was selected as this was final concentration of sodium citrate diluted with the platelets. Sodium citrate did not cause platelet aggregation, this was expected as sodium citrate is used as anticoagulant and can chelate with calcium ions (Ca^{2+}).

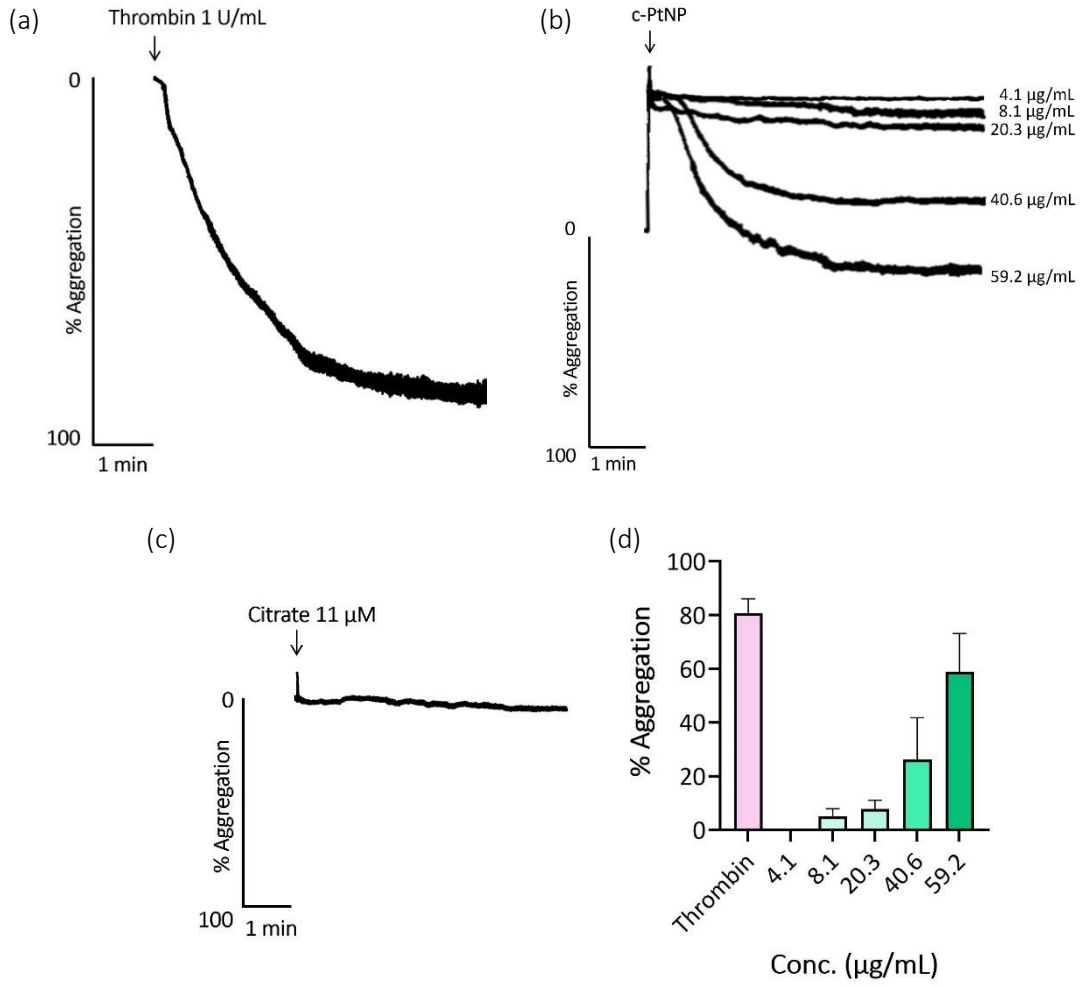

Figure 8.3 Human platelet aggregations with c-PtNPs. (a) representative control aggregation trace to 1U/mL Thrombin, (b) representative aggregation traces to c-PtNPs (4.1 – 59.2 µg/mL), (c) representative aggregation trace to sodium citrate 11 µM, (d) quantification of dose-response aggregations to c-PtNPs (4.1 – 59.2 µg/mL) presented as mean ± SEM. Results are representative of 3 experiments (n=3).

Although, the zeta potential data in section 8.2.1 demonstrated an increased surface charge from -34.8 to -23.5 mV, based on these values, it is indicated that citrates are still present on the PtNP surface and not all citrate ions were displaced. The degree of how much citrate ion capping was is displaced by the Tyrodes-HEPES buffer cannot be determined, it is likely that the citrate ions in the stern layer remain on the PtNP surface. It is presumed that platelet

aggregation could be a result of electrostatic interactions between the negatively charged citrate ions capping the PtNPs and the platelet surface receptors. Previous work by Alshehri et al.[101] revealed that washed platelets were activated by DEP through the transmembrane receptor glycoprotein VI (GPVI). It is well established that GPVI is the major signalling receptor for collagen on the surface of platelets and more recently fibrin.[215 216, 217] The structure of GPVI is shown in Figure 8.4. GPVI has two immunoglobulin (Ig) domains (D1, D2) which have a mixed surface charge, a mucin-like stalk which is rich in O-glycosylation site that has a negative surface charge. This is linked with the dimeric Fc receptor γ-chain (FcRγ) which includes the immunoreceptor tyrosine-based activation motif (ITAM) which is involved in the GPVI signalling cascade, which will be discussed later.[89, 216, 217] It is thought that the negative charge of the PtNPs has interacted with positive charges on the mixed surface charge of the D1 and D2 domain of the GPVI receptor.

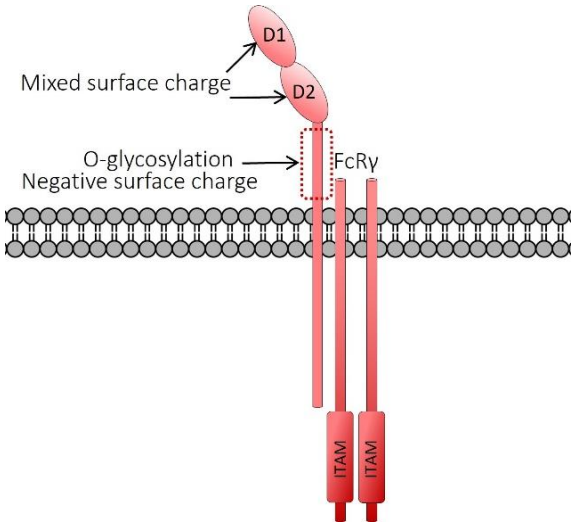

Figure 8.4 Structure of glycoprotein VI (GPVI).

Next, platelet function was assessed with PtNP-2-MOHA (negatively charged) and PtNP-11-MUHEG (neutrally charged). Stimulation by PtNP-2-MOHA at the maximum concentration of

59.2 µg/mL resulted in no change in light transmission, as shown in Figure 8.5 (a). One explanation for this could be the zeta potential, PtNP-2-MOHA had a zeta potential of 21.1 mV, see Table 8.1. If we compare this with c-PtNPs, the c-PtNPs had a higher (reduced) zeta potential of -34.9 mV. This difference suggests that PtNPs with high zeta potentials can interact with platelets causing them to activate and the aggregate. Conversely, PtNPs with low (increased) zeta potentials may not be able to interact with the platelets as there is not enough charge on the nanoparticle surface to interact with the platelets, therefore, no platelet activation and aggregation would occur.

Platelet aggregation could also be determined by measuring platelet aggregation in the presence of the GPIIb/IIIa antagonist eptifibatide. Additionally, P-selectin expression could be measured using flow cytometry and intracellular calcium release with the fluorescent dye fura-2-AM.

To test whether PtNP-2-MOHA is able to potentially block platelet aggregation, 1 U/mL of thrombin was added to the platelets and found to have a robust response, as shown in Figure 8.5 (a). The aggregation was repeated with 2-MOHA to ascertain whether the PEG thiol alone could cause platelet aggregation, however no platelet aggregation was observed. Potentially, the negative charge from the carboxylic acid functional head group of 2-MOHA and the polar charge from the PEG molecules is causing repulsion with the negatively charged ions constituting the Tyrodes-HEPES buffer.

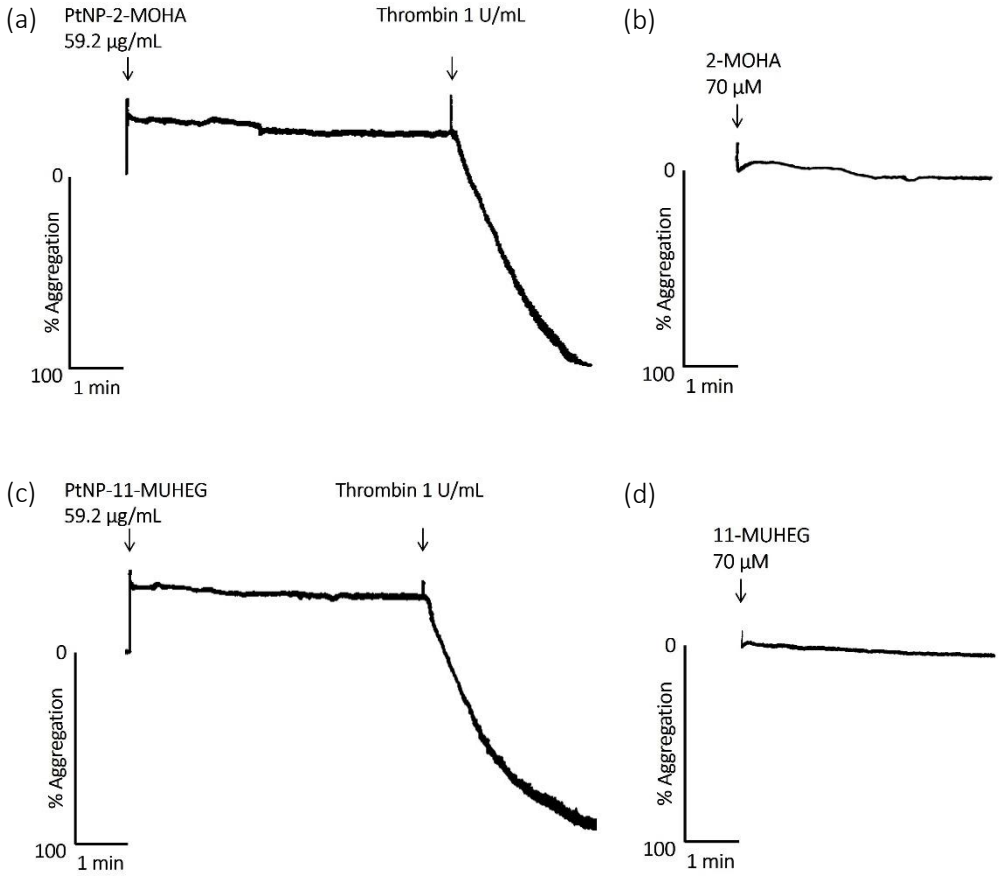

Figure 8.5 Human platelet aggregations with functionalised PtNP-2-MOHA and PtNP-11-MUHEG. (a) representative aggregation traces to PtNP-2-MOHA (59.2 µg/mL), (b) representative aggregation traces to 2-MOHA (70 µM), (c) representative aggregation traces to PtNP-11-MUHEG (59.2 µg/mL) and (d) representative aggregation traces to 11-MUHEG (59.2 µg/mL). Results are representative of 3 experiments (n=3).

Platelet function was also assessed with PtNP-11-MUHEG, as shown in Figure 8.5 (b). PtNP-11-MUHEG did not cause platelet aggregation. This was to be expected as the 11-MUHEG molecules carries a neutral charge from its hydroxyl functional head group, thus, it would not interact with the platelets. The zeta potential and XPS analysis of PtNP-11-MUHEG confirmed that citrate ions were still on the PtNP surface after ligand exchange, however the zeta potential

of PtNP-11-MUHEG was low at -23.1, as demonstrated by PtNP-2-MOHA, this would not be enough surface charge to induce platelet aggregation. To assess whether PtNP-11-MUHEG was not inhibiting platelet aggregation, platelets were treated with 1 U/mL thrombin in the presence of PtNP-11-MUHEG and were found to have a good response, as shown in Figure 8.5 (c). 11-MUHEG was also tested alone to confirm there was no platelet aggregation, as shown in Figure 8.5 (d). As the c-PtNPs demonstrated platelet aggregation, these nanoparticles were taken forward to elucidate the mechanism of platelet activation.

8.2.3 Mechanism of platelet activation by platinum nanoparticles

Previous work by Alshehri et al [101] revealed that washed platelets were activated by DEP through the GPVI receptor. The GPVI signalling pathway is illustrated in Figure 8.6. Upon ligand interaction, GPVI activates the phosphorylation of the Src family kinases (SKF) leading to the phosphorylation ITAM of the GPVI-FcRγ complex. In turn, this initiates the recruitment of Syk (spleen tyrosine kinase) which auto phosphorylates and induces the phosphorylation of linker for activation of cells (LAT) and leads to the recruitment of various adapter and effector proteins. Subsequently, 1-phosphatidylinositol-4,5-bisphosphate phosphodiesterase gamma2(PLCγ2) becomes activated and phosphorylated leading the final events where intracellular calcium (Ca^{2+}) is increased causing platelet aggregation. To deduce whether platelet activation by c-PtNPs was mediated by GPVI, the GPVI signalling pathway was investigated through a series of inhibitory and phosphorylation experiments. As tyrosine kinases Src and Syk are attributed to GPVI signalling, platelet aggregations were performed using the Src and Syk inhibitors PP2 and PRT-060318 respectively. PP2 is a selective inhibitor for Src, while PRT-060318 is selective inhibitor for Syk.

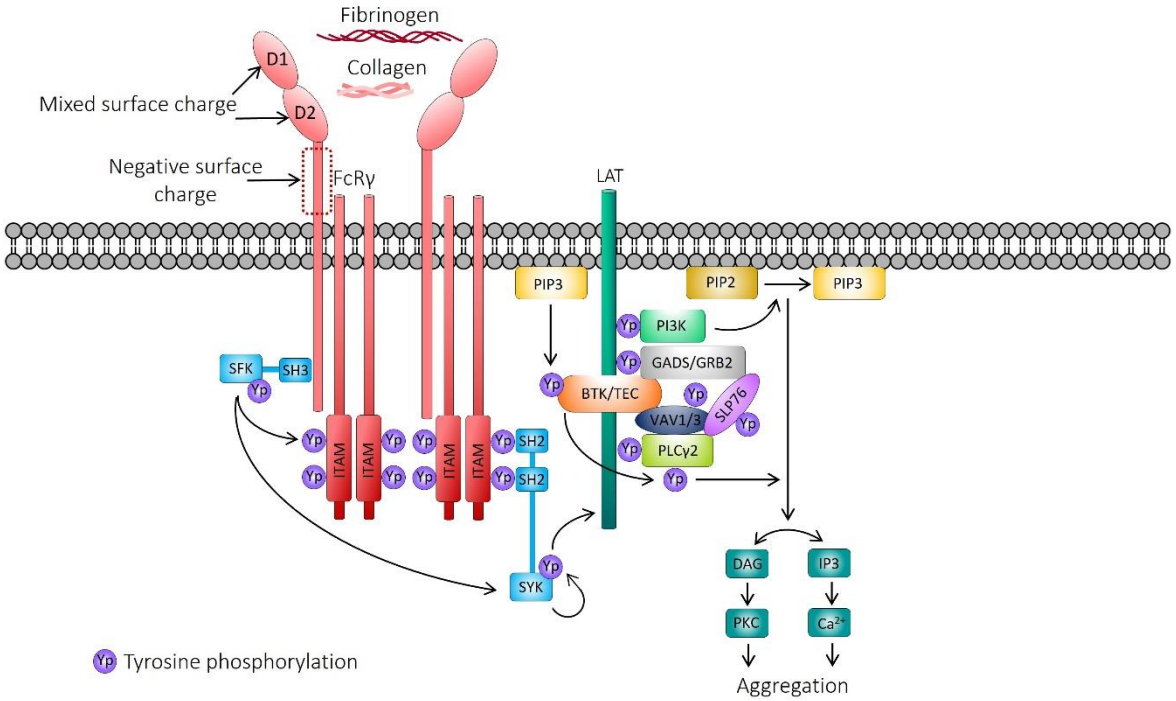

Figure 8.6 GPVI signalling pathway.

Collagen binding to GPVI is mediated via the glycine, L-proline and 3-hydroxy-L-proline (GPO) repeat units of collagen, thus, a control aggregation was first performed with the synthetic collagen-related peptide (CRP), which consists of repeat units of GPO.[218] Washed platelets were pre-incubated with 1% dimethyl sulfoxide (DMSO) prior to stimulation with 3 µg/mL CRP; DMSO was selected as vehicle reagent as the stock solutions of PP2 and PRT-060318 were prepared in DMSO. Next, washed platelets were pre-incubated with 20 µM PP2 followed by stimulation by 3 µg/mL CRP. The experiment was repeated with 3 µM PRT-060318. For c-PtNPs, washed platelets were pre-incubated with DMSO followed by stimulation by 59.2 µg/mL of c-PtNPs. To ascertain if platelet aggregation by the c-PtNPs was mediated by GPVI activation, inhibitory aggregations were conducted with the PP2 and PRT-060318. A control aggregation was conducted with the maximum c-PtNPs concentration of 59.2 µg/mL; again, washed

platelets were pre-incubated with 1% DMSO for 1 minute prior to stimulation with c-PtNPs. Subsequent aggregations involved pre-incubation with 20 µM PP2 and stimulation by 59.2 µg/mL of c-PtNPs, again this experiment was repeated with 3 µM PRT060318 and c-PtNP. Experiments were performed using 3 human donors, data was expressed as mean ± SEM.

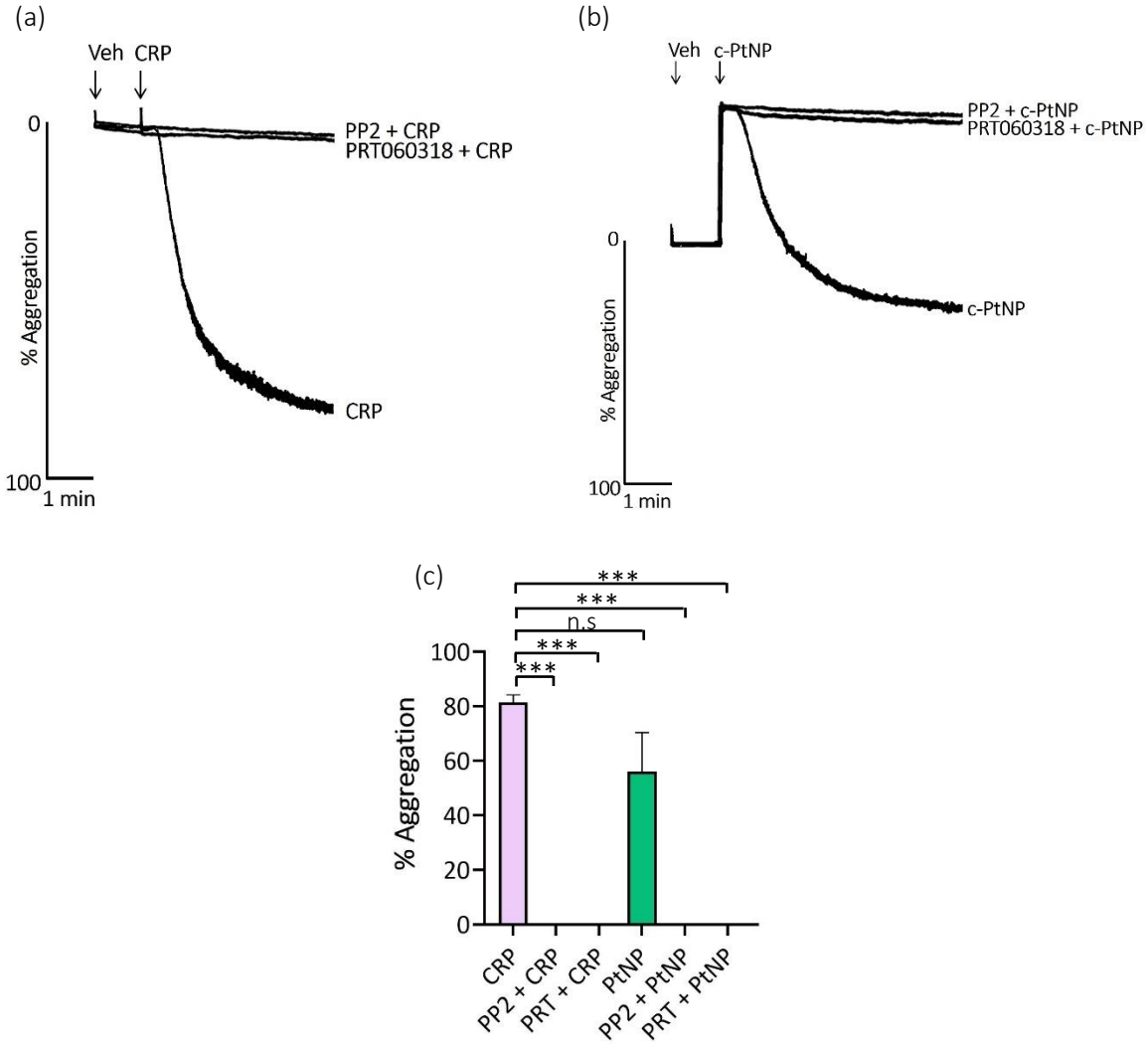

Figure 8.7 Human platelet aggregations with c-PtNPs and Src and Syk inhibitors. (a) representative control aggregation trace to 3 µg/mL CRP following pre-incubation with 20 µM PP2 and 3 µM PRT-060318, (b) representative trace to 59.2 µg/mL c-PtNP following pre-incubation with 20 µM PP2 and 3 µM PRT-060318, (c) quantification of maximal aggregation by CRP and c-PtNP with pre-incubation of with 20 µM PP2 and 3 µM PRT-060318 presented as mean ± SEM, (P<0.001). Results are representative of 3 experiments (n=3).

Upon stimulation by 3 μg/mL CRP, the washed platelets gave 81.5 ± 2.7% aggregation as illustrated in Figure 8.7 (a). Pre-incubation with the Src and Syk inhibitors completely blocked the light transmission, thus, no platelet aggregation was observed. These results give confidence that both inhibitors PP2 and PRT-060318 affectively blocked GPVI activation. Upon stimulation by the c-PtNPs, aggregation was observed at 56% ± 14.3. This was comparable to the previous result in section 8.2.1. No light transmission was observed in the presence of the Src and Syk inhibitors PtNPs, thus, no platelet aggregation was observed as shown in Figure 8.7 (b). The quantification of these aggregations are shown in Figure 8.7 (c), this data clearly demonstrates that the Src and Syk inhibitors effectively blocked GPVI activation and potentially c-PtNPs activate platelets through the GPVI receptor.

To further deduce whether the mechanism of platelet activation by the c-PtNPs is mediated by GPVI activation, phosphorylation of tyrosine, Syk and LAT in the GPVI signalling cascade were investigated by western blotting. Washed platelets were initially pretreated with EGTA (ethylene glycol-bis(β-aminoethyl ether)-N,N,N′,N′-tetraacetic acid) for 5 minutes prior to preincubation with inhibitors. EGTA chelates to Ca^{2+} preventing integrin activation and platelet aggregation which hinders protein solubilisation which is required for separation by SDS-PAGE. After pretreatment with EGTA, washed platelets were pre-incubated for 5 minutes with PP2 and PRT-060318 inhibitors followed by stimulation with c-PtNPs (59.2 μg/mL) for 5 minutes. Aggregations were terminated with 2X Laemmli sample buffer to produced whole cell lysates (WCL) for western blot investigations. Additionally, control WCL were prepared without

inhibitors with stimulation by DMSO, c-PtNP, CRP. Baseline control WCL were prepared without EGTA pre-treatment, followed by stimulations with DMSO, c-PtNP, CRP.

WCL were separated on 4-12% sodium dodecyl sulphate polyacrylamide (SDS) gels and transferred to a polyvinylidene fluoride (PVDF) membrane. Non-specific binding was blocked by incubation with 4% bovine serum albumin (BSA) prepared in tris-buffered saline with Tween 20 (TBST). Primary antibodies were diluted in 4% BSA with TBST (dilutions: phosphotyrosine (4G10), 1:1000, phospho Syk pY525/6, 1:500 and phosphor LAT, 1:500) and membranes were incubated overnight at 4^{o}C. Following primary antibody incubation, membranes were washed with TBST (3 x 10 minutes) and then incubated with the corresponding horseradish peroxidase (HRP) conjugated secondary antibody at 1:10000 dilution. Membranes were washed again with TBST (3 x 10 minutes) and developed on X-ray films with an enhanced chemiluminescence (ECL) substrate. Protein loading was assessed with antibodies for α-tubulin (1:1000) for 4G10 and total Syk 4D10 (1:200 dilution) for phospho Syk and phospho LAT. Results are demonstrated in Figure 7.8, experiments were performed using 3 human donors.

From the results presented in Figure 8.8, compared to the baseline controls, it is clearly evident that phosphotyrosine was highly expressed when platelets were pre-treated with EGTA and stimulated by CRP. Very faint phosphotyrosine expression was observed in the vehicle DMSO and PtNPs samples, with EGTA pre-treatment phosphotyrosine increased but not as much CRP. Platelets pre-incubated with the Src and Syk inhibitors had very faint phosphotyrosine expression. Phospho-Syk expression was not detected in the vehicle treated samples, by

contrast, phospho-Syk expression was detected at 72 kDa only in the CRP stimulated platelets. Faint phospho-LAT expression was observed in the baseline DMSO, c-PtNP and CRP samples, while EGTA treated samples demonstrated an increased phospho-LAT expression at 37 kDa for DMSO and PtNP but was dominate in the CRP stimulated platelets. The Src and Syk inhibitors blocked phospho-LAT expression when the platelets stimulated by with c-PtNPs.

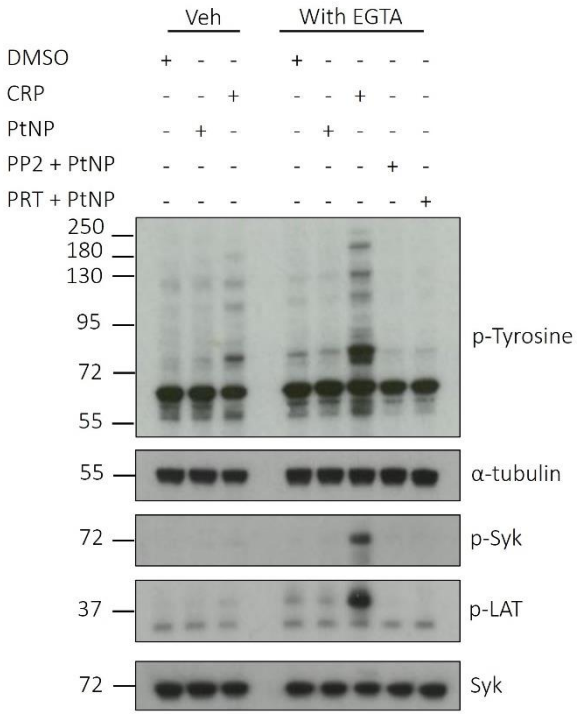

Figure 8.8 Expression of phospho-tyrosine, phospho-Syk and phospho-LAT from platelet whole cell lysates treated with EGTA, pre-incubated with Src and Syk inhibitors with PtNP stimulation. Results are representative of 3 experiments (n=3).

Overall, this data demonstrates that c-PtNPs did not stimulate tyrosine phosphorylation, thus, platelet activation was not mediated by GPVI. It could be that the zeta potential of c-PtNP was not high enough to activate platelets through the GPVI receptor. Alshehri et al.[101] demonstrated that platelet activation and aggregation by DEP in washed platelets was

mediated by through the GPVI receptor, however, the study did not focus on the how the physicochemical properties of DEP caused platelet activation. If we compare the citrated PtNPs to DEP, DEP are comprised of a mixture of carbon, polycyclic aromatic hydrogens (PAHs) and nitro-PAH and other metals and was reported to exhibit a surface charge of -39.1.[219] In the present study, the zeta potential of DEP standard reference material 2975 which was used by Alshehri et al.[101] was measured at -44.7 mV. This surface charge was greater than the c-PtNPs in this study. Thus, DEP with higher zeta potentials were able to induce platelet activation and aggregation by the GPVI receptor.

8.2.4 Platinum nanoparticle human platelet rich plasma aggregations

To understand how the PtNPs will interact with the platelets in a physiologically setting, platelet function with citrate capped PtNPs at its maximal concentration of 59.2 μg/mL were assessed in PRP as they were the only PtNPs from the functionalised PtNPs that demonstrated platelet aggregation in washed platelets. PRP is constituted with plethora of growth factors, clotting factors and proteins including albumin, fibrinogen and globulins.[220] Human PRP was prepared in a similar manner to washed platelet described in section 8.2.2. Whole blood was collected in with 3.2% (w/v) sodium citrate; ACD was not added to the blood as this would decrease the pH and the ACD can chelate with Ca^{2+}, thus, weakening the aggregation. The blood was centrifuged at 200 x g for 20 minutes at room temperature; the PRP was collected for LTA experiments. Platelet aggregations in PRP were undertaken in the same manner as the washed platelets. However, the PAR1 peptide was used as control agonist to assess platelet function in the PRP rather than thrombin, as thrombin is able to form fibrin[214] which is also an agonist for GPVI.[215, 221]

PRP was pre-warmed for 2 minutes at 37°C in aggregation tubes with stir bars, PRP was then stirred for 1 minute at 1200 rpm before the addition of agonists/nanoparticles. Aggregations were then recorded for 5 minutes. As before, the % aggregation was determined by measuring the height difference of the aggregation trace against the baseline and then calculating the % difference. Experiments were performed using 3 human donors, data was expressed as mean ± SEM.

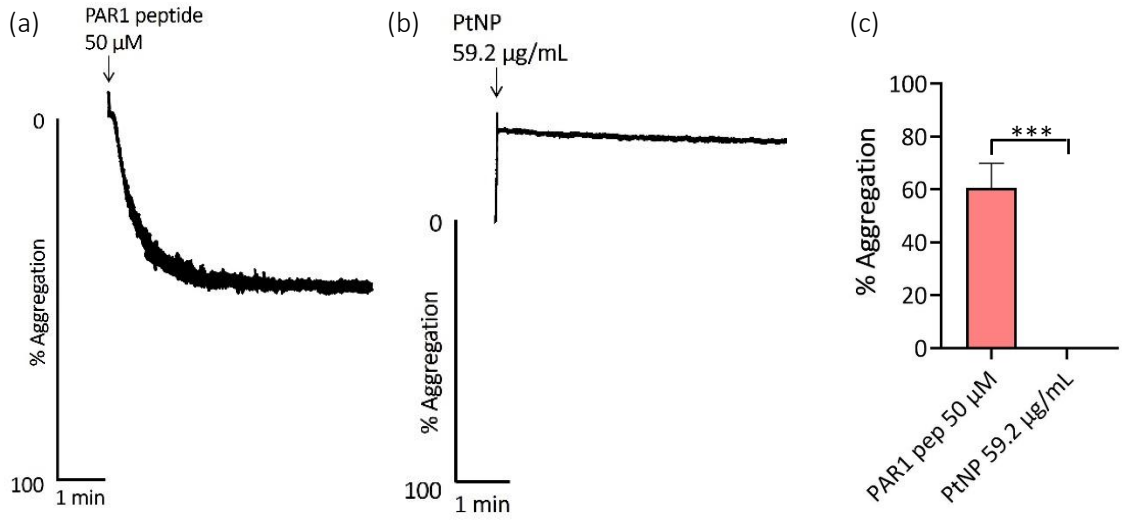

Figure 8.9 Human platelet rich plasma aggregations with PtNPs (a) representative aggregation traces to PAR1 peptide 50 µM, (b) representative aggregation traces to PtNP 59.2 µg/mL, (c) quantification of platelet aggregation in PRP with PtNPs. Results are representative of 3 experiments (n=3) and presented as mean ± SEM (P<0.001).

Figure 8.9 demonstrates the platelet aggregation stimulated by PtNPs in PRP. At a final concentration of 50 µM, the PAR1 peptide had a moderate response by 60% aggregation. Upon stimulation by the PtNPs, no aggregation was observed, presumably, the proteins in the PRP adsorbed onto the PtNP surface forming a protein corona. It is likely, that the negative charge

the c-PtNPs have interacted with proteins in the PRP via Van der Waals forces, electrostatic interactions, hydrophobic and hydrophilic interactions, leading to the formation of a protein corona. Thus, the c-PtNPs did not cause platelet aggregation in the PRP. This corresponds with previous platelet aggregations performed in PRP with charged nanoparticles including DEP, gold and silver nanoparticles.[93, 98, 101] To confirm protein corona formation by the PtNPs further investigation is required.

8.2.5 Protein corona of functionalised platinum nanoparticles

Functionalised PtNPs in Table 8.1 were examined for protein corona formation with human plasma. Although PtNP-2-MOHA and PtNP-11-MUHEG were the only two functionalised PtNPs selected for platelet function studies, all negatively charged carboxyl-terminated PtNPs and neutrally charged hydroxyl terminated PtNPs were utilised to assess if protein corona formation occurred. Utilising the method previously described in section 5.2.2 PtNPs were surface modified with alkanethiol and PEGylated thiols at the highest concentrations of 100 µM and 70 µM respectively for 3 hours at room temperature. Excess thiol and citrate ions were removed by centrifugation at 10000 x g for 10 minutes. The supernatant was discarded, and the functionalised PtNPs were resuspended in dH_2O and then characterised by DLS, zeta potential and pH.

Following characterisation, the functionalised PtNPs were incubated with commercial human plasma (mixed pool, TCS Biosciences Ltd, UK) for 30 minutes at 37^{o}C. Citrated capped PtNPs were used as control sample. All samples were centrifuged at 10,000 x g for 10 minutes;

supernatants were discarded and resuspended in phosphate buffered (PBS). For this experiment, DLS and zeta potential experiments were performed once as the high salt concentration from the PBS buffer degrades the electrodes on the capillary cells used for zeta potential measurements. Five DLS and zeta potential measurements were performed to obtain the mean for each sample, data is presented as mean.

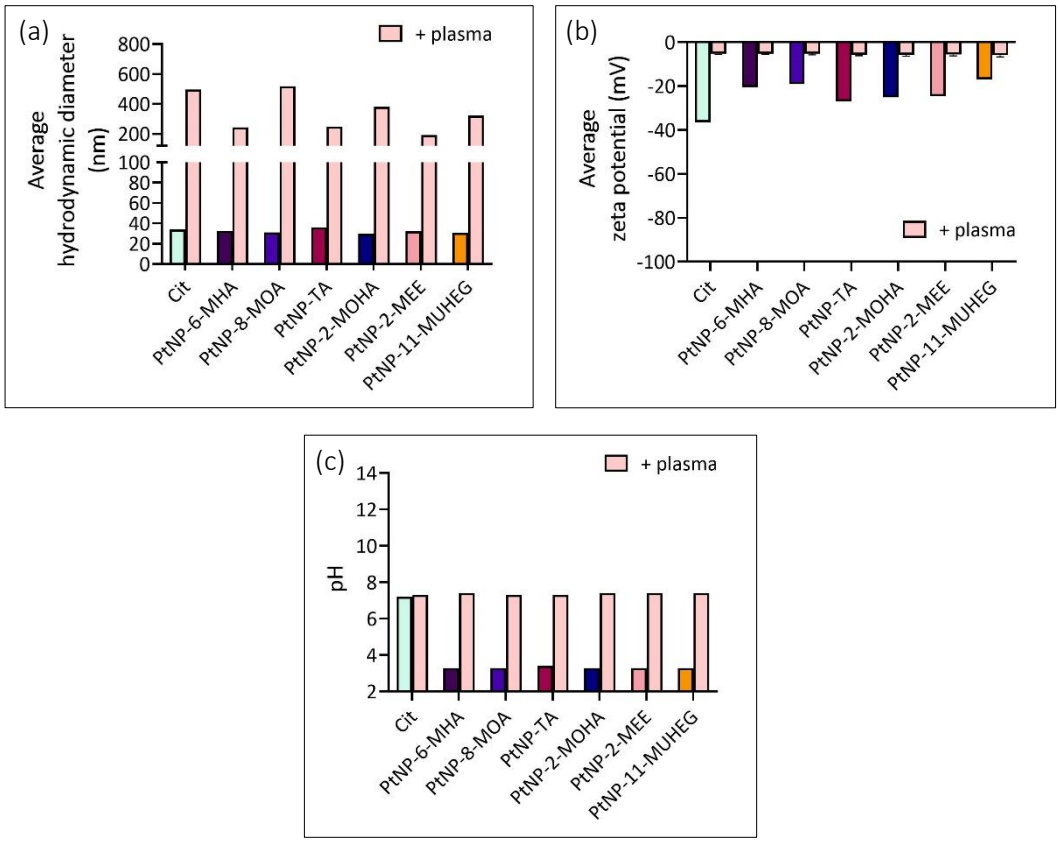

Figure 8.10 Protein corona of functionalised PtNPs. (a) hydrodynamic diameters with human plasma and (b) zeta potentials with human plasma. Results presented from 1 experiment (n=1).

The hydrodynamic dynamic diameters of the functionalised PtNPs before and after incubation are displayed in Figure 8.10 (a). The hydrodynamic diameters of c-PtNPs and all the functionalised PtNPs dramatically increased from about 30 nm to over 190 nm after incubation

with the human mixed plasma indicating the proteins had adsorbed onto the PtNP surface. Presumably, the proteins interacted with functionalised PtNPs to form a protein corona through Van der Waals forces, hydrogen bonds, electrostatic interaction and hydrophobic and hydrophilic interactions.[62, 66] Additionally, there may also be a sulphur-platinum interaction from the cysteine residues of the proteins and the PtNP core.[222] Interestingly, the hydrodynamic diameters of both neutrally charged PtNP-2-MEE and PtNP-11-MUHEG also observed increases in hydrodynamic diameters. A possible explanation for this, is that PtNP-2-MEE and PtNP-11-MUHEG were only partially functionalised, XPS analysis in chapter 7 indicated citrate ions were still present on the PtNP surface after ligand exchange. This would allow plasma proteins to bind to the functionalised PtNPs, thereby, increasing the hydrodynamic diameter.

Figure 8.10 (b) demonstrates the zeta potentials of the functionalised PtNPs. The citrated PtNPs (control) exhibited a zeta potential of -36.4 mV, after incubation with human mixed plasma, this increased to -5.3 mV. Similar results were observed with the negatively charged PtNPs, following incubation with human mixed plasma PtNP-6-MHA, PtNP-8-MOA, PtNP-TA and PtNP-2-MOHA all exhibited increased zeta potentials ranging from -5.2 to 5.7 mV. It is likely that the negatively charged PtNPs attracted positively charged protein residues first leading to the formation of a protein corona. The neutrally charged PtNP-2-MEE and PtNP-11-MUHEG also had demonstrated increased zeta potentials of -5.7 mV and -5.6 mV respectively. It is assumed the plasma proteins have interacted with the remaining citrate ions on the surface of PtNP-2-MEE and PtNP-11-MUHEG. The zeta potential of all the functionalised PtNPs assessed

demonstrated near a neutral charge, this was due to the charge of the human mixed plasma itself which measured a zeta potential of -5.5 mV at pH 7.3.

The pH of the functionalised PtNPs before and after incubation with human mixed plasma is presented in Figure 8.10 (c). The pH of the citrated PtNP solution was pH 7.2, this was comparable to the pH after incubation with human mixed plasma which was pH 7.3. After functionalisation by the alkane and PEGylated thiols the pH of these nanoparticle solutions decreased, which was previously observed in chapters 4 and 6, this is possibly a result of the thiol compounds having an acidic pH. This was similar to the data previously observed in chapters 4 and 6. By contrast, the pH of all the functionalised PtNPs solutions increased from a pH range of 3.3 to 3.4 to pH 7.3 to 7.4. This difference is a result of the pH of the PBS solution, PBS solution was utilised to resuspend the functionalised PtNPs after incubation with human mixed plasma to maintain protein structure. Collectively, the hydrodynamic diameters, zeta potential and pH data, provide evidence that the functionalised PtNPs bound with plasma proteins, thus, leading to protein corona formation. Furthermore, this data offers insight on the how functionalised PtNPs would interact with plasma proteins in a physiologically setting.

8.1 Conclusions

In the current study, the behaviour of the functionalised PtNPs were assessed in the platelet Tyrodes-HEPES buffer and demonstrated the PtNPs functionalised by PEGylated thiols were stable in Tyrodes-HEPES buffer. Of these PtNPs, citrated PtNPs (control, negative charge), PtNP-2-MOHA (negatively charged) and PtNP-11-MUHEG (neutrally charged) were taken forward in

platelet investigations. Platelet aggregation was observed by c-PtNPs in a dose-dependent manner in washed platelets, while PtNP-2-MOHA and PtNP-11-MUHEG had no effect on platelet aggregations. It was found that c-PtNPs exhibited a higher zeta potential of -38.9 mV compared to PtNP-2-MOHA at -21.1 mV, thus, platelets aggregation was induced by PtNPs with higher zeta potentials. The c-PtNPs were utilised to elucidate the mechanism of platelet aggregation in washed platelets by investigating the GPVI signalling pathway. Firstly, it was demonstrated that the pre-incubation of Src and Syk inhibitors PP2 and PRT-060318 blocked platelet aggregation by the c-PtNPs. However, c-PtNPs did not stimulate phosphotyrosine, Syk or LAT expression by western blotting to the same extent observed by CRP, thus, c-PtNPs they did not activate the platelets through the GPVI signalling pathway.

In a physiological setting with PRP, the PtNPs demonstrated no platelet aggregation indicating a possible protein corona formation. Lastly, all the functionalised PtNPs in this study formed a protein corona , this was confirmed by an increased hydrodynamic diameter and zeta potential when the PtNPs were pre-incubated with human mixed plasma.

8.2 Further work

Although PtNPs demonstrate platelet aggregation, it remains unclear if the c-PtNPs are binding to the platelet surface and causing their activation. To verify whether the PtNPs were binding to the platelet surface, field emission gun scanning electron microscopy (FEG-SEM) could be utilised. FEG-SEM provides high resolution images over traditional SEM, the technique would provide a high-resolution image of the platelet surface with the c-PtNPs. The technique does

not require contrast agents for observing the platelets. Previous work by Havrdova et al.[223] captured images of superparamagnetic iron oxide nanoparticle (SPIONs) within endosomes without the need for contrast agents and altering the morphology of the organelle. If c-PtNPs are confirmed to have adhered onto the platelet surface this would warrant further investigation to deduce which platelet surface receptors are involved in platelet activation and aggregation. Additionally, FEG-SEM could also be used to visual protein corona formation on the c-PtNP surface.

Further experiments to examine the cytotoxicity of PtNPs on human platelets could be tested by *in vitro* methods to measure lactate dehydrogenase (LDH), cell viability or cell proliferation using LDH, MTT or MTS assays respectively. The *in vivo* effects of the PtNPs on platelet aggregation could be examined by utilising mouse models of cardiovascular and inflammatory diseases. Platelets can be isolated and radiolabelled with ^{111}Indium oxine and infused back into the mice, where PtNPs can be intratracheally instilled, this would enable tracking of thromboembolism. The employment of cardiovascular and inflammatory mouse models would provide a wider insight on how charged PtNPs could potentially affect people with underlying conditions. In turn, raising public awareness to the health risks associated with nanoparticle exposure and the necessary health and safety management of nanomaterials.

Chapter 9 Conclusions and Future Work

9.1 Conclusions

The work presented in this thesis describes the synthesis and functionalisation used to prepare functionalised PtNPs and the characterisation methods employed to determine their physicochemical properties. Within this study, we assessed the functionalisation of various alkane and PEGylated thiols on c-PtNPs to create an array of PtNPs that exhibited a negative, positive, and neutral charge. Functionalisation was assessed by a selection of techniques, including zeta potential, DLS, TEM and XPS which are specific to surface analysis.

Initially, the core c-PtNPs were synthesised using a seed mediated synthesis approach. c-PtNP were grown from platinum seeds of 4 nm. Characterisation by TEM, DLS and zeta potential revealed c-PtNPs of 20 nm and 60 nm. Both 20 nm and 60 nm c-PtNPs exhibited a negative charge with good stability, the 20 nm c-PtNP had TEM diameters ranging from 20 to 23.4 nm with narrow particle distribution, while the larger 60 nm c-PtNPs had TEM diameters from 87.7 to 102 nm with a broad particle distribution. The 20 nm c-PtNPs were selected for subsequent experiments due to their narrow particle distribution. Large scale synthesis demonstrated that these 20 nm could be synthesised with reproducible sizes, surface charge and narrow particle distribution.

Using the newly synthesised 20 nm c-PtNPs, ligand exchange was attempted with carboxyl terminated alkanethiols 6-MHA, 8-MOA, and TA to functionalise the c-PtNPs to create sterically stable negatively charged PtNPs. Characterisation by zeta potential, pH and gel electrophoresis indicated that the citrate ions had been ligand exchanged for the alkanethiols. XPS analysis of PtNP-6-MHA and PtNP-8-MOA confirmed the presence of the platinum-thiol bond, thus, the thiols had chemisorbed onto the PtNP surface. However, the presence of the Na Auger peak revealed that citrate ions were still present on the PtNP surface after ligand exchange. Thus, the PtNPs were only partially functionalised by 6-MHA and 8-MOA. XPS analysis of PtNP-TA confirmed a platinum-sulphur bond, therefore, TA had chemisorbed on to the PtNP surface. Conversely, the Na Auger was not detected by XPS, indicating the citrate ions had been displaced by the TA molecules. The disulphide nature of TA enables two sulphur bonds with the platinum surface, therefore, more displacement of citrate ions allowing the more chemisorption by TA. Long alkanethiols pose the challenge of non-polar tendencies, to overcome this issue, the PEGylated thiol 2-MOHA was employed to functionalise the PtNPs using the same ligand exchange method. Again, characterisation by zeta potential, pH and gel electrophoresis indicated that the citrate ions had been ligand exchanged for 2-MOHA. Unfortunately, the XPS analysis of PtNP-2-MOHA was unable to confirm the platinum-thiol bond due to low signal, indicating ligand exchange was not sufficient. These findings provide insight into the ligand exchange of c-PtNPs with carboxyl terminated alkane and PEG thiols. Citrate ions were not fully displaced by the thiol molecules, thus, the PtNPs were partially functionalised by the alkane and PEG thiols.

Amino-terminated alkanethiols CSH, 6-AHT and 11-AUT were found to be unsuitable to functionalise the c-PtNPs through the ligand exchange method. Both SH and NH_2 groups could bind simultaneously to the PtNP core and citrate on capping respectively. The positive charge of the NH_2 group can electrostatically interact with negative charge of carboxylic acid groups of the citrate ions, thus, leading to aggregation. To functionalise the PtNPs to with a positive charge, two approaches were examined. First, positively charged PtNPs were synthesised with the cationic surfactant CTAB. TEM, DLS and zeta potential demonstrated PtNP-CTAB with 50.2 nm diameter and a positive charge. Ligand exchange of the CTAB capping for the quaternary ammonium compound 6-ATA proved to be successful by zeta potential and pH. However, this success was limited as the PtNP-6-ATA aggregated the following day rendering the 6-ATA unsuitable for functionalised PtNPs. In a second attempt, the alkanethiol DEA was used to synthesise positively charged PtNPs. Characterisation of PtNP-DEA by TEM, DLS and zeta potential revealed that successful synthesis was on the reaction taking place at pH 2. Although positively charge PtNPs were synthesised using DEA as a capping agent, the PtNP-DEA were found to be unstable as they also aggregated the following day. These studies demonstrated that positively charged PtNPs cannot be created in the same manner as the negatively charge PtNPs. This work demonstrates that ligand exchange and synthesis methods of positively charged PtNPs is challenging.

Neutrally charged PtNPs were functionalised in a similar manner to the negatively charged PtNPs. Ligand exchange of c-PtNPs with the hydroxyl-terminated alkanethiol 6-MCH was attempted. Characterisation by zeta potential and pH demonstrated 6-MCH was unable to the

PtNPs to exhibit a neutral charge. 6-MCH was also directly tested to functionalise the PtNPs in synthesis, however, this approach proved to be unsuccessful. Literature indicated that 6-MCH would need to be in a deprotonated state in optimal synthesis conditions to adsorb onto the PtNP surface. To overcome this challenge, the hydroxyl-terminated PEGylated thiols 2-MEE and 11-MUHEG were utilised for ligand exchange with c-PtNPs. Zeta potential, pH and gel electrophoresis characterisation indicated that ligand exchange had occurred, however, the zeta potentials exhibited by PtNP-2-MEE and PtNP-11-MUHEG were not near neutral as expected, therefore, indicating citrate ions were still present on the PtNP surface after ligand exchange. This was further supported by XPS analysis by the presence of the Na Auger peaks. Nonetheless, XPS analysis did reveal platinum-thiol bonds for both PtNP-2-MEE and PtNP-11-MUHEG, thus, the PEGylated thiols had chemisorbed onto the PtNP surface. Overall, the ligand exchange method only partially functionalised PtNP-2-MEE and PtNP-11-MUHEG. This work provides insight into ligand exchange of c-PtNPs with hydroxyl-terminated alkane and PEG thiols. Similar to negatively charged PtNPs, the citrate ions were not fully displaced by the PEGylated thiols, thus, the PtNPs were partially functionalised by the PEGylated thiols.

Though the negatively and neutrally charged PtNPs were only partially functionalised, they were examined for platelet studies with the platelet physiological buffer Tyrodes-HEPES. PtNPs functionalised by PEGylated thiols were found to be the most stable. Consequently, c-PtNPs (control, negatively charged), PtNP-2-MOHA (negatively charged) and PtNP-11-MUHEG (neutrally charged) were carried forward for platelet investigations. c-PtNPs induced platelet aggregation in a dose-dependent manner in washed platelets while PtNP-2-MOHA and PtNP-

11-MUHEG had no effect on platelet aggregation. Although both c-PtNPs and PtNP-2-MOHA were a negative charged, c-PtNPs exhibited a higher zeta potential compared to 2-MOHA, therefore, was able to induce platelet aggregation. Although PtNP-11-MUHEG demonstrated a negative charge from the citrate ions remaining on the surface of after ligand exchange, the zeta potential was not high enough to induce platelet aggregation. c-PtNP platelet activation was found not to be mediated through the GPVI receptor as key proteins in the GPVI signalling cascade phospho Syk and LAT were not activated. Protein corona formation was observed DLS, zeta potential and pH with all the functionalised PtNPs, regardless of their partial functionalisation. These experiments provide novel insights on how the zeta potential and not the surface charge of PtNPs influences platelet aggregation.

9.2 Further work

For the negatively charged PtNPs, the ligand exchange incubation times for 6-MHA, 8-MOA, TA, and 2-MOHA could be extended to multiple time point up to 24 hours to assess if surface charge and % of bound sulphur on PtNP surface varies. This would provide a novel insight into the mechanism of ligand exchange on c-PtNPs, as currently all work on the mechanism of ligand exchange on metallic nanoparticles is focused on AuNPs.

Albeit PtNPs were synthesised/functionalised to produce positively charged PtNPs these were rendered unstable. The quaternary ammonium thiol 11-MABr could be assessed for functionalisation with 20 nm c-PtNPs. In theory, the ammonium group would sterically not be able to interact with citrate ion capping, therefore, the thiol head group could chemisorb on

the PtNP surface. If this was successful after a 3-hour ligand exchange, the incubation time could be extended up to 24 hours. An alternative capping agent which has been used for functionalising AgNPs is the cationic polymer PEI. Its multiple NH_2 groups therefore allowing more PEI bind on the PtNP surface.

For neutrally charged PtNPs, perform ligand exchange of c-PtNPs with 6-MCH under basic conditions to assist with deprotonation of the hydroxyl group. The ligand exchange incubation times for 2-MEE and 11-MUHEG could be extended to multiple time point up to 24 hours to assess if surface charge and % of bound sulphur on PtNP surface varies. Again, this would provide a novel insight into the ligand exchange mechanism of c-PtNPs by PEGylated hydroxy-terminated thiols.

For PtNP-platelet interactions, it is unclear what is causing platelet activation. To deduce the mechanism of platelet activation, first the c-PtNPs need to be examined to see if they are indeed binding to the platelet surface. This can be confirmed by FEG-SEM, where the platelets can be visualised together with the PtNPs on the surface. If the PtNPs have adhered to the surface than further mechanistic investigations can be carried out. Additionally, *in vitro* cytotoxicity assays such as MTT, MTS and LDH should be performed to assess the direct impact of the PtNPs on human platelets . Platelet aggregation experiments should also be *in vivo* by expanding the experiments to murine models of cardiovascular and inflammatory diseases.

Chapter 10 References

1. S. Bayda, M. Adeel, T. Tuccinardi, M. Cordani and F. Rizzolio, *Molecules*, 2019, 25, 112.
2. M. Vert, Y. Doi, K.-H. Hellwich, M. Hess, P. Hodge, P. Kubisa, M. Rinaudo and F. Schué, *Pure and Applied Chemistry*, 2012, 84, 377-410.
3. R. Feynman, in *Feynman and computation*, CRC Press, 2018, pp. 63-76.
4. I. Freestone, N. Meeks, M. Sax and C. Higgitt, *Gold Bulletin*, 2007, 40, 270-277.
5. M. Reibold, P. Paufler, A. A. Levin, W. Kochmann, N. Pätzke and D. C. Meyer, *Nature*, 2006, 444, 286-286.
6. N. V. Long, N. D. Chien, T. Hayakawa, H. Hirata, G. Lakshminarayana and M. Nogami, *Nanotechnology*, 2010, 21, 035605.
7. T. A. Salamone, L. Rutigliano, B. Pennacchi, S. Cerra, R. Matassa, S. Nottola, F. Sciubba, C. Battocchio, M. Marsotto, A. Del Giudice, A. Chumakov, A. Davydok, S. Grigorian, G. Canettieri, E. Agostinelli and I. Fratoddi, *Journal of Colloid and Interface Science*, 2023, 649, 264-278.
8. A. Abbaszadegan, Y. Ghahramani, A. Gholami, B. Hemmateenejad, S. Dorostkar, M. Nabavizadeh and H. Sharghi, *Journal of Nanomaterials*, 2015, 2015, 720654.
9. S. M. Dadfar, K. Roemhild, N. I. Drude, S. von Stillfried, R. Knüchel, F. Kiessling and T. Lammers, *Advanced Drug Delivery Reviews*, 2019, 138, 302-325.
10. M. Y. Ngun, N. Mohamad Nor, N. H. Ramli and K. Abdul Razak, *Materials Today: Proceedings*, 2022, 66, 2972-2976.
11. B. Fu, M. Dang, J. Tao, Y. Li and Y. Tang, *Journal of Colloid and Interface Science*, 2020, 570, 197-204.

12. H. W. Tan, J. An, C. K. Chua and T. Tran, *Advanced Electronic Materials*, 2019, 5, 1800831.

13. J. Im, G. F. Trindade, T. T. Quach, A. Sohaib, F. Wang, J. Austin, L. Turyanska, C. J. Roberts, R. Wildman, R. Hague and C. Tuck, *ACS Appl Nano Mater*, 2022, 5, 6708-6716.

14. A. Sels and V. Subramanian, *ACS Omega*, 2023, 8, 1929-1936.

15. Y. D. Herlambang, W. Sulistiyo, M. Margana, N. Apriandi, M. Marliyati, M. Setiyo and J. C. Shyu, *Automotive Experiences*, 2023, 6, 273-289.

16. P. C. Okonkwo, O. O. Ige, E. M. Barhoumi, P. C. Uzoma, W. Emori, A. Benamor and A. M. Abdullah, *International Journal of Hydrogen Energy*, 2021, 46, 15850-15865.

17. O. Holton and J. Stevenson, *Platinum Metals Review*, 2013, 57, 259-271.

18. M. Jeyaraj, S. Gurunathan, M. Qasim, M.-H. Kang and J.-H. Kim, *Nanomaterials*, 2019, 9, 1719.

19. P. G. Jamkhande, N. W. Ghule, A. H. Bamer and M. G. Kalaskar, *Journal of Drug Delivery Science and Technology*, 2019, 53, 101174.

20. P. Iqbal, J. A. Preece and P. M. Mendes, in *Supramolecular Chemistry*, 2012, DOI: https://doi.org/10.1002/9780470661345.smc195.

21. J. Turkevich, P. C. Stevenson and J. Hillier, *Discussions of the Faraday Society*, 1951, 11, 55-75.

22. C. R. Berry and D. C. Skillman, *Journal of Applied Physics*, 1971, 42, 2818-2822.

23. P. R. Van Rheenen, M. J. McKelvy and W. S. Glaunsinger, *Journal of Solid State Chemistry*, 1987, 67, 151-169.

24. G. Frens, *Nature Physical Science*, 1973, 241, 20-22.

25. N. T. K. Thanh, N. Maclean and S. Mahiddine, *Chemical Reviews*, 2014, 114, 7610-7630.

26. Y. H. Chen, C. Y. Tsai, P. Y. Huang, M. Y. Chang, P. C. Cheng, C. H. Chou, D. H. Chen, C. R. Wang, A. L. Shiau and C. L. Wu, *Mol Pharm*, 2007, 4, 713-722.

27. N. C. Bigall, T. Härtling, M. Klose, P. Simon, L. M. Eng and A. Eychmüller, *Nano Letters*, 2008, 8, 4588-4592.

28. K. R. Brown, D. G. Walter and M. J. Natan, *Chemistry of Materials*, 2000, 12, 306-313.

29. B. Baruah and M. Kiambuthi, *RSC Advances*, 2014, 4, 64860-64870.

30. R. Prajapati, S. Chatterjee, A. Bhattacharya and T. Mukherjee, *The Journal of Physical Chemistry C*, 2015, 119, 150521102948008.

31. H. Chen, L. Shao, Q. Li and J. Wang, *Chemical Society Reviews*, 2013, 42, 2679-2724.

32. A. Ulman, *Chemical Reviews*, 1996, 96, 1533-1554.

33. R. G. Nuzzo and D. L. Allara, *Journal of the American Chemical Society*, 1983, 105, 4481-4483.

34. P. E. Laibinis, G. M. Whitesides, D. L. Allara, Y. T. Tao, A. N. Parikh and R. G. Nuzzo, *Journal of the American Chemical Society*, 1991, 113, 7152-7167.

35. D. Y. Petrovykh, H. Kimura-Suda, A. Opdahl, L. J. Richter, M. J. Tarlov and L. J. Whitman, *Langmuir*, 2006, 22, 2578-2587.

36. C. Vericat, M. E. Vela, G. Benitez, P. Carro and R. C. Salvarezza, *Chemical Society Reviews*, 2010, 39, 1805-1834.

37. D. K. Schwartz, *Annu Rev Phys Chem*, 2001, 52, 107-137.

38. L. L. Rouhana, M. D. Moussallem and J. B. Schlenoff, *Journal of the American Chemical Society*, 2011, 133, 16080-16091.

39. R. Dinkel, B. Braunschweig and W. Peukert, *The Journal of Physical Chemistry C*, 2016, 120, 1673-1682.

40. S.-Y. Lin, Y.-T. Tsai, C.-C. Chen, C.-M. Lin and C.-h. Chen, *The Journal of Physical Chemistry B*, 2004, 108, 2134-2139.

41. J. C. Love, L. A. Estroff, J. K. Kriebel, R. G. Nuzzo and G. M. Whitesides, *Chemical Reviews*, 2005, 105, 1103-1170.

42. T. Yonezawa and T. Kunitake, *Colloids and Surfaces A: Physicochemical and Engineering Aspects*, 1999, 149, 193-199.

43. S. Cerra, T. A. Salamone, F. Sciubba, M. Marsotto, C. Battocchio, S. Nappini, F. A. Scaramuzzo, R. Li Voti, C. Sibilia, R. Matassa, A. M. Beltrán, G. Familiari and I. Fratoddi, *Colloids and Surfaces B: Biointerfaces*, 2021, 203, 111727.

44. C. Yee, M. Scotti, A. Ulman, H. White, M. Rafailovich and J. Sokolov, *Langmuir*, 1999, 15, 4314-4316.

45. S. E. Eklund and D. E. Cliffel, *Langmuir*, 2004, 20, 6012-6018.

46. G. H. Woehrle, L. O. Brown and J. E. Hutchison, *Journal of the American Chemical Society*, 2005, 127, 2172-2183.

47. Y. Wang and T. Bürgi, *Nanoscale Adv*, 2021, 3, 2710-2727.

48. E. U. Stolarczyk, A. Leś, M. Łaszcz, M. Kubiszewski, W. Strzempek, E. Menaszek, M. Fusaro, K. Sidoryk and K. Stolarczyk, *International Journal of Pharmaceutics*, 2020, 583, 119319.

49. K. Aslan and V. H. Pérez-Luna, *Langmuir*, 2002, 18, 6059-6065.

50. C. D. Bain, H. A. Biebuyck and G. M. Whitesides, *Langmuir*, 1989, 5, 723-727.

51. J. M. Abad, S. F. L. Mertens, M. Pita, V. M. Fernández and D. J. Schiffrin, *Journal of the American Chemical Society*, 2005, 127, 5689-5694.

52. I. Guzmán-Soto, M. Omole, E. I. Alarcon and C. D. McTiernan, *RSC Advances*, 2020, 10, 32953-32958.

53. M. U. Ahmed, V. Kaneva, S. Loyau, D. Nechipurenko, N. Receveur, M. Le Bris, E. Janus-Bell, M. Didelot, A. Rauch, S. Susen, N. Chakfé, F. Lanza, E. E. Gardiner, R. K. Andrews, M. Panteleev, C. Gachet, M. Jandrot-Perrus and P. H. Mangin, *Arterioscler Thromb Vasc Biol*, 2020, 40, 2127-2142.

54. M. Kus-Liśkiewicz, P. Fickers and I. Ben Tahar, *Int J Mol Sci*, 2021, 22.

55. D. S. Kohane and R. Langer, *Chemical Science*, 2010, 1, 441-446.

56. X. D. Zhang, H. Y. Wu, D. Wu, Y. Y. Wang, J. H. Chang, Z. B. Zhai, A. M. Meng, P. X. Liu, L. A. Zhang and F. Y. Fan, *Int J Nanomedicine*, 2010, 5, 771-781.

57. H. Buchtelova, S. Dostalova, P. Michalek, S. Krizkova, V. Strmiska, P. Kopel, D. Hynek, L. Richtera, A. Ridoskova, P. Adam, J. Kynicky, M. Brtnicky, Z. Heger and V. Adam, *Food Chem Toxicol*, 2017, 105, 337-346.

58. K. P. Steckiewicz, E. Barcinska, A. Malankowska, A. Zauszkiewicz-Pawlak, G. Nowaczyk, A. Zaleska-Medynska and I. Inkielewicz-Stepniak, *J Mater Sci Mater Med*, 2019, 30, 22.

59. C. M. Goodman, C. D. McCusker, T. Yilmaz and V. M. Rotello, *Bioconjugate Chemistry*, 2004, 15, 897-900.

60. M. Hashimoto, S. Yamaguchi, J.-I. Sasaki, K. Kawai, H. Kawakami, Y. Iwasaki and S. Imazato, *European Journal of Oral Sciences*, 2016, 124, 68-74.

61. M. Mahmoudi, M. P. Landry, A. Moore and R. Coreas, *Nature Reviews Materials*, 2023, 8, 422-438.

62. R. Rampado, S. Crotti, P. Caliceti, S. Pucciarelli and M. Agostini, *Frontiers in Bioengineering and Biotechnology*, 2020, 8.

63. T. Cedervall, I. Lynch, S. Lindman, T. Berggård, E. Thulin, H. Nilsson, K. A. Dawson and S. Linse, *Proc Natl Acad Sci U S A*, 2007, 104, 2050-2055.

64. L. Vroman and A. N. N. Lukosevicius, *Nature*, 1964, 204, 701-703.

65. L. Vroman, A. L. Adams, G. C. Fischer and P. C. Munoz, *Blood*, 1980, 55, 156-159.

66. R. García-Álvarez and M. Vallet-Regí, *Nanomaterials*, 2021, 11, 888.

67. A. C. G. Weiss, K. Krüger, Q. A. Besford, M. Schlenk, K. Kempe, S. Förster and F. Caruso, *ACS Appl Mater Interfaces*, 2019, 11, 2459-2469.

68. M. A. Dobrovolskaia, A. K. Patri, J. Zheng, J. D. Clogston, N. Ayub, P. Aggarwal, B. W. Neun, J. B. Hall and S. E. McNeil, *Nanomedicine: Nanotechnology, Biology and Medicine*, 2009, 5, 106-117.

69. M. Lundqvist, J. Stigler, G. Elia, I. Lynch, T. Cedervall and K. A. Dawson, *Proceedings of the National Academy of Sciences*, 2008, 105, 14265-14270.

70. S. Tenzer, D. Docter, S. Rosfa, A. Wlodarski, J. Kuharev, A. Rekik, S. K. Knauer, C. Bantz, T. Nawroth, C. Bier, J. Sirirattanapan, W. Mann, L. Treuel, R. Zellner, M. Maskos, H. Schild and R. H. Stauber, *ACS Nano*, 2011, 5, 7155-7167.

71. Z. J. Deng, G. Mortimer, T. Schiller, A. Musumeci, D. Martin and R. F. Minchin, *Nanotechnology*, 2009, 20, 455101.

72. R. García-Álvarez, M. Hadjidemetriou, A. Sánchez-Iglesias, L. M. Liz-Marzán and K. Kostarelos, *Nanoscale*, 2018, 10, 1256-1264.

73. M. R. Miller, J. B. Raftis, J. P. Langrish, S. G. McLean, P. Samutrtai, S. P. Connell, S. Wilson, A. T. Vesey, P. H. B. Fokkens, A. J. F. Boere, P. Krystek, C. J. Campbell, P. W. F. Hadoke, K. Donaldson, F. R. Cassee, D. E. Newby, R. Duffin and N. L. Mills, *ACS Nano*, 2017, 11, 4542-4552.

74. S. Zhang, X. Yuan, H. Wang, W. Mérida, H. Zhu, J. Shen, S. Wu and J. Zhang, *International Journal of Hydrogen Energy*, 2009, 34, 388-404.

75. S. Zhang, X.-Z. Yuan, J. N. C. Hin, H. Wang, K. A. Friedrich and M. Schulze, *Journal of Power Sources*, 2009, 194, 588-600.

76. M. R. Miller and D. E. Newby, *Cardiovascular Research*, 2019, 116, 279-294.

77. C. A. Weitekamp, L. B. Kerr, L. Dishaw, J. Nichols, M. Lein and M. J. Stewart, *Inhal Toxicol*, 2020, 32, 1-13.

78. M. Omrani, M. Goriaux, Y. Liu, S. Martinet, L. Jean-Soro and V. Ruban, *Environmental Pollution*, 2020, 257, 113477.

79. A. Solomon, E. Smyth, N. Mitha, S. Pitchford, A. Vydyanath, P. K. Luther, A. J. Thorley, T. D. Tetley and M. Emerson, *J Thromb Haemost*, 2013, 11, 325-334.

80. A. J. Lucking, M. Lundback, N. L. Mills, D. Faratian, S. L. Barath, J. Pourazar, F. R. Cassee, K. Donaldson, N. A. Boon, J. J. Badimon, T. Sandstrom, A. Blomberg and D. E. Newby, *Eur Heart J*, 2008, 29, 3043-3051.

81. K. R. Machlus, J. N. Thon and J. E. Italiano, Jr., *Br J Haematol*, 2014, 165, 227-236.

82. Z. Li, M. K. Delaney, K. A. O'Brien and X. Du, *Arterioscler Thromb Vasc Biol*, 2010, 30, 2341-2349.

83. A. Kasirer-Friede, M. L. Kahn and S. J. Shattil, *Immunol Rev*, 2007, 218, 247-264.

84. C. Lecut, A. Schoolmeester, M. J. E. Kuijpers, J. L. V. Broers, M. A. M. J. v. Zandvoort, K. Vanhoorelbeke, H. Deckmyn, M. Jandrot-Perrus and J. W. M. Heemskerk, *Arteriosclerosis, Thrombosis, and Vascular Biology*, 2004, 24, 1727-1733.

85. S. P. Watson and P. Harrison, in *Postgraduate Haematology*, 2010, DOI: https://doi.org/10.1002/9781444323160.ch40, pp. 772-792.

86. T. Renné, M. Pozgajová, S. Grüner, K. Schuh, H. U. Pauer, P. Burfeind, D. Gailani and B. Nieswandt, *J Exp Med*, 2005, 202, 271-281.

87. E. Smyth, A. Solomon, A. Vydyanath, P. K. Luther, S. Pitchford, T. D. Tetley and M. Emerson, *Nanotoxicology*, 2015, 9, 356-364.

88. A. Nemmar, M. F. Hoylaerts, P. H. Hoet, D. Dinsdale, T. Smith, H. Xu, J. Vermylen and B. Nemery, *Am J Respir Crit Care Med*, 2002, 166, 998-1004.

89. S. J. Montague, P. Patel, E. M. Martin, A. Slater, L. G. Quintanilla, G. Perrella, C. Kardeby, M. Nagy, D. Mezzano, P. M. Mendes and S. P. Watson, *Platelets*, 2021, 32, 1018-1030.

90. F. Zia, M. Kendall, S. P. Watson and P. M. Mendes, *RSC Advances*, 2018, 8, 37789-37794.

91. S. Deb, H. K. Patra, P. Lahiri, A. K. Dasgupta, K. Chakrabarti and U. Chaudhuri, *Nanomedicine*, 2011, 7, 376-384.

92. A. V. Aseychev, O. A. Azizova, E. M. Beckman, L. B. Dudnik and V. I. Sergienko, *Bull Exp Biol Med*, 2013, 155, 685-688.

93. N. Ajdari, C. Vyas, S. L. Bogan, B. A. Lwaleed and B. G. Cousins, *Nanomedicine: Nanotechnology, Biology and Medicine*, 2017, 13, 1531-1542.

94. S. A. Love, J. W. Thompson and C. L. Haynes, *Nanomedicine (Lond)*, 2012, 7, 1355-1364.

95. H. Huang, W. Lai, M. Cui, L. Liang, Y. Lin, Q. Fang, Y. Liu and L. Xie, *Scientific Reports*, 2016, 6, 25518.

96. E. A. Jun, K. M. Lim, K. Kim, O. N. Bae, J. Y. Noh, K. H. Chung and J. H. Chung, *Nanotoxicology*, 2011, 5, 157-167.

97. S. Shrivastava, T. Bera, S. K. Singh, G. Singh, P. Ramachandrarao and D. Dash, *ACS Nano*, 2009, 3, 1357-1364.

98. J. Laloy, V. Minet, L. Alpan, F. Mullier, S. Beken, O. Toussaint, S. Lucas and J. M. Dogné, *Nanobiomedicine (Rij)*, 2014, 1, 4.

99. S. Deb, S. O. Raja, A. K. Dasgupta, R. Sarkar, A. P. Chattopadhyay, U. Chaudhuri, P. Guha and P. Sardar, *Blood Cells Mol Dis*, 2012, 48, 36-44.

100. T. Liu, R. Bai, H. Zhou, R. Wang, J. Liu, Y. Zhao and C. Chen, *RSC Advances*, 2020, 10, 7559-7569.

101. O. M. Alshehri, S. Montague, S. Watson, P. Carter, N. Sarker, B. K. Manne, J. L. Miller, A. B. Herr, A. Y. Pollitt, C. A. O'Callaghan, S. Kunapuli, M. Arman, C. E. Hughes and S. P. Watson, *Biochem J*, 2015, 468, 459-473.

102. A. Radomski, P. Jurasz, D. Alonso-Escolano, M. Drews, M. Morandi, T. Malinski and M. W. Radomski, *Br J Pharmacol*, 2005, 146, 882-893.

103. J. Semberova, S. H. De Paoli Lacerda, O. Simakova, K. Holada, M. P. Gelderman and J. Simak, *Nano Lett*, 2009, 9, 3312-3317.

104. G. F. Guidetti, A. Consonni, L. Cipolla, P. Mustarelli, C. Balduini and M. Torti, *Nanomedicine*, 2012, 8, 1329-1336.

105. M. A. Dobrovolskaia, A. K. Patri, J. Simak, J. B. Hall, J. Semberova, S. H. De Paoli Lacerda and S. E. McNeil, *Molecular Pharmaceutics*, 2012, 9, 382-393.

106. H. Hu, A. Yu, E. Kim, B. Zhao, M. E. Itkis, E. Bekyarova and R. C. Haddon, *The Journal of Physical Chemistry B*, 2005, 109, 11520-11524.

107. P. S. Uttekar, S. H. Lakade, V. K. Beldar and M. T. Harde, *IET Nanobiotechnol*, 2019, 13, 688-696.

108. A. E. Enciso, B. Neun, J. Rodriguez, A. P. Ranjan, M. A. Dobrovolskaia and E. E. Simanek, *Molecules*, 2016, 21, 428.

109. R. José, L. María Luisa, N.-N. Leyre and V. Vicente, *Haematologica*, 2009, 94, 700-711.

110. N. K. Hante, C. Medina and M. J. Santos-Martinez, *Frontiers in Cardiovascular Medicine*, 2019, 6.

111. L. E. Franken, K. Grünewald, E. J. Boekema and M. C. A. Stuart, *Small*, 2020, 16, 1906198.

112. L. Zhang, W. Shi and B. Zhang, *Journal of Energy Chemistry*, 2017, 26, 1117-1135.

113. R. Sandhu, N. Singh, J. Dhankhar, K. Gandhi and R. Sharma, 2018, pp. 135-137.

114. A. Wishard and B. C. Gibb, *Supramolecular Chemistry*, 2019, 31, 608-615.

115. S. Mourdikoudis, R. M. Pallares and N. T. K. Thanh, *Nanoscale*, 2018, 10, 12871-12934.

116. C. N. Lunardi, A. J. Gomes, F. S. Rocha, J. De Tommaso and G. S. Patience, *The Canadian Journal of Chemical Engineering*, 2021, 99, 627-639.

117. B. V. Deraguin and L. Landau, *Acta Physicochim: USSR*, 1941, 14, 633-662.

118. E. J. Verwey, *J Phys Colloid Chem*, 1947, 51, 631-636.

119. J. Matusiak and E. Grządka, *Annales - Universitatis Mariae Curie-Sklodowska, Sectio AA*, 2017, LXXII, 33-45.

120. M. Hanauer, S. Pierrat, I. Zins, A. Lotz and C. Sönnichsen, *Nano Letters*, 2007, 7, 2881-2885.

121. X. Xu, K. K. Caswell, E. Tucker, S. Kabisatpathy, K. L. Brodhacker and W. A. Scrivens, *Journal of Chromatography A*, 2007, 1167, 35-41.

122. P. Van der Heide, *Journal*, 2012.

123. H. Bluhm, in *In Situ Characterization of Thin Film Growth*, eds. G. Koster and G. Rijnders, Woodhead Publishing, 2011, DOI: https://doi.org/10.1533/9780857094957.2.75, pp. 75-98.

124. G. V. Born, *Nature*, 1962, 194, 927-929.

125. A. M. Hvas and E. J. Favaloro, *Methods Mol Biol*, 2017, 1646, 321-331.

126. A. Pal, in *Protocols in Advanced Genomics and Allied Techniques*, ed. A. Pal, Springer US, New York, NY, 2022, DOI: 10.1007/978-1-0716-1818-9_6, pp. 119-127.

127. T. Gwozdz and K. Dorey, in *Basic Science Methods for Clinical Researchers*, eds. M. Jalali, F. Y. L. Saldanha and M. Jalali, Academic Press, Boston, 2017, DOI: https://doi.org/10.1016/B978-0-12-803077-6.00006-0, pp. 99-117.

128. L. Strong and G. M. Whitesides, *Langmuir*, 1988, 4, 546-558.

129. X. Qian, X.-H. Peng, D. O. Ansari, Q. Yin-Goen, G. Z. Chen, D. M. Shin, L. Yang, A. N. Young, M. D. Wang and S. Nie, *Nature Biotechnology*, 2008, 26, 83-90.

130. A. Chen and P. Holt-Hindle, *Chem Rev*, 2010, 110, 3767-3804.

131. J. C. Claussen, S. S. Kim, A. U. Haque, M. S. Artiles, D. M. Porterfield and T. S. Fisher, *J Diabetes Sci Technol*, 2010, 4, 312-319.

132. S. Hrapovic, Y. Liu, K. B. Male and J. H. Luong, *Anal Chem*, 2004, 76, 1083-1088.

133. D. Chen, C. Zhao, J. Ye, Q. Li, X. Liu, M. Su, H. Jiang, C. Amatore, M. Selke and X. Wang, *ACS Appl Mater Interfaces*, 2015, 7, 18163-18169.

134. J. Polte, *CrystEngComm*, 2015, 17, 6809-6830.

135. I. Römer, T. A. White, M. Baalousha, K. Chipman, M. R. Viant and J. R. Lead, *J Chromatogr A*, 2011, 1218, 4226-4233.

136. R. Bryaskova, D. Pencheva, S. Nikolov and T. Kantardjiev, *Journal of Chemical Biology*, 2011, 4, 185-191.

137. S. Skoglund, J. Hedberg, E. Yunda, A. Godymchuk, E. Blomberg and I. Odnevall Wallinder, *PLoS One*, 2017, 12, e0181735.

138. M. R. Ivanov, H. R. Bednar and A. J. Haes, *ACS Nano*, 2009, 3, 386-394.

139. O. J. Oziri, Y. Wang, T. Watanabe, S. Uno, M. Maeki, M. Tokeshi, T. Isono, K. Tajima, T. Satoh, S.-i. Sato, Y. Miura and T. Yamamoto, *Nanoscale Advances*, 2022, 4, 532-545.

140. E. Smyth, A. Solomon, M. A. Birrell, M. J. Smallwood, P. G. Winyard, T. D. Tetley and M. Emerson, *British journal of pharmacology*, 2017, 174, 2130-2139.

141. Y. Yuan, Y. V. Kaneti, M. Liu, F. Jin, D. F. Kennedy, X. Jiang, J. Huang and A. Yu, *Journal of Energy Chemistry*, 2015, 24, 660-668.

142. M. C. Biesinger, L. W. M. Lau, A. R. Gerson and R. S. C. Smart, *Applied Surface Science*, 2010, 257, 887-898.

143. T. L. Barr and S. Seal, *Journal of Vacuum Science & Technology A*, 1995, 13, 1239-1246.

144. I. Khalakhan, M. Vorokhta, X. Xie, L. Piliai and I. Matolínová, *Journal of Electron Spectroscopy and Related Phenomena*, 2021, 246, 147027.

145. B. V. Crist, *Journal*, 2019.

146. J. Chastain and R. C. King Jr, *Handbook of X-ray photoelectron spectroscopy*, 1992.

147. M. C. Biesinger, *Surface and Interface Analysis*, 2017, 49, 1325-1334.

148. K. Park, G. Tuttle, F. Sinche and S. L. Harper, *Arch Pharm Res*, 2013, 36, 125-133.

149. H. Perez, J. P. Pradeau, P. A. Albouy and J. Perez-Omil, *Chemistry of Materials*, 1999, 11, 3460-3463.

150. N. Hock, G. F. Racaniello, S. Aspinall, N. Denora, V. V. Khutoryanskiy and A. Bernkop-Schnürch, *Advanced Science*, 2022, 9, 2102451.

151. C. Albert, L. Bracaglia, A. Koide, J. DiRito, T. Lysyy, L. Harkins, C. Edwards, O. Richfield, J. Grundler, K. Zhou, E. Denbaum, G. Ketavarapu, T. Hattori, S. Perincheri, J. Langford, A. Feizi, D. Haakinson, S. A. Hosgood, M. L. Nicholson, J. S. Pober, W. M. Saltzman, S. Koide and G. T. Tietjen, *Nature Communications*, 2022, 13, 5998.

152. A. Ghosh, F. Stellacci and R. Kumar, *Catalysis Today*, 2012, DOI: 10.1016/j.cattod.2012.03.079.

153. J. Chen, B. Chang, S. Oyola-Reynoso, Z. Wang and M. Thuo, *ACS Omega*, 2017, 2, 2072-2084.

154. D. Pedone, M. Moglianetti, E. De Luca, G. Bardi and P. P. Pompa, *Chemical Society Reviews*, 2017, 46, 4951-4975.

155. Q. Guo and F. Li, *Physical Chemistry Chemical Physics*, 2014, 16, 19074-19090.

156. V. Lacour, K. Moumanis, W. M. Hassen, C. Elie-Caille, T. Leblois and J. J. Dubowski, *Langmuir*, 2019, 35, 4415-4427.

157. K. Cacua, F. Ordoñez, C. Zapata, B. Herrera, E. Pabón and R. Buitrago-Sierra, *Colloids and Surfaces A: Physicochemical and Engineering Aspects*, 2019, 583, 123960.

158. C. Dablemont, P. Lang, C. Mangeney, J.-Y. Piquemal, V. Petkov, F. Herbst and G. Viau, *Langmuir*, 2008, 24, 5832-5841.

159. M. C. Biesinger, *Applied Surface Science*, 2022, 597, 153681.

160. D. G. Castner, K. Hinds and D. W. Grainger, *Langmuir*, 1996, 12, 5083-5086.

161. G. K. Jennings and P. E. Laibinis, *Journal of the American Chemical Society*, 1997, 119, 5208-5214.

162. G. K. Jennings and P. E. Laibinis, *Colloids and Surfaces A: Physicochemical and Engineering Aspects*, 1996, 116, 105-114.

163. L. Ramin and A. Jabbarzadeh, *Langmuir*, 2011, 27, 9748-9759.

164. N. Nishi, D. Hobara, M. Yamamoto and T. Kakiuchi, *The Journal of Chemical Physics*, 2003, 118, 1904-1911.

165. J. Zhu, J. Chin, C. Wängler, B. Wängler, R. B. Lennox and R. Schirrmacher, *Bioconjugate Chemistry*, 2014, 25, 1143-1150.

166. J. Chen, S. K. Spear, J. G. Huddleston and R. D. Rogers, *Green Chemistry*, 2005, 7, 64-82.

167. W. Wang, Q. Q. Wei, J. Wang, B. C. Wang, S. H. Zhang and Z. Yuan, *J Colloid Interface Sci*, 2013, 404, 223-229.

168. N. Chandran, P. Janardhanan, M. Bayal, R. Pilankatta and S. S. Nair, *Biochimica et Biophysica Acta (BBA) - General Subjects*, 2023, 1867, 130372.

169. X. Qian, X. H. Peng, D. O. Ansari, Q. Yin-Goen, G. Z. Chen, D. M. Shin, L. Yang, A. N. Young, M. D. Wang and S. Nie, *Nat Biotechnol*, 2008, 26, 83-90.

170. Q. Xu, L. M. Ensign, N. J. Boylan, A. Schön, X. Gong, J.-C. Yang, N. W. Lamb, S. Cai, T. Yu, E. Freire and J. Hanes, *ACS Nano*, 2015, 9, 9217-9227.

171. G. Beamson and D. Briggs, *High resolution XPS of organic polymers*, Wiley, 1992.

172. A. Roy, A. K. Mukhopadhyay, S. C. Das, G. Bhattacharjee, A. Majumdar and R. Hippler, *Coatings*, 2019, 9, 551.

173. R. Cao and B. Li, *Chemical Communications*, 2011, 47, 2865-2867.

174. A. Stewart, S. Murray and S. E. J. Bell, *Analyst*, 2015, 140, 2988-2994.

175. S. F. Tan, U. Anand and U. Mirsaidov, *ACS Nano*, 2017, 11, 1633-1640.

176. H. Liao and J. H. Hafner, *Chemistry of Materials*, 2005, 17, 4636-4641.

177. H. Hegde, C. Santhosh and R. K. Sinha, *Materials Research Express*, 2019, 6, 105075.

178. L. Shen, F. Tu, Z. Shang, M. Ma, Y. Xia, Z. Zhao, L. Zhao, Z. Wang and G. Shao, *International Journal of Hydrogen Energy*, 2022, 47, 15001-15011.

179. S. Dasari and P. B. Tchounwou, *Eur J Pharmacol*, 2014, 740, 364-378.

180. N. Farrell, in *Transition Metal Complexes as Drugs and Chemotherapeutic Agents*, ed. N. Farrell, Springer Netherlands, Dordrecht, 1989, DOI: 10.1007/978-94-011-7568-5_3, pp. 46-66.

181. K. Malecka, S. Menon, G. Palla, K. G. Kumar, M. Daniels, W. Dehaen, H. Radecka and J. Radecki, *Molecules*, 2020, 25.

182. Y. Zhang, B. Newton, E. Lewis, P. P. Fu, R. Kafoury, P. C. Ray and H. Yu, *Toxicol In Vitro*, 2015, 29, 762-768.

183. N. A.-F. Aboul-Maaty and H. A.-S. Oraby, *Bulletin of the National Research Centre*, 2019, 43, 25.

184. R. Kalendar, S. Boronnikova and M. Seppänen, in *Molecular Plant Taxonomy: Methods and Protocols*, ed. P. Besse, Springer US, New York, NY, 2021, DOI: 10.1007/978-1-0716-0997-2_3, pp. 57-67.

185. H. Heinz, C. Pramanik, O. Heinz, Y. Ding, R. K. Mishra, D. Marchon, R. J. Flatt, I. Estrela-Lopis, J. Llop, S. Moya and R. F. Ziolo, *Surface Science Reports*, 2017, 72, 1-58.

186. R. Li, Z. Wang, X. Gu, C. Chen, Y. Zhang and D. Hu, *ACS Omega*, 2020, 5, 4943-4952.

187. M.-Z. Wei, T.-S. Deng, Q. Zhang, Z. Cheng and S. Li, *ACS Omega*, 2021, 6, 9188-9195.

188. J. He, S. Unser, I. Bruzas, R. Cary, Z. Shi, R. Mehra, K. Aron and L. Sagle, *Colloids and Surfaces B: Biointerfaces*, 2018, 163, 140-145.

189. P. Wand, J. D. Bartl, U. Heiz, M. Tschurl and M. Cokoja, *J Colloid Interface Sci*, 2016, 478, 72-80.

190. G. Testa, L. Fontana, I. Venditti and I. Fratoddi, *Beilstein J Nanotechnol*, 2016, 7, 1822-1828.

191. I. Venditti, C. Palocci, L. Chronopoulou, I. Fratoddi, L. Fontana, M. Diociaiuti and M. V. Russo, *Colloids and Surfaces B: Biointerfaces*, 2015, 131, 93-101.

192. I. Venditti, G. Testa, F. Sciubba, L. Carlini, F. Porcaro, C. Meneghini, S. Mobilio, C. Battocchio and I. Fratoddi, *The Journal of Physical Chemistry C*, 2017, 121, 8002-8013.

193. H. Nagao, M. Ichiji and I. Hirasawa, *Chemical Engineering & Technology*, 2017, 40, 1242-1246.

194. A. Sharonova, K. Loza, M. Surmeneva, R. Surmenev, O. Prymak and M. Epple, *IOP Conference Series: Materials Science and Engineering*, 2016, 116, 012009.

195. W. Tu, K. Takai, K.-i. Fukui, A. Miyazaki and T. Enoki, *The Journal of Physical Chemistry B*, 2003, 107, 10134-10140.

196. K. V. Sarathy, G. Raina, R. T. Yadav, G. U. Kulkarni and C. N. R. Rao, *The Journal of Physical Chemistry B*, 1997, 101, 9876-9880.

197. K. Vijaya Sarathy, G. U. Kulkarni and C. N. R. Rao, *Chemical Communications*, 1997, DOI: 10.1039/A700738H, 537-538.

198. M. J. Mitchell, M. M. Billingsley, R. M. Haley, M. E. Wechsler, N. A. Peppas and R. Langer, *Nature Reviews Drug Discovery*, 2021, 20, 101-124.

199. G. Vales, S. Suhonen, K. M. Siivola, K. M. Savolainen, J. Catalán and H. Norppa, *Nanomaterials*, 2020, 10, 271.

200. E. Okoampah, Y. Mao, S. Yang, S. Sun and C. Zhou, *Colloids and Surfaces B: Biointerfaces*, 2020, 196, 111312.

201. N. M. Schaeublin, L. K. Braydich-Stolle, A. M. Schrand, J. M. Miller, J. Hutchison, J. J. Schlager and S. M. Hussain, *Nanoscale*, 2011, 3, 410-420.

202. J. Bi, T. Li, H. Ren, R. Ling, Z. Wu and W. Qin, *Journal of Chromatography A*, 2019, 1594, 208-215.

203. Q. Lai, Y. Liu, L. Ge, Y. Yang, X. Ji and Z. He, *Analytical Methods*, 2021, 13, 2092-2098.

204. H. Tan, T. Zhan and W. Y. Fan, *The Journal of Physical Chemistry B*, 2006, 110, 21690-21693.

205. I. A. Mudunkotuwa and V. H. Grassian, *Journal of the American Chemical Society*, 2010, 132, 14986-14994.

206. R. P. Vasquez, *Surface Science Spectra*, 1998, 5, 279-284.

207. Y. Wu, K. X. Vazquez-Prada, Y. Liu, A. K. Whittaker, R. Zhang and H. T. Ta, *Nanotheranostics*, 2021, 5, 499-514.

208. X. Hu, Y. Zhang, T. Ding, J. Liu and H. Zhao, *Frontiers in Bioengineering and Biotechnology*, 2020, 8.

209. M. Fathi-Achachelouei, H. Knopf-Marques, C. E. Ribeiro da Silva, J. Barthès, E. Bat, A. Tezcaner and N. E. Vrana, *Frontiers in Bioengineering and Biotechnology*, 2019, 7.

210. E. C. Wang and A. Z. Wang, *Integr Biol (Camb)*, 2014, 6, 9-26.

211. K. Sasaki, M. Shao and R. Adzic, in *Polymer Electrolyte Fuel Cell Durability*, eds. F. N. Büchi, M. Inaba and T. J. Schmidt, Springer New York, New York, NY, 2009, DOI: 10.1007/978-0-387-85536-3_2, pp. 7-27.

212. C. McGuinnes, R. Duffin, S. Brown, L. M. N, I. L. Megson, W. Macnee, S. Johnston, S. L. Lu, L. Tran, R. Li, X. Wang, D. E. Newby and K. Donaldson, *Toxicol Sci*, 2011, 119, 359-368.

213. Y. Wang, J. E. Q. Quinsaat, T. Ono, M. Maeki, M. Tokeshi, T. Isono, K. Tajima, T. Satoh, S.-i. Sato, Y. Miura and T. Yamamoto, *Nature Communications*, 2020, 11, 6089.

214. J. W. Weisel and R. I. Litvinov, *Subcell Biochem*, 2017, 82, 405-456.

215. O. M. Alshehri, C. E. Hughes, S. Montague, S. K. Watson, J. Frampton, M. Bender and S. P. Watson, *Blood*, 2015, 126, 1601-1608.

216. S. P. Watson, J. M. Auger, O. J. McCarty and A. C. Pearce, *J Thromb Haemost*, 2005, 3, 1752-1762.

217. J. Rayes, S. P. Watson and B. Nieswandt, *J Clin Invest*, 2019, 129, 12-23.

218. P. A. Smethurst, D. J. Onley, G. E. Jarvis, M. N. O'Connor, C. G. Knight, A. B. Herr, W. H. Ouwehand and R. W. Farndale, *Journal of Biological Chemistry*, 2007, 282, 1296-1304.

219. H. Jung and D. B. Kittelson, *Aerosol Science and Technology*, 2005, 39, 1129-1135.

220. V. Pavlovic, M. Ciric, V. Jovanovic and P. Stojanovic, *Open Med (Wars)*, 2016, 11, 242-247.

221. P. Höök, R. I. Litvinov, O. V. Kim, S. Xu, Z. Xu, J. S. Bennett, M. S. Alber and J. W. Weisel, *Scientific Reports*, 2017, 7, 13001.

222. K. Nienhaus and G. U. Nienhaus, *Small*, 2023, 19, 2301663.

223. M. Havrdova, K. Polakova, J. Skopalik, M. Vujtek, A. Mokdad, M. Homolkova, J. Tucek, J. Nebesarova and R. Zboril, *Micron*, 2014, 67, 149-154.

224. J. Arblaster, *Platinum Metals Review*, 1994, 38, 119-125.

Chapter 11 Appendix

11.1 Platinum nanoparticles surface area calculations

The total surface area/mL of the PtNPs were calculated for surface modification and platelet experiments. The example below shows the calculations of 20 nm PtNPs on 10x reaction scale (reaction volume 305.5 mL) using 0.2 M $H_2PtCl_6.6H_2O$. Calculations were made in the following sequence.

Moles of platinum seeds

The moles of the Pt seeds were first calculated and included into the PtNP surface area calculations. 4 nm Pt seeds were synthesized using 17.42 mL of 0.2% (w/v) H_2PtCl_6, total reaction volume was 250 mL. The molar concentration of H_2PtCl_6 was calculated as follows:

$H_2PtCl_6.6H_2O$ was converted molar concentration.

$$\frac{0.2\ g}{100\ mL} \times \frac{10}{10} = \frac{2\ g}{1L}$$

The moles of $H_2PtCl_6.6H_2O$ stock solution were calculated using the weight of and molar mass of $H_2PtCl_6.6H_2O$ 517.90 g/mol using Equation 11.1.

$$moles = \frac{mass}{molar\ mass} \qquad \text{Equation 11.1}$$

$$moles = \frac{2\ g}{517.90\ g/mol} = 0.00386\ moles$$

The molar concentration was calculated as follows:

$$Molar\ concentration\ = \frac{moles}{Volume} \rightarrow \frac{0.00386}{1\ L} = 0.00386\ M\ or\ 3.86\ mM \qquad \text{Equation 11.2}$$

In the reaction, the moles of $H_2PtCl_6.6H_2O$ were calculated using Equation 11.3 as follows:

$$moles = stock\ molar\ concentration\ \times\ volume \qquad \text{Equation 11.3}$$

$$moles = 3.86\ mM\ \times\ 17.42\ mL$$
$$moles =\ 3.86\ \times\ 10^{-3}\ (mol/L)\ \times\ 1.74\ \times\ 10^{-2}\ (L)$$
$$moles =\ 6.73\ \times\ 10^{-5}\ (mol)$$

The moles of platinum (Pt) can be calculated using the moles of $H_2PtCl_6.6H_2O$, as the moles of $H_2PtCl_6.6H_2O$ is equal to the moles of platinum, see Equation 7.4 below:

$$H_2PtCl_6.6H_2O + 2\ NaBH_4 + 6H_2O \rightarrow Pt + 2B(OH)_3 + 6H_2 + 4HCl + 2NaCl \qquad \text{Equation 11.4}$$

The moles of $H_2PtCl_6.6H_2O$ are equal to the moles of platinum (Pt):

$$6.73\ \times\ 10^{-5}\text{moles}\ H_2PtCl_6.6H_2O =\ 6.73\ \times\ 10^{-5}\text{moles}\ Pt$$

As 10 mL of Pt seeds was used for the PtNP synthesis reaction, the moles of 1 mL of Pt seeds were calculated using Equation 11.3, see below:

$$moles = \frac{10\ mL}{250\ ml}\ \times\ 6.73\ \times\ 10^{-5}\ mol$$
$$moles =\ 2.69\ \times\ 10^{-6}$$

Moles of platinum nanoparticles

20 nm PtNPs were synthesized using 10 mL of 4 nm Pt seeds (template) with 450 µL of 0.2 M $H_2PtCl_6.6H_2O$, the total reaction volume was 305.5 mL. Equation 11.3 to calculate the moles of Pt.

$$moles = 0.2\ M\ \times\ 450\ \mu L$$
$$moles =\ 0.2\ (mol/L)\ \times\ 4.50\ \times\ 10^{-4}\ (L)$$
$$moles =\ 9.00\ \times 10^{-5}\ (mol)$$

The concentration of $H_2PtCl_6.6H_2O$ is equal to the Pt concentration:

$$9.00 \times 10^{-5}\text{moles } H_2PtCl_6.6H_2O = 9.00 \times 10^{-5}\text{moles } Pt$$

Total moles of Pt from both reactions were calculated with Equation 11.5:

$$Total\ moles = moles\ of\ Pt\ seeds + moles\ of\ Pt\ from\ PtNP\ synthesis \quad \text{Equation 11.5}$$

$$Total\ moles = 2.69 \times 10^{-6} + 9.00 \times 10^{-5}$$

$$Total\ moles = 9.27 \times 10^{-5}$$

Number of platinum atoms

The total number of atoms of platinum were calculated using Equation 11.6:

$$Number\ of\ atoms = Number\ of\ moles\ x\ Avogradro's\ number \quad \text{Equation 11.6}$$

$$Number\ of\ Pt\ atoms = 9.27 \times 10^{-5}\ moles \times 6.023 \times 10^{23}\ (\frac{1}{mol})$$

$$Number\ of\ Pt\ atoms = 5.58 \times 10^{19}\ mol$$

Average platinum nanoparticle volume

The mean diameter of the PtNP was determined by TEM as 21.9 nm, the volume was calculated using the volume of a sphere, see Equation 11.7.

$$V = \frac{4}{3}\pi r^3 = \frac{1}{6}\pi d^3 \quad \text{Equation 11.7}$$

V is the volume, is Pi, is the radius and is the diameter.

$$V = \frac{1}{6} \times \pi \times (21.9\ nm)^3$$

$$V = 5.50 \times 10^3\ nm^3$$

Average nanoparticle mass

Using the density of Pt and the average volume of a PtNP calculated above, the average particle mass was calculated using the density equation:

$$\rho = \frac{m}{V} \qquad \text{Equation 11.8}$$

ρ is the density, m is the mass and V is the volume. The equation was rearranged to find the mass:

$$m = \rho \times V$$

The density of Pt is 21.45 g/cm^3,[227] this was converted from g/cm^3 to g/nm^3

$$d_{Pt} = \frac{21.45\ g/cm^3}{1 \times 10^{21} nm^3/cm^3}$$

$$d_{Pt} = 2.145 \times^{-20} g/nm^3$$

Then

$$m_{NP} = 2.145 \times 10^{-20}\ g/nm^3 \times 5.50 \times 10^3\ nm^3$$

$$m_{NP} = 1.18 \times 10^{-16}\ g$$

Moles of platinum moles per nanoparticle and number of atoms per nanoparticle

With the average mass of the PtNPs, the moles of Pt per nanoparticle was calculated with Equation 11.1 the Pt moles per NP was calculated as follows:

$$moles_{Pt\ per\ NP} = \frac{1.18 \times 10^{-16}\ g}{195.08\ g/mol}$$

$$moles_{Pt\ per\ NP} = 6.05 \times 10^{-19}\ mol$$

Using the Pt moles per NP, the number of atoms per platinum nanoparticle was calculated using Avogadro's number.

$$Number\ of\ atoms\ per\ PtNP = 6.05 \times 10^{-19} moles \times 6.023 \times 10^{23} (\frac{1}{moles})$$

$$Number\ of\ atoms\ per\ PtNP = 3.64 \times 10^{5}$$

Number of nanoparticles in the reaction

The number of NP in the reaction was calculated using the number of atoms per PtNP nanoparticle and platinum moles, see equation:

$$Number\ of\ NPs\ in\ reaction = \frac{Number\ of\ Pt\ atoms\ \ in\ reaction}{Number\ of\ Pt\ atmos\ per\ NP}$$ Equation 11.9

$$Number\ of\ nanoparticles\ in\ reaction = \frac{5.58 \times 10^{19}\ mol}{3.64 \times 10^{5}\ mol}$$

$$Number\ of\ nanoparticles\ in\ reaction = 1.53 \times 10^{14}$$

Surface area of nanoparticle

The surface area of the nanoparticles (was calculated from the average TEM diameter 21.9 nm and the equation for the area of a sphere, Equation 11.10

$$A = 4\pi r^2 = \pi d^2$$ Equation 11.10

is the area, is Pi and is the radius, the diameter was 21.9 nm

$$A = \pi \times (21.9\ nm)^2$$

$$A = S_{NP} = 1506.74\ nm^2$$

Total surface area of nanoparticle

The total surface area of the platinum nanoparticle was calculated as with Equation 11.11:

$$S_T = S_{NP} \times No_{NP}$$ Equation 11.11

Where: is the total surface area, is the average surface area of a nanoparticle and is the number of nanoparticles in the reaction.

$$S_T = S_{NP} \times No_{NP}$$
$$S_T = 1506.74\,nm^2 \times 1.53 \times 10^{14}$$
$$S_T = 2.31 \times 10^{17}\,nm^2$$

Surface area per mL

The surface area per mL was calculated using the total reaction volume of 305.50 mL as follows:

$$Surface\ area/mL = \frac{2.31 \times 10^{17}\,nm^2}{305.50\,mL}$$
$$Surface\ area/mL = 7.56 \times 10^{14}\,nm^2/mL$$

11.2 Surface coverage of nanoparticles by alkanethiols calculations

For surface modification experiments, the surface coverage by alkanethiols was calculated using the total surface area of a batch 20 nm PtNP, the alkanethiol footprint 0.214 nm^2 and Avogadro's number. The alkanethiol footprint was obtained by experimental data from Strong and Whitesides 1988.[158]

The total surface previously calculated to be 1506.74 nm^2, the number of alkanethiol molecules occupying each PtNP was calculated as shown below in Equation 11.12:

$$Alkanethiol\ molecules\ on\ each\ PtNP = \frac{Surface\ area\ of\ nanoparticle\ nm^2}{Alkanethiol\ footprint\ nm^2}$$ Equation 11.12

$$Alkanethiol\ molecules\ on\ each\ PtNP = \frac{1506.74\,nm^2}{0.214\,nm^2}$$

$$Alkanethiol\ molecules\ on\ each\ PtNP = 7041$$

Thus, 7041 molecules will occupy each 20 nm PtNP. The molar concentration of alkanethiol required for surface coverage was determined using the previously calculated number of nanoparticles per reaction, Avogadro's constant and the number of alkanethiol molecules on each PtNP. First, the number of nanoparticles per reaction was calculated nanoparticles per mL using total reaction volume of 305.50 mL, see Equation 11.13.

$$Nanoparticles/mL = \frac{Number\ of\ NP\ in\ reaction}{Total\ reaction\ volume} \qquad \text{Equation 11.13}$$

$$Nanoparticles/mL = \frac{1.53 \times 10^{14}}{305.50\ mL}$$

$$Nanoparticles/mL = 5.02 \times 10^{11}$$

$$Nanoparticles/L = 5.02 \times 10^{11} \times 1000$$

$$Nanoparticles/L = 5.02 \times 10^{14}$$

The molar concentration was calculated using equation 11.14 as follows:

$$Molar\ concentration = \frac{Nanoparticles/L \times Avogrado's\ constant}{Number\ of\ alkanethiol\ molecules} \qquad \text{Equation 11.14}$$

$$Molar\ concentration = \frac{5.02 \times 10^{14} \times 6.02 \times 10^{23}}{7041}$$

$$Molar\ concentration = 5.9\ \mu M$$

For surface modification experiments, a 10x was used to ensure full surface coverage.

$$Molar\ concentration = 5.9\ \mu M \times 10$$

$$Molar\ concentration = 59\ \mu M$$

For experiments with PEGylated thiols the PEG footprint of 0.35 nm^2 was obtained from Qian et al 2008.[129] TA and 6-ATA footprints were derived using Chem3D, where the approximate width of both molecules was found, the square of the value was taken to get an approximate footprint. The footprint of TA and 6-ATA were approximated at 0.428 nm^2 and 0.145 nm^2 respectively. Surface coverage calculations of alkane and pegylated thiols are shown in Table 11.1 to Table 11.8

Table 11.1 Surface coverage calculations for PtNP with 6-mercaptohexanoic acid (6-MHA)

Average PtNP diameter (nm)	21.9
Pi	3.14
Total surface area (nm^2)	1506.74
Thiol footprint of 6-MHA (nm^2)	0.214
Molecules of 6-MHA on each PtNP	7040.84
Number of nanoparticles/mL	5.02×10^{11}
Number of nanoparticles/L	5.02×10^{14}
Avogadro's number	6.02×10^{23}
Molar concentration (M)	5.9×10^{-6}
Molar concentration 10x excess	5.9×10^{-5}

Table 11.2 Surface coverage calculations for PtNP with 8-mercaptooctanoic acid (8-MOA)

Average PtNP diameter (nm)	21.9
Pi	3.14
Total surface area (nm^2)	1506.74
Thiol footprint of 6-MHA (nm^2)	0.214
Molecules of 6-MHA on each PtNP	7040.84
Number of nanoparticles/mL	5.02×10^{11}
Number of nanoparticles/L	5.02×10^{14}
Avogadro's number	6.02×10^{23}
Molar concentration (M)	5.9×10^{-6}
Molar concentration 10x excess	5.9×10^{-5}

Table 11.3 Surface coverage calculations for PtNP with thioctic acid (TA)

Average PtNP diameter (nm)	21.9
Pi	3.141592654
Total surface area (nm^2)	1506.74
Thiol footprint of TA (nm^2)	0.428
Molecules of TA on each PtNP	3520.419
Number of nanoparticles/mL	5.02×10^{11}
Number of nanoparticles/L	5.02×10^{14}
Avogadro's number	6.023×10^{23}
Molar concentration (M)	2.9×10^{-6}
Molar concentration 10x excess	2.9×10^{-5}

Table 11.4 Surface coverage calculations for PtNP with O-(2-carboxyethyl)-O'-(2-mercaptoethyl)heptaethylene glycol (2-MOHA)

Average PtNP diameter (nm)	21.9
Pi	3.141592654
Total surface area (nm^2)	1506.74
Thiol footprint of EG7-COOH (nm^2)	0.35
Molecules of EG6-OH on each PtNP	4304.969
Number of nanoparticles/mL	5.02×10^{11}
Number of nanoparticles/L	5.02×10^{14}
Avogadro's number	6.023×10^{23}
Molar concentration (M)	3.59×10^{-6}
Molar concentration 10x excess	3.59×10^{-5}

Table 11.5 Surface coverage calculations for PtNP with (6-aminohexyl)trimethylammonium bromide hydrobromide (6-ATA)

Average PtNP diameter (nm)	50.2
Pi	3.141592654
Total surface area (nm^2)	7916.94
Theoretical footprint of 6-ATA (nm^2)	0.147
Molecules of 6-ATA on each PtNP	53856.729
Number of nanoparticles/mL	5.02×10^{11}
Number of nanoparticles/L	5.02×10^{14}
Avogadro's number	6.023×10^{23}
Molar concentration (M)	4.5×10^{-5}
Molar concentration 10x excess	4.5×10^{-4}

Table 11.6 Surface coverage calculations for PtNP with 6-mercaptohexanol

Average PtNP diameter (nm)	21.9
Pi	3.141592654
Total surface area (nm^2)	1506.74
Thiol footprint of 6-MHA (nm^2)	0.214
Molecules of 6-MHA on each PtNP	7040.838
Number of nanoparticles/mL	5.02×10^{11}
Number of nanoparticles/L	5.02×10^{14}
Avogadro's number	6.023×10^{23}
Molar concentration (M)	5.9×10^{-6}
Molar concentration 10x excess	5.9×10^{-5}

Table 11.7 Surface coverage calculations for PtNP with 2-{2-[2-(2-mercaptoethoxy)ethoxy]ethoxy}ethanol (2-MEE)

Average PtNP diameter (nm)	22.6
Pi	3.141592654
Total surface area (nm^2)	1604.60
Thiol footprint of EG6-OH (nm^2)	0.35
Molecules of EG6-OH on each PtNP	4584.571
Number of nanoparticles/mL	4.57×10^{11}
Number of nanoparticles/L	4.57×10^{14}
Avogadro's number	6.023×10^{23}
Molar concentration (M)	3.48×10^{-6}
Molar concentration 10x excess	3.48×10^{-5}

Table 11.8 Surface coverage calculations for PtNP with 11-mercaptoundecyl)hexa(ethylene glycol) (11-MUHEG)

Average PtNP diameter (nm)	22.6
Pi	3.141592654
Total surface area (nm^2)	1604.60
Thiol footprint of EG7-COOH (nm^2)	0.35
Molecules of EG6-OH on each PtNP	4584.571
Number of nanoparticles/mL	4.57×10^{11}
Number of nanoparticles/L	4.57×10^{14}
Avogadro's number	6.023×10^{23}
Molar concentration (M)	3.48×10^{-6}
Molar concentration 10x excess	3.48×10^{-5}

11.3 PtNP preparation for platelet experiments

For platelet aggregation experiments, the concentration of the PtNPs were calculated as follows:

$$Molar\ concentration\ = (9.27\ \times\ 10^{-5}/305.5)/1000$$

$$Molar\ concentration = 3.03\ \times\ 10^{-4}$$

$$Mass\ in\ reaction\ (g) = 9.27\ \times\ 10^{-5}\ \times\ 195.1$$

$$Mass\ in\ reaction\ (g) = 1.81\ \times\ 10^{-2}$$

$$Molar\ concentration\ (g/mL) = \frac{1.81\ \times\ 10^{-2}}{305.5}$$

$$Molar\ concentration\ (g/mL) = 5.92\ \times\ 10^{-5}$$

$$Molar\ concentration\ (g/mL) = 5.92\ \times\ 10^{-5}\ \times 1000$$

$$Molar\ concentration\ (mg/mL) = 5.92\ \times\ 10^{-2}$$

$$Molar\ concentration\ (\mu g/mL) = 5.92\ \times 10^{1}$$

A 10 mL aliquot of 20 nm PtNPs was concentrated by centrifugation. The supernatant was discarded, and the remaining nanoparticles were resuspended in 100 µL.

$$Molar\ concentration\ (mg/mL) = 5.92$$

For PtNP-platelet experiments the stock concentration of c-PtNPs and the functionalised PtNPs was 5.92 mg/mL, PtNPs were diluted down to 1/100 for platelet aggregations and western blots, bringing the final concentration to 59.2 µg/mL.